Single-Molecule Imaging of Electroporated Chemotaxis Proteins in Live Bacteria

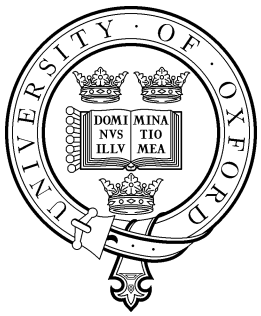

Diana Di Paolo

St Catherine's College

University of Oxford

Thesis submitted in partial fulfillment of the requirements for the degree of *Doctor of Philosophy* at the University of Oxford

Michaelmas Term, 2015

"Life is not easy for any of us. But what of that?
We must have perseverance and, above all,
confidence in ourselves.
We must believe that we are gifted for something
and that this thing must be attained."

1937, Marie Curie

Abstract

Single-Molecule Imaging of Electroporated Chemotaxis Proteins in Live Bacteria

Diana Di Paolo

St Catherine's College, University of Oxford

Submitted for the degree of Doctor of Philosophy, Michaelmas Term 2015

Many species of motile bacteria use rotating extracellular filaments to propel themselves through liquid media. Each filament is driven by a membrane spanning rotary nano-machine called the bacterial flagellar motor. In *Escherichia coli* and *Rhodobacter sphaeroides* the motor is powered by a transmembrane flux of H^+ and the chemical energy is converted into work through a ring of stator units pushing on a central rotor.

Chemotaxis is the biasing of movement towards regions that contain higher concentrations of beneficial, or lower concentrations of toxic, chemicals and is one of the most well-understood bacterial sensory pathways. Upon phosphorylation, the response regulator protein CheY transduces changes of environmental chemical gradients detected by specific transmembrane chemoreceptors to the flagellar motors: it binds to the N-terminus of the FliM proteins in the C-ring part of the motor inducing a cascade of conformational changes that modulate the direction of rotation (in *E. coli*) or the motor stopping (in *R. sphaeroides*).

In this project, a novel technique for protein internalisation in live bacteria based on electroporation and single-molecule imaging using a custom-built microscope are combined to perform an in-depth investigation of the interactions between wild type and mutant chemotaxis proteins, chemoreceptors and the motor complex *in vivo*.

Chemotaxis proteins are purified, labelled with organic dyes and inserted into live *E. coli* and *R. sphaeroides* cells by electroporation. In typical experiments exploiting this new capability, video fluorescence microscopy shows single molecules diffusing within cells, interacting with the sensory clusters and individual flagellar motors. The work described in this thesis allows for the first time imaging and tracking of single dye-labelled chemotaxis proteins performing their function as response regulators in real time. Diffusion as well as relevant binding constants and dwell times at each end of their journey are measured, providing also a comparison of such quantities across different protein mutants, genetic backgrounds and environmental conditions.

Declaration

The work in this thesis was undertaken at the University of Oxford in the Clarendon Laboratory, Department of Physics, and in the Department of Biochemistry. Work was performed from October 2012 to December 2015 under the supervision of Dr R. M. Berry. All the work in this thesis is my own unless stated and has not been submitted for a degree at this or any other University.

Acknowledgements

Firstly, I would like to express my sincere gratitude to my supervisor, Dr. Richard Berry, for having given me since the DTC short project and then on into the DPhil adventure constant guidance, continuous support and invaluable help in both experimental design and results' interpretation. Thank you for having always encouraged my research, maintained confidence in me, and allowed me to grow as a research scientist as well as a person. I have always admired your enthusiasm and critical approach to science, and am grateful to you for granting me the academic freedom to choose my own lines of inquiry and spend quite a big chunk of the DPhil exploring the new-for-me field of Biochemistry.

Secondly, I would like to thank everyone that has somehow helped me getting through those days in the lab when nothing was working or those times when MATLAB would not cooperate to analyse my data, making these set backs more easily bearable and helping me getting over them with both fruitful discussions and amusing distractions: the lovely people of the Berry, Kapanidis and Armitage labs, past and present, thank you all for sharing your knowledge and expertise with me as well as for the chatty coffee breaks, dance playlists in the lab, not to mention the one-year-old but already beloved Beaujolais Thursdays' tradition. A particular mention goes to Andrea, Matt, Chris, Marta and Caroline: my DPhil years would not have been the same without you guys.

Too many friends' names I would like to include in these acknowledgements. Most of them are sadly not in Oxford anymore and have gone on onto better (I hope) things, but nevertheless the thought of them arises from my heart and soul in this occasion. The families of the St. Cross and St. Catherine's Colleges MCRs, of the Oxford Females in Engineering, Science and Technology, of the Oxford Women in Physics and, of course, of the Oxford Italian Society have been a great home away from home for me during my life here, providing me with unique experiences and memories, which I will always treasure.

Paolo never wrote his thesis' acknowledgements, but definitely deserves a special place in these. He has been by my side from the very beginning of my DPhil, living and sharing with me through all of these years every single success and defeat, either academic or personal. Despite a distance of over 500 miles, he has always helped me getting over the hard times, finally managing to get us reunited in Oxford just in time to see me accomplishing such a big achievement as becoming a Doctor. He is a great physicist and a great person and I do hope that whatever the future holds for us we will be able to live it together "in the best of the possible worlds".

Finally, and most importantly, a huge *grazie* to my parents Carla and Antonio and to my (not-so-)little brother Edoardo. They haven't for once, even in the most difficult moments, stopped supporting me, encouraging me to pursuit my studies and my passions and believing in my capabilities. Without their love and their confidence in me there is absolutely no way I would be here today writing these lines.

Contents

List of Figures

List of Tables

Abbreviations

Amp	ampicillin
bp	base pairs
BF	bright-field
BFM	bacterial flagellar motor
CCD	charged coupled device
CCW	counter-clockwise
CFP	cyan fluorescent protein
CM	chloramphenicol
CW	clockwise
DIC	differential interference microscopy
DMSO	dimethyl sulphoxide
DNA	deoxyribonucleic acid
dNTP	deoxynucleoside 5'-phosphate
ds	double stranded
DTT	dithiothreitol
EP	electroporation/electroporated
FOV	field of view
FP	fluorescent protein
GFP	green-fluorescent protein
IPTG	isopropyl β-D-thiogalactosidase
Kan	kanamycin
kb	kilobase
K_D	Dissociation constant
kDa	kilo Dalton
LB	Luria-Bertani
LBA	Luria-Bertani agar
MB	motility buffer
MilliQ	ultrapure water
MSD	mean squared displacement
MCP	methyl-accepting chemotaxis protein
NA	numerical aperture
Nal	nalidixic acid

NEP	non-electroporated
Ni-NTA	nickel-nitrilotriacetic acid
OD_{600nm}	optical density at 600nm
OD_{700nm}	optical density at 700nm
PAGE	polyacrylamide gel electrophoresis
PBS	phosphate buffered saline
PCR	polymerase chain reaction
PMF	proton motive force
PSF	point spread function
RT	room temperature
SDS	sodium dodecyl sulphate
SOC	super optimal broth with catabolite repression
SUX	succinate medium
TB	tryptone broth
TCEP	tris(2-carboxyethyl)phosphine
TIRF	total internal reflection fluorescence
TRIS	2-amino-2-(hydroxymethyl)-1, 3-propandiol
UV	ultraviolet
WT	wild type
YFP	yellow fluorescent protein

Preamble

Many species of bacteria sense their environment and exploit rotating *flagella*, protruding from the cell body, to swim towards favourable conditions for growth and colonisation[1]. Directed movement is a signature of life, and essential to movement is the ability to generate force. In biological systems, this force is generated by motor proteins, which convert chemical energy into work and are responsible for motility across many levels, from intracellular transport to motion of an individual cell in its surroundings and in multi-cellular aggregates[2]. The bacterial flagellar motor is one of nature's most amazing and well-studied systems, an exquisite example of how directed motion can be generated by nanometre-scale devices[3]. It is nowadays a test-case in Biophysics for probing the properties of biomolecular motors, either because it can be genetically modified relatively easily, allowing for fluorescent labelling of its components, or because its function can be monitored in live cells in real time by direct observation of motor rotation in a light microscope. Furthermore, it is becoming clearer and clearer that bacteria are highly structurally organized, and that some protein components of macromolecular complexes, like the flagellar motor, are not fixed, but show dynamic exchange in response to a range of cellular signals. To understand both the role and mechanisms of protein exchange it is essential to study the behaviour of proteins in living bacterial cells. The preferred method of investigation in the last two decades has been the use of genetically fused fluorescent proteins (FPs); this has been widely and successfully exploited, but suffers from a number of serious limitations: in fact, not all fusions are fully functional,

making the interpretation of the data often cumbersome and narrowing the pool of proteins available for study; moreover, FPs are quite bulky and may interfere with the function of the wild type protein; finally, their chromophores usually have short half lives compared with the time scales of the biological processes under examination, requiring the inferral of protein global behaviour from a large number of very short individual tracks[4]. For many years researchers have been trying to find smaller, more stable fluorophores that could be used inside living cells. A new method recently developed in Oxford offers the exciting possibility of a new generation of single-molecule *in vivo* fluorescent labelling experiments in live bacteria[5]: purified proteins are labelled with organic dyes and put back into cells in small numbers using *electroporation*, a modification of a method that is well established for DNA transformation. The goal of the work described herein is to image and track single molecules of wild type and mutant chemotaxis proteins, in particular the response regulator CheY, labelled with organic dyes and re-introduced into live *Escherichia coli* and *Rhodobacter Sphaeroides* by electroporation. While performing their function as response regulators between the chemoreceptor clusters and the flagellar motors, the CheY diffusion coefficients, binding constants and dwell times at each end of this journey will be measured and compared for different environmental conditions and genetic backgrounds.

This thesis is organized as follows: **Chapter 1** starts with a general introduction to motility in prokaryotes, gives an overview of the structure and mechanism of the bacterial flagellar motor, explains the general concept of bacterial chemotaxis and illustrates chemotactic pathways in the two species of interest for this work, *E. coli* and *R. sphaeroides*; **Chapter 2** contains a comprehensive description of the materials and methods used, from molecular biology through protein purification and labelling to microscopy techniques employed to image cellular samples, either in bright-field or in fluorescence. **Chapter 3** explains how the principle of electropor-

ation was applied in this work and what precautions were taken during creation of the labelled protein samples; **Chapter 4** gives statistics on internalisation efficiency and summarises viability studies' results. **Chapter 5** includes a detailed description and analysis of the single-molecule colocalisation and motility experiments carried out in *E. coli*. In **Chapter 6** the main results of this thesis are reported, with estimation of diffusion coefficients and binding kinetics of different CheY mutants in three background strains and in the presence or absence of chemotactic stimuli. Finally, in **Chapter 7** the electroporation approach is extended to *R. sphaeroides*, and the encouraging preliminary results obtained for this species are illustrated. Immediate remarks and conclusions are provided for the reader's convenience in the Discussion/Summary sections in each chapter, with the broader implications of this work addressed in **Chapter 8**.

Chapter 1

Introduction

1.1 Motility in prokaryotes

The ability of an organism to self-propel is called motility. Some bacteria are non-motile, relying entirely upon Brownian motion for dispersal. Motile bacteria, instead, have the capability to adapt to varying environments by moving towards suitable areas for survival, a process known as *taxis*. They can swim away from toxic substances and toward nutrients (chemotaxis, more in section 1.3), optimal light (phototaxis) and oxygen (aerotaxis) concentrations. Genes for motility have been identified in over 50% of sequenced bacterial species[6]. Motile bacteria move through liquids or over moist surfaces exploiting an impressive diversity of motility mechanisms (reviewed in 7). Gliding and twitching refer to movement across solid substrates while swimming refers to movement through aqueous environments.

Gliding motility

Gliding is defined as the *"translocation along solid bodies ... during which no wriggling, contraction or peristaltic alterations are visible, the change of shape being*

restricted to bending ..."[8] and can be achieved by different bacterial species via a number of different mechanisms. Cells of *Flavobacterium johnsoniae* rely on proteins that are unique to the phylum *Bacteroidetes*, the motility adhesins SprB and RemA, which interact with the surface resulting in translocation of the cell. SprB and RemA are delivered to the cell surface by the type IX secretion system (T9SS). T9SSs are confined to but common in the phylum *Bacteroidetes*. Transmembrane components of the T9SS may perform roles in both secretion and gliding motility[9]. *Mycoplasma mobile* forms gliding machinery at a cell pole and glides continuously in the direction of the cell pole at up to 4.5 μm per second on solid surfaces. *M. mobile* uses ATP energy to repeatedly catch, pull, and release sialylated oligosaccharides on host cells with its approximately 50 nm long legs. This system may have developed from an accidental combination between an adhesin and a rotary ATPase, both of which are essential for the adhesive parasitic life of *Mycoplasmas*[10]. In the *myxobacteria*, gliding motility is called Adventurous, or A-motility, because it can drive the movement of isolated bacteria, even when pili are not present. A-motility appears to require the secretion of slime; in *myxobacteria* these include a viscous polysaccharide gel[11]. An early model for myxobacterial gliding suggested that the cell was driven by the hydration and extrusion of slime from protein 'nozzles' that cluster mostly at the cell poles[11]. However, recent experimental data suggest that the motion of internal proteins rather than the extrusion of polysaccharides drives cell movement[12].

Twitching motility

Twitching motility is driven by the extension, adhesion, and retraction of fibrous cellular protrusions called Type IV pili (fine filaments, 6 nm in diameter with lengths that might exceed 10 μm). In *Myxococcus xanthus* this is called Social, or S-motility, since the extended pili stick not only to the substrate but also to other cells, and

so are important for coordinated group movements of the bacteria. Microbes performing this type of motility include proteobacteria such as *Neisseria gonorrhoeae*, *Pseudomonas aeruginosa* and *Myxococcus xanthus*, unicellular and filamentous cyanobacteria such as *Nostoc punctiforme* and those belonging to the *Synechocystis* sp. PCC6803, and Gram-positive (i.e. lacking an outer membrane but having a much thicker peptidoglycan layer) bacteria such as *Clostridia*[13–15].

Flagellate motility

Swimming in a liquid medium is usually accomplished by flagellate motility, which is the type of motility relevant to the work described in this thesis. It involves one or more helical surface appendages, about 20 nm in diameter and up to 10 μm long, called flagella (sing. flagellum) or filaments, protruding from the cell body and turned like a screw by a rotary motor embedded in the cell membrane. The bacterial flagellar motor is described in detail in section 1.2. There are mainly four different types of flagellar arrangements, illustrated in Figure 1.1:

- Monotrichous: a single flagellum protruding from either polar, sub-polar, or random position (e.g. *R. sphaeroides*, *P. aeruginosa*, *Vibrio cholerae* and *Vibrio alginolyticus*);
- Lophotrichous: several flagella (tuft) protruding from one or both poles of the cell (e.g. *Helicobacter pylori* and *Alcaligenes faecalis*);
- Amphitrichous: a single flagellum (or multiple flagella) protruding from both cell poles (e.g. *Spirillum volutans* and other bacteria of the *Spirillum* genus);
- Peritrichous: multiple flagella randomly distributed over the entire cell body (e.g. *E. coli*, *Salmonella typhimurium* and *Bacillus subtilis*).

Comprising in *E. coli* 1% of the proteome and about 2% of the genome (about 50 genes) for their synthesis and control[17], bacterial flagella are among the most com-

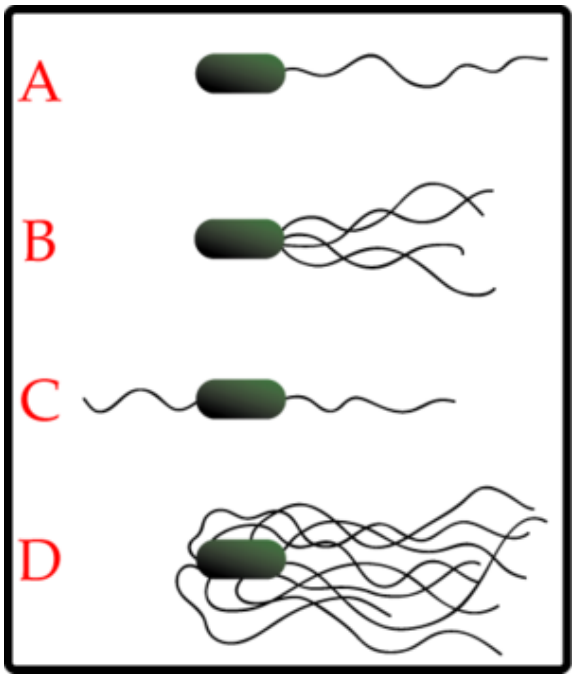

Figure 1.1: Different bacterial flagellation patterns as described in the main text. **A**: Monotrichous; **B**: Lophotrichous; **C**: Amphitrichous; **D**: Peritrichous. Taken from 16.

plex of all prokaryotic organelles. The names of the component proteins (also applied to the genes that encode them) were devised by bacterial geneticists according to the defects that resulted from the relative null mutations, for example, *fla* (no flagellum) or *mot* (flagellated but non-motile)[18]. Genes with similar mutant phenotypes were labeled with different ending letters (i.e. FliG, FliH, FliI, or FliJ) to indicate that they belonged to different sets of genes on the chromosome. Besides chemotactic control, perhaps the main advantage of flagellar propulsion is the high velocities achieved: in fact, despite a great variation in speed between species, flagellated bacteria are the fastest, with *E. coli* moving at a rate of 25-35 μm per second[19] and *Bdellovibrio bacteriovorus* up to 160 μm per second[20]. In contrast, speeds for gliding motility range from 1-10 μm and twitching occurs even more slowly, at rates of 0.05-1 μm per second, with close proximity of one cell to another usually required for movement[7]. Flagella-based swimming, therefore, allows bacteria to respond faster to changes in stimuli and environmental conditions and enhances dispersal over a large area, features closely linked with an efficient performance of chemotaxis, the

ability to orientate along certain chemical gradients, which will be described more in detail in section 1.3.

1.2 The bacterial flagellar motor

The bacterial flagellar motor is a macromolecular protein complex that spans all the layers of the cell envelope, the outer membrane, the peptidoglycan cell wall, the periplasm, through the inner membrane into the cytoplasm and is one of the largest molecular machines in bacteria, with a molecular mass of ∼11 MDa. It is powered by a flux of H^+ or Na^+ ions across the cytoplasmic membrane driven by an electrochemical gradient, the proton-motive force (as in *E. coli*) or the sodium-motive force (as in the polar flagella of *Vibrio* species). Being the most thoroughly studied of all prokaryotic motility structures, it has become a model system for molecular motors in general[21].

1.2.1 Architecture

Structural studies of the motor to date have been hampered by the motor's size, complexity, membrane localisation and attachment to the cell envelope, factors making motors difficult if not impossible to purify intact[3]. Cryo-electron microscopy (cryo-EM) and X-ray crystallography[22,23] have been invaluable tools to unveil the overall architecture and the finer details of the flagellar motor, complemented by genetic and biochemical studies that have elucidated the localisation, domain structure and relevant membrane topology of the constituent proteins, as well as regions critical for function and protein-protein interactions (see 1 for a review). Single-particle cryo-EM studies have produced nanometre-resolution structures of the purified *Salmonella enterica* motor, albeit without stators or the export apparatus[23] (Figure 1.2, c). More recently, the development of electron cryotomography (ECT)[24,25] has

made it possible to image the structures of complete motors within intact cells in 3D to several nanometres resolution (Figure 1.2, a and b).

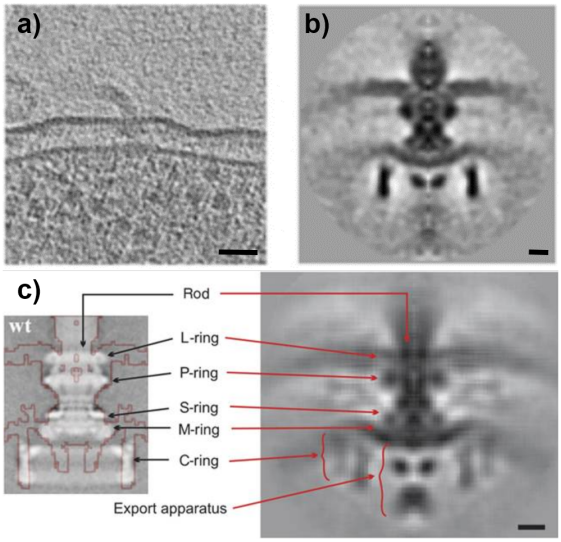

Figure 1.2: Flagellar motor structures obtained by ECT and subtomogram averaging. **a)** 20-nm thick central slice through the tomogram of an individual *E. coli* cell exhibiting a flagellar motor. Scale bar 50 nm. **b)** axial slice through an average reconstruction of such motor. Scale bar 10 nm. **c)** Left: isosurface of the *S. enterica* motor obtained by ECT and subtomogram averaging (red line) superimposed on an earlier single-particle reconstruction of purified basal bodies from the same organism[23]. Right: a generic motor structure obtained by aligning and averaging the axial slices of flagellar motors structures from 11 phylogenetically diverse bacteria. Scale bar 10 nm. Image taken from 3.

Unless explicitly stated otherwise, the experiments described in this thesis involved motors from *E. coli* or *R. sphaeroides*. In both these species, the flagellar motor is about 45 nm in diameter, is H^+-driven and consists of a core, called the "basal body", rotating against a ring of stator units, anchored to the cell wall. The core of the basal structure is highly conserved. In Gram-negative (i.e. having a thin peptidoglycan cell wall surrounded by an outer membrane containing lipopolysaccharide) bacteria, it consists of a central rod functioning as both the secretion channel and the drive shaft that transmits torque, on which four rings embedded in the inner cell membrane are mounted (Figure 1.3). These are the L (lipopolysaccharide outer membrane), the P (peptidogylcan cell wall), the MS (inner membrane) and the C (cytoplasmic) rings. The L and P rings are inserted in the outer lipopolysaccharide

membrane and peptidoglycan cell wall, respectively, and work as a bushing between the rotor and the outer parts of the cell envelope. Whether they rotate relative to the cell envelope, the rod, or both is not known. The MS-ring consists of ∼26 copies of a single protein, FliF, and is the first part of the motor to assemble, thus it can be thought of as the platform on which the rest of the motor is built.

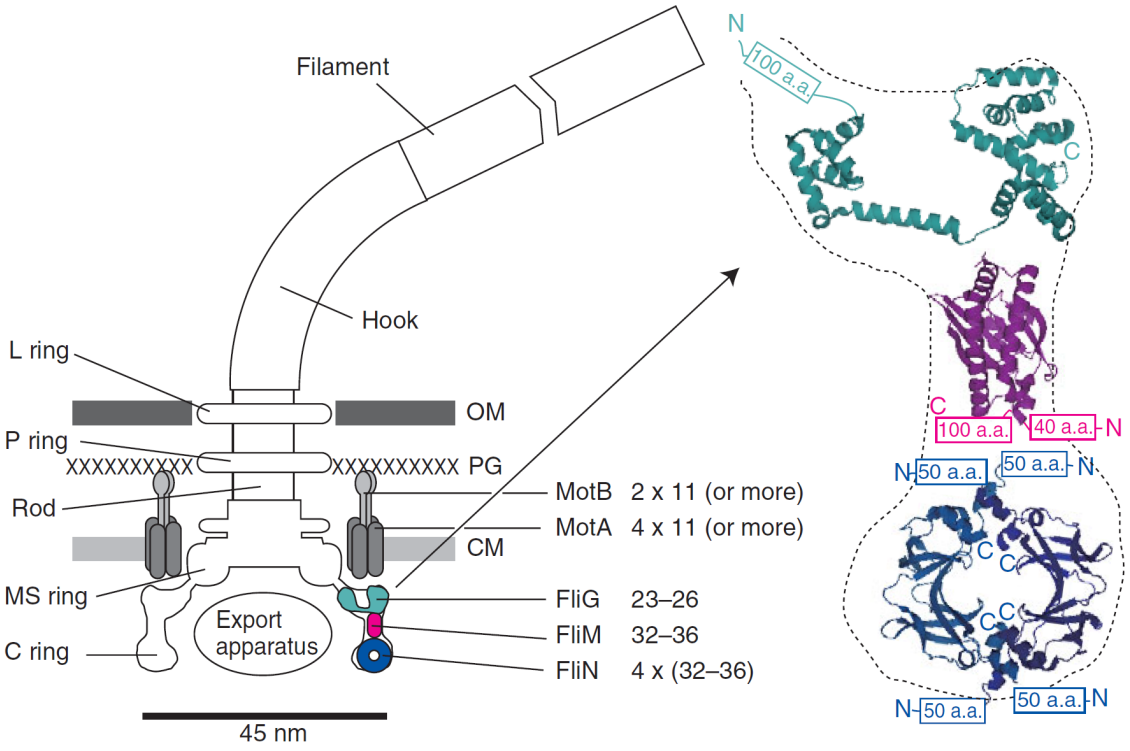

Figure 1.3: Left: Schematic side view of the structure of a H^+-driven bacterial flagellar motor, spanning the three layers of the cell envelope: the outer membrane (OM), the peptidoglycan wall (PG), and the cytoplasmic membrane (CM). In evidence, the four rings and rod of the motor, the stator units, formed by MotA and MotB proteins with stoichiometry $MotA_4MotB_2$, and the proposed location and copy number of the proteins involved in torque generation. As mentioned in the main text, note that a later published paper suggests that FliG stoichiometries different from 23-26 could also be possible in order to have a functional motor[26]. Right: X-ray crystal structures of truncated FliG (cyan), FliM (magenta), and FliN (blue) in their predicted docked position into the C-ring. N/C termini and missing amino acids (a.a.) are indicated. Image taken from 1.

1.2.2 The switch complex

The switch complex, thought to be the site of torque generation, corresponds structurally to the C-ring and is formed from about 23-26 copies of FliG, 32-36 copies of FliM, and 4×(32-36) copies of FliN (Figure 1.4). FliG consists of three domains, $FliG_N$, $FliG_M$ and $FliG_C$. $FliG_N$ directly binds to the MS ring, $FliG_C$ interacts with the stator protein MotA and $FliG_M$ provides a binding site for FliM. FliM and FliN form a stable complex with a 1:4 FliM:FliN stoichiometry[27]. Motors with FliF-FliG fusion proteins were found to be motile[28], indicating that FliG directly associates with FliF on the cytoplasmic face of the MS ring with a 1:1 stoichiometry in a 26-fold ring; moreover, analysis of *S. enterica* motors at high spatial and temporal resolution showed 26 equal steps per rotation in either direction[29,30]. However, C-rings of different sizes with symmetries ranging 31-38 were observed without a corresponding increase in MS-ring size[3,31]. From these considerations, the authors in 26 infer that also FliF:FliG stoichiometries different from 1:1 are compatible with functional motors. Structurally speaking, this hypothesis is supported by the existence of two linkages, one in $FliG_{NM}$ (assigned to the inner lobe) and one in $FliG_C$ (assigned to the outer lobe), that might provide flexibility to accommodate the symmetry mismatch between FliG and FliM[32].

1.2.3 The stator

In H^+-driven flagellar motors each stator unit is composed of two copies of MotB and four copies of MotA integral membrane proteins ($MotA_4MotB_2$)[33,34]. MotA consists of four transmembrane helices (TMs), two short periplasmic loops and two extensive cytoplasmic regions[27]. MotB consists of an N terminal cytoplasmic region, one TM and a C terminal periplasmic domain containing a well-conserved peptidoglycan binding (PGB) motif. Asp32 of *E. coli* MotB is a highly conserved residue critical for proton translocation through the channel[35]. The transmembrane domain of MotB

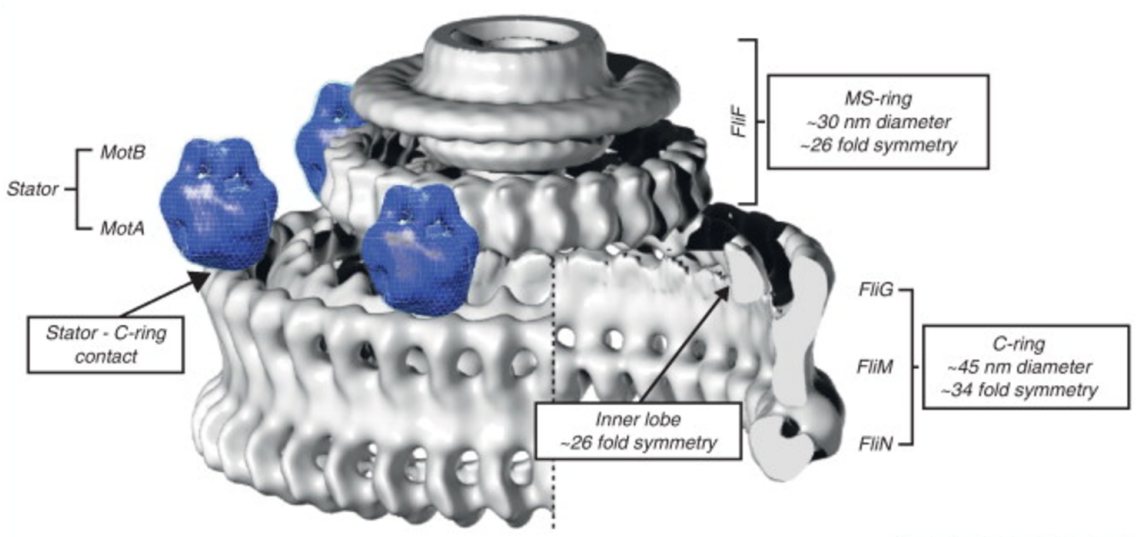

Figure 1.4: A 3D EM reconstruction of the MS-ring and the switch complex of *Salmonella typhimurium*, with stator units shown in blue and positioned above the outer lobe of the C-ring where they are seen in electron cryotomograms. Image taken from 26.

forms an ion channel along with the TM-3 and TM-4 helices of MotA, conducting protons through the cytoplasmic membrane and thus powering the motor. The C terminal periplasmic domain of MotB, MotB_C, is required not only for proper anchoring of the stator to the PG layer[36] but also for proper alignment of the stator relative to the rotor[37].

1.2.4 Self-assembly

In *E. coli*, after assembly of the MS-ring, the C-ring is next; then, the export apparatus is built, which allows for construction of the axial structures, assembled in turn in the order: rod, hook, hook-associated proteins, cap and filament. The export apparatus uses both the ion-motive force and the energy of ATP hydrolysis to complete the export process[25]. It is structurally and functionally homologous to the type III secretion system (T3SS) that directly injects virulence factors into host cells[38]. It is located at the bottom of the MS-ring (Figure 1.5) and is composed of six membrane proteins (FlhA, FlhB, FliP, FliQ, FliR, and FliO) and three sol-

uble proteins (FliI, FliH, and FliJ) in the cytoplasm[39]. The membrane components are thought to form an export gate for secretion of the substrates, while the three soluble proteins form a complex that promotes the export process by binding and delivering export substrates to the export gate. Genes encoding these components are expressed in a similar sequence, whereas P- and L-ring proteins (FlgH and FlgI) are exported into the periplasm via the Sec pathway instead of through the dedicated flagellar T3SS[40,41].

Each flagellum is a left-handed helical, semi-rigid protein filament, made up of polymerised strands of up to 20,000 copies of a single protein called flagellin (51.3 kDa), the product of the *fliC* gene. Less commonly, it is composed of several different flagellins. More precisely, the filament is made up of 11 longitudinal "protofilaments", arranged to leave a hollow core, and polymerises at the distal end by assembling FliC proteins. These are exported unfolded through a central channel ∼3 nm in diameter that runs for the entire length of the flagellum[42,43]. Protofilaments can have two different configurations: R-type or L-type according to their right- or left-handed twist, respectively. If all the protofilaments are in the same form, filament and hook form a straight rod. Different proportions of R- and L-type of protofilaments confer the helical structure to each filament[44]. The incorporation of newly exported flagellin is regulated by the pentameric cap protein FliD[45]. At the tip of the flagellum is the capping protein HAP2. As the axis of the filament generally runs at an angle different from that of the motor, the two are coupled by a flexible coupling or universal joint called the hook (Figure 1.3): this is a curved structure about 20 nm in diameter and 50 nm long composed of about 120 copies of the protein FlgE (42 kDa) arranged in a right-handed helix, whose export and incorporation are regulated in the same way as FliC. The junction of the hook and filament requires the presence of a small number of two hook-associated proteins called HAP1 and HAP3.

A still open question is how the many different substrates used in the structure of the flagellum are recognized and assembled in the proper order, and what triggers

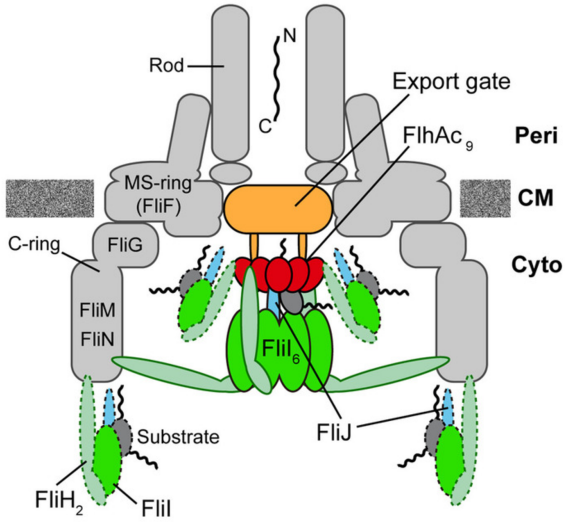

Figure 1.5: Schematic of the bacterial flagellar export apparatus. The export gate made of FlhA, FlhB, FliO, FliP, FliQ and FliR is embedded in the MS-ring; the cytoplasmic ATPase complex consisting of FliH, FliI and FliJ transports flagellar proteins from the cytoplasm to the distal end of the growing flagellar structure for self-assembly in a proton motive force-dependent manner. The C terminal cytoplasmic domain of FlhA ($FlhA_C$ in figure) forms a nonameric ring structure and projects into the cavity of the C-ring formed by FliG, FliM, and FliN. FliI forms a homohexamer ($FliI_6$) with a narrow central pore[46]. FliJ binds to the center of the $FliI_6$ ring to form the $FliI_6$FliJ ring; FliH in turn binds to FliI and anchors the $FliI_6$FliJ ring complex to the export gate through interactions of FliH with the C-ring protein FliN and FlhA. In this way, the $FliI_6$ ring can act as a substrate loader to promote the initial entry of the substrate into the gate. Image from 47.

their switching as one part of the structure is completed and another is to be started. This process seems to depend on a number of factors ranging from characteristic chaperones to specific sorting signals within their N terminal 100 amino acids, and appears to involve the soluble protein FliK and the integral membrane protein FlhB. FliK regulates the length of the hook, acting as an internal molecular ruler[48–50]. FlhB, a key component of the T3SS that is thought to act as the export gate[51], undergoes autocleavage and its C terminal domain interacts with FliK to change the export specificity of the system from rod or hook to filament-type substrates[52,53].

1.2.5 Mechanism of torque generation

FliG is the rotor protein most directly involved in torque generation and motor switching (see section 1.2.6) via interactions between conserved charged residues of the stator protein MotA. MotB holds the stator in place by binding to the PG layer; protonation and deprotonation of the conserved residue Asp32 are thought to induce conformational changes of the cytoplasmic loop between TM2 and TM3 of MotA (the "power stroke"), which push FliG and turn the rotor around[54,55]. The deletion of the genes encoding MotA and MotB results in a non-motile phenotype. However, when functional stator units are expressed from an inducible plasmid in such strains, the motile phenotype is resumed and motor speed increases in discrete increments, a process known as "resurrection" [56,57]. The authors in 57 demonstrated that torque is generated by up to 11-12 independent stator units; moreover, they observed transient speed changes even in wild type motors, and speculated that stators were not fixed but rather in a process of constant turnover in and out of the motor. This hypothesis was confirmed by total internal reflection fluorescence microscopy of green fluorescent protein labelled MotB (GFP-MotB) at the single-molecule level in spinning motors in live cells[58]. Fluorescence recovery after photobleaching showed exchange of MotB proteins in the motor on a timescale of minutes, confirming that stator units are dynamic rather than static. This may allow the replacement of damaged stators or it may be a mechanism for regulating motility in response to environmental conditions.

1.2.6 Switching in *E. coli*

An average size *E. coli* bacterium, about 0.5-1 μm in diameter and 2 μm long, has about six[59] independently functioning motors distributed over the cell surface, each able to rotate clockwise (CW) and counter-clockwise (CCW). As previously mentioned, each motor rotates a single helical filament at several hundreds of re-

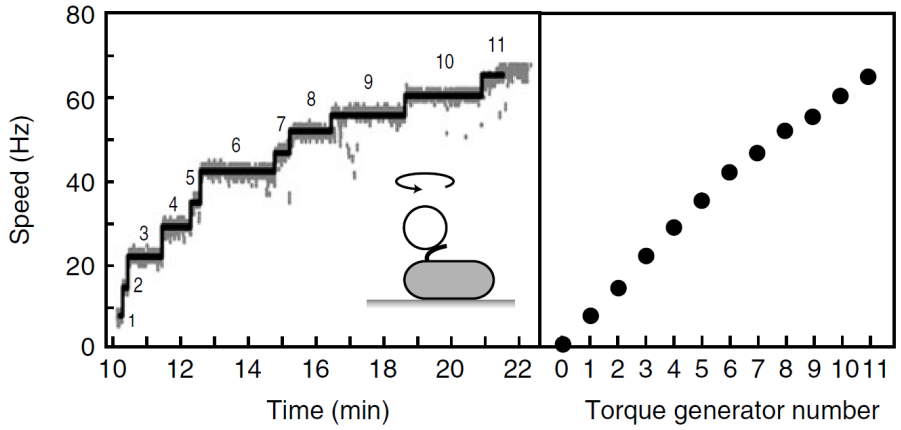

Figure 1.6: Experimental evidence that torque is generated by independent stator units in *E. coli*. Left: the speed of motors with defective stator proteins "resurrects" upon expression of functional stator proteins from an inducible plasmid. Right: motors labelled with 1 μm beads show an occupancy of up to 11-12 stators. The speed per stator decreases slightly at high stator number. Black lines show fits using a step-finding algorithm. Image adapted from 1 with data from 57.

volutions per second (hertz). Motors driven by sodium ions spin about five times faster[18]. When all the left-handed filaments are rotating CCW (looking down the filament towards the cell body), they form a single bundle due to hydrodynamic interactions, pushing the cell forward in long, smooth runs. When one or more of the motors switches to CW rotation, the associated filament undergoes a torsionally induced polymorphic transformation to a right-handed state that rapidly propagates from one end to the other, driving the bundle apart and making the cell start "tumbling" on the spot, randomly reorienting itself[60–63]. When the bundle reforms, the cell is usually facing a different direction (see Figure 1.7). This is called the "run and tumble" behaviour. CCW rotation, associated with the "runs", is the ground energy state of the filaments, which are in this case left-handed (pitch $\sim$2.5 μm, diameter $\sim$0.5 μm); during CW rotation, instead, each filament is turned by torsion into a form called semi-coiled, which is right-handed (roughly half the normal pitch but same amplitude), and then into a form called curly, which also is right-handed (roughly half the normal pitch and also half the normal amplitude)[18]. When the motor switches back to CCW, the curly filament relaxes back to normal. Filament

waveforms can also be affected by pH and ion concentrations[64,65].

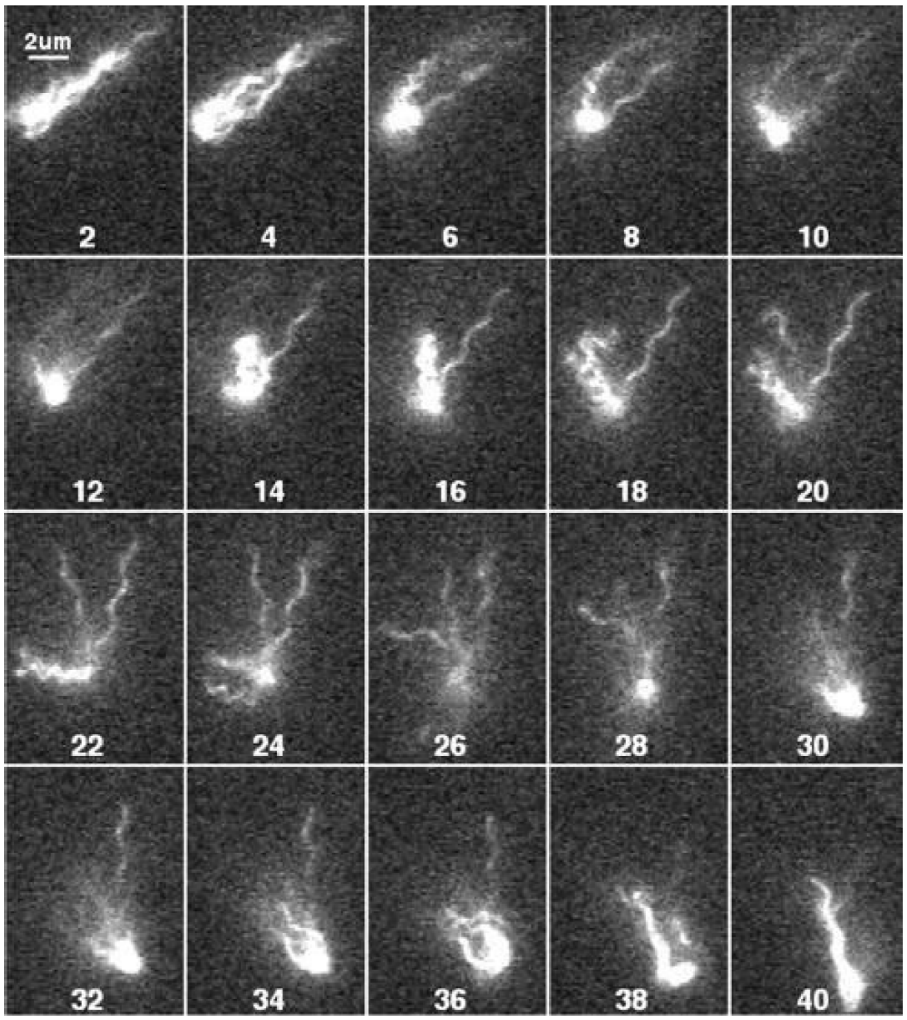

Figure 1.7: A swimming *E. coli* cell, with body and filaments fluorescently labelled with Alexa Fluor 532, illuminated by an argon-ion laser. In the sequence, only one of the filaments retains a constant waveform and orientation, while all the others undergo a polymorphic transformation as a result of the motor's CW switching, disrupting the bundle and causing the cell to tumble and reorient itself. Every other frame is shown, with a frame-rate of 60 Hz. Image taken from 61.

1.2.7 Stopping in *R. sphaeroides*

R. sphaeroides is a rod-shaped, gram-negative, purple non-sulfur photoheterotrophic bacterium belonging to the α-3 subclass of Proteobacteria. It is slightly smaller than *E. coli*, i.e. about 1×2 μm[66], and very versatile, in that it can grow under aerobic conditions, anaerobically in the light using photosynthesis or anaerobically in the

dark using alternative electron acceptors[67]. It is motile and chemotactic under all of these conditions. As previously mentioned, it is monotrichous, i.e. it has a single flagellum, between 1 and 9 μm long, that rotates unidirectionally and stops periodically to allow the cell to reorient[68,69]. A stop is equivalent to a bundle break-up in *E. coli*. Forward swimming occurs during CCW motor rotation. When the motor stops, the cell is randomly reoriented by Brownian motion[70,71].

1.3 Bacterial chemotaxis

Being too small in size to sense gradients directly across their body length, swimming cells sample their environment with time comparing the current conditions with those of a second or so ago[72]. Moreover, bacteria often live in environments with a low Reynold's number R = $lv\rho/\eta$ (where l = length, v = velocity, ρ = density and η = viscosity), i.e. $\sim 10^{-6}$, where inertial forces are roughly a million times smaller than viscous ones[73,74]. For these reasons, bacteria are unable to move directly linearly towards a food source and are readily displaced from their trajectories by Brownian motion in the absence of the propulsive force of the flagella. In homogenous environments with no chemical gradients, *E. coli* exhibits a random walk movement with alternating run/tumbles approximately every 1 s[60]. However, in a chemical gradient, cells tend to move towards attractants or away from repellents, with runs extended up to ~10 s. This is chemotactic behaviour[75,76]. Runs do not exceed the 1-10 s range due to physical considerations[77]: in fact, below 1 s, the cell does not travel far enough to outrun diffusion and make a fresh estimate of stimuli concentration; meanwhile, running for longer than 10 s is futile since the cell drifts off course by more than 90° due to Brownian motion.

Chemotaxis is the process by which bacteria can migrate towards more favourable environments for growth by moving along chemical gradients towards attractants and away from repellents. There is a wide range of chemical moieties sensed by

bacteria including peptides, amino acids, sugars and organic acids, in addition to smaller molecules and ions such as oxygen, nitrate and nickel. The precise molecules that are detected by a cell and whether they are harmful or beneficial depend on the bacterial species and, sometimes, this changes within the same species under different environmental conditions. For instance, acetate is a chemoattractant for *R. sphaeroides* but repels *E. coli*. In any species, however, the motors receive instructions to modulate the frequency of switching, via a very sophisticated intracellular signal transduction pathway, which is reviewed in the next two sections for *E. coli* and *R. sphaeroides*, respectively.

1.3.1 Two component signaling systems

While many eukaryotic signaling cascades involve protein kinases that phosphorylate both themselves and other protein substrates at specific serine, threonine or tyrosine residues, thereby regulating protein activities, traditional two component signalling (TCS) systems, or histidine-aspartate phosphorelay (HAP) systems are the predominant prokaryotic mechanism for coordination of signal transduction with extracellular sensing. Generally, they utilise two proteins for detection and response - the detector protein is a sensor kinase, also called histidine protein kinase (HPK) which is a homodimer, containing an input domain and transmitter (or dimerisation) domain; this interacts with the response regulator protein (RR) which contains an output domain. HAP-system signalling is initiated by trans-autophosphorylation within the HPK dimer: the phosphoryl group of an adenosine-tri-phosphate (ATP) molecule that is bound to the kinase domain of one monomer is transferred to a specific His residue in the other monomer. The phosphoryl group is then transferred to the conserved Asp residue of the RR, which results in the activation of the output domain of the RR and generation of the signaling pathway's response. RRs can then undergo spontaneous dephosphorylation by losing the phosphoryl group to the solu-

tion, with phosphorylated half-lives varying from a few seconds to hours. However, in many cases, the half-life is reduced by the presence of a specific phosphatase. The chemotaxis system is a modified two-component system in which the HPK doesn't have an input domain and relies on other components of the chemosensory network to detect the signal and transduce external stimuli. Moreover, the RR lacks an output domain. Chemotaxis has become a paradigm for the two-component superfamily of receptor-regulated phosphorylation pathways and has been extensively investigated with a range of experimental and computational methods (for reviews see 74, 78–80).

1.3.2 The chemotaxis signaling pathway in *E. coli*

E. coli's chemotaxis pathway is one of the best-characterised bacterial chemosensory networks and it is incredibly sensitive, being able to sense a chemical gradient even if just 1% of the chemoreceptors has a ligand bound[81]. For simplicity, it can be depicted as being composed of two temporally distinct phases, phosphosignaling and adaptation[78]. In the former, the sensing that is usually performed by the input domain of the HPK, is performed by homodimeric transmembrane chemoreceptors, known as methyl-accepting chemotaxis proteins (MCPs), which detect attractant and repellent external stimuli. Each is ∼380 Å long, with an 80 Å periplasmic ligand binding domain at the interface between the two monomers, a 40 Å transmembrane domain and a 260 Å conserved cytoplasmic signalling domains[82]. In *E. coli*, the transmembrane and signalling domains are connected by the HAMP (histidine kinases, adenylyl cyclases, methyl-binding proteins and phosphatases) domains, for which there is no crystal structure yet. Despite their overall conserved architecture, MCPs have very diverse ligand binding capabilities due to variations in their periplasmic domain. There are four main chemoreceptors: Tap, Trg, Tsr and Tar. They are homologous but have a hierarchy of affinity for different signals: Tap and Trg

sense dipeptides and ribose-galactose concentration respectively; Tar senses aspartate and maltose levels, whereas Tsr senses pH, temperature and serine levels. Tar and Tsr are the major receptors, comprising ∼7500 molecules per cell, while the minor receptors are present in a few hundred copies. The chemoreceptors' signaling domains contain two adaptation regions, each with four to six specific glutamic acid residues (open and filled circles in Figure 1.9) that can be reversibly methylated[83,84] and play a key role in the adaptation phase of the pathway, discussed later in this section. A fifth MCP-like protein, Aer, mediates aerotactic responses (i.e. responses to changes in oxygen levels) by monitoring redox potential in the electron transport chain. Despite having the same conserved cytoplasmic signalling domain that is found in all other MCPs, Aer undergoes sensory adaptation through a different, methylation-independent mechanism[85,86].

The five MCPs in *E. coli* rely on a number of cytoplasmic signaling proteins to control flagellar rotation and sensory adaptation (Figure 1.9): once an external stimulus is detected, conformational changes are induced in the receptors and the linker protein CheW transduces the signal to the histidine protein kinase CheA, which is a homodimer. CheW and CheA form the "sensory complex", which respond to signal propagation from the MCPs over a time scale of milliseconds. However, there is also evidence for a direct CheA-MCP interaction[87]. CheA is expressed in two forms: full-length $CheA_L$ and short-length $CheA_S$, which lacks a phosphorylation site. Each $CheA_L$ monomer is 71 kDa and consists of five modular domains, P1-P5. P1 is a five helical bundle with a solvent-accessible histidine at position 48[88]. His48 is trans-autophosphorylated by the other CheA monomer in the dimer using ATP bound to P4. P2 binds to the response regulators which receive the phosphoryl group from His48-P (see Figure 1.8). P3 is the dimerisation domain. P4 is the catalytic domain. P5 bears a very similar fold to CheW, to which it binds. The phosphoryl group is transferred to the response regulator CheY protein on the timescale of tenths of seconds. CheY-P is then released and diffuses through the cytoplasm to the

motors on a timescale of milliseconds, where its binding triggers a switch to clockwise motor rotation, cell tumbling and ultimately cell reorientation. A more detailed description of CheY and of its interactions with FliM are included in the next section. Interestingly, CheA that lacks a P2 domain can still phosphorylate CheY, although this occurs at a much slower rate than for full-length CheA. This indicates that the P1 domain of CheA might also contribute to the rate of phosphotransfer. CheA trans-autophosphorylation is inhibited by increases in attractants or decreases in repellents, leading to a decrease in CheY-P concentration and related increased probability of CCW rotation. Deletion of either *cheW* or *cheA* genes in *E. coli* results in a smooth-swimming phenotype, because CheY remains unphosphorylated.

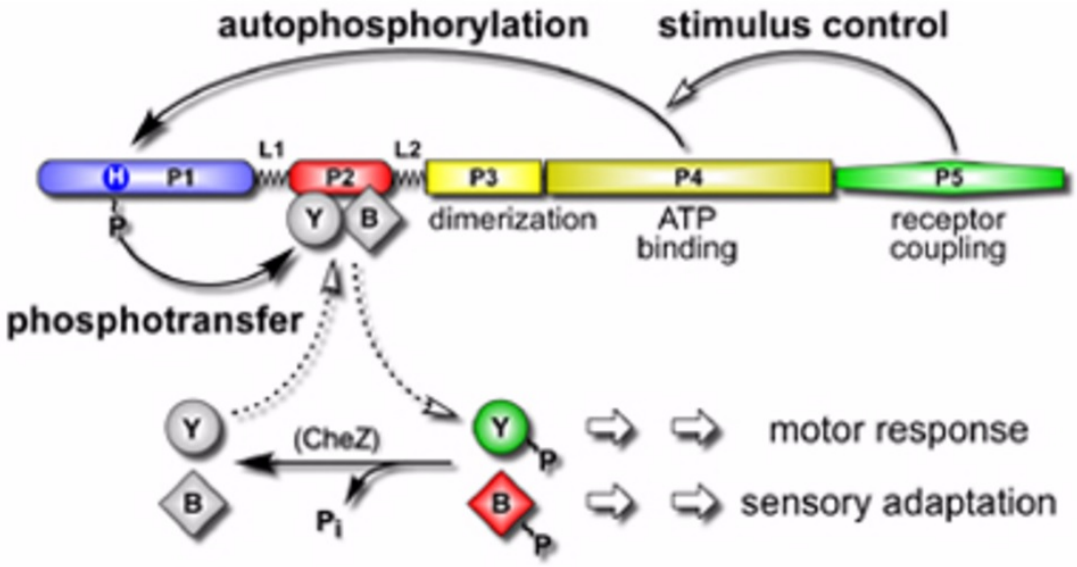

Figure 1.8: Domain organization and phosphotransfer from CheA to response regulators in *E. coli*. CheA regulates flagellar movements and stimulus sensitivity by activating the effector proteins CheB and CheY through phosphorylation from the P2 domain. Figure taken from `http://chemotaxis.biology.utah.edu/Parkinson_Lab/posters/chemotacticsignalingwithoutatarget/chemotacticsignaling.html`.

One requirement of biological signalling systems is a dynamic response. To ensure continuous sensing, the signal must be terminated i.e. dephosphorylation must occur. CheY-P undergoes rapid auto dephosphorylation on the time scale of approx-

imately 20 s, a time scale characteristic of a fast signaling pathway because response regulators from slower two-component pathways can remain phosphorylated for up to an hour or longer (Stock and Surette 1996). However, if temporal sensing is to occur in *E. coli*, termination must occur within 100 ms (the time that it takes to perform a tumble)[89]. This accelerated rate of dephosphorylation is achieved by CheZ, a 24 kDa phosphatase. Δ*che*Z *E. coli* mutants exhibit a never-ending tumbling phenotype due to build up of CheY-P levels. CheZ has been shown to mostly localise at the chemoreceptor cluster[90] but has also been suggested to associate into highly active oligomers in the presence of CheY-P and chemotactic stimuli[91,92]. In 93, the authors suggest that high CheY-P levels reached upon exposure to a repellent promote the oligomerisation of CheZ dimers at the polar clusters by $CheA_S$, whilst attractants and low CheY-P would lead to the formation of cytoplasmic dimers. As CheZ is more active in the oligomeric state[92], movement of CheZ to the clusters would be coupled with an increased rate of CheY-P dephosphorylation, sharpened cellular response to chemoeffectors, increase in the range of detectable ligand concentrations and more precise and robust adaptation.

Adaptation is the second phase of chemotaxis, which is achieved through reversible demethylation/methylation of MCPs by CheB and CheR. CheB is a methylesterase whose activity increases 100 fold following phosphorylation by CheA-P. CheB-P demethylates methylation sites on the MCPs and acts antagonistically to CheR, a constitutively active methyltransferase. Methylation allows tighter packing of the MCP helices resetting CheA activity[94]. CheB-P demethylates the receptors allowing the adaptation sites to pack less tightly (resulting in lowered chemoreceptor sensitivity) and hence CheA to be deactivated. This allows the cell to reset its signalling machinery to the new chemoattractant concentration, preventing desensitisation. Mutant cells deficient in this adaptation machinery become locked in smooth swimming or tumbling states[95,96]. CheY and CheB compete for binding to the P2 domain of CheA but the probability of being phosphorylated is greater for CheY than for

CheB due to the low CheB copy number of ∼300 compared to ∼8000 CheY[97]. The time frame between MCP signalling and methylation/demethylation is ∼1 s, hence smooth runs typically last about 1 s, as previously stated. This is to ensure that the response occurs before adaptation[75,76]. For a better understanding of the results

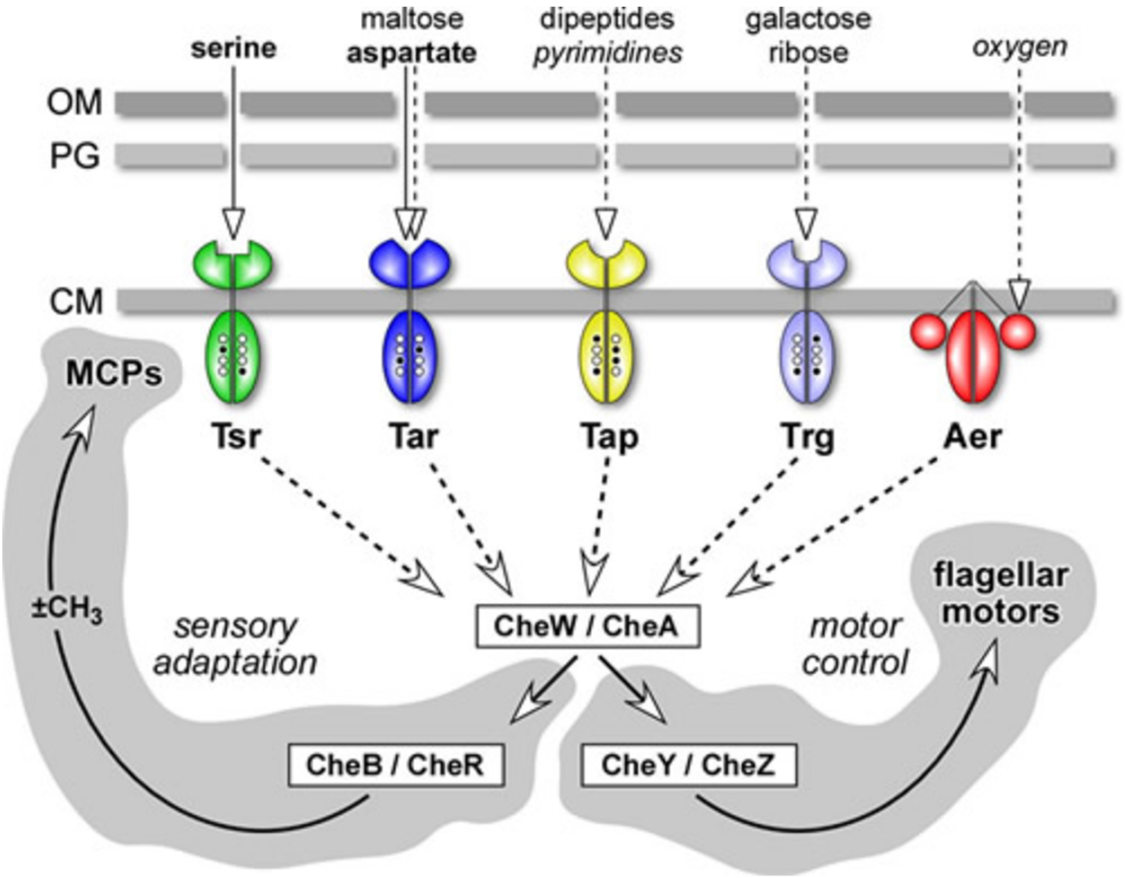

Figure 1.9: Schematic diagram of the chemotaxis signalling pathway in *E. coli*. The five transmembrane chemoreceptors detect external stimuli, CheW transduces the signal to the chemotaxis histidine protein kinase CheA, which phosphorylates either of the two response regulators - CheY and CheB. CheY-P binds to FliM triggering a switch in the direction of rotation of the bacterial flagellar motor from anticlockwise to clockwise. CheB is a methylesterase which demethylates the MCPs resulting in lower levels of phosphorylated CheA. CheR is the antagonist of CheB, a constitutively active methyltransferase. The actions of CheB and CheR allow adaptation of the system. Receptor modification sites are shown as white (unmethylated) and black (methylated) circles. CheZ phosphatase increases the rate of CheY spontaneous dephosphorylation to reset the system and bring it back to steady state. Figure taken from `http://chemotaxis.biology.utah.edu/Parkinson_Lab/projects/ecolichemotaxis/ecolichemotaxis.html`.

illustrated in Chapters 4 and 5, it is worth spending a few words on the cellular localisation of the methyl-accepting chemotaxis proteins in *E. coli*. Immunolabeling and electron microscopy studies[98] indicated that, in WT cells, MCPs cluster in patches ∼200 nm in diameter at one (primarily) or both poles of the cell[98]. They associate into "trimers of dimers"[99,100] that span the inner membrane and complex with CheA, through the coupling protein CheW. Clustering depends not only on the MCP itself but also on the latter two MCP-associated cytoplasmic proteins[90]: in the absence of CheA, the MCP-CheW complex continues to localise to the cell poles, however, in the absence of CheW, MCP-CheA does not[98]. Chemical crosslinking has confirmed that these trimers occur *in vivo*[101]. The recently resolved crystal structure of the cytoplasmic domain of the Tsr receptor has furthermore revealed that the tails of three dimer receptors come together and form a trimeric structure[99]. Considering this structure, the authors in 102 predict that chemoreceptors are arranged in higher order arrays in a two-dimensional 12-nm hexagonal lattice, built from trigonal units each composed of three MCP dimers, three molecules of CheW, and three monomers of CheA. The architecture of these arrays is not specific to *E. coli*, but is universal among bacteria[103] and is likely to be key to the high signal sensitivity, wide dynamic range, integration between receptors and feedback control of the chemotaxis system[100,104].

1.3.3 The response regulator CheY

CheY is the response regulator for *E. coli*'s chemotaxis system. Its structure has been determined by X-ray crystallography and Nuclear Magnetic Resonance (NMR) under different conditions in several laboratories[105–107]: it is a 14 kDa single-domain receiver protein having the classic RR structure, with a central five-stranded parallel β-sheet domain sandwiched between five α-helices. CheY is phosphorylated on Asp57[105] by the histidine kinase CheA through phosphotransfer. This site, which is

highly homologous to those of other aspartate kinases, is illustrated in Figure 1.10 together with other relevant conserved catalytic residues: Asp13, which coordinates Mg^{2+} [26,108,109], Thr87 which likely serves as a general acid-base catalyst,and Lys109 which provides acid-base catalysis and electrostatic stabilisation. The Lys109 side chain could also serve as a molecular switch by forming a salt bridge to Asp57 or phospho-Asp57 [26,108–110]. *In vitro*, CheY can also be phosphorylated by small inorganic phosphodonors, such as acetyl phosphate [111], and it is subject to acetylation at a number of sites [112]. Although acetyl phosphate is present within the cell and its level varies with the growth phase and conditions [113,114], the rate at which it phosphorylates CheY is much lower than that of CheA-mediated phosphorylation (0.05-0.5 s^{-1} vs 800 s^{-1} and K_D values 10-600 mM vs $\sim$60 μM) [115]. This CheA-independent phosphorylation indicates that CheY, like other response regulators, can catalyse its own phosphorylation. The potential biological relevance of acetylation and phosphorylation by such inorganic phosphodonors is not fully understood, but mutants in acetyl-CoA synthetase show abnormal behaviour [112], which indicates that some aspects of chemotactic behaviour might be modulated by metabolic activity. In the thesis, this question will be extensively addressed in section 6.6 of Chapter 6.

Interaction of CheY with the switch

As illustrated in section 1.2.2, the switch complex corresponds structurally to the C-ring, at the bottom of the basal body, and is formed from an array of FliN tetramers alternating with FliM C terminal ($FliM_C$) domains [117] and from 23-26 copies of FliG. FliM is believed to interact with FliG, triggering conformational changes in $FliG_C$, which in turn communicates the bound-state of FliM to the stator complexes through MotA. It is a widely shared opinion in the field that FliG is predominantly involved in motor rotation and torque generation and that FliM is predominantly involved in switching. However, there is still much debate as to how FliM actuates the motor's

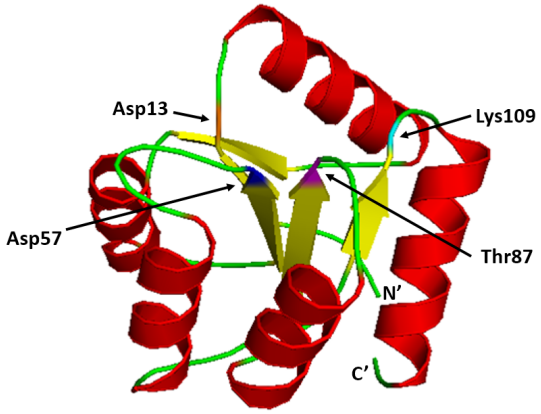

Figure 1.10: Active sites on CheY. Shown are Asp57 (blue), the phosphorylation site, Thr87 (magenta) which acts as acid-base catalyst, Lys109 (cyan) which directly coordinates the phosphoryl group at Asp57[116] and Asp13 (orange), responsible for Mg^{2+} coordination. Mg^{2+} ions serve as essential cofactors in both the autocatalytic phosphorylation and dephosphorylation reactions[78].

switching. The CheY docking surface with FliM has been implicated by genetic studies[118–120], but it does not appear to directly overlap the kinase phosphorylation site. Instead, the available evidence indicates that the phosphorylation-induced conformational change, rather than the presence of acyl phosphate on the protein surface, is responsible for regulating the docking.

For example, some CheY mutants are phosphorylated but fail to promote tumbling, whereas others are not phosphorylated but do stimulate tumbling[108,110,121,122], suggesting that tumbling is modulated by a specific conformational change at the motor-docking surface. Sockett et al.[119] were the first to suggest FliM as the primary target for CheY binding; later biochemical studies showed interaction between FliM and CheY-P *in vitro*[123]. The conserved aromatic residue Tyr106 (Y106) in CheY is believed to play an important role in FliM-CheY interaction: in 124, the combined results from *in vivo* behavioral and *in vitro* biochemical studies on bacteria where Y106 was substituted with a range of other amino-acids, suggested that the diverse phenotypes of such mutants were not due to a variation in phosphorylation or dephosphorylation ability nor in affinity for the switch, but to the altered signal

transduction of CheY to FliM. These data imply that the binding of CheY-P to the flagellar motor is a necessary, but not sufficient, event for switching generation. It was previously suggested that CheY activation might be a multistep event[107,110] with Y106 likely involved in the propagation of the chemotactic signal within the CheY molecule. According to such multistep model, it was recently suggested in 125 that CheY-P is first captured by a flexible 16 amino-acids linker to the N terminus of FliM and then interacts with a conserved hydrophobic patch on FliN to induce a small shift of the FliN tetramers relative to $FliM_C$ and CW rotation of the flagellar motor[126]. However, the possibility that these residues do not form the whole CheY-binding site cannot be eliminated. In 127, data gathered from mutant experiments indicate that the N terminal region of FliM is primarily important for CheY-P binding and generation of CW rotation, the middle region for FliG interaction and motor rotation and both the extended N terminal and the C terminal regions for flagellar assembly via FliM-FliM polymerisation. In 128 the middle domain of FliM ($FliM_M$) was demonstrated to also be a low affinity binding site for CheY, but its functional significance in clockwise motor rotation was not determined. The importance of low affinity binding sites, especially of $FliM_M$, for switching regulation will be further discussed in Chapter 6 of this thesis. In *E. coli*, CW rotation of the motor normally requires presence of CheY-P but can occur in a CheY-deletion strain if the temperature is lowered to 5°C or below. Such temperature dependence in the function of a protein assembly is expected to arise mainly from the hydrophobic effect and could be explained in the present case by the exposure of an additional hydrophobic surface area of about 2500 Å in the CW state. In fact, some residues at the $FliM_M$-$FliM_M$ interface in the *E. coli* protein are hydrophobic (Ile56, Met67, and Phe70 on one edge and Val98 and Phe188 on the other) and so might contribute to the observed temperature dependence of switching[117]. Certain CheY-P mutants do not bind to FliM[122], further indicating that the switch protein recognizes the conformation of CheY rather than its phosphoryl group[78,108,110,121].

Evidence for post-binding cooperativity

As previously mentioned, chemoreceptors can detect small changes in environmental chemicals' concentrations over a wide dynamic range, providing the basis for rapid and efficient chemotaxis response. Early investigation explored the rotational response of a tethered cell (attached by a single antibody-treated filament to a microscope coverslip) following exposure to small steps in aspartate concentration delivered iontophoretically[72]. According to estimates of receptor number and aspartate dissociation constant, steps leading to a change in the aspartate receptor occupancy of just 0.2% (∼20 out of the ∼10000 receptors) resulted in a 23% change in CW bias (the probability of CW rotation). The amplification of the pathway, defined as the fractional change in CW bias divided by the fractional change in receptor occupancy, therefore stands at a factor of ∼100. Amplification in biology is generally a hallmark of allosteric cooperativity. The concept of binding cooperativity was developed by Hill in 1913. It has classically been classified as either concerted[129] or sequential[130], the former describing coupling between ligand binding and subunit conformation, and the latter coupling of conformations between different subunits. In the concerted model, coupling between subunits occurs first and all subunits switch conformation simultaneously, even if not all have bound ligand. In the sequential model, coupling between ligand binding and conformation is prior, then, as soon as a ligand binds a subunit, that subunit switches conformation[131]. More recently, a mathematical model of the general allosteric scheme[132] was constructed in which both types of coupling coexist in the mechanism of conformational spread, with the stochastic growth and shrinkage of domains of adjacent subunits sharing a particular conformational state. The classical binary view of the kinetic states of the switch, i.e. either CW or CCW, has currently been questioned. The conformational spread model applied to a ring of identical protomers seems to most accurately be able to account for the rotary motor's multistate switching, switch-

ing at low temperatures in the absence of CheY and experimentally measured Hill coefficient values[133–135]. In fact, the switch response showed a steep sigmoidal relationship between the concentration of the response regulator CheY-P and motor rotational bias (the fraction of time spent rotating in a given direction), compatible with a Hill coefficient of ∼10 (ref. 136); however, binding of CheY-P to FliM protein subunits of the complex was shown to be much less cooperative, with a Hill coefficient <2 (refs. 137, 138). What and where the source of cooperativity in switching is, remains an open question. If such cooperativity required the nearly simultaneous arrival of many CheY-P molecules by diffusion, switching would be slow. A possible way around this issue would be the recently suggested two-step capture of CheY-P (Afanzar et al., personal communication) which, through the FliM N terminal segment, would recruit a pool of active proteins in the proximity of a low affinity binding site, either on $FliM_M$ or FliN, thus increasing switching probability. Along these lines, in a recent study aimed at determining how many FliM molecules within a single flagellar motor should be occupied by CheY-P to generate CW rotation, wild type FliM ($FliM_{WT}$) and a mutant FliM protein almost locked in CW rotation ($FliM_{CW}$) were coexpressed in a Δ*che*Y gutted strain[139]. Surprisingly, a probability of 50% of CW rotation was achieved only when ∼90% of the FliM molecules at the motor were in clockwise locked conformation. Around this fraction of $FliM_{CW}$ molecules within the complex, the gain of CW rotation as a function of the increased fraction of $FliM_{CW}$ was very steep. This steepness suggests that if $FliM_{CW}$ correctly reflects $FliM_{WT}$ state occupied by CheY-P, the source for high cooperativity relies at least in part in a post-binding step. The findings in 137 provide further evidence in support of the notion that the chemotactic signal is amplified within the switch rather than at the preceding binding step of CheY-P to the switch. On a related note, it has also been proposed that the sensitivity of the motor to CheY-P is dependent on its composition and can change in response to CheY-P occupancy[140]. In particular, the number of FliM subunits in the

flagellar-ring increases in response to decreasing CheY-P concentration, resulting in increased motor sensitivity. This shift in sensitivity could also explain why motors show signal-dependent FliM turnover[141].

1.3.4 The chemosensory pathway in *R. sphaeroides*

Differently from *E. coli*, in addition to a polar cluster of transmembrane MCPs, *R. sphaeroides* also presents a cytoplasmic cluster of soluble chemoreceptors, as shown in Figure 1.11 (see 84 for a comprehensive review). Both are essential for chemotaxis under laboratory conditions, neither of them being capable of supporting chemotaxis alone[142,143]. The physiological advantage of having two distinct chemosensory pathways is unclear, but genome sequences indicate that the existence of different pathways is not an uncommon feature in bacteria[144]. Three operons that could potentially encode complete chemosensory pathways have been recognized in *R. sphaeroides*: *cheOp*1, *cheOp*2 and *cheOp*3. While a role for *cheOp*1 has yet to be identified under laboratory conditions, *cheOp*2 and *cheOp*3 have been found to encode the two separate chemotaxis machineries described above[142,145]. Interestingly, whereas the genes encoding membrane-spanning chemoreceptors are scattered around the genome, those encoding the soluble chemoreceptors (Tlps) are within the chemotaxis operons[146]. The chemosensory proteins encoded in *cheOp*2 mostly localise at the cell polar clusters, while those encoded in *cheOp*3 are targeted with Tlps to the cytoplasmic clusters[147]. *cheOp*2 and *cheOp*3 have been shown to be expressed in cells at different relative levels in aerobic or anaerobic conditions: expression of *cheOp*2 ∼4- and 15-fold higher than that of *cheOp*3 under anaerobic and aerobic conditions, respectively, clearly indicating that cells can adapt their chemotaxis system according to the local environmental conditions[67]. In the *R. sphaeroides* genome there are also two sets of flagellar genes, *fla*1 and *fla*2, each encoding functional flagella[148]. The number and the positioning of the two types

of flagella differ: wild type cells expressing the fla1 genes have a single randomly positioned flagellum with a 20 nm diameter filament, whereas cells expressing the fla2 genes have 2-4 unipolar flagella with a 10 nm diameter filament. The Fla1 and Fla2 flagella are controlled by different chemotaxis proteins: rotational behaviour of the Fla1 flagellum is assumed to be controlled jointly by the products of *cheOp*2 and *cheOp*3, whereas rotation of the Fla2 flagellum is assumed to be controlled by the products of *cheOp*1. It has been observed that both kinds of flagella support swimming motility in liquid culture[149]. However, under laboratory growth conditions, wild type cells only express the Fla1 flagellum genes[149]. The reason for the existence of the *fla*2 genes and of *cheOp*1 is not clear, although the presence of these intact genes in the genomes of all sequenced *R. sphaeroides* strains suggests that they are probably expressed under growth conditions different from those used in the laboratory[150]. Only the Fla1-mediated chemotaxis will be discussed in this thesis. As a result of such complex chemotaxis pathway, *R. sphaeroides* has 13 chemoreceptors (nine transmembrane MCPs and four cytoplasmic Transducer-Like Proteins (Tlps)), four CheA homologues, four CheW homologues, two CheB homologues, three CheR homologues and six CheY homologues (with no CheZ homologue). *In vitro* phosphotransfer assays have shown that the different CheA proteins phosphorylate different subgroups of response regulators[151]: $CheA_2$ phosphorylates all of them, whereas $CheA_3$ and $CheA_4$ phosphorylate $CheY_6$ and $CheB_2$ from *cheOp*3 and to some extent $CheY_1$ from *cheOp*1. $CheA_3$ and $CheA_4$ form a heterodimer ($CheA_3A_4$) that uses the kinase domain of $CheA_4$ to phosphorylate the P1 domain of $CheA_3$[143]. Although $CheA_2$ can phosphotransfer to all of the response regulators *in vitro*, it is not enough to support chemotaxis alone in $CheA_3$-$CheA_4$ deletion mutants. This might be because of the spatially separate localisation (i.e. either at the polar MCPs or at the cytoplasmic Tlps) of the proteins encoded by the two operons. $CheW_2$, $CheW_3$ and $CheW_4$ in the receptor clusters are responsible for transducing the signal to the relative CheAs[152]. Unlike in *E. coli*, the two CheB

proteins do not seem to be specifically localised in *R. sphaeroides*, whereas the CheR proteins are partially localised[153]. The fact that phosphate groups from $CheY_3$ and $CheY_4$ can be transferred to $CheY_6$ through reverse phosphotransfer to $CheA_2$ (very slow process *in vivo*[84]), and that $CheA_3$ has phosphatase activity for $CheY_6$[154] account for the absence of a CheZ homologue in *R. sphaeroides*.

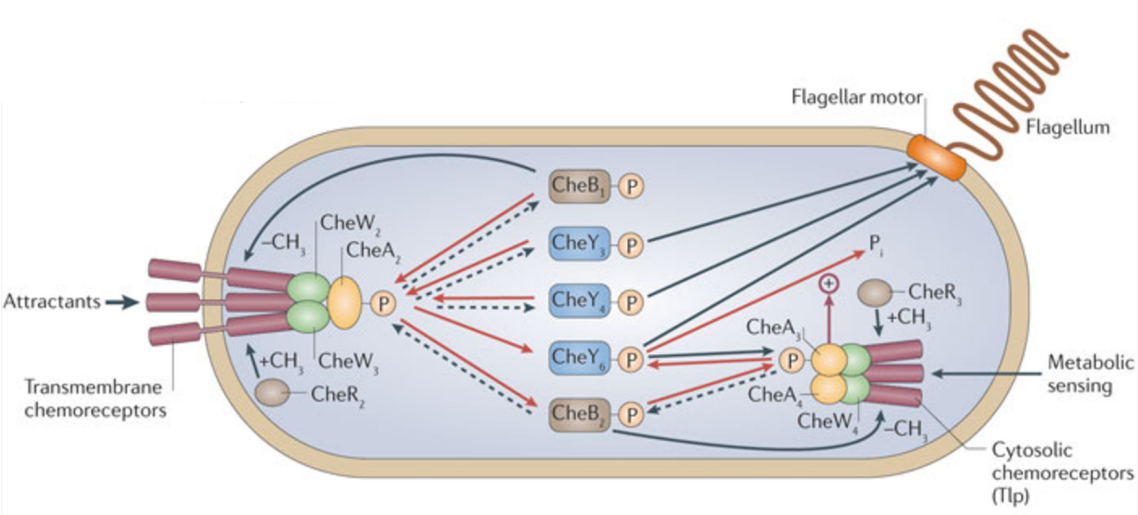

Figure 1.11: Schematic diagram of the Fla1-mediated chemotaxis network in *R. sphaeroides*. Differently from *E. coli*, *R. sphaeroides* exhibits two distinct signalling clusters, one of transmembrane chemoreceptors sensing extracellular concentration gradients, and another of cytoplasmic chemoreceptors detecting the metabolic state of the cell. The histidine kinase analogue of *E. coli*'s CheA is thought to be $CheA_2$ which, upon autophosphorylation, transfers phospho groups to a range of response regulators including $CheY_3$, $CheY_4$, $CheY_6$, $CheB_1$ and $CheB_2$ (red arrows). When the cytosolic cluster is active, $CheA_3$-P phosphorylates $CheY_6$ and $CheB_2$, which in turn triggers the response regulators' phosphorelay cascade by phosphorylating $CheA_2$ at the polar cluster (dashed arrows). Figure reproduced from 84.

1.3.5 Localisation of Che proteins

It has been shown in the literature that phosphosignals from $CheA_2$, $CheA_3$, and $CheA_4$ plus $CheY_6$ and either of $CheY_3$ or $CheY_4$ are essential for chemotaxis in *R. sphaeroides*[155]: in this paper, the intracellular localisation of $CheY_3$, $CheY_4$, and $CheY_6$ was studied using CFP/YFP fusions; the functionality of the fusions was tested using swarm plates and it was found that, while N terminal fusions to

both $CheY_3$ and $CheY_4$ were fully functional, strains with either N or C terminal fusions to $CheY_6$ were non-chemotactic. Moreover, western blotting using an antibody against $CheY_6$ showed that the $CheY_6$ fusions were expressed at much lower levels than wild type (undetectable in the case of the N terminal fusion), which could explain why strains containing these fusions were non-chemotactic.

R. sphaeroides cells typically have a chemotaxis cluster at each pole and a single cytoplasmic cluster located approximately at mid-cell[84]. A key feature of the cytoplasmic cluster is that its chemoreceptors lack transmembrane regions and are soluble - unlike those of the polar cluster - allowing them to sense the cytoplasmic, rather than periplasmic, concentration of ligands. The identities of the ligands sensed by the cytoplasmic chemoreceptors are unknown; however, chemotaxis towards many attractants (for example, alanine, ammonia, glutamate and sugars) requires their transport and metabolism, suggesting that the ligands sensed could include common metabolites derived from these chemoeffectors[84]. $CheA_3$ and $CheA_4$ were previously shown to localise at the cytoplasmic chemotaxis cluster, whereas $CheA_2$ localises to the polar chemoreceptor clusters[147]. The polar clusters are proposed to sense the external environment, while the cytoplasmic one the metabolic state of the cell. $CheY_6$ is phosphorylated by both $CheA_2$ and $CheA_3A_4$ *in vitro*[143,151]. $CheY_3$ and $CheY_4$ are phosphorylated by $CheA_2$ but not by $CheA_3A_4$. If the *R. sphaeroides* CheYs localised to the sites of their cognate kinases, then $CheY_6$ would be expected to be found at both the cytoplasmic and polar clusters, whereas $CheY_3$ and $CheY_4$ would be found only at the cell poles. In 155, fluorescence microscopy showed that the majority of YFP-$CheY_3$ was delocalised throughout the cytoplasm, instead; no polar clusters were observed, although some protein was localised to cytoplasmic clusters. In contrast, CFP-$CheY_4$ mainly localised to discrete regions at both the cell poles and in the cytoplasmic cluster with some diffuse fluorescence throughout the cytoplasm. The fluorescence from $CheY_6$-YFP was mainly localised to cytoplasmic clusters, although a substantial amount of dif-

fuse fluorescence was seen throughout the cytoplasm; no polar clusters were visible. However, since the $CheY_6$ fusions were nonfunctional, their localisation was also determined by immunogold electron microscopy in the same paper: this method suggested that $CheY_6$ is delocalised throughout the cytoplasm, instead, which is consistent with the requirement of response regulators to be mobile to allow communication between the signaling clusters and the flagellar motor. The presence of the YFP tag on $CheY_6$-YFP may have increased the affinity of the protein for the cytoplasmic cluster possibly by stabilising a conformation that enhances affinity for the cluster or the lower amount of ChY_6-YFP may have altered its localisation pattern. The unexpected result that both $CheY_3$ and $CheY_4$ localise to the cytoplasmic chemotaxis cluster even though no known cognate kinase for these proteins is found there, suggests that $CheY_3$ and $CheY_4$ may interact with a component of the cytoplasmic chemotaxis cluster, although it is not known which yet. The schematic in Figure 1.12 offers a visual summary of the localisation of the chemotaxis proteins in *R. sphaeroides*.

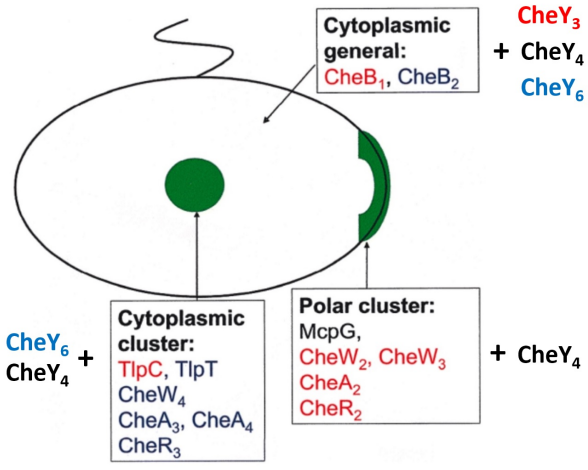

Figure 1.12: Known localisation of chemotaxis proteins in *R. sphaeroides*. Proteins from *cheOp*2 are shown in red, those from *cheOp*3 in blue and those at unlinked loci in black. Image taken from 156.

1.3.6 $CheY_6$-FliM interaction

A wide range of techniques has been used to probe the $CheY_6$-FliM interaction in *R. sphaeroides*. Surface Plasmon Resonance (SPR) experiments have been attempted (Christian Bell, unpublished): $CheY_6$ was attached to a chip surface and a FliM peptide (1-20) was flowed over the surface. No $CheY_6$-FliM binding was detected. *In vitro* pull down assays showed that all six *R. sphaeroides* CheYs bind FliM, the binding being enhanced two- to three-fold by CheY phosphorylation[157]. However, in experiments with fluorescently tagged fusion proteins *in vivo*, it was not possible to distinguish $CheY_6$-FliM binding. In fact, with thousands of $CheY_6$ copies per cell, the relatively small amount of proteins interacting with the flagellar motor could not be visualised. It was also observed that deletion or inactivation of $CheY_6$ results in a non-chemotactic strain (smooth swimming), indicating $CheY_6$ is the only CheY able to stop the motor and make the cell reorient[155]. $CheY_3$ and $CheY_4$ are also believed to interact with FliM, although not triggering a change in flagellar rotation[157]. These results suggest that despite some of the *R. sphaeroides* CheYs may be unable to stop the motor, they might still compete for binding to FliM. This competition could be central to integrating the signals from both the cytoplasmic and polar chemoreceptor clusters. This kind of control would require a complex balance among all of the reactions in which the response regulators are involved (i.e. binding to FliM and to CheA, phosphorylation and dephosphorylation rates, etc.); therefore, the biochemical characterisation of the affinity of each CheY protein for FliM is currently one of the main interests in the field. In particular, the interaction between $CheY_6$ and FliM remains to be characterised at the molecular level, and will be object of the studies reported in chapter 7.

1.4 Microscopy Techniques

1.4.1 Bright-field illumination

Bright-field microscopy is the simplest of all the optical microscopy illumination techniques, not involving the use of any devices that alter the properties of light, such as polarizers or filters. White light is transmitted through the specimen from below and observation is made from above. Contrast in this type of imaging depends on differences in light absorption, refractive index or colour: as light passes through the sample, regions that alter the direction, speed, and/or spectrum of the wavefronts generate optical disparities (contrast) when the rays are gathered and focused by the objective. However, the general lack of contrast in bright-field mode when examining unstained specimens, and even more when imaging transparent bacterial cells, which have a very thin contour (see Figure 1.13), renders this technique capable of providing only a limited degree of information.

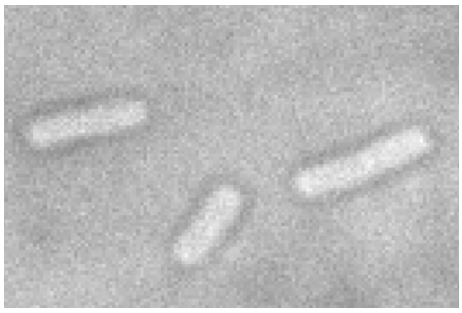

Figure 1.13: Typical bright-field image of *E. coli* cells (example image recorded during this work).

1.4.2 Contrast enhancement methods

Contrast enhancement methods are important for visualising without loss of resolution thin, transparent specimens which modulate the phase but not the amplitude of transmitted light. As most bacterial cells are transparent and are usually imaged within media with refractive index similar to that of water, such as agarose

pads or tunnel slides (see section 2.6.1), they will appear just as bright as the surrounding medium using standard bright-field microscopy and would therefore be very difficult to spot. Prior to the introduction of such techniques, cells and other semi-transparent specimens were rendered visible in bright-field microscopy by artificial staining techniques. Contrast enhancement methods convert the differences in optical density (i.e. the refractive index) of the bacterial cells into different shades of brightness, instead, and are therefore much less invasive and more accurate in the study of biological systems. The optical configuration is designed to exploit the interference of the light which passes through the specimen (the bacteria) with the light that goes around the medium. Two common methods, phase-contrast and differential interference contrast (DIC), are illustrated in Figure 1.14.

Phase contrast

The phase contrast technique employs an optical mechanism to translate minute variations in phase into corresponding changes in amplitude, which can be visualised as differences in image contrast (see 158–160 for extensive reviews). During their journey through cell nuclei, cytoplasm, or water, the light waves are delayed by small degrees, since these media have slightly different refractive indices (the higher the refractive index of a medium, the smaller the speed of light in the medium). The amount of lag is called a phase shift. The amount of the phase shift depends on what media (refractive index) the waves have passed through on their paths, and how long the paths were through these media. The human eye cannot see these phase shifts in the microscope image, it is only able to distinguish between different intensities and colours. Therefore, the phase contrast technique uses optical tricks to translate phase shifts into grey values. Presented in the left side of Figure 1.14 is a schematic illustration of the phase contrast optical configuration. Light from a source, usually a tungsten-halogen lamp, passes through a phase stop (the size of which depends upon objective and condenser numerical aperture) and illuminates the specimen via

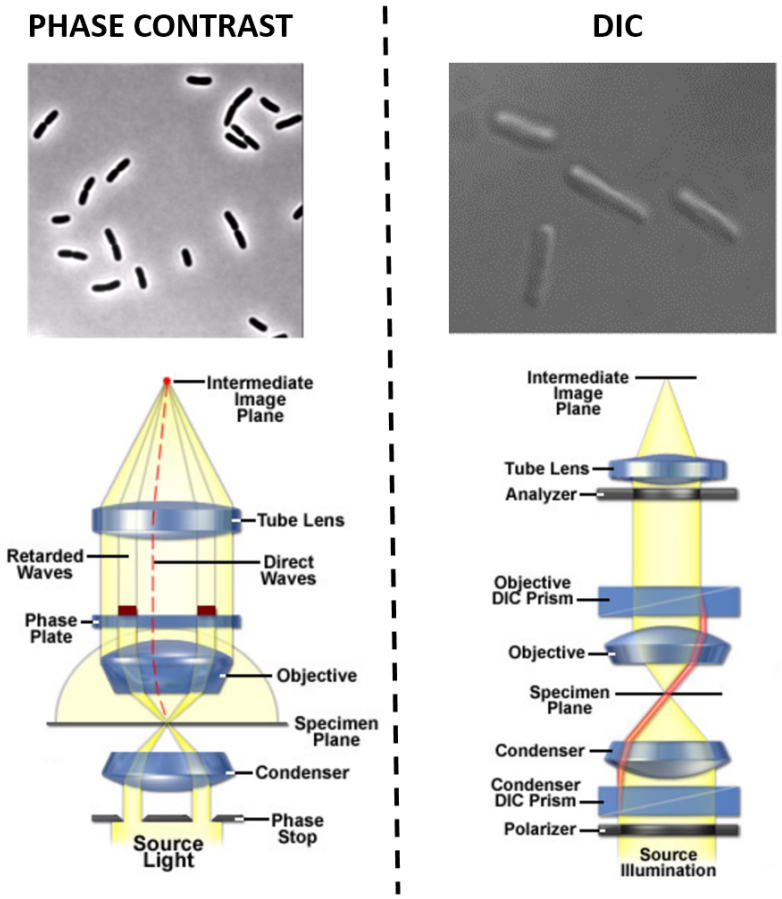

Figure 1.14: Left: typical phase contrast image of *E. coli* cells (top) and phase contrast optical path schematic (bottom). Defocused, parallel light from a source illuminates the sample after passing through a phase stop, which is typically constructed as an opaque flat-black (light absorbing) plate with a transparent annular ring, and is positioned in the front focal plane of the condenser. If the specimen contains sub-structures that have mixed refractive indices, these entities guide the light from the direct waves into new paths (red dotted line). All of the wavefronts are ultimately recombined to form the intermediate image by the tube lens. Right: typical DIC image of *E. coli* cells and DIC optical path schematic. The single starting beam is split into two adjacent beams with orthogonal polarisations by a condenser DIC prism; these beams pass through the specimen before being focused onto a second objective DIC prism which recombines them on the intermediate image plane. Optical configuration images adapted from 158–160.

the condenser optical components in a hollow cone of light. Wavefronts either pass through undeviated or are diffracted (red dotted line) and retarded in phase by structures and phase gradients present in the specimen. Undeviated and diffracted light collected by the objective is segregated at the rear focal plane by a phase plate and focused at the intermediate image plane to form the final phase contrast

image observed in the eyepieces. A major artifact of this type of imaging is the bright halo of light appearing around the cell contour (Figure 1.14, top left). Halos occur in phase contrast microscopy because the circular phase-retarding (and neutral density) ring located in the objective phase plate also transmits a small degree of diffracted light from the specimen. The problem is compounded by the fact that the width of the non-diffracted light (zeroth-order) wavefront projected onto the phase plate by the condenser annulus is smaller than the actual width of the phase plate ring. Nevertheless, phase contrast microscopy allows imaging of living cells in their natural state without necessity of fixing or staining them. As a result, the dynamics of ongoing biological processes, such as in our case directed motion compatible with motor rotation and chemotactic response, can be observed and recorded in high contrast with sharp clarity and minute specimen detail.

Differential Interference Contrast

Differential interference contrast microscopy (Figure 1.14, right side) requires plane-polarised light and additional light-shearing (Nomarski or Wollaston) prisms to exaggerate minute differences in specimen thickness gradients and refractive index (see 158–160 for extensive reviews). Lipid bilayers in the bacterial cell membranes, for example, produce excellent contrast in DIC because of the difference in refractive index between aqueous and lipid phases of the cell. In addition to the increased contrast, DIC exhibits decreased depth of field at wide apertures, creating a thin optical section of the thick specimen. In a typical differential interference contrast optical system, two birefringent prisms are inserted into the optical path, one in the condenser and the second near the objective pupil. The condenser prism performs a vectorial decomposition of the previously linearly polarised light into two beams that are perpendicularly polarised to each other, and laterally shifts these partial beams in such a way that a small lateral displacement of the wavefronts occurs where regions of thickness or refractive index vary. If the two partial beams now

pass through exactly the same structures, no further path difference will occur in the specimen; however, if the two partial beams see slightly different conditions, each of them will run through a slightly different path length on the remaining trip to the intermediate image plane and toward the eyepiece, where an image of the sample can be observed as differences in intensity and colour. The design results in one side of a specimen detail appearing bright while the other side appears darker. This shadow-cast effect often renders the specimen in a pseudo three-dimensional relief (Figure 1.14, top right), which is not however an indicator of any actual topographical structure. Annoying halos, often encountered in phase contrast, are absent in DIC images, but one should keep in mind, however, that since DIC is based on polarised light principles, highly birefringent specimens or those embedded in birefringent materials should not be observed with this technique.

1.4.3 Fluorescent methods

In the last two decades, fluorescence microscopy has become an essential tool in microbial cell biology due to attributes that are not readily available in other contrast modes with traditional optical microscopy. The quantitative nature and high temporal resolution of fluorescence microscopy make it particularly useful for studies of intracellular dynamic systems, such as macromolecular complexes like the bacterial flagellar motors or signalling networks like the chemotaxis one. Several fluorescence-based techniques, in fact, allow not only for static localisation studies, but also for real-time investigation of signal propagation, protein-protein interaction, protein dynamics, diffusion and exchange. In a typical application, the chosen target is marked with a fluorescent probe (e.g. a fluorescent protein or an organic dye, respectively genetically or synthetically encoded) and the fluorescence emission is excited by means of a properly filtered source, observed with an optical microscope and collected by a suitable detector. Through the use of multiple fluorescent

labels it is possible to identify and monitor several target molecules simultaneously.

Principles

The main concepts needed to understand the fluorescence imaging results illustrated in chapters 3-5 and some definitions of related quantities will now briefly be introduced (see 161, 162 for extensive reviews). Fluorescence is the property of some atoms and molecules to absorb light at a particular wavelength and to subsequently emit light of longer wavelength after a brief interval, known as the fluorescence lifetime. The difference between the exciting and emitted wavelengths is called the Stokes shift. By completely filtering out the exciting light without blocking the emitted fluorescence, it is possible to see only the objects that are fluorescent, even down to single molecules if the background is dark enough. The Jablonski diagrams, first conceived by Alexander Jablonski in the 1930s, are a useful graphic tool to understand the details of the excitation and emission process: in these schemes, each molecular level is indicated by a horizontal line, and the electronic levels are in turn split in several horizontal parallel lines, to represent the partition in rotational and vibrational sublevels. In Figure 1.15, radiative transitions like excitation, fluorescence and phosphorescence are drawn as blue, green and orange vertical arrows, respectively, while dark red vertical arrows represent vibrational relaxation due to loss of vibrational excitation energy through energy transfer to the environment caused by collisions with other molecules and solvent interactions; finally, horizontal arrows indicate conserved energy processes like internal conversion and inter-system crossing, where conversion from an electronical to a vibrational excited state occurs. Following radiation absorption, a fluorophore is excited to some vibrationally excited state of a higher electronic level S_i. Internal Conversion is the decay from a molecular state to a lower one with the same spin multiplicity and it is due to loss of energy by collisions with solvent or by dissipation through internal vibrational modes. This process increases as the temperature is raised and has typical times of

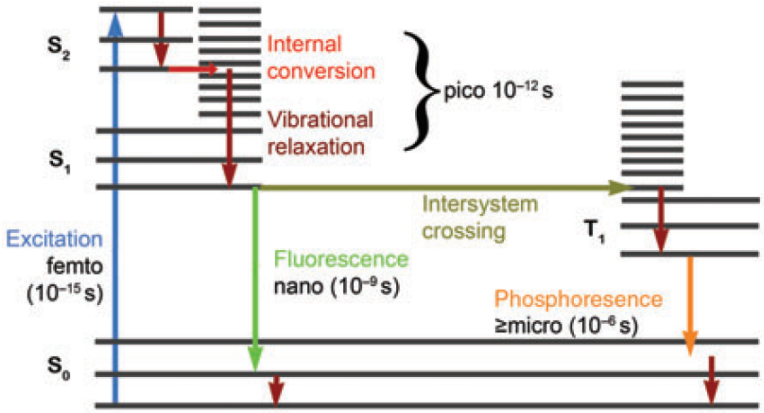

Figure 1.15: General form of a Jablonski diagram: on the left side of the diagram are the singlet states. S0 is the ground state and represents the energy of a molecule that is not being excited by light. In this state, a pair of electrons has the normal configuration with opposite spins. S1 and S2 are more energetic, excited singlet states in which an outer electron is boosted into a different orbital. On the right of the diagram are the triplet states in which an outer electron, boosted to a new orbital, has also undergone a subsequent reversal in spin so that a former pair of electrons has now parallel spins. Also shown, the times that the various steps in fluorescence excitation and emission and phosphorescence take. Image taken from 161.

10^{-12} s or less, thus occurring prior to emission. After excitation, the fluorophore returns to the electronic ground state, but usually on a vibrational level of higher energy, which then thermically relaxes to the fundamental one in about 10^{-12}s. An interesting consequence of emission to higher vibrational ground states is that the emission spectrum is typically a mirror image of the absorption spectrum of the $S_0 \rightarrow S_1$ transition. This similarity occurs because electronic excitation does not greatly alter the nuclear geometry. Hence the spacing of the vibrational energy levels of the excited states is similar to that of the ground state. As a result, the vibrational structures seen in the absorption and the emission spectra are similar. The quantum yield of a fluorophore is a measure of the total light emission over the entire fluorescence spectral range. It is measured as the ratio of fluorescence emission to nonradiative energy losses. A high quantum yield not only increases fluorescence intensity but also means alternative competing photochemical processes associated with intersystem crossing, such as bleaching and free radical formation, are less likely.

Molecules in the S1 state can also undergo a spin conversion to the first triplet state T1. Emission from T1 can occur either by phosphorescence, or by internal conversion, and, since the triplet state generally is lower in energy than the excited singlet, phosphorescence is usually shifted to longer wavelengths relative to fluorescence. Conversion of S1 to T1 is an example of Intersystem Crossing. Transition from T1 to the singlet ground state is forbidden in electric dipole approximation, and as a result the rate constants for triplet emission are several orders of magnitude smaller than those for fluorescence, and therefore the triplet state will display an extremely long radiative lifetime (seconds or longer instead of nanoseconds typical of excited singlets). This means that collisions with other molecules or internal conversion can effectively compete with phosphorescence. This is why it is rarely observed in solution, but rather in solid and de-oxygenated samples, conditions usually very far from biological.

Single-Molecule Fluorescence

Common bioscience experiments observe a large number of molecules, revealing the ensemble average of the measured properties. When observing a single molecule there is no ensemble averaging, allowing one, for instance, to distinguish between homogeneous and inhomogeneous broadening in a distribution of parameters. Fluorescence single-molecule experiments can also reveal dynamic, fast processes like for instance conformational changes and protein exchange in a biological system, and allow for tracking of such molecules in real time. However, imaging experiments of single molecules in cells present many practical challenges: optical signals from single molecules or labels are extremely weak and thus are easily drowned out in a noisy background - they therefore require special care in cleaning the sample from unwanted fluorescent species and the microscope coverglass from possible dirt on the surface, to avoid false positives; it is essential to collect as much signal (i.e. photons) as possible from individual targets and suppress the unwanted noise from

the environment by choosing optimal probes and illumination setting parameters for detection.

Wide-field imaging

The simplest, most common form of wide-field fluorescence microscopy used is epi-illumination (Figure 1.16, a)). Because the excitation volume is very large in the z direction in this kind of illumination, the residual fluorescence from emitters out of the focal plane is also collected, leading to a low contrast in the resulting image. This hinders imaging of thick samples. However, if the sample is thin enough (e.g. bacteria), it is still possible to image single FP-labeled molecules inside the cell with a reasonable signal-to-noise ratio[58,163,164]. A more popular form of wide-field imaging is Total Internal Reflection illumination, which takes advantage of the evanescent field induced by TIR, whose intensity decays exponentially with distance, resulting in a sectioning excitation with a typical probing depth of 100-160 nm along the z direction from the interface for visible light[165] (Figure 1.16, c)). By reducing the region of a signal's provenance, in this way decreasing the background, this method improves the signal-to-noise ratio dramatically compared to epi-illumination. Even with less emissive probes such as FPs, a good signal-to-noise ratio can be achieved. However, one drawback of this technique is that the sectioning effect in turn limits the imaging depth. Therefore, only molecular events occurring at or near the membrane of cells can be probed. This is however not a crucial point for the work described in this thesis, as bacterial flagellar motors are embedded within the cell membrane and therefore good targets for such technique. For photobleaching lifetimes estimation (section 4.1), near-TIR (nTIRF) was sometimes used, a type of illumination that extends the probing depth while minimising background signals by using an incident angle slightly smaller than the critical angle[166] (Figure 1.16, b)).

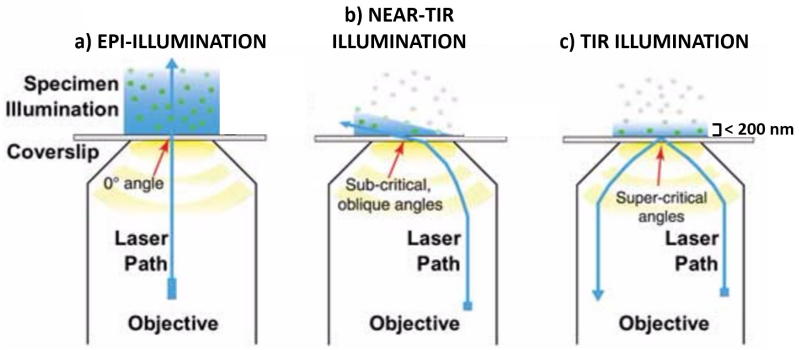

Figure 1.16: Illustration of the three most common wide-field imaging techniques. **a)** Epi-fluorescence microscopy illuminates the whole sample evenly, suffering from a low signal-to-noise ratio. **b)** Near-TIR illumination employs beams directed at subcritical angles to trade-off between increased penetration depth and background minimisation. **(c)** Total internal reflection fluorescence (TIRF) microscopy exploits beam incidence at the critical angle, where total reflection occurs, to establish an evanescence field that penetrates for less than 200 nm into the sample and excites nearby fluorophores, thus reducing the background from other fluorescent components in the cell. Image adapted from 167.

1.5 Aims

The aims of this research are of two kinds: firstly, to establish a suitable procedure to apply the electroporation technique to the study of chemotaxis (and eventually other) proteins in bacteria, namely by:

- Developing a reliable protocol to produce electrocompetent cells with a motile phenotype (both *E. coli* and *R. sphaeroides*);
- Tuning the electroporation parameters (i.e. voltage, amount to incubate with) to introduce a suitable number of labelled proteins in the cell to carry out single-molecule experiments (in both *E. coli* and *R. sphaeroides*);
- Studying the correlation between cell loading and viability (in both *E. coli* and *R. sphaeroides*);
- Studying the correlation between cell electroporation and motility recovery (in both *E. coli* and *R. sphaeroides*);
- Studying the correlation between cell loading and motility recovery (in *E.*

coli);

Secondly, to exploit such technique to investigate the interaction of *E. coli* CheY and *R. sphaeroides* $CheY_6$ with FliM, quantify their dynamic behaviour and compare the results obtained with both what previously reported in the literature and between the two species. Specifically:

- Image and track single CheY proteins, labelled with a fluorescent organic dye of choice, while diffusing within the cell, binding to the sensory cluster(s) and to individual flagellar motors;
- Measure their diffusion coefficient, binding constants and dwell times at the switch complex;
- Correlate fluorescence and motility in electroporated tethered cells;
- Present evidence that supports recently proposed hypotheses (see section 6.2).

Chapter 2

Materials and Methods

Recipes for all media and buffers are included in appendix A.

2.1 Strains and Plasmids

Strains and plasmids used in this study are summarised in Table 2.1 and Table 2.2, respectively. Strains EW668 and EW669 were obtained by P1 phage transduction of JPA945 strain with JW1877-1 and JW1870-2 strains from the KEIO collection[168] as described in 169.

2.1.1 Storage

Stationary-phase cultures of *E. coli* and *R. sphaeroides* strains were preserved in a 3:2 mixture of appropriate growth medium and sterile glycerol (50% v/v). Cryotubes (Sarstedt) containing 1 ml of this mixture were flash-frozen in liquid nitrogen and stored at -80°C.

Strain	Species	Genotype/Description	Source/Reference
XL1-Blue	*E. coli*	General cloning strain, used for plasmid creation and modification. Tet^R	Stratagene
DH5α	*E. coli*	General cloning strain, derived from K12, used for plasmid creation and modification.	Life Technologies
BL21(DE3)	*E. coli*	Competent *E. coli* cells used for the expression of recombinant proteins with pET vectors.	Life Technologies
BL21(DE3)pLysS	*E. coli*	Competent *E. coli* cells used for the expression of recombinant proteins with pET vectors. CM^R	Life Technologies
M15[pREP4]	*E. coli*	Strain - containing pREP4 plasmid - used for the expression of recombinant proteins with pQE60 vectors. Kan^R	QIAGEN
RP437	*E. coli*	Wild type for motility	170
JPA802	*E. coli*	RP437, *fliC(sticky)*	M. Tipping
RP5232	*E. coli*	RP437, $\Delta cheY$	170
JPA2900	*E. coli*	RP437, $\Delta cheY$, *fliC(sticky)*	Gift from N. Delalez
JPA1814	*E. coli*	RP437, *fliM-yPet*, *fliC(sticky)* , 6aa linker	Gift from N. Delalez
JPA945	*E. coli*	RP437, *fliM-yPet*, 6aa linker	Gift from N. Delalez
EW668	*E. coli*	RP437, *fliM-yPet*, $\Delta cheA$, Kan^R	Gift from O. Afanzar
EW669	*E. coli*	RP437, *fliM-yPet*, $\Delta cheZ$, Kan^R	Gift from O. Afanzar
UU2689	*E. coli*	RP437, *cheZ-cfp*	Gift from S. Parkinson
WS8N	*R. sphaeroides*	Spontaneous nalidixic acid resistant strain of the wild type strain WS8.	171
JPA1447	*R. sphaeroides*	WS8N *cfp-cheW*$_3$, *yfp-cheW*$_4$	153
JPA1674	*R. sphaeroides*	WS8N *yPet-fliM*	M. T. Brown

Table 2.1: Strains used in this work.

2.2 Growth conditions

- *E. coli* liquid cultures for protein expression were grown aerobically at 37°C with shaking at 225 rpm in Luria-Bertani (LB) medium and/or in 2X TY rich medium. Electrocompetent *E. coli* cells were grown aerobically with shaking at 225 rpm in TB medium at 30°C.

Plasmid	Description	Source/Reference
pFN29A	T7 RNA polymerase-driven protein expression vector, N terminus 6xHis-Halo Tag. Amp^R	Promega
pIND4	IPTG inducible plasmid for gene expression. Kan^R	172
pIND4-Y	pIND4 containing *E. coli* WT *cheY*.	This study
pQE60	Protein expression vector, C terminus 6xHis tag, inducible *lac* promoter. Amp^R Used to express WT CheY and mutants.	QIAGEN
pQE60-Y	pQE60 containing *E. coli* WT *cheY*.	This study
pQE60-YNC	pQE60 containing *E. coli cheY* with Cys at N terminus.	This study
pQE60-YCC	pQE60 containing *E. coli cheY* with Cys at C terminus.	This study
pQE60-**YNC	pQE60 containing *E. coli cheY*** [173] with Cys at N terminus.	This study
pQE60-**YCC	pQE60 containing *E. coli cheY*** with Cys at C terminus.	This study
pFloat	Entero-bacterial protein expression vector derived from pET30a (Novagen), 6xHis and solubility tags, human rhinovirus 3C protease cleavage sequence.	174
pFloat-YNC-His	pFloat containing *E. coli cheY* with Cys at N terminus, 6xHis-tag at C terminus and cleavage site.	This study
pFloat-SUMO-YNC	pFloat containing *E. coli cheY* with Cys at N terminus, 6xHis-SUMO tag at N terminus and cleavage site.	This study
pCA24N	Protein expression vector, N terminus 6xHis tag, GLCGR C' linker, IPTG inducible *lac* promoter. CM^R. Used to express CheY(I95V) [175] mutant.	176
pBAD33	Arabinose protein expression vector. CM^R. Used to test *E. coli* cells' electrocompetency.	Beckwith Lab
pQE80	Protein expression vector, N terminus 6xHis tag, inducible *lac* promoter and *lacI*.	QIAGEN
pQE80-Y6(A134C)	pQE80 containing *R. sphaeroides* $cheY_6$with (A134C) point mutation.	This study (M. W. Smith)

Table 2.2: Plasmids used in this work.

Frozen stocks or liquid samples requiring selection were streaked out on solid LB agar plates (2% w/v agar) and grown at 37°C.

- *R. sphaeroides* liquid cultures were grown in Succinate medium (SUX) at 30°C, either aerobically with shaking at 225 rpm, or photoheterotrophically in sealed containers with minimal air space, under white light and without shaking. In

both cases, two to three days' growth was required for a stationary culture.

Electrocompetent *R. sphaeroides* cells were grown aerobically with shaking at 225 rpm in SUX medium at 30°C without additional antibiotic.

Frozen stocks or liquid samples requiring selection were streaked out on LB agar plates containing 2% w/v agar and nalidixic acid and incubated for at least 48 hours at 30°C.

2.2.1 Antibiotics

When required, the appropriate antibiotic(s) was (were) added to either liquid or solid growth media at the working concentrations given in Table 2.3. Stock solutions were prepared 1000-fold more concentrated than such concentrations, filter sterilised, aliquoted and stored at -20°C.

Antibiotic	**Concentration for *E. coli* (μg/ml)**
Kanamycin	25
Chloramphenicol	34
Ampicillin	100
Tetracycline	25
Antibiotic	**Concentration for *R. sphaeroides* (μg/ml)**
Nalidixic Acid	25

Table 2.3: Antibiotic concentrations used in this work.

2.3 Genetic techniques

2.3.1 DNA extraction

Plasmid extraction

E. coli cultures containing the plasmid of interest were grown overnight in LB broth and the appropriate antibiotic at 37°C. Sequencing quality plasmid DNA was extrac-

ted using the QIAprep Spin Miniprep Kit (Qiagen) for high copy number plasmids, following the instructions provided. DNA was eluted in MilliQ water and stored at -20°C.

Extraction of *R. sphaeroides* genomic DNA

Cultures were grown aerobically to stationary phase (∼48 hours). 1 ml of culture was centrifuged and flash-frozen in liquid nitrogen. The frozen pellet was resuspended in 500 μl of lysis buffer (see appendix A) and heated up to 65°C. 100μg of proteinase K was added before incubation at 45°C for 2 hours. Chromosomal DNA was extracted twice with phenol:chloroform:isoamyl-alcohol (500 μl , 25:24:1) and precipitated with 100% ethanol at -20°C for 30 mins. The sample was then centrifuged (16000 x g, 15 mins), the pellet washed with 70% ethanol, and centrifuged again as above. The pellet was finally dried at 37°C overnight, resuspended in 50 μl sterile water and stored at -20°C.

2.3.2 Cloning

Polymerase Chain Reaction (PCR)

PCRs for amplification of a section of genomic of plasmid DNA were carried out with reaction mixture composition as described in Table 2.4 in a final volume of 50 μl of liquid. Unless stated elsewhere, reaction mixtures were then run in a Techne TC-3000 thermocycler using the program described in Table 2.5, annealing temperatures were chosen based on the melting temperature (T_M) of the primers. Amplifications for *E. coli cheY* gene and its mutants were performed using Phusion High-Fidelity HF DNA Polymerase (New England Biolabs), while amplifications for *R. sphaeroides* $cheY_6$ were performed using *Pfu* DNA polymerase (Promega). All primers (listed in appendix B) were synthesised by Sigma-Genosys.

Component	Quantity (μl)
Template DNA	0.5-1
Primers	1 of each at 100 μM
	2.5 of each at 10 μM for Gibson cloning (section 2.3.2)
DNA Polymerase	0.5
DNA Polymerase Buffer	5 (10x *Pfu*) / 10 (5x HF)
dNTPs	5 at 2.5 mM
DMSO	2.5 for 5%
MilliQ	Make up to total volume of 50 μl

Table 2.4: Composition of PCR reaction mixtures.

Step	Temperature (°C)	Time
Initial denaturation	98	10 min
Repeat the following cycle 30 times:		
Denaturation	98	2 min
Annealing	T_M specific	1 min
Extension	72	15-30 seconds per kbp of DNA
Final extension	72	5 min
Hold sample	4	indefinite

Table 2.5: PCR reaction program. For $cheY_6$'s gene amplification only, denaturation time was set to 1 minute and extension time to 2 min per kbp of DNA.

Gibson Assembly

Plasmids pFloat-YNC-His and pFloat-SUMO-YNC were constructed using seamless cloning methods (Gibson Assembly, New England Biolabs)[177]. The entero-bacterial expression vectors pFloat[174], derived from pET30a (Novagen) and engineered to include N terminal His6- and Small Ubiquitin-like Modifier (SUMO) solubility tags, and a human rhinovirus 3C protease cleavage sequence (LEVLFQ/GP) were used. SUMO proteins are small, around 100 amino acids in length and 12 kDa in mass. SUMO modification has the function of enhancing protein stability, cytosolic transport, and transcriptional regulation. Such tag was removed after expression and purification of Cys-modified CheY using PreScission Protease, a genetically engineered fusion protein consisting of human rhinovirus 3C protease and GST (Gluta-

thione S-transferase) which specifically cleaves between the Gln and Gly residues of the recognition sequence of LeuGluValLeuPheGln/GlyPro.

Restriction enzyme digests

Unless stated elsewhere, DNA digests were carried out using restriction enzymes from New England Biolabs (NEB) following the instructions provided by the manufacturer. Restriction digests were carried out using the supplied buffers in a total volume of 50 μl (no need to use Bovine Serum Albumine - BSA). Restriction enzyme digest reaction mixtures (as described in Table 2.6) were incubated for at least 2 hours at 37°C.

Component	Quantity (μl)
DNA	1
10 x buffer	5
Enzyme	1 of each
MilliQ	Make up to total volume of 50

Table 2.6: Restriction enzyme digest reaction mixture composition.

Gel electrophoresis

DNA fragments were separated using gel electrophoresis. Multi-purpose agarose (Roche) was dissolved in 0.5x TBE buffer (see appendix A) at concentrations ranging between 0.8 and 2% (w/v) to optimise separation of the particular size of DNA fragments expected. DNA samples mixed with DNA loading dye were loaded on the gel alongside 1kb-plus DNA ladder (Invitrogen) and electrophoresed at a constant voltage of 130 V for ∼1 hour through 0.5x TBE buffer. The gel was stained in 1 ng/ml ethidium bromide for 10-15 min, rinsed in water and the position of DNA fragments visualised using a UV transilluminator (λ = 360nm). Bands of interest were then excised using a clean razor blade for further purification.

Purification of DNA fragments

DNA fragments were purified from agarose gel bands using the QIAquick Gel Extraction Kit (QIAGEN). Purified DNA was eluted in 50 μl MilliQ water and stored at -20°C.

DNA ligation

Digested products were ligated in 20 μl final volume mixtures containing T4 DNA ligase (New England Biolabs) and the appropriate buffer according to the manufacturer's instructions. The volumes of vector and insert DNA were adjusted to give a molar ratio of about 1:3 (total amount of DNA present $\sim$1 μg); the mixtures were incubated overnight at 16°C and subsequently transformed into freshly made competent cells (section 2.3.3 and 2.3.4).

Sequencing

DNA sequencing was performed by the Automated DNA Sequencing Service from Geneservice (Source BioScience). Sequences were analysed using Clone Manager Professional version 9.0 (Sci Ed Central) or the EMBOSS Needle Pairwise Sequence Alignment tool (`http://www.ebi.ac.uk/Tools/psa/emboss_needle/nucleotide.html`).

2.3.3 Competent cells

Cells were made either chemically competent, using the rubidium chloride method, or electrocompetent. In the former case, cells were used for cloning purposes, whereas in the latter cells were used for electroporation experiments (see chapter 3).

Chemically competent *E. coli*

E. coli cells were made chemically competent as follows: 50 ml of LB-broth were inoculated with 1 ml of stationary phase *E. coli* and incubated at 37°C until it reached an OD_{600nm} of 0.3-0.5. The culture was then transferred to a 50 ml falcon tube and incubated on ice for 15-30 minutes, before being centrifuged at 1000 x g for 10 minutes at 4°C. The pellet was resuspended in 16 ml of ice cold TFB-I buffer (see appendix A) and incubated on ice for 1 hour, before being centrifuged again at 750 x g for 10 minutes at 4°C. The pellet was this time resuspended in 2 ml ice cold TFB-II buffer (see appendix A); resuspended cells were divided into 100 μl aliquots, flash frozen in liquid nitrogen and stored at -80°C.

Electrocompetent *E. coli*

An ad-hoc, slightly modified version of the traditionally adopted protocol from 178 was used to prepare electrocompetent *E. coli* cells. In order to ensure that electrocompetent cells were motile (both swimming and spinning) before starting the electroporation protocol (see chapter 3), the growth temperature was reduced to 30°C instead of the prescribed 37°C , and the LB rich medium was replaced with TB medium, both modifications known to yield optimal motility[179]: 500 ml of Tryptone Broth (TB) medium (see appendix A) were inoculated with ∼4 ml of an overnight culture and incubated in a 2L flask at 30°C with agitation. The OD_{600nm} of the culture was measured every 30 min, until it reached about 0.4. Growth was then stopped by putting the flask on ice and swirling it gently to ensure homogeneous cooling. In this protocol, to achieve maximum efficiency of transformation, it is crucial that the temperature of the bacteria does not rise above 4°C at any stage. From here onwards, the same steps as in 178 were carried out, namely a 20 min wash with MilliQ water plus 3x20 min washes with 10% Glycerol, all at 4°C and 1000 x g, to reduce the ionic strength of the cell suspension and avoid arcing during application

of the electric pulse (see section 3.3.3). The cell pellet was then resuspended in 1 ml of GYT medium (see appendix A) and 40 μl aliquots, fast-frozen in liquid nitrogen and stored at -80°C.

Cell motility before and after the washing steps was checked by microscopic examination and confirmed. Electrocompetence was tested qualitatively by incubating cells with 1 μl of pBAD33 plasmid carrying a resistance gene to Chloramphenicol antibiotic and performing electroporation (see chapter 3); cells plated on LB-agar+Chloramphenicol and incubated overnight at 37°C showed unaffected growth, whereas, as a control, electroporated cells without pBAD33 did not grow at all.

Electrocompetent *R. sphaeroides*

Cells from frozen stocks of interest were streaked on LB agar plates and incubated at 30°C for 48 hours. 2 ml of SUX + Nal (1:1000 dilution from a 20 mg/ml stock in water) were then inoculated and liquid cultures grown photoheterotrophically in 1.7 ml eppendorfs upside down at room temperature for 24-36h. 500 ml of SUX medium in a 2L flask was inoculated with 125 μl (1:4000 dilution) of the stationary phase bacterial culture and grown aerobically at 30°C with agitation at 225 rpm overnight. Next morning, the OD_{700nm} of the culture was measured every 30 min, until it reached about 0.4. Growth was then stopped by putting the flask on ice and swirling it gently to ensure homogeneous cooling. As with *E. coli*, to achieve maximum efficiency of transformation, it is crucial that the temperature of the bacteria does not rise above 4°C at any stage. Cells were washed twice with MilliQ water and then once with 10% Glycerol for 15 min, all at 4°C and 3000 x g, to reduce the ionic strength of the cell suspension and avoid arcing during application of the electric pulse. The cell pellet was then resuspended in 1 ml of ice-cold 10% Glycerol and 40 μl aliquots, flash-frozen in liquid nitrogen and stored at -80°C.

2.3.4 Internalisation methods

Transforming *E. coli* by heat-shock

Fully formed plasmids were inserted into *E. coli* by heat-shock. A 100 μl frozen aliquot of chemically competent cells was thawed on ice and incubated, always on ice, with plasmid DNA for 30-45 min. For ligation products, 25 μl of ligation mixture was added, for purified plasmid 1 μl was added. The cells were then heat-shocked by immersing them in a 42°C water bath for 45 s and then immediately put on ice for 2 min. 800 μl of LB medium was then added and cells incubated at 37°C for *at least* 1 hour. Cells were finally spread onto LB agar plates containing appropriate selective antibiotics and incubated overnight at 37°C.

Internalisation by electroporation

In this work, a MicroPulser^{TM} Electroporator (Bio-Rad) was used to apply an electric field of chosen intensity and allow for internalisation of dye-labelled proteins of interest. Figure 2.1 shows a visual summary of a typical experiment: first, electrocompetent cells were incubated with the fluorescent dye labelled protein of interest; secondly, an electric field of opportunely chosen strength was applied to allow for internalisation of part of the fluorescent molecules in solution; cells were then recovered and washed several times to remove non-internalised molecules; imaging was finally performed in white-light and in fluorescence. A more detailed procedure is described in the following: one 40 μl aliquot of electrocompetent cells of a chosen strain was thawed on ice for 10-20 minutes; one 0.1 cm electroporation cuvette and one 1.7 ml sterile eppendorf tube labelled NEP (Non-Electroporated, *Positive Control*) were put on ice, as well; other 2 sterile eppendorf tubes labelled *Negative Control* and EP (Electroporated) were lined up in a rack at room temperature.
The *Negative control* sample was prepared by adding 1 μl of cells from the above

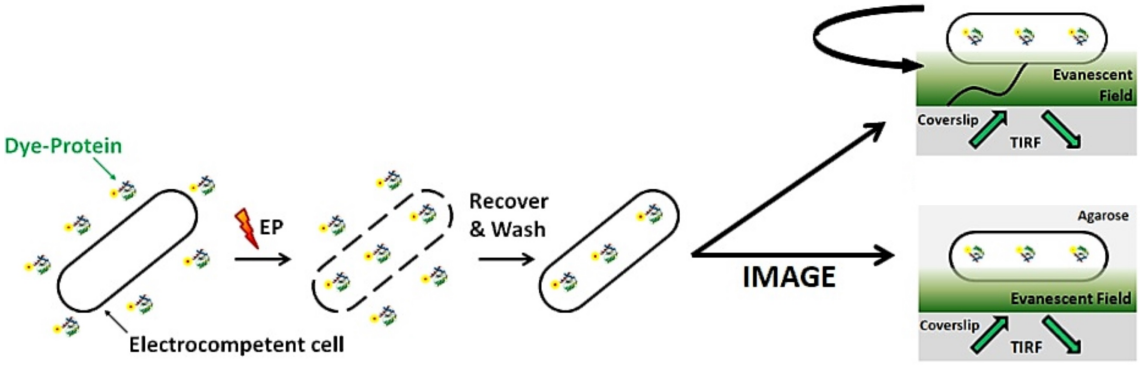

Figure 2.1: Steps of a typical electroporation experiment: electrocompetent cells were incubated with the fluorescent molecules of interest prior to electroporation; after internalisation, they were recovered in rich medium, extensively washed and imaged.

aliquot to either 9 μl of Motility Buffer (MB) for *E. coli* or SUX medium for *R. sphaeroides* (see appendix A for recipes). Half volume of the starting aliquot of cells ($\sim$20 μl) was then transferred into the chilled NEP eppendorf and the remaining named as EP cells; the chosen quantity of fluorescently labelled protein was then added to both EP and NEP samples; using a thin gel-loading tip, the EP sample was transferred into the chilled electroporation cuvette and incubated on ice for 1-2 minutes; after wiping out very well the cuvette to remove possible water on the electrodes, an electric field of the chosen strength was applied to the cell suspension (details for each experiment are reported in chapter 3). 500 μl of SOC for *E. coli* and SUX for *R. sphaeroides* was immediately added to both EP and NEP samples, the EP cells transferred to the clean eppendorf tube previously prepared at room temperature and EP and NEP samples recovered at 30°C, 450 rpm in a Thermo-mixer (Eppendorf). The recovery time varied according to the kind of experiment that was being carried out. EP and NEP cells were washed with either MB (*E. coli*) or SUX (*R. sphaeroides*) for 1 minute at 7000 rpm in a bench-top centrifuge, for 4 times; cell pellets resuspended in 90-150 μl of MB/SUX and prepared for imaging in one of the two ways described in section 2.6.1.

2.4 Protein Techniques

2.4.1 Overexpression of Cys-modified *E. coli* CheY/CheY**

In a first attempt, genes of interest were cloned into a pFN29A 6xHis-Halo Tag vector configured to append the 6xHis-Halo Tag to the amino-terminus of the protein fusion partner, providing T7 RNA polymerase-driven protein expression in *E. coli*. This approach was not successful, as there was very little or no protein overexpression, as verified via expression trials. In a second, this time successful, attempt, Cys-modified *cheY* and *cheY*** genes were cloned in a pQE60-His6Tag vector. In the case of N terminal cysteine modification, a Cys was inserted after the first aminoacid (M1) in WT CheY sequence; in the case of C terminal cysteine modification, a Cys was inserted after the last aminoacid in WT CheY sequence (M129), but before the 6xHis tag of pQE60. Formation of correct constructs was checked by sequencing. Recombinant pQE60-derivative plasmids encoding for the different proteins of interest were transformed into *E. coli* M15[pREP4] competent cells by heat-shock (see section 2.3.4), plated onto LB agar + Amp and incubated overnight at 37°C. Before starting large scale cultures, expression trials were carried out at four conditions of temperature and duration to assess which one would yield the best overexpression: 18°C overnight, 25°C overnight, 25°C 5h, 30°C 5h, with the latter resulting the best trade off between time required and yield. Single colonies were picked for a 25 ml overnight culture containing appropriate antibiotics (Amp and Kan, in this case). 500 ml of 2X TY rich medium (see appendix A) were inoculated with 10 ml of stationary overnight culture. Two 2L flasks were used per protein, i.e. 1L of growth media. Cells were grown at 37°C with shaking at 225 rpm until midlog phase. At this stage, IPTG was added to a final concentration of 0.1 mM to induce protein expression. Cells were incubated for another 5h at 30°C before being centrifuged at 7000 x g for 20 min at 4°C and harvested.

2.4.2 Purification of Cys-modified *E. coli* CheY/CheY**

In preliminary studies, a purification protocol presented in 180 was tested, based on CheY's affinity to cibacron blue dye and therefore presenting the advantage of not involving the use of any tags or labels on the protein itself. In fact, such modifications, despite simplifying purification procedures, might alter to a certain extent the native structure/function of the protein, and, where applicable, involve also cleaving steps after purification. However, despite successful overexpression of WT CheY from BL21(DE3)PLysS *E. coli* cells transformed with the inducible expression vector pIND4, no purified protein was obtained.

A different approach was then followed. Exploiting the presence of a C terminal 6xHis tag, proteins were purified using nickel affinity chromatography: cell pellets from section 2.4.1 were resuspended in lysis buffer (see appendix A) in presence of 1 mM DTT, a disulphide bond reducing agent, one tablet of SIGMAFAST^{TM} Protease Inhibitor Cocktail EDTA-Free and Benzonase nuclease (Sigma-Aldrich); cells were lysed by sonication on ice using the Vibracell sonicator with settings 60% amplitude, 4 mins sonication time, 5 s on, 15 s off (total time 16 minutes per protein). Lysates were cleared by centrifugation at 36000 x g for 45 min and filtered through a 0.45 μm filter. A nickel affinity chromatography column was prepared by pouring 1 ml Ni-NTA Agarose slurry (Bio-Rad) into a chromatography drip column, allowing to settle for 10 min and equilibrating with 30 column volumes (30 ml) of lysis buffer. The filtered cleared lysate was applied to the column and run through. Protein was allowed to bind and the column was washed with at least 50 ml of lysis buffer before being eluted with 10 ml of elution buffer (see appendix A) with TCEP, an even stronger reducing agent. Six 1 ml fractions of the eluate were collected and stored at 4°C (protein usually elutes mostly in the first three fractions).

2.4.3 SDS-PAGE

Overexpressed proteins' purity and identity were assessed by size comparison using SDS-PAGE (sodium dodecyl sulfate polyacrylamide gel electrophoresis). An appropriate amount of 4x RunBlue LDS Sample Buffer (Expedeon) and β-mercaptoethanol reducing agent (in a volume ratio of 1:5) were added to samples to be visualised. Protein samples and cell pellets were boiled at 100°C for 10 min to denature, loaded on a precast 4-20% acrylamide gel, alongside a Benchmark Protein Ladder (Invitrogen). Gels were run for 1 hour in SDS-PAGE running buffer (see appendix A) at 165 V, 110 mA (per gel), stained and visualised using Instant Blue, a Coomassie based staining solution.

2.4.4 Overexpression and purification of Cys-modified *E. coli* CheY(I95V)

E. coli DH5α cells containing plasmids of interest were aerobically grown in 1 L of LB (see appendix A) with the appropriate antibiotic at 37°C, 225 rpm. After reaching OD_{600nm} 0.5, cells were induced with 1 mM IPTG at 37°C and further incubated for 3 hours. Cells were harvested by centrifugation for 10 min at 7000 x g and resuspended in 5 ml of 50 mM sodium-phosphate buffer, pH 7 supplemented with 300 mM NaCl, 0.1% Triton x100, 10mg DNase1 and 10mg lysozyme at 4°C. Cells were lysed by sonication on ice using 60% amplitude, 4 mins sonication time, 5 s on, 15 s off (total time 16 minutes per protein). The lysate was then centrifuged at 10000 x g for 20 min at 4°C to remove cellular debris, the supernatant collected, and incubated with 2 gr of Protino Ni-TED beads[181] for 30 min at 4°C. The beads were washed for 5 times with 50 ml of 50 mM sodium-phosphate buffer, pH 7 supplemented with 300 mM NaCl at 4°C. The protein was eluted from the beads for 5 times with 3 ml (each) of 50 mM sodium-phosphate buffer, pH 7 supplemented with 300 mM NaCl

and 200 mM Imidazole at 4°C. The eluted protein was filtrated and de-salted with an Amicon centrifugal device (3 kDa Molecular Weight Cut-Off) for 3 hours at 7000 x g at 4°C. The flow-through was discarded and the sample diluted with 50 mM sodium-phosphate buffer, pH 7 supplemented with 1 mM $MgSO_4$. The dilution step was repeated three times. Finally, the sample was concentrated to 200-500 μl in volume. The protein yield obtained was in the range 2-20 mg/ml.

2.4.5 Overexpression and purification of *R. sphaeroides* $CheY_6$(A134C)

E. coli BL21 (DE3) cells containing plasmids of interest were aerobically grown in 1L of 2xTY rich medium (see appendix A) with appropriate antibiotic/s at 37°C, 225 rpm. After reaching OD_{600nm} 0.6-0.8, cells were induced with 1 mM IPTG at 18°C and incubated overnight. Cells were harvested by centrifugation for 20 min at 7000 x g and resuspended in 30 ml of lysis buffer (see appendix A). Cells were lysed by French Press (3 passes, 1000 psi) and lysate centrifuged (36000 x g, 1 hour) to remove cell debris and insoluble material. The supernatant was then filtered through a 0.45 μm filter and applied to a Ni-NTA Agarose (QIAGEN) column. The column was pre-equilibrated with 5 volumes of lysis buffer, the protein allowed to bind, then washed with other 5 volumes of lysis buffer and the protein eluted in lysis buffer (no protease inhibitor) containing 200 mM imidazole. Protein purity was assessed using SDS-PAGE gels.

2.4.6 Size exclusion chromatography

To remove impurities still present in the protein samples purified by Ni-NTA affinity chromatography, size exclusion chromatography (gel filtration) was used. The protein fractions were centrifuged at 10000 x g for 10 min at 10°C to precipitate eventual

aggregates, injected onto a S75 gel filtration column (HiLoad 16/600 Superdex 75 pg, GE Healthcare) connected to an AKTA system and run through with Labelling buffer (see appendix A) at a flow rate of 1 ml/min. The void volume (50 ml) was discarded and fractions of 1 ml collected for approximately 80 ml. UV absorption at 280 nm was used to identify fractions containing protein and SDS-PAGE was used for size confirmation. Fractions containing the protein of interest, usually 3-10 ml total, were combined and concentrated using a centrifuge concentrator (5 kDa Molecular Weight Cut-Off). The column was washed in MilliQ, then 20% ethanol after every run.

2.4.7 Protein concentration determination

Final protein concentration was determined using the Bradford assay[182]. To form the standard curve, 20 μl serial dilutions of bovine serum albumin (BSA) in MilliQ from a stock at 1.5 mg/ml were made, concentrations ranging between 0 mg/ml to 0.8 mg/ml (minimum 5 different concentration points required). Triplicates of each concentration were made for greater accuracy. The Bradford solution was prepared mixing 1 part of concentrated Bradford reagent (stored at 4°C) to 4 parts of MilliQ and filtered through Whatman paper. 1 ml of Bradford solution was added to each of the 20 μl BSA solutions and these were incubated for 5 min; at the end of this time, Abs_{595nm} measured and values plotted to give a standard curve. Protein samples were diluted in 20 μl such that their concentrations fell within the straight portion of the standard curve (0.3-0.6 mg/ml)and treated in the same way. Abs_{595nm} readings were compared to the standard curve to estimate protein concentration.

2.5 Protein-dye conjugation

2.5.1 Labelling

Pure protein aliquots from 2.4.6 were stored in a buffer suitable for maleimide dye labelling (Labelling buffer, see appendix A) in presence of TCEP reducing agent to avoid aggregation and oxidation of the cysteine's -SH groups and with optimal pH for the cysteine-maleimide reaction to occur ($\sim$7.4). An appropriate number of aliquots of pure protein were thawed on ice. 280 nm absorption of all of them was re-measured on a spectrophotometer, respective concentrations compared with values found in section 2.4.7 and confirmed; if necessary, protein was diluted with Labelling buffer to reach a final concentration in solution of 50-100 μM, and a reaction volume of 200-300 μl. Between 6x and 20x molar excess of the chosen maleimide dye resuspended in dimethyl sulphoxide (DMSO) was then added. For compounds with low aqueous solubility, like most fluorescent dye maleimides, use of organic co-solvent, such as DMSO is essential. Percentage of DMSO to protein was always kept $< 3\%$ vol/vol. Labelling reactions were allowed to proceed in the dark overnight or for one hour either at 4°C or at room temperature; for each of these conditions, sensitivity of the labelling buffer to temperature was taken into account when adjusting the reaction's pH to 7.4.

2.5.2 Free dye removal

Removing free, unreacted dye after labelling was essential in order to avoid false fluorescent positives during microscopy imaging. The dye-protein labelling reaction products were therefore run on a suitable size exclusion column (i.e. Superdex 75 HR 10/30 or Hiload 16/600 Superdex 75 pg) connected to an AKTA machine. The latter was provided with UV and Visible detector lamps to monitor elution profiles of both free dye and labelled (or unlabelled) protein. In the following, presence of

some unlabelled proteins in the final sample was not an issue, as these were not fluorescent and therefore did not constitute false positives or background for the labelled proteins once internalised inside the cells.

The column was equilibrated first with water and then with Electroporation buffer (see appendix A). The sample was spun down for 2 min at max speed in a bench-top centrifuge to pellet eventual aggregates at the bottom of the tube and avoid column clogging. Supernatant was separated from the pellet and injected onto the column using a Hamilton syringe and run through electroporation buffer at the recommended flow rate of the column in use (0.5-1 ml/min). The pellet was in turn resuspended in 200 μl of Labelling buffer and stored at 4°C to run on a gel together with purified fractions. The void volume of the column was discarded and fractions of 500 μl collected in a "raster scan" fashion. The column was washed in MilliQ, then 20% ethanol after every run.

Fractions corresponding to labelled protein were distinguished from those containing only free dye or other side products by careful analysis of the elution profiles: chromatograms for absorption at 280 nm and absorption at the dye's maximum excitation wavelength were compared and overlap of the two peaks confirmed.

2.5.3 Visualisation, concentration, storage

In order to decide which elution fractions to mix to make the final sample, selected ones both in the proximity of the peak of interest (i.e. labelled protein) and away from it were run on a SDS PAGE gel. Bands were then scanned for dye's fluorescence using a UV-Vis Pharos FX Plus Molecular Imager (Bio-Rad) and subsequently stained with Instant Blue (see section 2.4.3) to check for protein presence. Fractions positive for both dye's and protein's presence were then combined and concentrated down to a final working concentration of 2-60 μM and stored either in 50% Glycerol at -20°C or at 4°C.

2.5.4 Quantification of labelling yield

The degree of labeling, i.e. the dye/protein ratio in the final labelled protein sample, was estimated by measuring the absorption spectra of the species involved on a spectrophotometer and inserting the resulting quantities into the standard formula[183]:

$$\frac{Dye}{Protein} = \frac{A_{max}\,\varepsilon_{Protein}}{[A_{280} - (correction\,factor)\,A_{max}]\,\varepsilon_{Dye}} \tag{2.1}$$

where A_{max} is the maximum absorption of the dye at its excitation peak, A_{280} is the maximum absorption of the protein at 280 nm, $\varepsilon_{Protein}$ and ε_{Dye} are the protein's and the dye's extinction coefficients (in units of $M^{-1}cm^{-1}$) respectively, and the $correction\,factor$ accounts for absorption of the dye at 280 nm.

2.6 Visualising bacterial cells

2.6.1 Sample preparation

According to the particular kind of experiment carried out, described in chapters 6 and 7, samples for imaging were prepared in two alternative ways, using agarose pads or tunnel slides, respectively.

Agarose pads

Agarose pads for *E. coli* cells deposition were created by pipetting a droplet (∼300 μl) of 1% agarose (BD/DIFCO) in Motility buffer (MB) (see appendix A) on the centre of a coverslip and leaving it to spread a little until naturally set. The pad should not be too flat, but raised about 0.5 - 1 mm from the bottom glass. In the case of internalisation and viability tests, MB was replaced with EZ Rich Defined Medium (RDM, non-autofluorescent) to ensure cell growth and division. For *R.*

sphaeroides, pads were made using a solution of 1% agarose in Succinate medium (SUX) (see appendix A). The pad was left to dry out for 10-15 min, after which 5 μl of cells to be imaged were pipetted onto it and a burned[1] coverslip added on top. Coverslips were burned in order to remove undesired residual dirt and stains before imaging. The sample thus prepared was inverted and placed on the microscope with the burned coverslip closest to the objective.

Tunnel slides

Tunnel slides for motility studies were made by attaching two strips of double-sided tape (3M) to the longer sides of a rectangular microscopy slide and placing a glass coverslip on top of it (Figure 2.2). The glass coverslips used each have a thickness of 170 μm. The height of the tunnel is determined by the thickness of the tape used which is about 100 μm. Solutions were flushed in the tunnel through the small air space between the slide and the coverslip. In the case of *E. coli* , thanks to the *fliC(sticky)* mutation (various regions in the *fliC* gene truncated so that hydrophobic regions are exposed, see Table 2.1), cells would tether to the glass via their flagella and they could therefore be incubated in a dark humidity chamber in presence of a wet piece of tissue upside down for 10 min without any further addition. In the case of *R. sphaeroides*, before flushing in the cells, a 1:1000 dilution in water of anti-flagellin antibody stock would be first flushed in, incubated for 5 min and excess washed away with 100 μl of SUX medium. For both *E. coli* and *R. sphaeroides*, non-stuck cells were removed by washing the slide with 100 μl of either MB or SUX media, respectively, three times, adsorbing liquid from the opposite side with a Kimwipe (KIMTECH). The open ends of the tunnel were finally sealed with nail varnish to prevent evaporation and the sample imaged upside down.

[1]The procedure for burning coverslips is: ramp up the heat in the furnace at 90°C per hour until 500°C; burn at 500°C for one hour; cool down at 150°C per hour to 90°C until room temperature is reached.

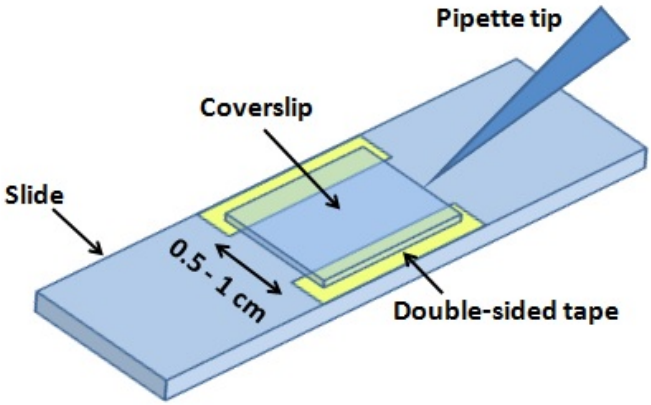

Figure 2.2: Schematic of a tunnel slide. The central chamber has a volume of ∼25-50 μl.

2.6.2 Motility checks

For quick confirmation of motility, 8 μl of cells were visualised between a slide and a coverslip using white light and a 40x magnification on a Nikon Optiphot phase-contrast microscope. A field of view was found with rotating cells lying separate from each other, and, where necessary, videos were recorded using a Generic Interface for Cameras (GenICam, Stemmer Imaging).

2.6.3 Epi-fluorescence microscopy

Epi-fluorescence microscopy was mostly carried out on an inverted Nikon Eclipse Ti system connected to an Andor iXON CCD camera. A 100x oil objective (Nikon) was used. The microscope was controlled using NIS Elements software (Nikon). The Perfect Focus System (PFS) feature was activated when time courses or multiple fields of view were captured in order to maintain a stable focus. For epi-fluorescence acquisition, a mercury lamp with appropriate excitation and emission filters for the fluorescent proteins/labelled proteins/dyes being imaged was used. In addition, a Nikon Eclipse TE200 microscope was also used (sections 5.2, 5.3), samples iluminated by a mercury lamp with the appropriate excitation and emission filters

(Chroma) and images captured with a Hamamatsu ORCA-ER CCD camera. This microscope was controlled using the Simple PCI 6 software package.
For both setups, exposure times were in the range 50-800 ms and white light images were taken using a halogen lamp for illumination in DIC configuration.

2.6.4 TIRF microscopy

TIRF and n-TIRF (also known as HILO[166]) fluorescence microscopy of electroporated labelled proteins in live *E. coli* and *R. sphaeroides* was performed on a customised inverted Olympus IX-71 microscope equipped with two lasers, a 637 nm "red" diode laser (Vortran Stradus; Vortran Laser Technology, Sacramento, CA, USA) and a 532 nm "green" DPSS laser (MGL-III-532nm-100mW, CNI). Laser light was combined into a single-mode optical fiber (Thorlabs, Newton, NJ, USA) and collimated before focusing on the objective. nTIRF and TIRF illumination was achieved by adjusting the position of the focused excitation light on the back focal plane of the objective (UPLSAPO, 100x, NA 1.4, Olympus). Cellular fluorescence was collected through the same objective, filtered to remove excitation light through a long-pass filter (HQ545LP; Chroma, Taoyuan Hsien, Taiwan) and a notch filter (NF02-633S; Semrock, Rochester, NY, USA), and spectrally separated by a dichroic mirror (630DRLP, Omega, Brattleboro, VT, USA). Each channel was imaged onto separate halves of the chip of an EMCCD camera (iXon+, BI-887, Andor, Belfast, UK). The illumination for white-light images comprised a white-light lamp (IX2-ILL100; Olympus, Shinjuku, Tokyo, Japan) and condenser (IX2-LWUCD; Olympus) attached to the microscope. Movies and images were recorded using manufacturer's software (Andor). All measurements were carried out in continuous wave (CW) mode for both green and red lasers. For the viability experiments described in section 4.3, the exposure times and excitation powers were 100 ms, 1 mW for the green laser and 0.6-2.5 mW for the red laser; for the single-molecule and motility experi-

ments described in chapters 6 and 7, the exposure times and excitation powers were 1-10 ms, 1 mW for the green laser and 2.5-19 mW for the red laser.

Contributions

Cloning of *cheY*$_6$(A134C) gene into pQE80, overexpression and purification of CheY$_6$ (A134C) were carried out by Matthew W. Smith (Armitage Lab, Department of Biochemistry, University of Oxford). Cloning of *cheY*(I95V) gene into pCA24N, overexpression and purification of Cys-modified CheY(I95V) were carried out by Oshri Afanzar (Department of Biological Chemistry, The Weizmann Institute of Science, Israel).

Chapter 3

The Electroporation Technique

3.1 Rationale

To perform an accurate study of the interactions between chemotaxis proteins and the motor complex it is essential to investigate their behavior *in vivo*. Most current research relies on the use of proteins fused to Fluorescent Proteins (FPs). Over the last 20 years, these have revolutionized cell biology via their use as genetically encoded protein labels: Green Fluorescent Protein (GFP)[164,184,185] and its mutated allelic forms, blue, cyan, and yellow fluorescent proteins are used to construct fluorescent chimeric proteins that can be expressed in living cells, tissues, and entire organisms, after transfection with the engineered vectors[186–188]. Red fluorescent proteins have also been isolated from other species, including coral reef organisms, and are similarly useful[189,190]. The fluorescent protein technique avoids the problem of purifying, tagging, and introducing labelled proteins into cells or the task of producing specific antibodies for surface or internal antigens. These fluorescent tags have allowed studies of the copy number, diffusion patterns and intracellular localisation of proteins involved in processes such as gene expression or membrane transport[58,191,192]. Moreover, this method has allowed researchers in the bacterial

flagellar motor field to measure stoichiometry of different components in single motors and has led to the discovery that both rotor and stator proteins exchange on a timescale of minutes with cellular pools of spares[58,193,194]. However, as mentioned in the Preamble, these methods suffer from a number of serious limitations. To start with, being genetically encoded, they label essentially all target proteins, which is of course a great advantage for counting molecules, but is less good for tracking single molecules due to spots-overlapping issues; also, FPs are much less bright (∼6-fold for GFP)[195,196] and photo-stable (∼100-fold for GFP)[5] than commercially available small organic dyes and are therefore far from ideal for single-molecule tracking purposes. Furthermore, not all fusions are fully functional, limiting the interpretation of the data and the proteins available for study, and they usually involve quite big tags, meaning the function of the wild type protein could in principle be affected.

For many years researchers have been trying to find smaller, more stable fluorophores that could be used inside living cells. Organic dyes remain the prime choice for *in vitro* experiments due to their greater photostability, small size (up to 100-fold smaller volume than FPs) and ease of intramolecular labelling (mainly through the use of cysteine residues)[195,196]. All these factors are particularly important for single-molecule fluorescence imaging and tracking.

However, since these are not compatible with genetic tagging, a means for re-introducing externally dye-labelled proteins into cells is required for *in vivo* studies. Several internalisation methods combining the advantages of organic labeling and *in vivo* detection have been introduced over the past decade, some employing relatively large polypeptides tags (e.g., TMP, HALO, or 20 kDa SNAP tags)[41,197,198] not ideal for bacterial application and others were limited to large, single-membrane eukaryotic cells (e.g., scrape loading, syringe loading, microinjection)[199–202]. A new method recently developed in Oxford overcomes these limitations, offering the exciting possibility of a new generation of single-molecule *in vivo* fluorescence experiments in live bacteria[5,203]. Purified proteins are labelled with organic dyes of choice

and put back into cells in small numbers using *electroporation*, a modification of a method that is well established in molecular biology and exploits the phenomenon that application of an external electrical field to a low ionic strength cell suspension creates transient pores in the membrane, allowing for the uptake of DNA or other macromolecules.

The driving idea for the research described in this thesis is to combine electroporation with single-molecule microscopy in live *E. coli* and *R. sphaeroides* to image and track chemotaxis proteins of interest while performing their function as response regulators between the chemoreceptor clusters and the motors. As explained above, upon electroporation cells internalise the organic dye-labelled proteins which, at the illumination powers used and compared to if they were labelled with a FP, emit a higher number of photons before bleaching and therefore allow for longer, faster and more accurate single-molecule tracking. As with every new method, there are of course some challenges, which will be addressed in this chapter and in the following ones: just to mention some, tuning electroporation's conditions to trade off between cell survival and internalisation efficiency; recovering electroporated cells to a healthy, motile state as quickly as possible; imaging fluorescence from internalised molecules before this is reduced by cell division or degradation.

3.2 Overview of electroporation theory

The electroporation mechanism has long been investigated, both experimentally and, more recently, computationally (see 204, 205 for a review). Electrically, the cell membrane can be viewed as a thin insulating sheet surrounded on both sides by aqueous electrolyte solutions. During electroporation, the cell membrane is exposed to an external electric field of sufficient magnitude and duration to cause electrical breakdown and breaching. What happens next is best described by the theory of aqueous pore formation: permeabilising structures (pores) form almost instantan-

eously, allowing transmembrane transport of molecules that are otherwise unable to cross, like the fluorescently labelled proteins at issue[206]. The main molecular constituents of every cell membrane are the lipids. The most abundant in bacteria are phospholipids (Figure 3.1). Each of these three major lipid classes has a polar (hydrophilic) and a nonpolar (hydrophobic) part. Typically, the polar part is rather compact and the nonpolar part is more elongated, so they are often referred to as the "head" and the "tails" of the lipid molecule, respectively.

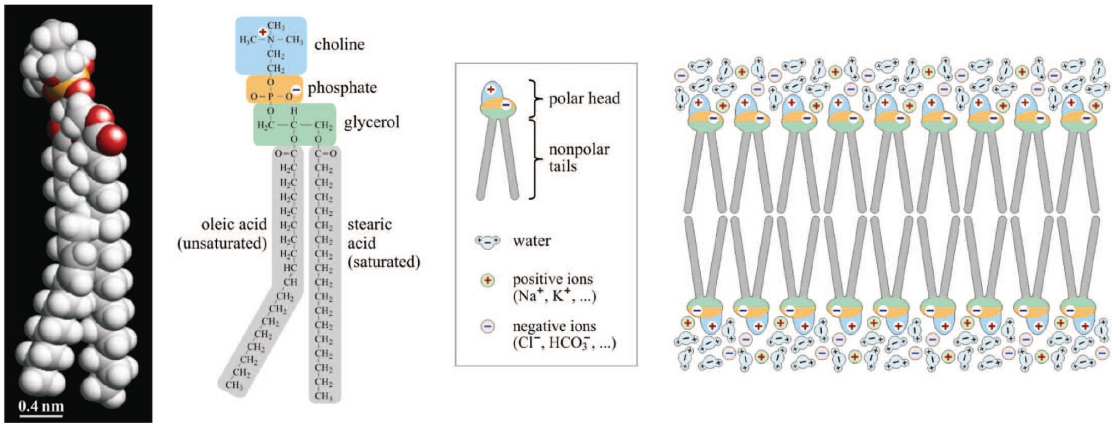

Figure 3.1: Left: space-filling model and structural formula of the SOPC (1-stearoyl-2-oleoyl-phosphatidylcholine) molecule, a typical membrane lipid. Right: schematic of a bilayer of such lipids in an aqueous electrolyte solution, with explicit charges. Taken from 207.

Lipids are held together only by weak (noncovalent) interactions, and at sufficiently high temperatures, the bilayer behaves as a two-dimensional liquid[207]. Because of its nonpolar interior, it is also an almost impenetrable barrier for polar molecules dissolved in the aqueous electrolyte on both its sides. Nevertheless, water and some monoatomic ions permeate through it at rates too high to be explainable by diffusion through an entirely intact bilayer[208,209]. Under certain conditions, e.g., sufficiently high temperature, surface tension, or both, this permeation can be attributed to the formation and rapid resealing of very small aqueous pores in the lipid bilayer, with radii below a nanometer and lifetimes below a nanosecond; they form and reseal because of thermal and mechanical fluctuations. Therefore, pores can form without

an external electric field acting on the membrane, but they are inherently unstable. Upon electroporation, instead, the applied transmembrane voltage reduces the energy required for spontaneous formation of aqueous pores facilitating the formation of a higher number of pores which are also more stable than in the absence of the electric field, with lifetimes ranging from milliseconds up to minutes after the field is removed. The formation of these pores in the membrane caused by electroporation has not yet been observed directly, however, convincing evidence is provided by Molecular Dynamics (MD) simulations. Such simulations already provide some support for pore formation in the absence of an electric field[207]; moreover, if a sufficiently strong electric field perpendicular to the bilayer is added in them, there is a clear increase in the rate of pore formation and stabilisation based on the transition from the hydrophobic to the hydrophilic pore form (Figure 3.2).

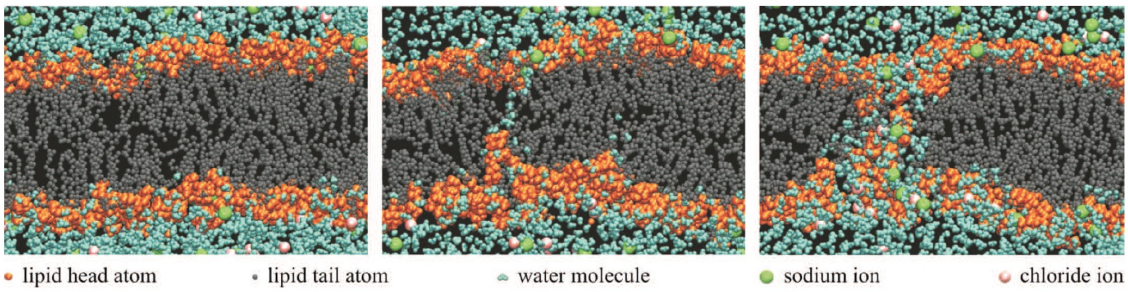

Figure 3.2: A Molecular Dynamics simulation of an aqueous pore forming in a lipid bilayer exposed to an electric field perpendicular to the bilayer plane. Left: bilayer at steady state. Middle: water molecules from one side of the bilayer meet water from the opposite side to form a bridge. Right: the adjacent lipids reorient with their heads toward the water molecules in the middle lining the periphery of the pore and stabilising it, allowing for internalisation of the labelled molecules in solution. Taken from 207.

3.3 Protein Labelling

3.3.1 Choice of proteins

The wild type forms of CheY and $CheY_6$ were the obvious choice of proteins to electroporate in *E. coli* and *R. sphaeroides*, respectively, for the aims described in section 3.1. Two more mutants of *E. coli* CheY were also produced in order to compare their binding affinities to FliM with those obtained for the WT protein. In the following, the replacement of an amino-acid A present in the protein's WT sequence in position X with another amino-acid B is indicated as AXB:

- CheY(D13K/Y106W) also known as CheY**, a constitutively active form of CheY which promotes clockwise flagellar rotation in the absence of phosphorylation[173,210], is not supposed to interact with the chemoreceptor cluster at all and has slightly inferior binding affinity to FliM than WT CheY-P ($K_{D(\text{CheY-P})} = 26\ \mu M$, $K_{D(\text{CheY(D13K/Y106W)})} = 55\ \mu M$[211]);
- CheY(I95V), a hyperactive form of CheY showing increased CW bias *in vivo*[175] and enhanced FliM binding affinity *in vitro*, namely three-fold with respect to unphosphorylated CheY when unphosphorylated and seven-fold with respect to phosphorylated CheY when phosphorylated[211]. This mutant's characteristics suggest a role for Ile95 in switch interaction: it could either directly interact with the switch or alter the nearby proposed FliM binding surface; alternatively, it could influence the side chain conformation of the adjacent residue Tyr106. Moreover, this mutant has reduced CheZ sensitivity, which in WT backgrounds, could potentially increase the concentration of phosphorylated CheY in the cell thereby leading to the observed stronger CW rotational bias.

A prominent difference between the various studied mutants of CheY, as revealed from their X-ray structures, is the orientation of the side chain of Tyr106, located on the face of the molecule[79]. This side chain appears in WT CheY as a mixture

of inward and outward conformations, whereas in all the other studied mutant proteins and analogs, the side chain is found in only one orientation, specifically in the outward one for both our mutants of interest CheY** and CheY(I95V)[79,211]. This is however inconsistent with the suggestion that phosphorylation of Asp57 initiates conversion of Tyr106 from a solvent-exposed orientation to a more internal position[79]. This notion is supported by the observations that in the analogs phosphono-CheY[212] and BeFX·CheY[213], the side chain of residue 106 is oriented inwardly. The finding that the side chain of Tyr106 is oriented outwardly in the complex between CheY and the P2 domain of CheA[214] further suggests that repositioning of Tyr106 might be involved in the release of CheY from CheA and in its subsequent binding to FliM. It thus seems that the rotameric state of Tyr106 plays an important role in determining the level of CheY activity, but it is still controversial how.

3.3.2 Cysteine insertion

Sulfhydryl groups (SH), also called thiols, are encountered in proteins and peptides as cysteine residues and are useful targets for bioconjugation and labelling. First, sulfhydryls are present in most proteins but are not as numerous as primary amines; thus, crosslinking via sulfhydryl groups is more selective and precise than via NHS (N-HydroxySuccinimide) esters. Second, sulfhydryl groups in proteins are often involved in disulfide bonds (-S-S-) within or between polypeptide chains as the basis of native tertiary or quaternary protein structure, so crosslinking at these sites typically does not significantly modify the underlying protein structure or block binding sites. Third, the number of available sulfhydryl groups can be easily controlled or modified: they can be generated by reduction of native disulfide bonds, or they can be introduced into molecules through genetic manipulation, as in this work.

Maleimides are electrophilic compounds which show high selectivity towards thiols. Reaction of thiols in the cysteine residues with a maleimide modification of the

chosen organic dye is nowadays one of the most widely used mechanisms for protein labelling. It proceeds as illustrated in Figure 3.3.

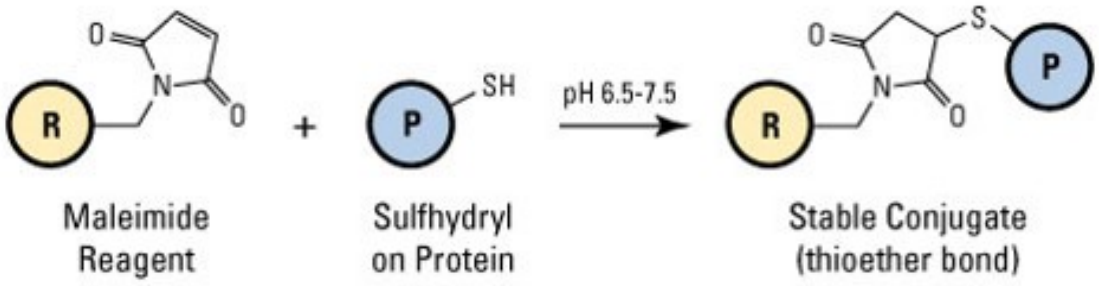

Figure 3.3: Maleimide reaction mechanism for chemical conjugation to a sulfhydryl group. (R) represents a labeling reagent having the maleimide reactive group; (P) represents a protein or other molecule that contains the target functional group SH on one or more cysteine residues.

The maleimide group reacts specifically with sulfhydryl groups when the pH of the reaction mixture is between 6.5 and 7.5, with the optimal value being 7.4[215] to form a stable, covalent thioether linkage; note that the choice of pH for the labelling buffer depends on the temperature at which the reaction is carried out (see section 2.5.1). During the labelling reaction, thiol-containing reducing agents like dithiothreitol (DTT) and β-mercaptoethanol (βME) must be excluded because they would otherwise compete for coupling sites. However, the tris(2-carboxyethyl)phosphine (TCEP) disulfide-reducing agent, not containing any thiols, does not have to be removed and was for this reason chosen for this work.

Wild type CheY and CheY** proteins do not have any native cysteine in their aminoacid sequences and $CheY_6$ proteins have only a very buried one in position 80. Therefore, in order to label them with an organic dye through maleimide-thiol reaction as described above, a cysteine residue in exposed position had to be engineered. An appropriate site had to be chosen in order to both satisfy such requirement and not disrupt the protein's function or affect its binding/interacting to/with other proteins: suitable candidates satisfying such requirements were the N and C termini in all the chemotaxis proteins used in this work, for both *E. coli* and *R. sphaeroides*.

In fact, as shown in Figure 3.4 for *E. coli* CheY and in Figure 3.5 for *R. sphaeroides* $CheY_6$, the proteins' N and C termini are far away from all the crucial residues for function. The CheY(I95V) protein used was a modified form derived from the ASKA library[176] having a C' linker with the sequence GLCGR and N' linker with the sequence MRG(6xHis)TDPALR. It therefore already had a C terminal cysteine. This and the CheY** mutants are structurally almost indistinguishable from WT CheY[211].

To further ensure suitability for dye labelling, solvent exposure of such residues on both proteins' surfaces was checked and confirmed using PyMol[218], as shown in Figure 3.6.

3.3.3 Labelling procedure

To prepare the protein samples to electroporate, N' and C' cysteine mutants of CheY and CheY** and C' cysteine mutants of CheY(I95V) and $CheY_6$ were first cloned according to criteria discussed in 3.3.2, overexpressed and purified as described in sections 2.4.1-2.4.6; each was then labelled with a maleimide modification of the organic dyes of choice according to the protocol described in 2.5.1; finally, unreacted dye was removed by size exclusion chromatography to avoid false positives during fluorescence imaging (sample chromatogram shown in Figure 3.7). In this step, the labelled protein was also buffer-exchanged into Electroporation buffer (see appendix A), then concentrated and stored either at -20°C in 50% glycerol for long-term or at 4°C for short-term storage. The ionic strength of the buffer in which cells are electroporated should be high enough to maintain protein integrity but low enough to avoid the occurrence of an electrical short circuit (arcing). The electroporation time constant describes the exponential decay of the applied voltage with time and is indicative of whether a certain level of electrical discharge has occurred in the medium. For a standard electroporator such as the one used in this work, 5 to

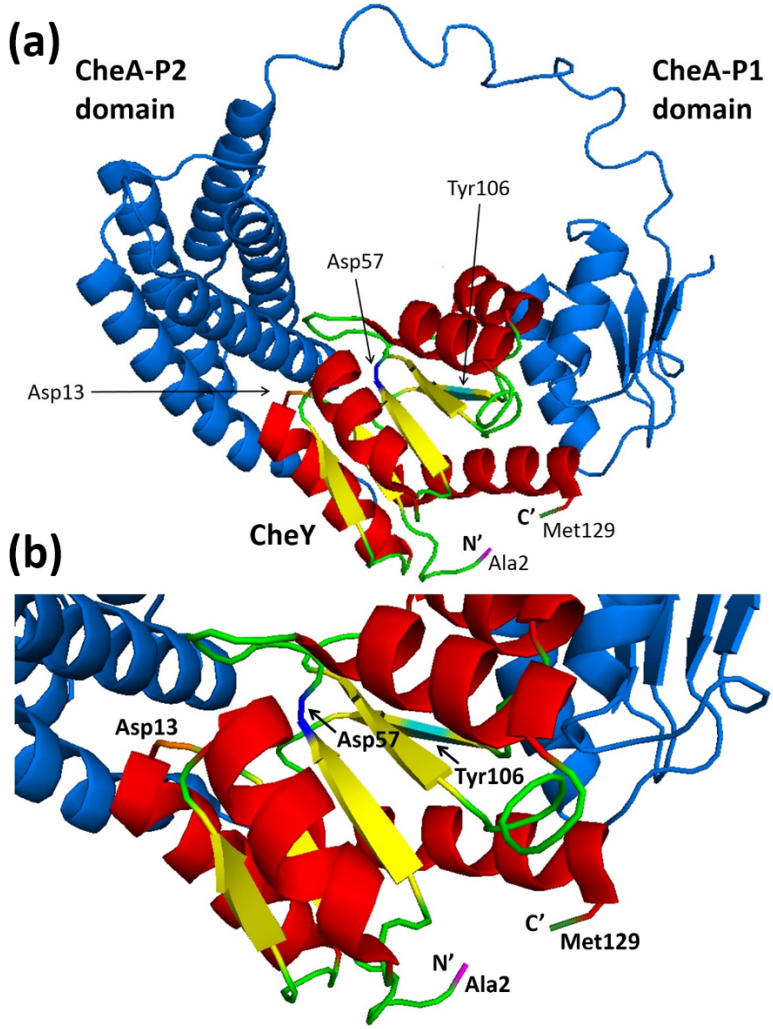

Figure 3.4: Evaluation of suitable protein sites for cysteine insertion in *E. coli*. **(a)** Solution structure of CheY in complex with P1-P2 domains of CheA (PDB entry 2LP4[216]). Both proteins are shown in cartoon representation, with CheY coloured according to secondary structure (red α-helices, yellow β-sheets, green loops) and CheA-P1/P2 in blue marine. **(b)** Specific interaction sites of CheY with the phosphatase CheZ and the histidine kinase CheA-P1 (Asp57, blue) and with FliM (Tyr 106, cyan). CheA-P2 interacts with CheY through the latter residue, as well. The Asp13 residue, involved in Mg^{2+} binding and catalysis, is also shown (orange)[108]. Detail from **(a)**).

6 ms are considered acceptable values to yield good cell loading while preserving cell viability. Since the chemotaxis proteins involved in this work are all quite stable in relatively low salt conditions, a working electroporation buffer of 50 mM Tris, 25 mM NaCl (pH 7.5 at RT) was used, similar to what previously reported in the literature[219]. In 219, it was also shown that the presence of glycerol in the

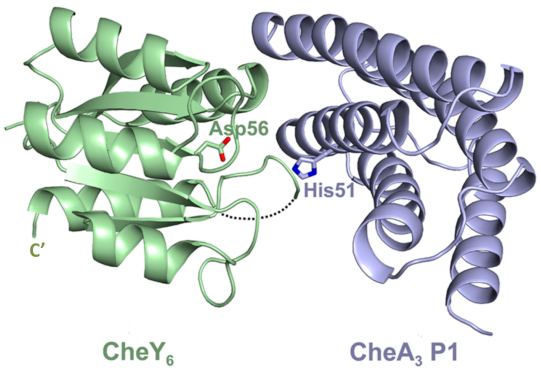

Figure 3.5: Evaluation of suitable protein sites for cysteine engineering in *R. sphaeroides*. Asp56, the major site of interaction between $CheY_6$ (pale green) and the P1 domain of $CheA_3$ (light blue) is shown. The interaction site of $CheY_6$ with FliM is not known; however, it can be inferred based on homology with *E. coli* CheY that this is not likely to be situated in proximity of the protein's C terminus (shown in the picture), where the cysteine for this work was engineered. Residues 113-118 of $CheY_6$ correspond to a highly flexible loop which was only partially ordered in the crystal structure and could not therefore be traced (dotted line). Reproduced from 217.

electroporation buffer, often added for storage purposes to maintain protein integrity and mitigate the effects of freezing and thawing, is compatible with electroporation, and does not compromise cell loading.

To test specificity of cysteine labelling, wild type (cysteine-free) CheY was also overexpressed, purified and incubated with 4x molar excess of Cy3B-maleimide dye O/N at 4°C . Following the same procedure described for the preparation of positive ones, this negative control sample was also loaded on the size-exclusion column and run with the same program parameters. From the resulting chromatogram, shown in Figure 3.8, it is possible to infer that the wild type protein corresponds to the first peak, whereas the two later ones correspond, respectively, to dye reacted with TCEP reducing agent and free dye. A closer look reveals that, compared to the labelled cysteine mutant CheY, here the peak in the absorption at 559 nm curve overlapping with the main protein peak looks broader, slightly shifted to the left and less intense, suggesting it does not represent a labelled protein. Comparison between Coomassie Blue staining and UV-Vis scan of a SDS-PAGE gel of selected fractions for the three peaks confirmed that cysteine-free WT CheY had not been selectively labelled as

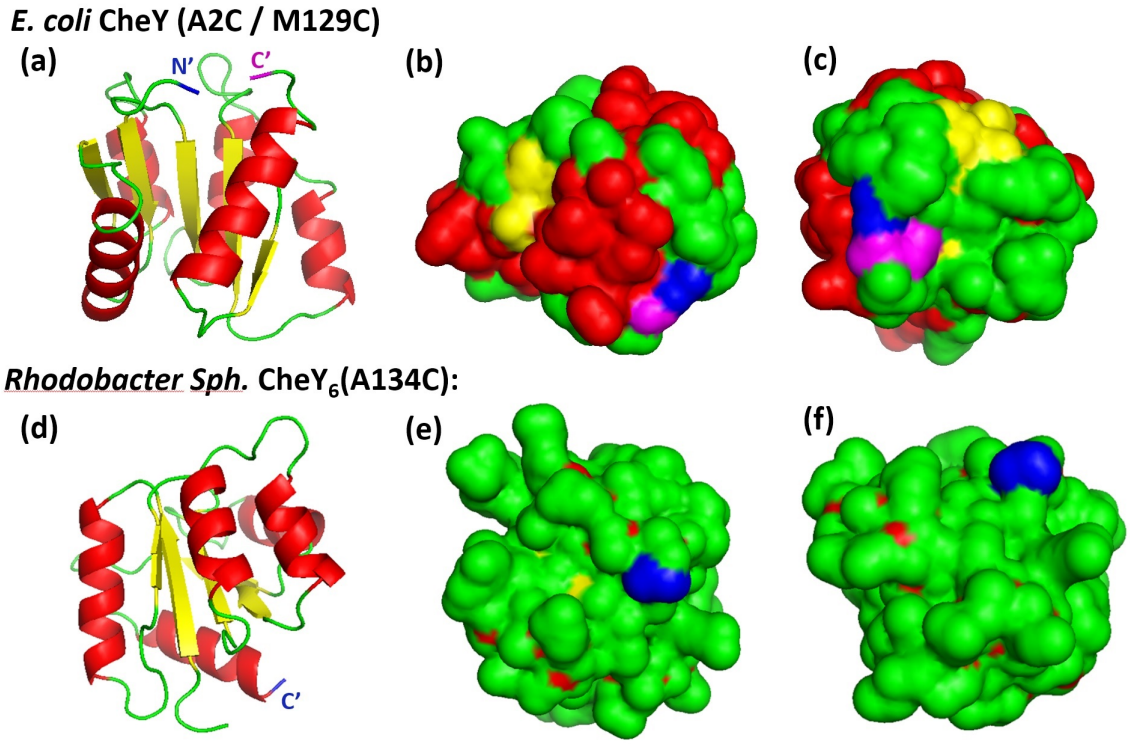

Figure 3.6: Testing exposure of selected sites for cysteine insertion in *E. coli* and *R. sphaeroides*. Both CheY and $CheY_6$ are coloured according to their secondary structure (red α-helices, yellow β-sheets, green loops). **(a)** Cartoon representation of *E. coli* CheY (PDB entry 3CHY[106]) showing the protein's N and C termini, selected sites for cysteine insertion, coloured in blue and magenta, respectively: it is already clear from this schematic illustration that these look quite exposed; **(b), (c)** Surface representation of CheY with the same colours convention as in **(a)**: this time, the solvent-accessible surface area is shown, confirming exposure of the N/C termini. **(d)** Cartoon representation of *R. sphaeroides* $CheY_6$ (PDB entry 3KYJ[217]) showing the protein's C terminus, selected site for cysteine insertion, coloured in blue: again, exposure is already clear from this schematic illustration; **(e), (f)** Surface representation of $CheY_6$ with the same colour convention as in **(d)**: exposure of the C terminus is further supported by visualisation of the solvent-accessible surface area.

the cysteine-modified mutants and hence the control was effectively negative (Figure 3.9).

With this procedure, a free dye contamination of only 1.2% (quantified in Fiji image-processing software using the 'Plot Profile' function, and integrating the peaks in OriginPro) was achieved in the final labelled sample, ∼15-fold lower than the starting amount of contamination before SEC.

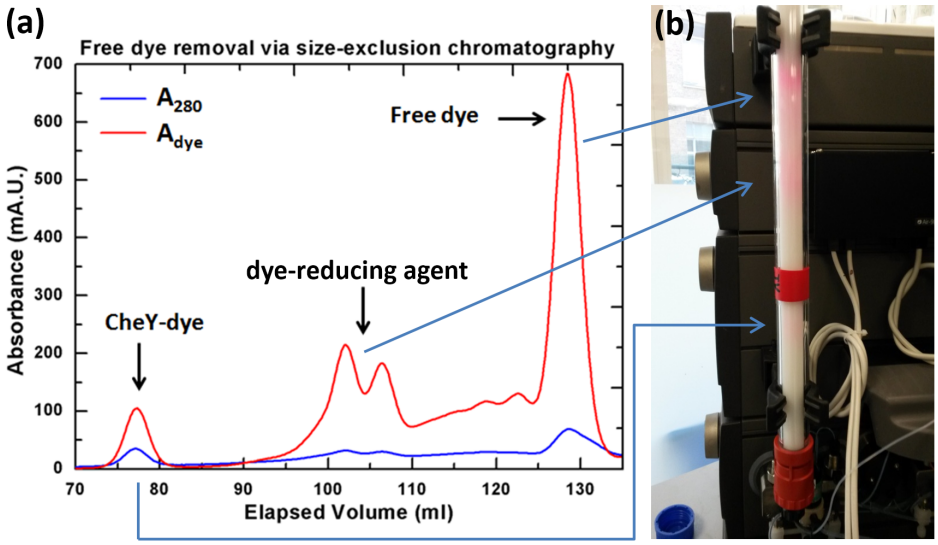

Figure 3.7: Free dye removal after labelling via size exclusion chromatography. **(a)** Example chromatogram showing in separate peaks labelled product, dye reacted with reducing agent and free dye. **(b)** Coloured bands corresponding to the different elution products on a Hiload 16/600 Superdex 75 pg column.

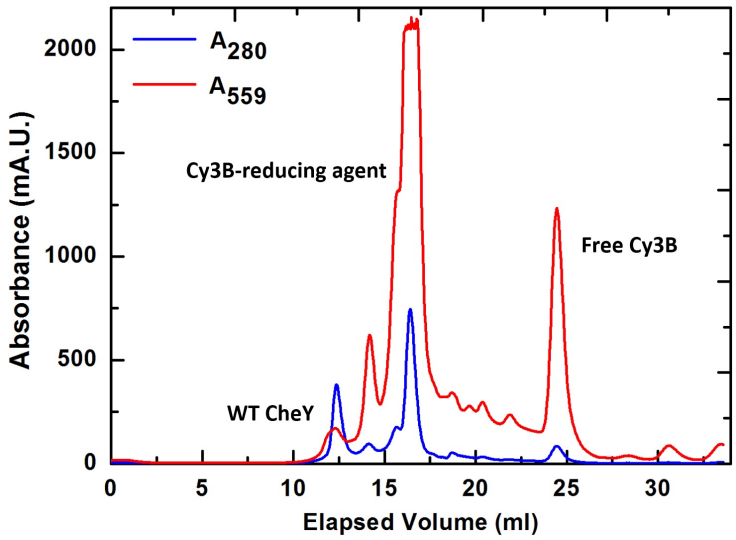

Figure 3.8: Negative control of cysteine-maleimide labelling specificity: absorption curves at 280 nm (blue) and 559 nm (Cy3B excitation wavelength, red) of WT CheY incubated with Cy3B-maleimide dye showing in separate peaks labelled product, dye reacted with reducing agent and free dye upon size exclusion chromatography on a Superdex^{TM} 75 HR 10/30 column.

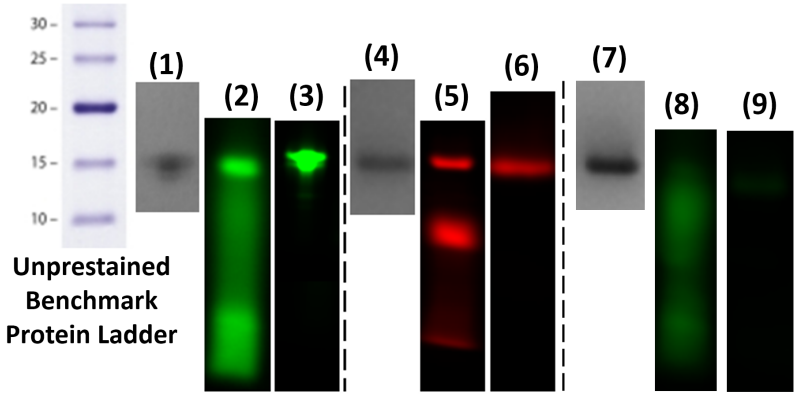

Figure 3.9: Contamination evaluation through SDS-PAGE. Lanes (1), (4) and (7) show a Coomassie Blue stained pure CheY protein running at a height compatible with its molecular weight of 15 kDa; lanes (2) and (5) contain, respectively, the reaction products of a labelling reaction carried out with Cy3B-maleimide dye (in green) and Cy5-maleimide dye (in red); lanes (3) and (6) show the same samples as in lanes (2) and (5) after free dye removal. The comparison between lanes (2) and (3) and lanes (5) and (6) clearly shows that the free dye contamination is successfully removed by SEC. Lane (8) shows the reaction products of a WT cysteine-free CheY protein incubated with Cy3B-maleimide dye (negative control): in this case, the band looks much more smeared than those in lanes (2) and (5), and the purified labelled protein fluorescent band in lane (9) is almost invisible, indicating hight specificity of the cysteine-maleimide labelling method. Fluorescent bands were quantified in Fiji image-processing software using the 'Plot Profile' function, and the peaks integrated in OriginPro. A free dye final contamination of ¡1.2% was found.

3.3.4 Samples created

Twelve samples were overall created and used: *E. coli* CheY was labelled with maleimide modifications of the Atto647, Cy3B, Atto647N and Cy5 dyes, CheY** and CheY(I95V) with maleimide modifications of the Atto647 and Cy3B dyes and *R. sphaeroides* $CheY_6$ with a maleimide modification of the Atto647 dye. See section 4.1 for a discussion about fluorophores' choice and Table 3.1 for photophysical properties of the dyes used.

A comprehensive summary of all the samples produced, with characteristics such as final concentration of labelled protein in solution, excess-fold of dye added, reaction volume, concentration of TCEP in solution and Degree of Labelling (DoL) is reported in Table 3.2. All the reactions were conducted O/N at 4°C , unless otherwise

Dye	Molecular Weight (Da)	λ_{exc} (nm)	λ_{em} (nm)	Extinction Coefficient ($\times 10^5$, $M^{-1}cm^{-1}$)	Correction Factor (280 nm)
Cy3B	796	559	570	1.3	0.08
Atto647	832	645	669	1.2	0.04
Atto647N	868	644	669	1.5	0.05
Cy5	817	649	670	2.5	0.05

Table 3.1: Photophysical properties of the organic dyes used in this work. Because fluorescent dyes also absorb at 280 nm, a correction factor must be used to adjust for amount of absorbance at 280 nm A_{280} contributed by the dye. The correction factor equals the A_{280} of the dye divided by the A_{max} of the dye. Correction factors' values in the Table were taken from the manufacturer's data sheet for each dye.

stated. The DoL was determined using the formula reported in section 2.5.4 using as correction factors the values reported in Table 3.1. The variety of proteins, dyes and bacterial species listed here supports the statement that this technique is particularly powerful in that it can be easily applied to a wide range of targets, probes and organisms.

3.4 Modifications to standard protocols

As for transformation of bacteria with plasmid DNA, cells must be treated prior to electroporation to ensure their electrocompetency. This procedure, consisting of several washing steps with water and glycerol, increases the membrane permeability and lowers the ionic strength of the cell suspension to avoid arcing in the electroporation cuvette. *E. coli* and *R. sphaeroides* cells were made electrocompetent as described in section 2.3.3. Two main modifications were introduced with respect to the standard electroporation parameters and procedure for DNA delivery:

- The recommended voltage for efficient DNA delivery inside *E. coli* , i.e. yielding 10^9 - 10^{10} transformants/μg of DNA, is reported in the literature to be 1.80 kV for 0.1 cm cuvettes, corresponding to a field strength of 18 kV/cm (ref. 220); in order to recover electroporated cells to a healthy, motile state

Organism	Sample	C (μM)	Excess Dye	Reaction Volume (μl)	[TCEP] (mM)	DoL (%)
E. coli	CheY(Cys)-Cy3B	25	20	200	>10	20
E. coli	CheY(Cys)-Atto647N	15	10	300	>10	3
E. coli	CheY(Cys)-Atto647N	43	6	250	0.4	41
E. coli	Cy5-(Cys)CheY	32	9	250	0.4	100 [a]
E. coli	Atto647-(Cys)CheY	4	9	250	0.4	0.5
E. coli	Atto647-(Cys)CheY	4	9	250	0.4	6
E. coli	Atto647-(Cys)CheY	2	9	250	0.4	0.5
E. coli	Atto647-(Cys)CheY†	7	9	250	0.4	0.7
E. coli	CheY**(Cys)-Cy3B	34	10	300	>10	6
E. coli	CheY**(Cys)-Atto647	60	9	250	0.4	0.7
E. coli	CheY(I95V)(Cys)-Atto647	3	7	300	0.5	0.3
R. sphaeroides	$CheY_6$(A134C)-Atto647	1.4	10	300	0.1	0.14

Table 3.2: Dye-labelled protein samples created in this work: the convention is that when the complex dye-(cys) is written *before* the protein name, the labelling is via the N terminus; when the complex (cys)-dye is written *after* the protein name, the labelling is via the C terminus. C is the final concentration of labelled protein (measured from A_{max}(dye)), DoL in the purified samples and information on labelling conditions used (molar excess of dye added, reaction volume, concentration of TCEP reducing agent) are listed.
†: the labelling reaction in this case was run O/N at RT.

[a] See section 3.6 for comments on such value.

as soon as possible after application of the electric pulse, such voltage was lowered to limit cell/motor damage and increase cell survival rate and motility recovery chances. A voltage found in this work to be a good trade-off between internalisation efficiency and the requirements just listed for *E. coli* was 1.2 kV, corresponding to a field strength of 12 kV/cm. For *R. sphaeroides*, instead, the only references present in the literature about electroporation in such species report the use of a 0.2 cm cuvette and an applied pulse of 2.5 kV corresponding to a field strength of 12.5 kV/cm (refs. 221, 222); however, preliminary experiments carried out in this work revealed that such bacteria looked more robust and viable than *E. coli* after electroporation, recovering growth and division ability on a quicker time scale after start of recovery. A

slightly higher voltage, 1.4 kV for a 1 mm cuvette, was therefore chosen for *R. sphaeroides*, and the amount of fluorescently labelled $CheY_6$ molecules for incubation reduced accordingly.

- In standard protocols for *E. coli*, upon electroporation with DNA, cells are usually incubated in a rich medium like the Super Optimal broth with Catabolite repression (SOC) at the bacteria's optimal temperature (37°C) for an hour or more to allow recovery and expression of the plasmid, followed by culture on agar plates; in this case, instead, the recovery time in rich medium (SOC for *E. coli* and SUX for *R. sphaeroides*) was reduced to only 5-10 minutes at 30°C (optimal temperature for bacterial motility in both species) to avoid loss of internalised fluorescence consequently to cell division and intracellular degradation. Cells were then washed and imaged straight away instead of proceeding to plating.

Each experiment always featured at least 3 samples:

1. Electroporated (EP) cells, incubated with 0.3-30 pmoles of fluorescently labelled protein (final concentration of labelled protein in solution 15 nM-1.5 μM to 10^8 cells in each electrocompetent cells' aliquot, estimated by having grown them to OD_{600nm}=0.4);

2. Non-Electroporated (NEP) cells, incubated with the same amount of fluorescently labelled protein as EP cells, but to which no electric pulse was applied;

3. *Negative Control* cells, which were never in contact with the fluorescently labelled protein.

Each time a microscopy experiment was carried out, it was very important to image at least some fields of view of the last sample to keep a consistent track of possible sources of background, i.e. autofluorescence from intracellular substances, agarose pads' solution, contamination of washing buffers etc.

3.5 Characterisation of cysteine CheY mutants

ProtParam (`http://www.expasy.org/tools/protparam.html`) computes various physicochemical properties that can be deduced from a protein sequence. No additional information is required about the protein under consideration apart from the raw sequence. In this work, such tool was used to estimate the extinction coefficient and the intracellular half life of CheY.

Extinction coefficient of cysteine modified CheY

Amino acids containing aromatic side chains (i.e., tyrosine, tryptophan and phenylalanine) exhibit strong UV-light absorption. Consequently, proteins and peptides absorb UV-light in proportion to their aromatic amino acid content and total concentration. Only the amino acids tryptophan (Trp, W) and tyrosine (Tyr, Y) and to a lesser extent cysteine (Cys, C) contribute significantly to peptide or protein absorbance at 280 nm. Phenylalanine (Phe, F) absorbs only at lower wavelengths (240-265 nm). The extinction coefficient ε indicates how much light a protein absorbs at a certain wavelength and is an essential quantity in order to estimate the Degree of Labelling using formula 2.1 in section 2.5.4. It has been shown[223] that it is possible to estimate the molar extinction coefficient of a protein from knowledge of its amino acid composition. Since CheY mutants produced in this work contain only one Trp residue, their ε at 280 nm is mostly accounted for by the extinction coefficients of the two Tyr residues and of the inserted cysteine in their sequences. For them, ProtParam yields a value of ε=8480 $M^{-1}cm^{-1}$ using the equations reported in 224. For CheY**, containing this protein the Y106W mutation and therefore having one more Trp in its sequence, ProtParam yields a $\sim$50% higher extinction coefficient

value of 12490 $M^{-1}cm^{-1}$. The conditions at which these estimations are valid are pH 6.5, 6.0 M guanidium hydrochloride, 0.02 M phosphate buffer. Taking into account the composition and pH of our storage buffer (Labelling Buffer, see appendix A for recipe), the real extinction coefficients of the proteins in it could be somewhat different. Moreover, ProtParam sums the contributions of the different amino acids as if they were independent, not taking into account secondary or tertiary structure. Both these observations could be source of inaccuracy in the estimation of the mutant CheY and CheY** extinction coefficients (see section 3.6).

CheY's half-life

The half-life is a prediction of the time it takes for half of the intracellular amount of a protein to turnover. This is a relevant value for the aims of this project in that it poses an upper limit to the amount of time cells can be allowed to recover upon electroporation before internalised labelled proteins start being degraded by cellular internal mechanisms. ProtParam estimates the half-life by looking at the N terminal amino acid of the sequence under investigation: in fact, it has been shown[225–227] that the identity of the N terminal residue of a protein plays an important role in determining its stability *in vivo*. For the CheY mutants used in this work, ProtParam yields a half life of > 10 hours in *E. coli*, which is a long enough time to allow for both a long recovery time and a still satisfactory observation of internalised fluorescent molecules.

Extinction coefficient of cysteine modified $CheY_6$

Since $CheY_6$ cysteine mutants produced in this work do not contain any Trp residue, their ε at 280 nm is only accounted for by the extinction coefficients of the two Tyr residues and of the two cysteines (one of which genetically engineered) in their

sequences. As the ProtParam tool is not very reliable for proteins not containing any Trp residues, it gave the quite low value of ε ~3000 $M^{-1}cm^{-1}$; however, if experimentally calculated according to the method described in 228 [1], the slightly higher value of ε ~3775 $M^{-1}cm^{-1}$ is found for the wild type protein. The latter value for ε was considered in this work for the calculation of the Degree of Labelling of the $CheY_6$-Atto647 sample.

3.6 Variability in Degree of Labelling

One source of inaccuracy in the labelling yield values reported in Table 3.2 calculated using formula 2.1, is, as mentioned in section 3.5, the difficulty in determining precise values for the extinction coefficient of the CheY/CheY**/$CheY_6$ mutants, due to the low abundance in these proteins of the highly absorbing residues Trp, Tyr, and cystine (disulfide bonds). For the CheY(Cys)-Cy5 sample, for instance, a calculated DoL close to 100% could mean that the extinction coefficient of the protein used was overestimated. The extinction coefficients of the dyes are known very accurately and are not subject to significant variations due to pH or chemical environment changes. However, even taking this into account, the question why the labelling yield of some samples listed in Table 3.2 is significantly low ($< 1\%$) remains. Experimental results show that Cy5-maleimide reacts with Cys-CheY much better than Cy3B-maleimide and, even more, than Atto647 and Atto647N-maleimide. Despite an in-depth theoretical and experimental investigation, the source of such low values is still not clear. Nevertheless, a list of all checks, tests and protocol modifications that were carried out to rule out possible affecting factors and try to increase the labelling yield is included below for completeness:

- **Exposure checks:** as discussed in section 3.3.2, sites for cysteine residues

[1] The authors of 228 suggest using the formula ε(280 nm) = 5500(#Trp) + 1490(#Tyr) + 125(#cystine) to predict the extinction coefficient value for a folded protein in water at 280 nm (cystine = disulfide bonds, none for $CheY_6$).

engineering were carefully selected in the proteins' sequences to be solvent-exposed on the surface to allow for efficient labelling with the maleimide dyes; despite them looking as such in Figure 3.6, interactions of electrostatic/hydrodynamic kind might be taking place that hinder the dye from binding. From inspection of table 3.3, illustrating polarity and hydrodynamic properties of the 4 different dyes used in this work, no clear trend arises that could easily explain the experimental variability identified.

Dye	Labelling efficiency	Polarity	Hydrodynamic behaviour	Reference
Cy3B	++	Neutral	Highly hydrophobic	229
Atto647N	+	Cationic	Hydrophobic	230, 231
Atto647	−	Neutral (zwitterionic)	Highly hydrophilic	232
Cy5	++	Neutral	Hydrophilic	233

Table 3.3: Visual comparison of polarity and hydrodynamic properties of dyes whose maleimide modifications were used in this work for protein labelling. The evaluation of the fluorophore labelling performance is based on the values reported in column *DoL* in Table 3.2: ++ = very high, + = high, − = low.

- **Duration/temperature of labelling reaction:** three conditions were tried out, O/N at 4°C, 1 hour at RT and O/N at RT. The latter two were tested because, CheY being a very stable protein, it is possible to work with it at RT for a reasonable amount of time. However, the cysteine-maleimide reaction is supposed to take place instantaneously so that usually even just half an hour or one hour incubation are enough to achieve yields of $\sim 100\%$[183,234]; interestingly, when the reaction was run for 1 hour at RT, the same percentage of labelled protein as when left O/N at 4°C was obtained. Incubation time was then increased to O/N, always at RT, hoping that allowing the reaction to proceed for longer would help, but again the same degree of labelling was obtained. Increasing the temperature did not yield a significant improvement, suggesting that this reaction is probably limited by steric hindrance or electrostatic interactions more than by low collision rate of the two compounds

involved. The first listed duration/temperature conditions (O/N, 4°C) were therefore selected for all the samples used in further experiments unless otherwise stated, as they guaranteed a good trade off between duration and protein preservation.

- **Reaction volume/protein concentration:** based on experimental experience of the author, and on consultations with people working in the field, the ideal volume for optimal proceeding of the labelling reaction is around 200-300 μl and protein concentration in solution around 50-100 μM. The labelled samples listed in Table 3.2 were produced observing these guidelines, so it is probable there was no negative effect of the reaction volume and protein concentration parameters on the labelling efficiency.

- **Excess dye:** a cysteine-maleimide reaction is supposed to occur almost instantaneously with very high specificity between the moieties involved, and therefore even a 1:1 molar ratio of protein:dye would theoretically be enough to achieve a satisfactory yield of labelled sample (close to 90%). It was however discussed earlier in this section how, since the very first trials with WT CheY, all response regulator proteins considered have been particularly hard to label. Therefore, in the reactions listed in Table 3.2 dye was added in a 6-20 fold molar excess, this modification still did not positively affect the low labelling efficiency obtained.

- **% DMSO in solution:** for compounds with low aqueous solubility, like most fluorescent dye maleimides, use of an organic co-solvent like Dimethylformamide (DMF) or dimethylsulfoxide (DMSO) to dissolve them is essential. The latter was used to resuspend the dye powder to a 5-10 mM final concentration. However, once the dye is mixed with the protein for labelling, the minimum volume of DMSO added is required. Ideally, DMSO in the protein solution should be <3% vol/vol. This upper limit was scrupulously respected for all of

the samples listed in Table 3.2, therefore eventual unavailability of the protein for the reaction due to precipitation or degradation by DMSO also cannot explain such a low yield of labelled molecules.

- **TCEP concentration:** the two most commonly used thiol reductants are 2-mercaptoethanol and dithiothreitol (DTT)[235]. However, disulfide reduction by thiols can be inconvenient when reacting protein sulfhydryls with thiol-reactive extrinsic labels like maleimide dyes, as the SH groups of the reductant compete directly with those of the protein for attachment. Therefore, thiol-based reductants are typically removed by dialysis or gel filtration before the protein is labeled. Unfortunately, such removal is sometimes accompanied by air oxidation of the thiols back to the disulfides. Tris(2-carboxyethyl)phosphine (TCEP) is an alternative reducing agent which has been commercially available since 1992[236]. In aqueous solutions, TCEP stoichiometrically and efficiently reduces disulfides; it has been shown to be significantly more stable than DTT at pH values above 7.5 and high temperatures, and a faster and stronger reductant than DTT at pH values below 8.0[237]. In addition, TCEP has been advertised as being noncompetitive with protein sulfhydryls for attachment of thiol-reactive dyes, thereby eliminating the need to remove it before labeling[238]. However, it has been reported that TCEP might indeed react with maleimides at concentrations higher than 2.5 mM[239,240]. For this reason, in this work the final concentration of TCEP in the volume of those reactions involving Atto647-maleimide dye for single-molecule experiments was kept to less than 500 μM, as this was low enough to avoid undesired interactions with the protein's cysteine but it was at the same time 5-fold the typical protein molar concentration used for labelling ($\sim$ 100 μM), assuring its reducing efficacy - still only a 0.14-6% labelling yield was obtained for the relative products (see Table 3.2).

3.7 Discussion

From Table 3.2, a clear correlation between the yield values obtained and the illustrated labelling reaction parameters does not seem to emerge. Nevertheless, some partial conclusions can be drawn. Note that the Cy5 case will be left out, as estimation of the DoL for such reaction is probably not accurate for the reasons stated in section 3.6.

- It is unlikely that the low labelling efficiency is only due to TCEP competitivity for sulfhydryl groups on the proteins. In fact, for instance in the reactions of CheY and CheY** with Cy3B-maleimide dye, where up to 10 mM TCEP was present, the labelling yield did not seem to be affected by such concentration of reducing agent, but by the amount of dye in solution instead. It however never reached values greater than 20% even upon addition of 20 fold molar excess of Cy3B, nor showed a linear relationship between yield and molar excess of dye, as the addition of 10 fold molar excess of the same dye, in the presence of the same amount of TCEP, gave only 6% labelled molecules. This suggests that in the Cy3B case the difference was made by the increased amount of added dye.

- The only case where there seems to be some sort of correlation between the TCEP concentration and the labelling yield obtained is that of Atto647N: here, a yield >40% was achieved when 0.4 mM TCEP was present, whereas this was reduced to 3% upon addition of ∼10 mM TCEP, despite the fact that the excess dye in the former reaction was only half of that in the latter. This suggests that in the Atto647N case the difference was made by the reduced TCEP concentration.

- From the above considerations, the author feels confident inferring one major conclusion: the main cause underlying the diverse labelling yield values ob-

tained in this work is the different affinity of the maleimide modifications of the dyes used for the cysteine site in the modified chemotaxis proteins. The Cy3B-maleimide dye gives the best labelling yield, whereas Atto647 performs the worst. Atto647N seems to be placed in between these two. This empirical deduction could be due to the structural, electrostatic or hydrodynamic properties of such dyes as well as of the proteins themselves.

Chapter 4

Internalisation and Viability

4.1 Photostability of organic dyes *in vivo*

The photostability and brightness of the four organic dyes in Table 3.3 was evaluated for their use *in vivo* in *E. coli*. An example analysis for Cy3B and Atto647, the two main fluorophores used in the experiments illustrated in chapters 6 and 7, is reported below. Based on the approach described in 241, the single-cell photobleaching lifetime of cells electroporated with a 1.5 μM concentration of CheY(Cys)-Cy3B, Atto647-(Cys)CheY, Atto647N-(Cys)CheY and Cy5-(Cys)CheY was taken as a measure for photostability. Example frames that were recorded for the electroporated cells and for the positive control cells (NEP) are shown in Figure 4.1. Cells were segmented by adapting the MATLAB implementation Schnitzcells for bright-field cell images[242]. The manually adjustable cell masks were saved and then used to extract fluorescence data by calculating the total fluorescence intensity per cell area within each cell mask for each movie frame. The cell autofluorescence per cell area after photobleaching was subtracted using a custom-written MATLAB script (The MathWorks, Natick, MA, USA). Thus, single-cell photobleaching timetraces were obtained (Figure 4.2, black curves). The raw single-cell photobleaching timetraces

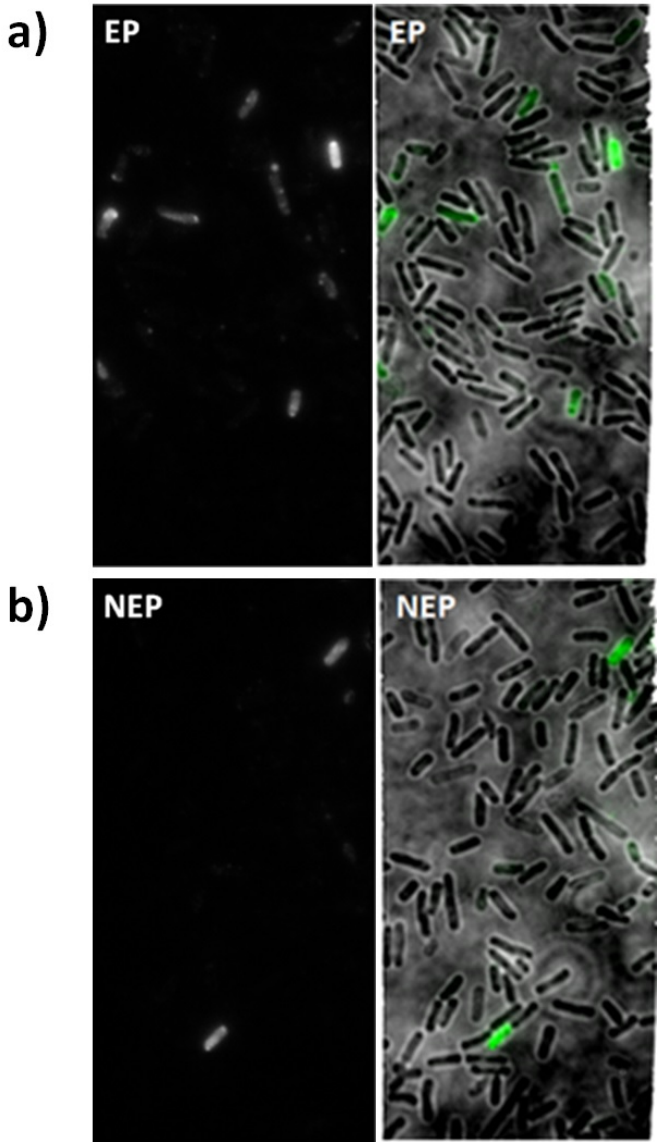

Figure 4.1: Example frames recorded for photostability studies. Fields of view of RP437 FliCst cells **(a)** electroporated with 1.5 μM (i.e. 30 pmoles) CheY(Cys)-Cy3B and **(b)** positive control (cells incubated with the same amount of dye but not electroporated): left panels, fluorescence at 532 nm; right, overlay of bright-field and green fluorescence in false colour. Images were recorded using nTIRF illumination and 100 ms exposure time; settings for Cy3B: 532 nm laser, 1 mW.

were fitted with a single-exponential (Figure 4.2, red curves). Cy3B showed a photobleaching lifetime of (19.9±8.9)s (mean ± standard deviation over 500 cells), Atto647 of (26.7±13.8)s (400 cells), Atto647N of (29.5±16.8)s (200 cells) and Cy5 of (3.8±1.8)s (200 cells). The first three values are in the range of results previously reported for such fluorophores in similar acquisition conditions (all dyes 100 ms exposure time - Cy3B: 532 nm laser, 1 mW; Atto647 and Atto647N: 637 nm laser, 300 μW)[241]; the photobleaching time for Cy5 was obtained in this work using a 637 nm laser with power of 600 μW, i.e. twice the one used in the cited paper: it is therefore consistent with the lifetime reported in 241 of (10±5) s for a laser of the same wavelength, same exposure time and 300 μW power, as the dose (i.e. power per area) on the sample was half than the one used in this work. As a comparison, photobleaching times for *Negative Control* cells (i.e. electrocompetent but never been incubated with the dye) is <4 s in the green channel and <8 s in the red channel with the same laser power settings and exposure times.

Based on these values, the pool of candidates for protein labelling was narrowed down to Cy3B, Atto647N or Atto647 which showed comparable photostability *in vivo*. Cy-Dyes are a group of highly fluorescent molecules that cover a wide spectral range and they are used as probes in many biological applications; however, most Cy-Dyes are vulnerable to cis/trans isomerisation about their polymethine linker which leads to loss of fluorescence upon excitation[243]. Cy3B is a conformationally locked version of Cy3, the green emitting dye in this series: it means it is not prone to photo-isomerisation and has superior fluorescence properties. The reason why this dye was used for the bulk fluorescence experiments shown in section 5.2 but not for single-molecule experiments reported later in chapter 6 and in chapter 7, is that bacterial cells exhibit a quite pronounced autofluorescence in the green region of the spectrum due to endogenous flavins, essential metabolic coenzymes[244]. Flavins comprise a category of molecules that include riboflavin (RF, vitamin B2) and its derivatives flavin adenine dinucleotide (FAD) and flavin mononucleotide

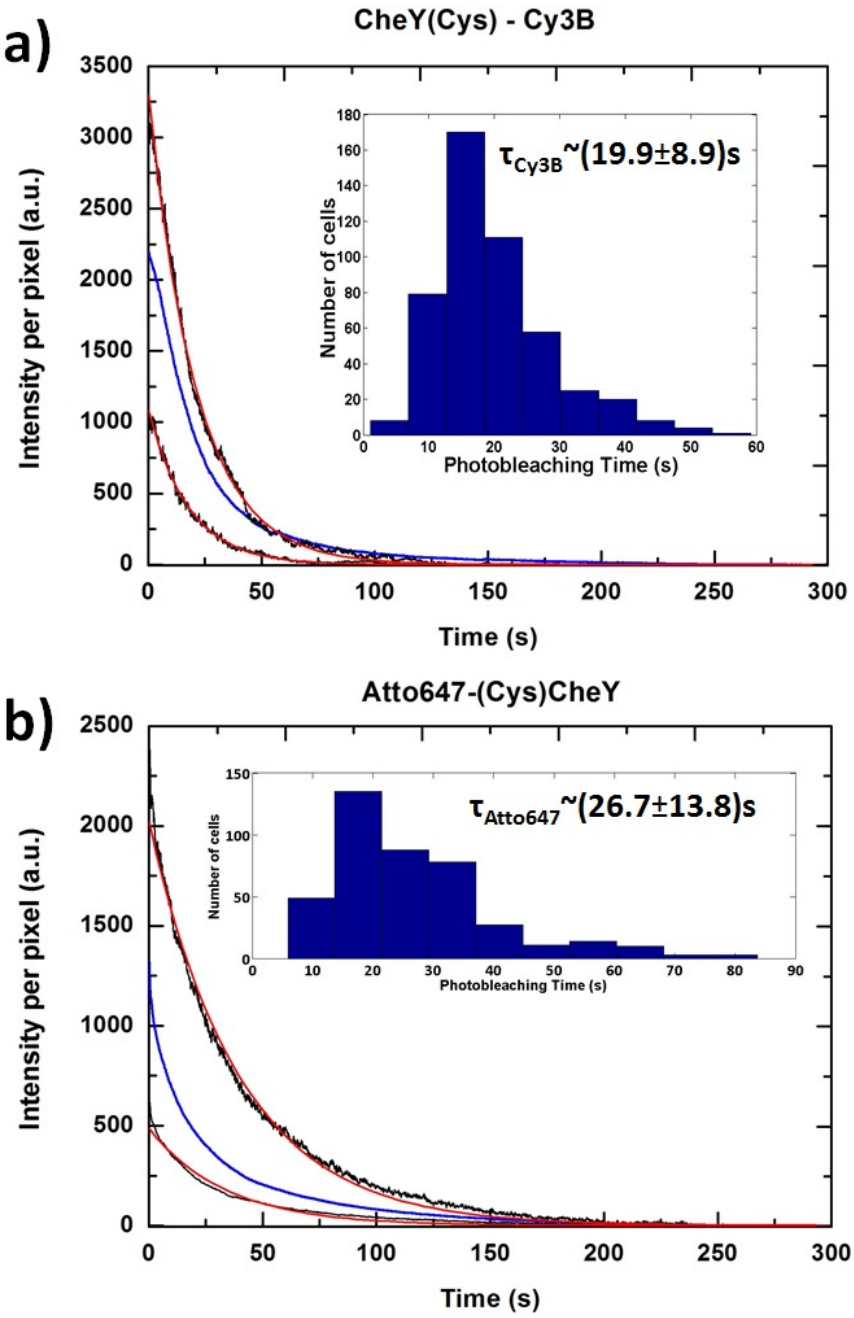

Figure 4.2: **a)** Cell-based photobleaching study of internalised CheY(Cys)-Cy3B into live *E. coli* as a measure for photostability. Main panel: two examples of single-cell photobleaching traces over time (black, raw data), respective single exponential fit (red, solid line) and average timetrace (blue) over 50 cells. Inset: a histogram of photobleaching lifetimes obtained by the single-exponential fit of single-cell photobleaching traces. **b)** Single-cell photobleaching lifetime measurements of Atto647-(Cys)CheY (main panel and inset as described in a). The average timetrace (blue) is in this case over 400 cells. Each histogram is based on a data set consisting of 400-500 cells. Data for both dyes were recorded using nTIRF illumination and 100 ms exposure time; settings for Cy3B: 532 nm laser, 1 mW; settings for Atto647: 637 nm laser, 300 μW.

(FMN). The oxidised form of flavin is excited at 450-490 nm and emits at 500-560 nm, whereas the reduced state exhibits no fluorescence. Due to the aerobic experimental conditions adopted in this work, the presence of some of such coenzymes in the oxidised, green-fluorescent form in the cell suspension could not be excluded. Cy3B was deemed suitable for high-loading experiments such those described in 5.2, where the background fluorescence from various sources can be disregarded due to a much brighter signal from the internalised probes; however, a dye emitting in a different channel was selected to carry out single-molecule measurements reported in chapters 6 and 7, where precise measurement of brightness and accurate tracking of a single labelled protein could suffer more from cellular autofluorescence. The ultimate choice of dye therefore ended up being between Atto647N and Atto647, both emitting in the red region of the visible spectrum. Diode laser excitation at wavelengths greater than 635 nm and red-absorbing fluorescent dyes were shown to reduce autofluorescence of biological samples and cell damage when working with live cells[245]. Atto647N is a popular dye in single-molecule experiments due to its outstanding brightness and photostability; however, its positive charge and hydrophobicity[230] cause molecules labelled with this dye to stick non-specifically to, for example, microscope cover slides or to cell walls when internalised[246,247]. As a consequence, Atto647N has proved difficult for study of single-molecule dynamics *in vivo*[241]. For all these considerations, the dye of choice for the single-molecule work reported in chapters 6 and 7 of this thesis is Atto647 (excitation 647 nm, emission 669 nm, extinction coefficient 120000 $M^{-1}cm^{-1}$).

4.2 Brightness of Cy3B and Atto647 dyes *in vivo*

One of the main goals of this work was to carry out single-molecule tracking of dye-labelled CheY molecules while performing their function as response regulator in live cells, diffusing in the cytoplasm between the chemoreceptor clusters and the

motors, binding to each of the latter in turn. Collecting a large number of emitted photons per frame (N) from the organic dyes is essential to localise and track the electroporated labelled proteins with high-precision, since lateral localisation precision scales with $1/\sqrt{N}$, neglecting pixelation and background noise[248]. Moreover, in order to avoid artifacts caused by overlapping spots, it was also fundamental to quantify the cellular uptake of labelled proteins upon electroporation and tune the initial incubating concentration to yield internalisation of very few proteins per cell (ideally less than 5 in average). Both Cy3B and Atto647 have been previously shown to have very high, comparable brightnesses *in vivo* when attached to dsDNA[241]; brightness values in the same range of those reported in 241 were found in this work for the case of dye-labelled proteins, as well. Single-molecule photobleaching steps in the fluorescence decay timetraces of *E. coli* cells electroporated with a 15 nM concentration (100 times lower than in photostability studies) of CheY(Cys)-Cy3B and Atto647-(Cys)CheY were taken as a measure of fluorophore brightness *in vivo*. Single-step photobleaching timetraces from cells loaded with less than 6 fluorescent molecules were fitted by Hidden Markov Modeling (HMM) as previously described[5] and the photobleaching step heights were obtained for 45 and 60 cells, respectively (Figure 4.3 a) and b), left panels, blue curves: raw data, red curves: HMM fit). In this specific case, timetraces were modelled as a sequence of up to 10 hidden states and transitions (i.e. photobleaching); the steps thus obtained were fitted with the Viterbi algorithm and a comprehensive MATLAB script performing the latter and HMM was run recursively. It is noticeable that the baseline in the photobleaching curves for both dyes does not reach zero. This is probably caused by autofluorescence from the agarose pads used or from other spurious sources. Being only one dye species present in each experiment, step-heights data were fitted with a single Gaussian. The center of the latter (right panels, red curves) for the binned photobleaching step heights is the unitary fluorophore intensity, and corresponds to the *in vivo* brightness of a single fluorophore. The single-Gaussian fit is centered

at (3.5±8.1) a.u., corresponding to a unitary fluorophore intensity of (3100±7200) photons per second for Cy3B, and at (8.1±5.6) a.u., corresponding to a unitary fluorophore intensity of (7000±4800) photons per second for Atto647. The photons per second values were obtained from comparison with those reported in 241 using the same imaging setup and acquisition parameters, and were found to be in agreement. The error on the estimate for Cy3B is bigger than the one on Atto647 due to lower sampling. In this case, to have an idea of how much the estimate given by the centre value of the Gaussian fit is close to the real unitary fluorophore intensity it is worth looking at the Standard Error on the Mean (SEM) (standard deviation divided by $\sqrt{N}$), as this takes into account the different sample sizes (N) for the two dyes: for Cy3B, the Gaussian fit is then centred at (3.5±1.2) a.u. (mean±SEM) whereas for Atto647 the Gaussian fit is centred at (8.1±0.7) a.u. (mean±SEM). This means that for Cy3B the unitary fluorophore intensity determined as the centre of the fitted Gaussian is within 35% of the true value, while for Atto647 the unitary fluorophore intensity determined as the centre of the fitted Gaussian is within 9% of the true value. In Figure 4.3 c), histograms of the number of fitted steps for Atto647(Cys)-CheY (left) and CheY(Cys)-Cy3B (right) are shown: these give an indication of how many labelled proteins were internalised per cell, and, as desired, despite cell-to-cell variability, they are indeed centered at (5±2) for CheY-Atto647 and (3.6±1.7) for CheY-Cy3B on average, estimated as the μ and σ of the fitted Gaussians (red curves in Figure 4.3, c) calculated using the *lsqcurvefit* MATLAB in-built function). For all the fits (red curves) shown in Figure 4.3, goodness was determined by calculating their R-squared (R^2) value (reported in the Figure's caption). R-squared is a statistical measure of how close the data are to the fitted regression line. It is also known as the coefficient of determination, or the coefficient of multiple determination for multiple regression.

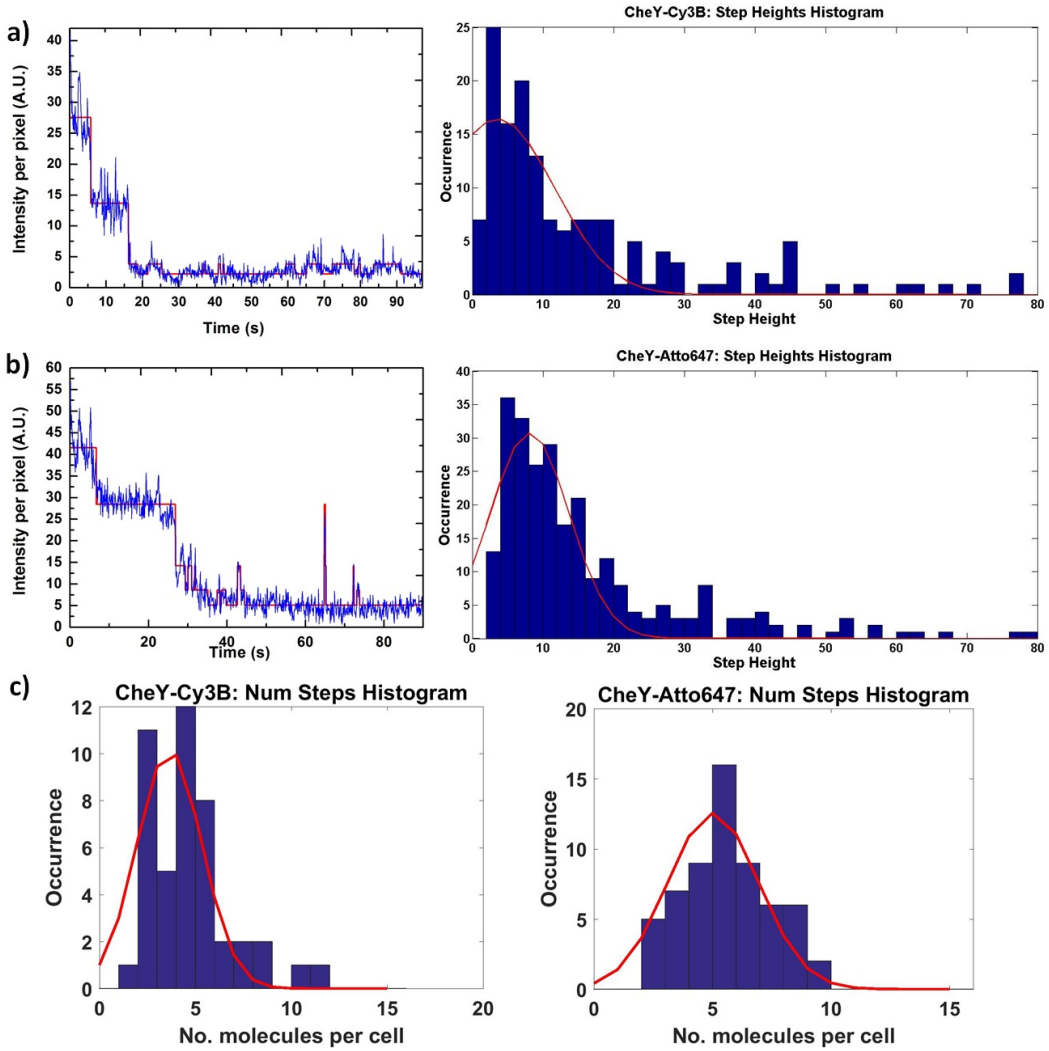

Figure 4.3: Photobleaching step size analysis as a measure of Cy3B and Atto647 dyes' brightness in live *E. coli*. **a)** Internalisation of CheY(Cys)-Cy3B. Left: example of single-cell photobleaching timetrace (blue: raw data, red: Viterbi path). Right: histogram of single-step height intensities from fitted steps (45 cells, red: Gaussian fit calculated using the *lsqcurvefit* MATLAB in-built function - $R^2 = 0.77$). **b)** Internalisation of Atto647-(Cys)CheY and same graphs as for **a)** (60 cells, $R^2 = 0.83$). Here is also visible an example of a blinking event just after a minute acquisition. See main text for estimation of unitary fluorophore intensities. **c)** Histograms of the number of steps per cell for Atto647-(Cys)CheY (left) and CheY(Cys)-Cy3B (right), confirming that the used loading conditions are suitable for single-molecule experiments as less than 5 molecules are internalised in average per cell (red curves Gaussian fits, $R^2 = 0.75$ for Cy3B, $R^2 = 0.91$ for Atto647).

4.3 Viability

Electroporation is a harsh procedure which damages and inevitably kills many cells. In fact, according to the most-widely shared understanding of the electroporation mechanism as described in section 3.2, both reversible and irreversible electroporation result in transient openings (pores) forming through the membrane. These pores may allow significant molecular transport between the intra- and extracellular volumes which could lead to a significant chemical imbalance which might negatively affect the cell. Electroporated bacteria are usually recovered in rich medium for one hour or more in case of DNA delivery to allow for replication and gene expression. However, in this work, the recovery time was reduced to only a few minutes, the main interest being to image fluorescence from internalised molecules on a timescale shorter than that for cell division, fluorescence degradation or intracellular protein breakdown. Minimising any damage caused to cells was the key factor guiding the formulation of the delivery protocol illustrated in section 3.4. Viability is defined as the ability of bacterial cells to grow and divide in favourable conditions on agar plates or in liquid medium. In contrast to viable cells, dying/dead cells have irreversibly lost their capability of growth and multiplication. Besides these two mutually exclusive conditions, upon microscopic investigation on agarose pads some electroporated cells in a sort of "persistent" state were observed in this work, nor growing nor dividing neither showing any sign of damaged membranes, previously described as "identical" in the literature[219]: these cells could be in a still viable but stressed state after application of the electric pulse and in need of further recovery time to resume growth/division and motility. It should be in fact pointed out that a cell can be "alive" in the sense of functional motility and chemotaxis without being able to divide or grow (as shown in 249, cell envelopes without cytoplasm (*ghosts*) still rotated when artificially energised). A multi-approach assessment of cell viability, characterisation of protein internalisation efficiency and fluorescence persistence

over time upon electroporation of labelled chemotaxis proteins is included in the following.

4.3.1 Viable plate counting

Complete cell viability, not just membrane recovery, is usually important for biological applications of electroporation, but determination of cell death following such treatment is nontrivial. If the cells in question can be cultured, assays based on clonal growth should provide the most stringent test, and this can be carried out relatively rapidly assessing microcolony formation, as explained below.

- EP sample: electrocompetent *E. coli* cells were electroporated without previous incubation with fluorescent species using standard parameters and recovery/washing procedure (1.2 kV, 5 minutes recovery in SOC medium and 4 washing steps in MB); they were plated on LB-agar in 10^{-3}, 10^{-5}, 10^{-6}, 10^{-7}, 10^{-8} and 10^{-9} dilutions in MB.

- NEP sample (equivalent in this case to the *Negative Control* one, as cells were not incubated with any fluorescent molecule): same treatment as EP sample; the same dilutions in MB as for EP sample were plated, except for the 10^{-3} one as it would have been too dense to yield single colonies.

- Wild Type (WT) sample: cells from an O/N culture were diluted in fresh TB, grown to OD_{600nm}=0.4 to reproduce as much as possible the same growth conditions in which cells were before being made electrocompetent and plated on LB agar in 10^{-6}, 10^{-7}, 10^{-8}, 10^{-9} dilutions in MB.

All plates were incubated O/N at 30°C. At the end of the incubation period, only the plates containing between 30 and 300 colonies were selected and the colonies on each one were counted. This particular choice was made as this range of colonies is conventionally considered statistically significant: in fact, if there are less than 30

colonies on a plate, small errors in dilution technique or the presence of few contaminants will have a drastic effect on the final count; likewise, if there are more than 300 colonies, there will be poor isolation and colonies will be difficult to count flawlessly. The number of colonies in each plate was multiplied by the respective dilution factor, in this way determining the number of Colony-Forming Units (CFUs) per ml, i.e. the number of viable (living) cells in the original electroporated sample. Results from such test showed that, out of a starting sample with 10^8 (i.e. OD_{600nm}=0.4) cells:

- EP cells had 172×10^5 CFUs per ml;
- NEP cells had 110×10^6 CFUs per ml;
- WT cells had 30×10^6 CFUs per ml.

The difference between NEP and WT cells can be accounted within the pipetting error. The number of viable cells in the EP sample is ∼20% of those in the NEP and WT samples, meaning that about 80% of the initial cells in the EP sample died upon electroporation. This value is in agreement with estimates previusly reported in the literature for electroporation in *E. coli* of RNAP ω subunit (10 kDa) labelled with Cy3B at the same voltage (but after 1-2 hours recovery vs 5 minutes here), i.e. growing/dividing cells were (30±15)% of the starting ones[219].

4.3.2 Optical Density versus recovery time

A second approach to test cells viability upon electroporation based on ensemble measurement of optical density is described in the following.

- EP sample: electrocompetent *E. coli* cells were electroporated without incubation with fluorescent species using the same parameters and recovery/washing procedure described in the previous section;

- NEP sample: same treatment as EP sample, but no electric pulse applied;
- *Negative Control* sample: these were just electrocompetent cells thawed on ice, no electroporation nor washing steps applied.

All samples were resuspended in SOC and recovered for 2 hours 30 minutes at 30°C, 225 rpm, measuring the OD_{600nm} and checking for motile phenotype every 30 minutes under 40x phase-contrast microscope.

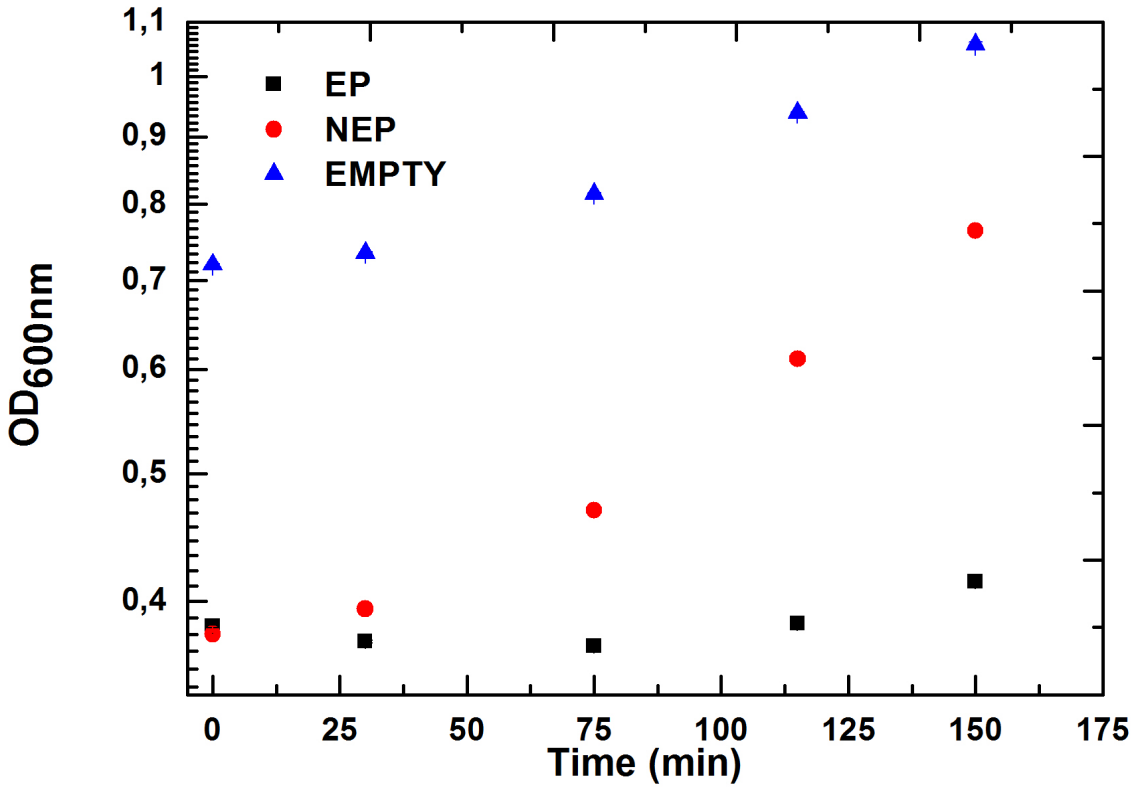

Figure 4.4: Semi-log plot of OD vs recovery time curves for EP, NEP and *Negative Control* cell suspensions over 2 hours 30 minutes recovery in SOC at 30°C. Where applicable, electroporation was performed 30 minutes before the first data point was taken. The red arrow indicates the time when spinners started to appear in both EP and NEP samples (75 minutes into recovery). Illustrative of one single culture; error bars estimated as ±0.01 uncertainty on the OD measurement returned by the spectrophotometer.

Figure 4.4 shows a plot of the OD curves of the three samples as a function of the recovery time: comparing them, it is possible to infer that, while NEP and *Negative Control* cells basically resumed growth and division at the wild type rate straight

away (i.e. one generation every 40-50 minutes at 30°C), there is a delay of ∼2 hours before the bulk effect of cell division becomes evident in the EP sample growth curve. Motility-wise, a lag time was observed for both EP and NEP cells, instead, before retrieval of any spinning/swimming phenotype, which occurred after 75 minutes from the start of recovery with different levels in the two samples (few spinning tethered cells over several Fields of View (FoVs) in the EP sample (¡1%) vs ∼1 per FoV in the NEP sample - about 20 cells in each FoV (5%)). Such lag time in motility recovery might be due to disruption of either the motor itself or the proton motive force or to other kind of intracellular unbalance - either at the rotor or stators level - as a combined result of the several washing steps performed during the electrocompetent process and, in the case of the EP cells, of the electric shock inflicted. While the delay in motility recovery for NEP and EP cells was similar, this turned out to be however shorter than the time required for the EP cells to start dividing again, indicating that it is in principle possible to image fluorescence and motility at the same time in the very cells present in solution at the moment of electroporation, losing none or, in the worst case, only some of the initial fluorescence signal due to cell growth/division. This was an unprecedented and very promising result for the aims of this work, as cell division over many generations would inevitably "dilute" the fluorescence signal from the electroporated molecules[5]. More motility studies are reported in chapter 7.

4.3.3 Single-cell growth

A third, this time single-cell, approach to assess resumption of division upon electroporation is described in this section.

- EP sample: electrocompetent *E. coli* cells were electroporated with ∼17 pmoles (∼0.9 μM) of CheY**(Cys)-Cy3B using standard parameters and recovery/washing procedure described above;

- NEP sample: same treatment as EP sample, but no electric pulse applied;
- *Negative Control* sample: these were just electrocompetent cells thawed on ice and diluted 1:10 in MB, no incubation, electroporation or washing steps applied.

Growth and division for NEP and EP cells deposited onto 1% EZ Rich Defined Medium (RDM)[250] agarose pads was monitored on a microscope in DIC over 3.5 hours at room temperature (∼156 cells). In this experiment, approximately 68% of the electroporated cells (106 out of 156) resumed growing/dividing within one hour, 20% remained intact but not growing (31) and 12% (19) showed evident signs of damaged membranes or other altered features. The 68% value obtained here is higher than the 20% one obtained in section 4.3.1 for colonies formed upon electroporation and recovery on LB-agar plates. This discrepancy could be due to the different growth media used in section 4.3.1 and in this section: in the former, LB agar was employed, a widely used bacterial culture medium mainly made of tryptone and yeast extract, which supply essential growth factors, such as peptides, peptones, trace elements (e.g. sulfur, magnesium), minerals and vitamins (see recipe in Appendix A). Sodium ions for transport and osmotic balance are provided in this medium by sodium chloride, which can be added in different concentrations - in this case 5 g/L NaCl (i.e. low salt). In the formulation adopted in the experiment in section 4.3.1, however, LB agar provided only small amounts of utilisable carbon sources, with catabolisable amino acids recovered from breakdown of oligopeptides the principal ones. In fact, a dedicated carbon source like glucose or glycerol was lacking from the composition, and the bacteria would therefore probably feed on peptides of varying length, in a much slower fashion than on sugars. There is, moreover, a clear size limit at about 650 Daltons for the peptides usable by a cell, which corresponds to the exclusion limit of porin channels[251]. The smaller, usable peptides are a minority, perhaps a quarter of the entire LB agar mixture, and free amino acids are an even

smaller minority, approximately 1% or less of the entire preparation[252]. Another factor may have an even more profound influence on the difference observed: the availability of divalent cations, Mg^{2+}, Ca^{2+} or similar, needed by the cells to link the highly negatively charged lipopolysaccharide (LPS) molecules in their outer membrane[253]. The experimentally determined value for the Mg^{2+} content of LB broth cited by Papp-Wallace and Maguire in 254 is quite low, only 30-40 μmol per litre. In the single-cell growth experiment described in this section, the EZ RDM was used, instead: differently from LB, it has 2 g/l, i.e. 0.2% by weight, glucose, which is *E. coli*'s preferred carbon source[255,256], and up to 500 μmol of Mg^{2+} per liter. The presence of these two factors may well have helped to improve the bacteria's recovery and growth from the electroporation protocol in this experiment with respect to the first one.

4.4 Internalisation efficiency

Here the question of how many cells in the population of electroporated bacteria had taken up a significant number of dye-labelled proteins was addressed. Movies of electrocompetent *E. coli* cells onto agarose pads electroporated with up to 30 pmoles of labelled CheY protein were recorded. Following the approach described in 5, 241, as for section 4.1, cells were segmented automatically by adapting the MATLAB implementation Schnitzcells[242] for bright-field cell images and the total fluorescence intensity per cell area within each cell mask for each movie frame was calculated. Apparently dividing cells were segmented as 2 cells if at an advanced division state. A suitable brightness threshold was set to take into account autofluorescence from the cellular background using the *Negative Control* cells and this was subtracted from both EP and NEP samples' intensities; cells were considered as "loaded" when the initial cell intensity normalised by the cell area was larger than the mean plus three times the standard deviation of non-electroporated NEP cells,

a criterion previously used in 219, 241. Loaded cells contained about 50-300 CheY molecules. The internalisation efficiency was defined as the ratio of loaded cells to the total number of cells visible in the bright-field image. However, since these corresponded only to very bright ones, the cells classified as "loaded" in this way may be less than the total number of cells that have undergone at least some degree of internalisation. Using the standard electroporation protocol, an internalisation efficiency of (11.9±6.1)% was estimated as an average from separate experiments incubating with 10-30 pmoles (i.e. 0.5-1.5 μM) of different labelled proteins and dyes, counting ∼2800 cells overall. Namely, CheY(Cys)-Cy3B, KF-Cy3B (KF = Klenow Fragment), Cy5-(Cys)CheY, CheY(Cys)-Atto647 and CheY(Cys)-Atto647N samples were used. This internalisation efficiency is slightly lower than the reported (24±5)% in the literature for electroporation of 2.5 μM RNAP ω-Cy3b at 1.2 kV[219]: in the first instance, the concentration of labelled protein the cells were incubated with in the experiment described here was a bit smaller than in 219, i.e. 1.5 μM vs 2.5 μM; quantitatively, being this ∼1.6-fold the amount of protein used in this work, the calculation 11.9 × 1.6 would yield ∼20% internalisation efficiency, in agreement with (24±5)% reported by 219. Secondly, a reason for this could be the smaller molecular weight of the ω subunit with respect to CheY (10 kDa vs 14 kDa), which would facilitate electric-field driven internalisation of the former; thirdly, it might also be due to the fact that cells classified as "loaded" in this paper were those exhibiting average fluorescence intensity higher than the mean intensity of *Negative Control* cells plus three standard deviations, whereas in this work NEP cells were used to set a threshold for considering a cell loaded. Ideally, *Negative Control* and NEP samples should have the same average fluorescence intensity, but, having measured both intensities, the author found this was not exactly the case in reality: in fact, having the NEP sample been incubated with the fluorescent molecules, it might retain some fluorescence even after extensive and careful washing, for instance if some molecules stick on the outside of the cell membrane or if some

free dye escaped from the removal steps described in section 2.4.6 has entered the cell. Moreover, electrocompetent NEP cells with compromised membranes could also allow internalisation even without electroporation. In this work, NEP cells were therefore chosen when setting a threshold for defining what a loaded cell was in order to take into account the described sources of false positives. Signal from internalised molecules was still visible in cells not growing nor dividing (classified as "intact but not growing") for more than 6 hours after electroporation and for more than 3.5 hours in cells classified as "growing" or "growing and dividing".

4.5 Correlation between cell loading and viability

In this section, the results of a simultaneous evaluation of cellular loading and viability upon electroporation are reported: 50 fields of view of cells electroporated with CheY**(Cys)-Cy3B were imaged on 1% EZ agarose pads both in bright-field and epi-fluorescence for 3.5 hours using an automated microscope stage and time lapse measurement. The EZ RDM was chosen over SOC for this experiment because of its low autofluorescence. Out of the cells displaying some degree of internalisation, the number remaining intact but not growing, growing but not dividing, actively dividing and showing damaged membranes or other altered features during the 3.5 hours of acquisition was monitored. The internalisation efficiency was ∼9.8% (21 loaded out of 215 cells), in agreement with the estimate reported in the previous section, with 19% (4 out of 21) of the fluorescent cells growing but not dividing, 19% growing and dividing (i.e. 38% overall growing AND/OR dividing) (Figure 4.5, a)), 43% (9 out of 21) intact but not growing and 19% damaged over the 3.5 hours of imaging (Figure 4.5, b)). It is therefore possible to conclude that fluorescence uptake is not lethal for the loaded cells, which are largely still viable upon internalisation, and cell viability is independent of fluorescence load (in agreement with findings reported in reference 5). Comparing these values with those repor-

ted in 219 for a 12 kV/cm field strength and 1-2 hours recovery, it is evident that, thanks to the damage-minimising protocol applied and despite recovering cells only for 5 minutes, both the proportion of loaded cells which can grow/divide after electroporation (38% vs 11%) and of cells remaining intact but not growing up to 3.5 hours from application of the electric pulse (43% vs 32%) were increased, reducing the percentage of damaged cells from 59% to only 19%, as well. Fluorescence from internalised molecules was shown to decay exponentially over time for all the cases (growing/dividing, intact but not growing and damaged cells) but with different time constants, namely (118±4) min for the growing/dividing, (180±35) min for the intact but not growing and (101±13) min for the damaged cells (Figure 4.5, c)). These values are consistent with the hypothesis that damaged cells have "leaky" membranes through which the internalised fluorescent molecules can escape into the outer solution more quickly than through intact membranes; moreover, the fact that between the time constants for growing/dividing and intact but not growing cells there is a factor of ∼1.5 is consistent with the assumption that whenever a loaded cell grows/divides it redistributes the internalised fluorescent molecules to a more elongated shape/its daughters, respectively.

4.6 Motility assessment and recovery

Application of the electroporation technique for the internalisation of proteins into live bacteria is something only recently attempted by colleagues in the Physics Department[5,219,241] and is not reported anywhere else. However, neither in this work nor in the literature reporting more "canonical" uses of electroporation in *E. coli* has recovery of electroporated cell motility and the state of the motor after electroporation been investigated. A functional motor is paramount for the study of the interactions between the *E. coli* chemotaxis system's response regulator CheY and the motor's switch complex. Since the start of this project, therefore, much

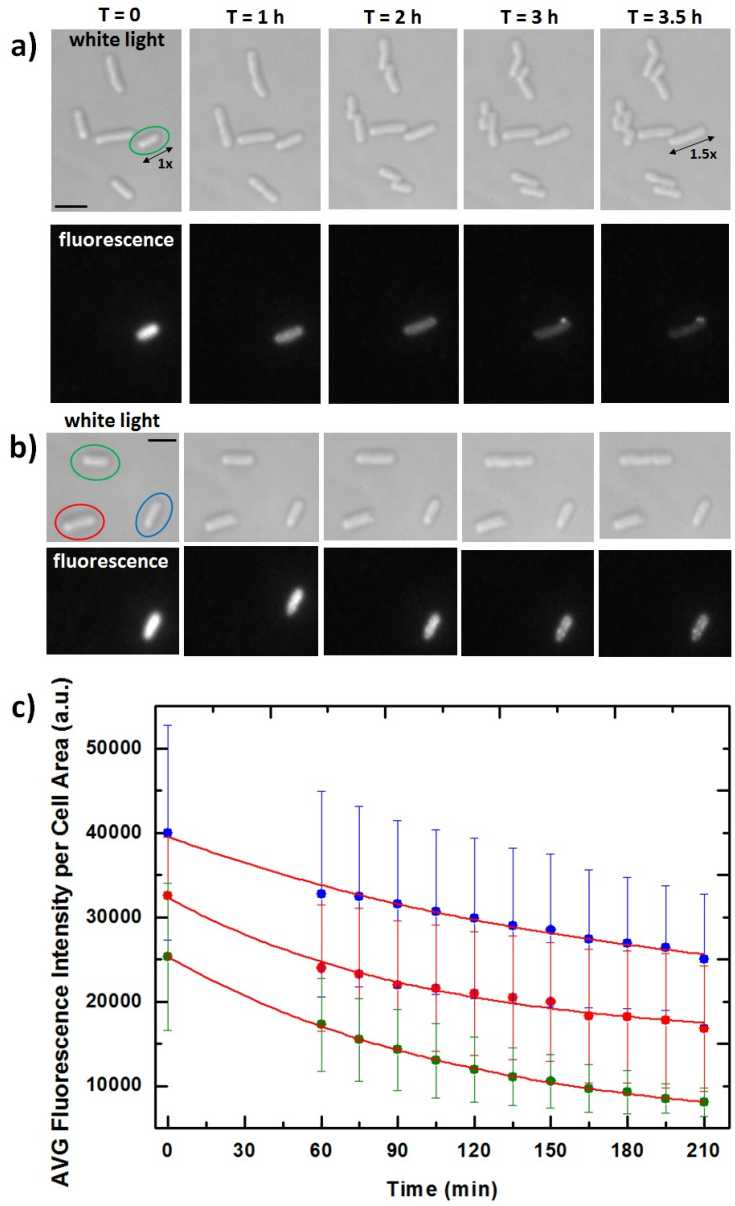

Figure 4.5: Electroporated *E. coli* cells imaged in white light (top panels) and in fluorescence (bottom panels) during a 3.5h time-lapse experiment on rich medium agarose pad: **a)** in this field of view, all but one are growing/dividing after one hour (top, white light), including the only cell that has uptaken some fluorescence (green oval) and which increases its size 1.5x by the end of the acquisition. **b)** in this field of view, a growing/dividing cell (green oval), a damaged cell (red oval) and an intact but not growing cell (blue oval) are visible. The latter remains in its lag state at least until the end of the acquisition, without showing any evident sign of membrane degradation. **c)** in **a)** (green dots, single exponential fit in red with τ = (118±4) min), **b)** (blue dots, single exponential fit in red with τ = (180±35) min)) and **c)** (red dots, single exponential fit in red with τ = (101±13) min)) the internalised fluorescence decays exponentially over time and single-molecules start being distinguishable in the cells from T = 3h onwards. As stated in section 4.5, the three fluorescence decays are averages over time for the observed 8 growing/dividing, 4 intact but not growing and 4 damaged cells. Errorbars represent standard deviations on the values measured for the different cells, reflecting internalisation variability. Scale bars in white light images 3 μm (translate to fluorescence images).

effort was put into recovery of cells to a motile phenotype upon electroporation. If the exposure to the electric field is sufficiently short and the membrane recovery sufficiently rapid for the cell to remain viable (see discussion in section 4.3), electroporation is said to be reversible (i.e. Reversible Electrical Breakdown, REB), irreversible otherwise. There is some experimental evidence that the membrane recovery (or, microscopically, pore resealing) consists of several stages: a fast phase (occurring in microseconds after the end of the pulse) is followed by several slower phases lasting from milliseconds to tens of seconds, or even minutes[257,258]. Recovery of the membrane after pulsing is clearly essential to achieving motility. Presently, however, relatively little is known about the kinetics of membrane recovery after the membrane has been damaged by REB. Some studies have used "delayed addition" of molecules to determine the integrity of cell membranes at different times after pulsing[259,260]: such experiments suggest that a subpopulation of cells has a delayed membrane recovery, as they are able to take up molecules after the pulse. This observation will be useful in order to understand some of the experimental results reported in the following.

In these studies, motility was rapidly assessed via phase-contrast microscope examination, simply sandwiching cells between a slide and a coverslip. Such an approach was also useful for determining how consistent cellular shape and arrangement were among different days. One disadvantage over tunnel slides was that, since no washing was applied, not all cells were tethered and in some cases the motion seen was due only to Brownian motion and convection currents in the fluid, making it therefore difficult to distinguish between real directed motion and diffusion. The purpose of this simple test was, however, to observe at least *some* rotating tethered cells to judge whether the bacteria had already started recovering motility from the electroporation shock and could therefore be used for further experiments.

4.6.1 Results

The effect of electroporation on cell motility was first investigated without anything being actually internalised. It is important to keep in mind that by the point the motility of electroporated cells is assessed, the cells will have gone through two quite stressful treatments, i.e. the process that made them electrocompetent (including freezing and thawing) and the electroporation itself. Whether the former had any effect on cell motility was addressed first: to start with, it was checked that the RP437, FliCst cells in the starting frozen stock were actually motile by phase-contrast microscopic examination as described above. A stock of electrocompetent cells was then prepared applying the protocol from 178 without any modifications, using LB medium at 37°C throughout all the growing steps and flash-freezing the cells in 20 μl aliquots. After electroporation and 5 minutes recovery in TB at 30°C with agitation, non-electroporated (NEP) and electroporated (EP) samples (prepared as illustrated in section 3.4) were observed under a 40x phase contrast microscope and deemed NOT motile. However, EP cells were not all dead, as they started dividing again upon extensive recovery in TB at 30°C, with motile daughter cells after about 3 hours (see Figure 4.6, black data points). A similar behaviour was found for NEP cells, which were not electroporated but were subject to the same recovery procedure as EP cells. These data clearly indicated that the process of making the cells electrocompetent was affecting the motor's function, even before application of the electric pulse. This was likely due to the particular temperatures and media used: in fact, it is known that the optimum temperature for *E. coli* motility is 25-37°C[179]. Moreover, LB is an extremely rich medium in which cells grow very rapidly: in fact, as visible from the blue and green data points in Figure 4.6, the LB-grown electrocompetent cells were in a stationary phase when the electric pulse was applied, and organisms from this phase are known to be distinctly inferior for motility than those from an exponential phase. These reasons

could account for a 3 hours-delay before re-gaining a motile phenotype. In order to restore motility as quickly as possible after electroporation to limit fluorescence loss consequent to cell division, the protocol from[178] was modified as described in section 3.4. Cells made electrocompetent in this way were motile both when freshly made and after being frozen and thawed, as judged by phase-contrast microscopic examination of both samples. Nevertheless, comparing the optical density curves over time of NEP and EP cells made electrocompetent using LB or TB (Figure 4.6), it was found that also TB-grown EP cells' OD started increasing again after about 3 hours from electroporation upon recovery in TB at 30°C. However, while only few (<1%) spinning tethered cells (*spinners*) were visible in LB-grown electrocompetent cells after 3 hours' recovery (most probably being already daughter cells), more (10%, i.e. 112 out of 1106 cells) were present in TB-grown electrocompetent cells already after 50 minutes recovery. Eventually, however, SOC was selected as the best medium for early cell recovery upon electroporation: in fact, comparing the black curve in Figure 4.6 and the red curve in Figure 4.4, it is possible to notice that while in the former there is a percentage decrease of about 38% in the OD_{600nm} between the value immediately after electroporation and the minimum at ∼80 min after electroporation (i.e. before cells resume division), such percentage decrease is only 3.4% for the latter, where cells were recovered in SOC for the same amount of time and with the same shaking settings. This physiological decrease in optical density in the first minutes after electroporation is likely due to the presence of damaged cells which do not manage to recover their membranes to a healthy state and lyse as a consequence. As explained in section 4.3.3, divalent cations like Mg^{2+}, Ca^{2+} and similar, are needed to link the highly negatively charged lipopolysaccharide (LPS) molecules in their outer membrane; moreover, glucose, the carbon source preferred by *E. coli*, could also help to re-establish intracellular energetic levels. Differently from TB, SOC contains both these elements, and is therefore likely to provide the electroporated cells with more necessary nutrients to recover from electroporation

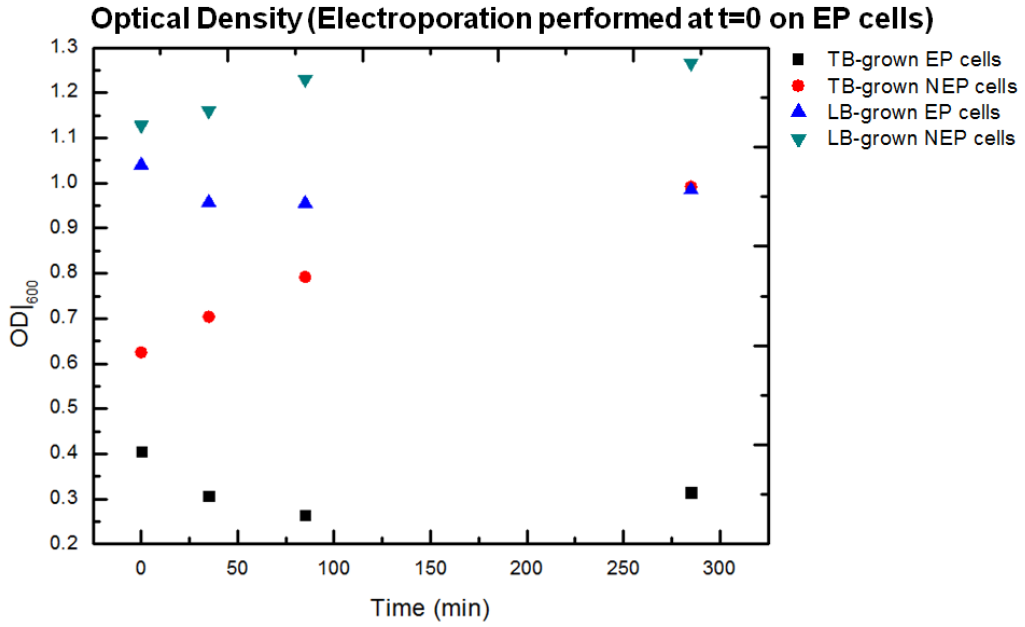

Figure 4.6: Comparison between OD values for LB-grown and TB-grown NEP and EP cell suspensions over 4 hours 45 min recovery in TB at 30°C. Where applicable, electroporation was performed at t=0. It is possible to see that both curves corresponding to LB-grown and TB-grown EP cells start slowly rising again after about 3 hours' recovery. Illustrative of one single culture; error bars estimated as ±0.01 uncertainty on the OD measurement returned by the spectrophotometer.

faster and more efficiently. Furthermore, the percentage of electrocompetent cells spinning in SOC after 50 minutes recovery was comparable to that in TB (i.e. (11±4)%, average of 4 experiments over 2 different days, 152 out of 1328 cells) indicating that similar motility capability was retained despite the medium being richer.

4.7 Summary

In this chapter, photostability of the four chosen CheY-dye complexes was characterised by measuring their photobleaching lifetime *in vivo*. CheY(Cys)-Cy3B, Atto647-(Cys)CheY and Atto647N-(Cys)CheY performed equally well with lifetimes of the order of 20-30 s; however, due to the high "stickiness" of Atto647N previously found, and in these experiments confirmed, CheY(Cys)-Cy3B and Atto647-(Cys)CheY con-

jugates were in the end selected to perform high-load and single-molecule experiments, respectively. The brightness of these two dyes was therefore evaluated *in vivo*, as well, using Hidden Markov Modeling and was found to be on average ∼3100 photons per second for Cy3B, and ∼ 7000 photons per second for Atto647, in agreement with previously measured values for the same dyes[241]. An estimate of the number of labelled proteins internalised using 1.2 kV and 15 nM concentration in the electroporation cuvette was also determined, with less than 5 molecules per cell found on average.

Studies of cell viability upon electroporation were then reported: in the light of the results from different types of assays, i.e. viable plate counting, optical density and single-cell growth, it was possible to conclude that, upon recovery in rich medium, up to 68% of the cells resume growth/division within one hour from electroporation. The existence of a correlation between cell loading and viability was assessed next. Fluorescence uptake was shown to be not lethal for the loaded cells, which were largely still viable upon internalisation, and cell viability was demonstrated to be independent of fluorescence load (in agreement with what previously reported in 5.) Finally, evidence for the existence of a minimum lag time of ∼50 min before cells start spinning/swimming again after application of the electric pulse and recovery in TB was presented. This is probably mostly due to the electric shock inflicted by electroporation, in terms of either disruption of membrane integrity, of proton motive force or both. Such delay, however, turned out to be less than the time required for cells to start dividing again, thus meaning that it is indeed possible to image fluorescence from the internalised molecules and a motile phenotype at the same time in the very cells present in solution at the moment of electroporation, losing none or, in the worst case, only some of the initial signal.

Contributions

Anne Plochowietz (Kapanidis group, Department of Physics, University of Oxford) provided MATLAB software used to produce the results illustrated in sections 4.1, 4.2 and carried out Hidden Markov Modeling analysis of the experimental data collected by the author.

Chapter 5

Motility and functionality in electroporated *E. coli*

In the previous chapter, independence between cell loading and viability upon electroporation was shown; furthermore, as a complementary check, the possibility for the cells to recover a motile phenotype upon electroporation was also assessed and confirmed. The main results of this work will be described in chapters 6 and 7. However, in these experiments cells had to be imaged onto agarose pads for the sake of precise localisation of the internalised molecules; it was therefore not possible to infer with certainty the motor's state, i.e. whether it was functioning and intact or damaged, despite the behaviour shown for CheY reflecting the expected response regulator's one suggested that the cell retained a functioning chemotaxis machinery. In the following, experiments that aim to explicitly show CheY's interaction with FliM in rotating tethered cells are reported.

5.1 Motility and electroporation in *E. coli*

In this section, results of motility experiments carried out on *E. coli* electroporated tethered cells are presented. The disadvantage of the method used in section 4.6 for a first assessment of motility is that the slide quickly dries out, rendering the organisms immotile or however less motile due to lack of oxygen. For this reason, for all the following experiments, cells were imaged in tunnel slides, prepared as illustrated in section 2.6.1.

5.1.1 Shearing or not shearing?

The RP437 strain of *E. coli* bacteria used in all the experiments reported in this chapter has a *fliC(sticky)* mutation (various regions in the *fliC* gene truncated so that hydrophobic regions are exposed), so cells would naturally tether to the glass via their flagella, with further shearing usually not necessary. However, since the percentage of rotating tethered cells obtained above was not very high (i.e. $\sim$11% in SOC), a test was carried out to establish whether shearing cells would increase such number. Cells were passed through a shearing device, usually about 50 times; this was made of a plastic loop about 20 cm long, with an overall inner volume of about 100 μl; at each end of the loop there was a 0.45 mm-diameter needle: due to the turbulent flow which occurs inside this small aperture, cells' filaments break at random points along their length and are shortened from about 10 μm down to $\sim$200-600 nm. This way, the yield of tethered cells should increase, as cells with multiple, long, sticky filaments would stick flatly to the coverslip without possibility of moving, instead. However, no big difference was detected, as about $\sim$8% of the cells were found to be tethered and rotating upon shearing, versus (11$\pm$4)% in the case of not-shearing. Non-sheared sticky filaments were therefore chosen as preferred tethering method for all the experiments in *E. coli* reported in the following.

5.1.2 Motility is independent of loading

The first question that was addressed was whether the uptake of fluorescent molecules upon electroporation would affect cell motility on top of the stress caused by the application of the electric pulse itself. Figure 5.1 shows a tethered electrocompetent *E. coli* cell electroporated with ∼100 times the amount of CheY protein employed for single-molecule tracking experiments in chapter 6, i.e. 1.25 μM or 25 pmoles, (same procedure as described in section 2.3.4, 5 min recovery in SOC at 30°C) imaged in fluorescence in TIRF: this cell is still live and rotating CW at a speed comparable with the average one of wild type cells, i.e. 3-10 Hz, proving that motility recovery upon electroporation is not depending on the number of internalised fluorescent molecules, in the same way as cell viability is independent of cell loading, as shown in section 4.5.

5.1.3 Single-molecule interaction with FliM in motile cells

Once established that uptake of fluorescent molecules was not somehow negatively affecting the electroporated cells more than the application of the electric pulse alone, the interaction of single labelled CheY molecules with FliM (and with other possible loci) in real time in a rotating tethered cell was investigated. Figures 5.2 and 5.3 show two example tethered cells electroporated with Atto647-(Cys)CheY and CheY**(Cys)-Atto647, respectively, imaged both in bright-field (left) and in fluorescence (TIRF, right): the convention is red for internalised proteins and green for FliM-YPet spots. The electroporation procedure was as described in section 2.3.4, 5 min recovery in SOC at 30°C. Throughout the movie from which the frames in Figure 5.2 are extracted, it is possible to clearly see a persistent red spot overlapping with the green one at the centre of rotation, and another, dimmer red spot at one of the cell's poles. In the frames shown in Figure 5.3, it is possible to see colocalisation of green and red spots in the cell, as well, showing the real time in-

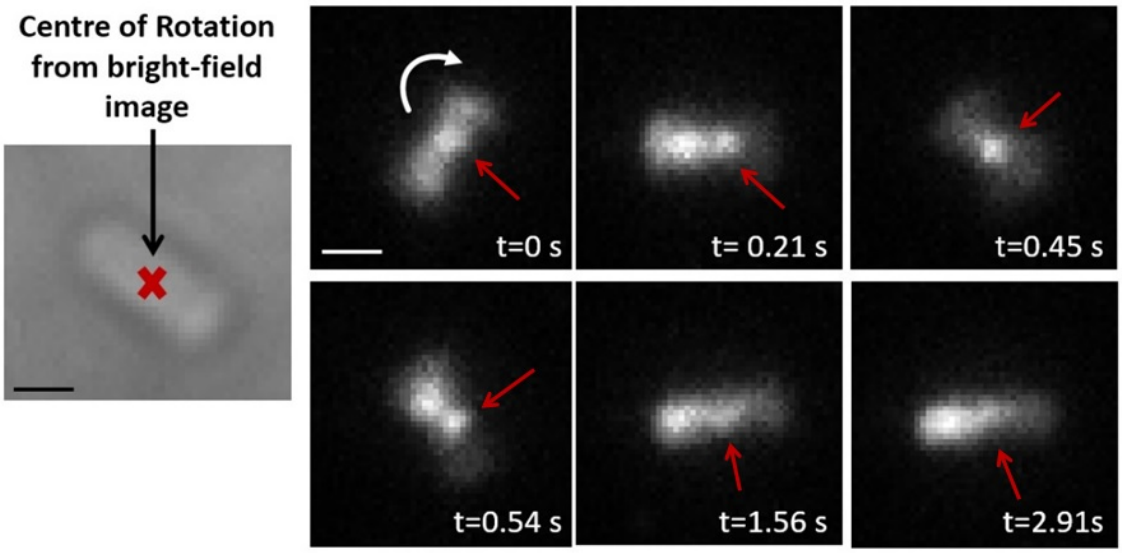

Figure 5.1: Frames from video fluorescence microscopy performed over 3 s showing single molecules diffusing/binding inside a tethered rotating electrocompetent *E. coli* RP437, FliC(sticky) cell electroporated with 1.25 μM , i.e. 25 pmoles, CheY(Cys)-Cy3B. At times during the movie (for example at t = 0 s, t = 0.21 s and t = 0.45 s), it is possible to clearly see a bright spot on top of the center of rotation. These colocalisation events last for much longer than just one frame and therefore suggest a possible interaction of CheY with the motor: it is in fact very unlikely that a free diffusing CheY molecule, moving at about 4 $\mu m^2/s$ in the cytoplasm, would stay fixed in the same location in the cell if it was not interacting with other protein complexes. At other times (for example at t = 1.56 s and t = 2.91 s), the bright spot localises at one pole of the cell; finally, in some frames (for example at t = 0.21 s and t = 0.54 s), it is possible to observe two bright spots in the cell, one of which is always at the centre of rotation and the other seems to be located at - or travelling to - the cell pole. Exposure time 30 ms, settings for Cy3B: 532 nm laser, 2 mW. Scale bar = 1 μm. (Substack of full video found on USB stick, *CheYmot1* movie (20 fps)).

teraction of the labelled CheY** with the motor; moreover, the cell imaged in this movie switched direction of rotation 10 times in 30 s of acquisition, proving that the chemosensory pathway was still indeed correctly functioning despite the harsh electroporation treatment and the presence of "externally re-introduced" chemotaxis proteins in the cytoplasm.

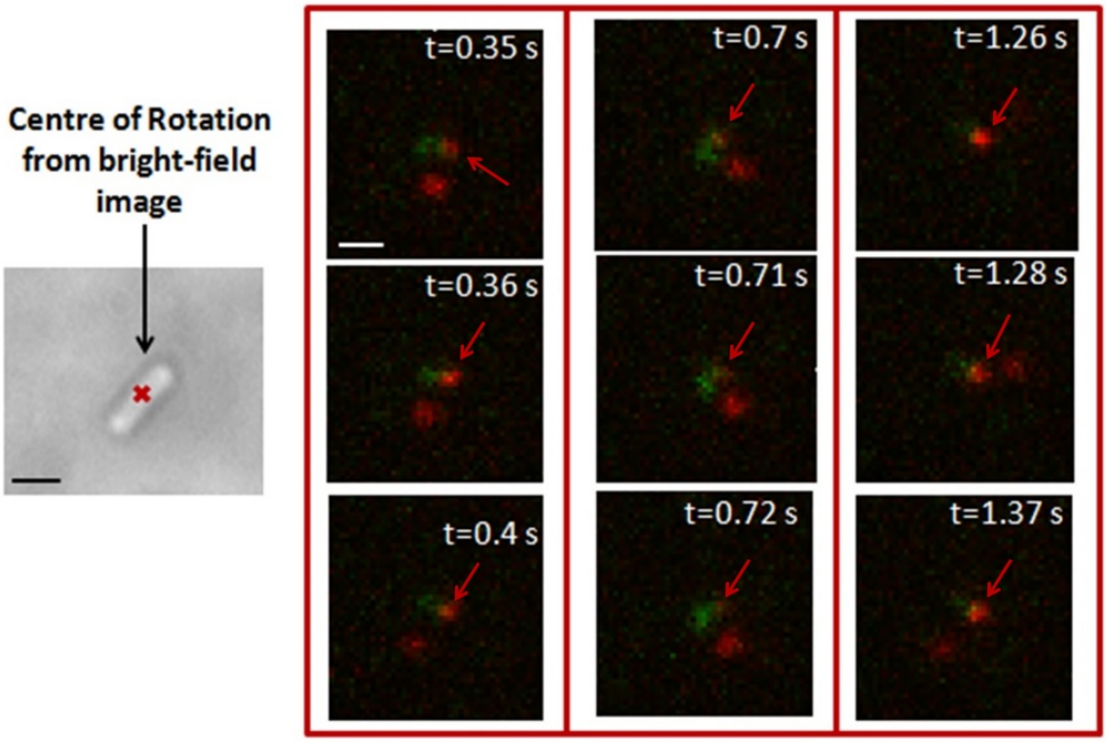

Figure 5.2: Frames from two-colours fluorescence video microscopy performed over 3 s (substack) showing single molecules diffusing/binding inside a tethered rotating *E. coli* RP437 (FliM-YPet, FliC(sticky)) electrocompetent cell electroporated with 20 nM, i.e. 0.4 pmoles, Atto647-(Cys)CheY: for most of the movie, it is possible to see very clearly a bright red spot on top of the center of rotation (green). Such long colocalisation events suggests a possible interaction of CheY with the motor: it is in fact very unlikely that a free diffusing CheY molecule, moving at about 4 $\mu m^2/s$ in the cytoplasm, would stay fixed in the same location in the cell if it was not interacting with other protein complexes. At other times (for example at t = 0.35 s and t = 0.71 s), it is possible to see also a second bright spot which localises at one pole of the cell. Exposure time 10 ms, settings for YPet: 532 nm laser, 1 mW; settings for Atto647: 637 nm laser, 2.5 mW. Scale bar in bright-field image (in black) = 1 μm; scale bar in fluorescence image (in white) = 500 nm. (Substack of full video found on USB stick, *CheYmot2* movie (40 fps)).

5.1.4 Time-lapse measurements

In the examples shown so far, cells were recovered for only 5 minutes after electroporation in order to not lose the internalised fluorescence due to protein degradation or cell division; finding a cell which was both spinning and fluorescent at the same time was therefore an extremely low yield process, with very few, i.e. 4 or 5, ro-

tating tethered cells found in one whole sample. Ideally, cells should be recovered for longer after electroporation in order to be in a healthier state at the time of imaging, this way increasing the probability of observing spinners, as well. For this purpose, a time lapse experiment was carried out in which cells were recovered for several hours after the application of the electric pulse and periodically imaged in bright-field and in fluorescence for a simultaneous evaluation of motility and loading: the aim was to find an optimal time point where cells had recovered enough that the efficiency of the spinners-searching procedure was improved but a sufficient amount of fluorescence from the internalised molecules to perform single-molecule imaging was still retained. In this type of experiment cells were therefore deliberately allowed to grow and divide; in order to have some fluorescence inside daughters as well, cells were initially incubated and electroporated with 3-fold the amount of labelled protein used in single-molecule experiments, namely 50 nM (i.e. 1 pmole) Atto647-(Cys)CheY. Cells were first recovered for 5 minutes in SOC, then diluted 1:10 in TB to a starting volume of 4 ml ($OD_{600nm,\ t=0} = 0.076$) and incubated at 30°C, 225 rpm in a sterile tube. The OD_{600nm} was measured every 30-40 minutes, 200 μl of cells washed and quickly imaged using phase contrast microscopy for a general assessment of motility; cells were then flushed into a tunnel slide, left upside down in a humidity chamber for 10 minutes and washed extensively with MB to remove unstuck cells; the tunnel's edges were sealed with nail polish to prevent evaporation and the sample in this way prepared was imaged in both bright-field and fluorescence. A NEP sample was prepared in the same way. The percentage of spinning cells kept increasing steadily with time up until 2.5 hours of experiment, meaning that, at least up to such time point, de-oxygenation was not a problem. Figure 5.4, a) shows the optical density curves for EP and NEP cells over time: as previously observed, the latter grow faster than the former by about 20%; although shown, data points with OD_{600nm} greater than 1 should not be deemed as fully reliable, as the spectrophotometer is known to lose linearity at high cell densities. In

panel b), a comparison of the number of tethered cells with a spinning phenotype over time in samples EP and NEP is shown: for the reason just stated, only measurements up to OD_{600nm}=1 are included in the graph, and it is possible to see that the two curves are quite in agreement. This indicates that the adopted protocol is a good recovery procedure for electroporated cells, yielding as many motile cells as the non-electroporated sample. Finally, in panel c), the probability curves over time of observing in the EP sample a fluorescent cell (black), a rotating tethered cell (red) and a fluorescent spinning cell (blue) are shown. These values are normalised to the total number of cells imaged (20-80) for each time point. As expected, the probability of observing a fluorescent cell decreases exponentially with time, whereas the probability of observing a spinning cell increases, at least until about 3 hours from start of recovery, where it starts to decrease in correspondence to OD_{600nm} reaching values above 1 and cells entering stationary phase. The curve given by the product of the first 2 probabilities is also shown (green): in fact, if the probabilities of a cell being motile and of being fluorescent are independent, then the probability of them both occurring is the product of the probabilities of each occurring. In this case, the blue experimental curve and the green one, obtained multiplying the black and red curves, are in good agreement, supporting once again the hypothesis that motility and fluorescence are indeed independent. From the blue curve shown in Figure 5.4, b) it is possible to infer that the optimal trade-off between observing a spinning cell and the probability of observing a fluorescent one is reached after a recovery time of about 2.5 hours. Moreover, it was possible to observe some cells containing internalised fluorescence still up to about 4 hours from electroporation, data consistent with the finding reported in section 4.4 that signal from internalised molecules was still visible in growing or growing and dividing cells up for more than 3.5 hours after electroporation (see *CheYTimeLapseBrightField* and *CheYTimeLapse* movies on USB stick, recorded after 3.5 hours from electroporation (60 fps)).

5.2 Electroporated CheY localises at the cell pole

The question as to whether the re-introduced labelled chemotaxis proteins were functional in general, without particular regard to the motor, was then posed: in figure 5.5, the three panels in a) show, respectively, a sparse field of view of *E. coli* cells electroporated according to the protocol described in section 2.3.4 with 1.5 μM (30 pmoles) CheY(Cys)-Cy3B imaged in fluorescence with the internalised molecules in false colours, and an overlap with the same field of view illuminated by white-light in DIC. No fluorescence was observed in the negative controls with cells incubated with the same molecules but not electroporated (b). In $\sim$80% of the cells that had internalised some fluorescence (20 out of 26 fluorescent cells over 60 imaged cells), an interesting trend arose of the internalised proteins to localise at the poles where the chemoreceptors are known to cluster Figure 5.5, (c). This result, widely reported for wild type CheY in the literature in colocalisation experiments carried out using genetically fused fluorescent tags[90,261], seemed to indicate that the proteins internalised by electroporation were still intact and retained their function inside the cells. As a further control, cells electroporated with free dye did not show any sign of localisation in particular regions of the cells (d).

5.3 CheY-CheZ colocalisation

As a further check that the fluorescence at the poles was actually the protein performing its function, i.e. binding to the chemoreceptors' cluster as previously described, and not an artifact due, for instance, to the introduced proteins aggregating at the cell poles, colocalisation of the electroporated CheY molecules with the phosphatase CheZ, which has been shown to mostly localise at the chemoreceptor cluster at the cell pole[90,262], was investigated. Using a strain featuring a Cyan Fluorescent Protein (CFP) genetically fused to CheZ (UU2689, see Table 2.1) and

two-colour imaging, unambiguous identification of the chemoreceptor cluster was possible. Colocalisation of CheY(Cys)-Cy3B and CheZ-CFP in electroporated *E. coli* cells was confirmed in 22 out of the 53 cells showing some degree of fluorescence internalisation (42%), as an example field of view in Figure 5.6 shows. It should be mentioned that in the remaining 58% of the cases, the fluorescence in the imaged cells was very diffuse, and no other locus different from the pole where electroporated proteins tended to localise could be individuated. This was a good indication that the re-introduced fluorescently labelled CheY was still intact and functioning *in vivo* upon electroporation and that the trend observed in section 5.2 could be real and not due to artifacts.

5.4 Summary

In this chapter, results from joint motility and fluorescence microscopy experiments in *E. coli* were reported, as well as a functionality assay of the externally re-introduced CheY proteins. Firstly, as a complementary check to what shown in chapter 4.3 about cell viability, the possibility for the cells to recover a motile phenotype upon electroporation was assessed and confirmed. Secondly, cell motility was shown to be independent of loading, as growth/division were demonstrated to be in chapter 4.3. The interaction of single labelled CheY molecules with FliM (and with other possible loci) in real time was therefore investigated and observed in rotating tethered bacteria recovered for a short amount of time (few minutes) as well as for hours (in a time-lapse experiment) in rich medium. Finally, good indication of general functionality of the electroporated CheY labelled proteins apart from interaction with the motor was shown by means of two-fluorescence colocalisation studies with CheZ-CFP at the cell poles.

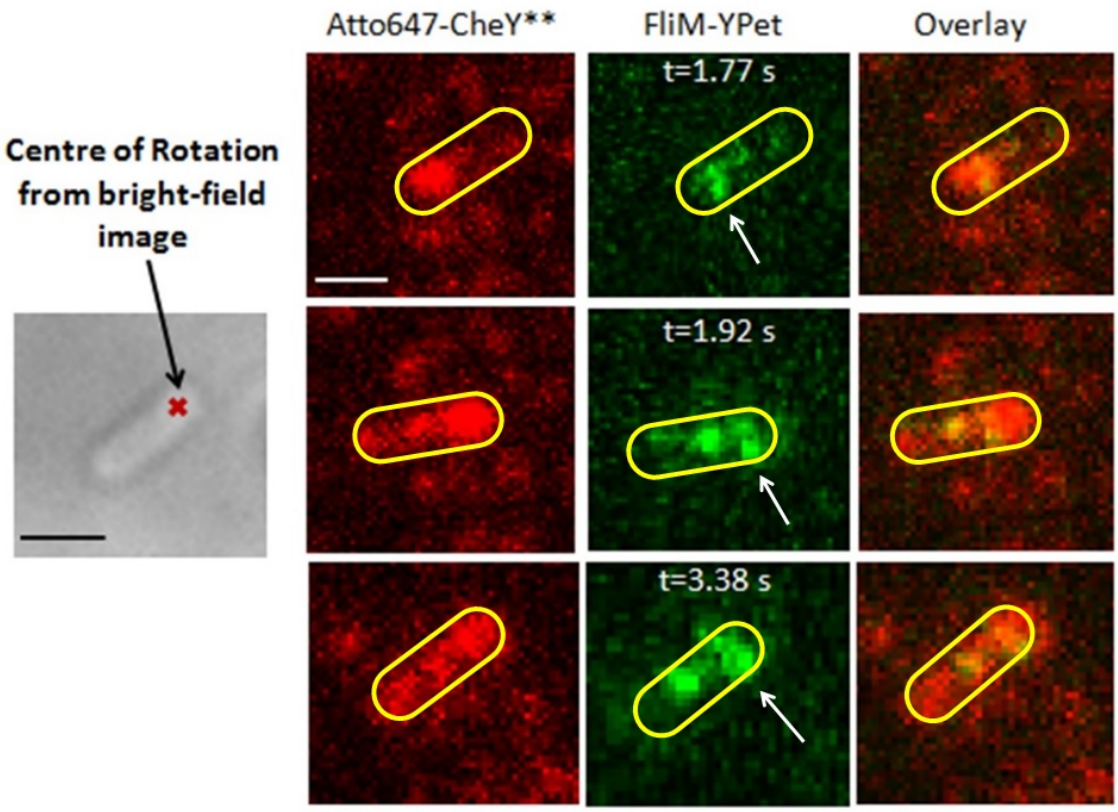

Figure 5.3: Frames from fluorescence video microscopy performed over 30 s showing single molecules diffusing/binding inside a tethered rotating *E. coli* RP437 (FliM-YPet, FliC(sticky)) electrocompetent cell (yellow outline) electroporated with 30 nM, i.e. 0.6 pmoles, CheY**(Cys)-Atto647. For each of the 3 chosen frames (rows), images acquired in separate channels for CheY**(Cys)-Atto647 and FliM-YPet (in red and green false colours, respectively) and an overlay of the two are shown. Throughout the whole movie, it is possible to see very clearly a bright red spot on top of the center of rotation (gree, white arrows). Such a long colocalisation event suggests a possible interaction of CheY with the motor: it is in fact very unlikely that a free diffusing CheY molecule, moving at about 4 $\mu m^2/s$ in the cytoplasm, would stay fixed in the same location in the cell if it was not interacting with other protein complexes. At other times (as shown for example in frames at t = 1.92 s and t = 3.38 s), it is possible to see two red spots localising with two green ones: the second green spot, not corresponding to the tethered motor, could either represent another motor (complete or partially formed) which has come into the TIRF zone from somewhere in the membrane which was not illuminated as a consequence of cell movement or some FliM-YPet aggregates; finally, a bright spot at the cell pole opposite to the motor's location is also sometimes visible, not corresponding to any green spot, and likely due to transient interaction of CheY** with the chemoreceptors through CheA. Note: the red fluorescence background in this experiment is slightly higher than in Figures 5.1 and 5.2 because of the ∼1/3 greater initial concentration that the cells were electroporated with. Extra fluorescence background in the green channel could be due to cell lysis, instead. Exposure time 10 ms, settings for YPet: 532 nm laser, 1 mW; settings for Atto647: 637 nm laser, 2.5 mW. Scale bars in bright-field image (in black) and in fluorescence image (in white) = 1 μm. (Substack of full video found on USB stick, *CheYStarStarmot1* movie (60 fps)).

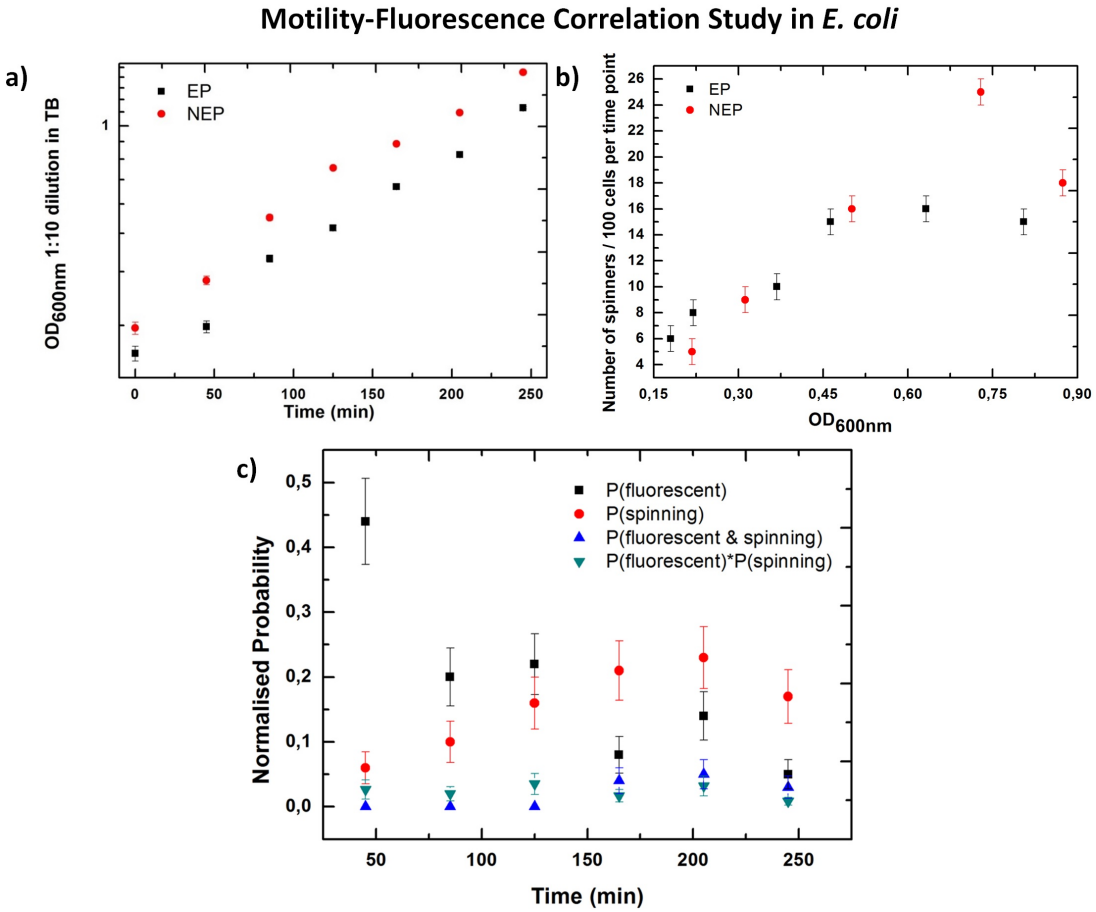

Figure 5.4: Correlation study of motility and fluorescence in *E. coli* cells electroporated with 50 nM (1 pmole) CheY-Atto647: **a)** Semi-log plot of optical density curves for EP and NEP cells over time; **b)** number of spinners versus time in EP and NEP samples; **c)** Probabilities normalised to the total number of cells imaged (20-80) for each time point of observing in the sample a fluorescent cell (black), a rotating tethered cell (red) and a fluorescent spinning cell (blue). The curve given by the product of the first 2 probabilities is also shown (green). Error bars on each data point are given by the normalised percentage error assuming 1 cell miscounting.

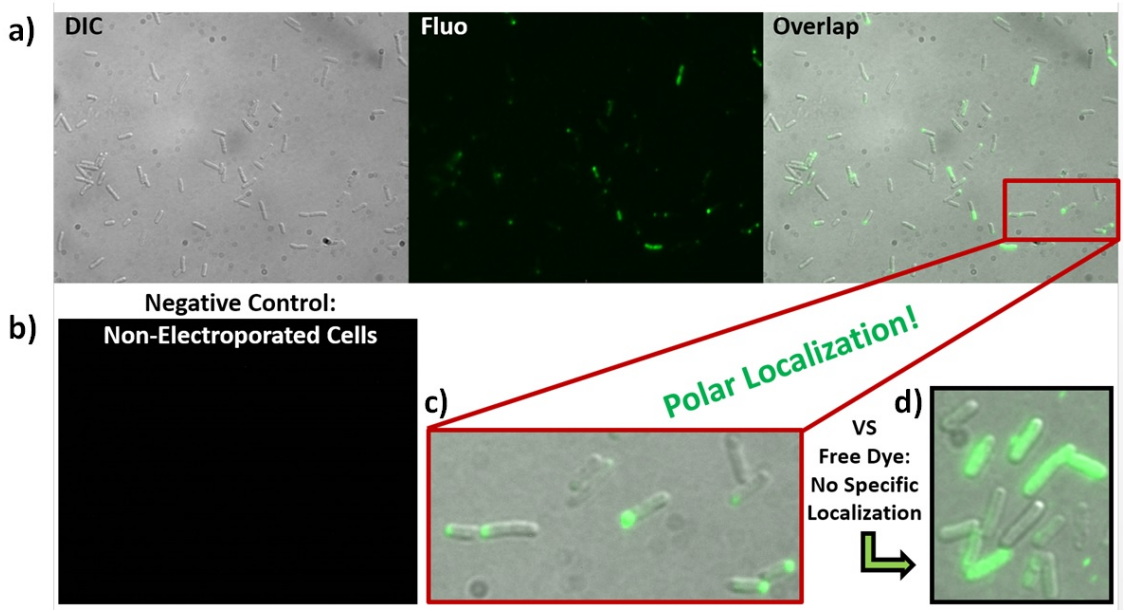

Figure 5.5: **a)** Fluorescence images in false colours of electrocompetent *E. coli* cells electroporated with 1.5 μM (30 pmoles) CheY(Cys)-Cy3B imaged in DIC, fluorescence and an overlap of the two; **b)** Electrocompetent cells incubated with the same amount of protein but not electroporated showed little or no fluorescence internalisation. **c)** Detail showing polar localisation of electroporated CheY-Cy3B proteins inside the cells; **d)** Further control: electroporated free Cy3B-maleimide dye shows no specific localisation. Epi-fluorescence, 150 ms exposure time. Electroporation parameters and procedure as described in section 2.3.4.

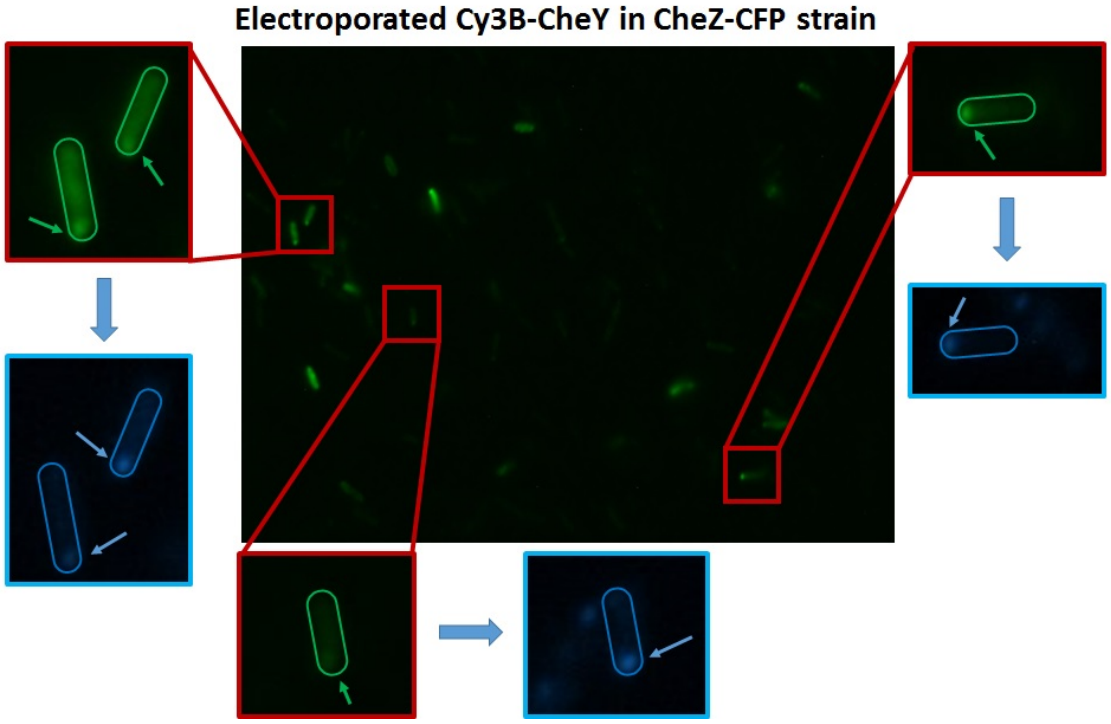

Figure 5.6: Colocalisation of electroporated CheY-Cy3B (green) and CheZ-CFP (blue) in false colours in *E. coli*. Two-colour imaging revealed that Cy3B labelled CheY molecules localise at the same cell pole as the phosphatase CheZ in electroporated cells showing polar fluorescence. Epi-fluorescence, 150 ms exposure time, electroporation parameters and protein used for electroporation were the same as in the experiment described in section 5.2.

Chapter 6

Fluorescence Microscopy in *E. coli*

6.1 Single-molecule experiments

The goal of this type of experiments was to observe and quantify the working cycle of various CheY mutants in different genetic backgrounds. Single molecules were detected and tracked in their journey between the receptor clusters and the motors, via diffusion through the cytoplasm, in live cells. Binding kinetics to both motor and MCP array, as well as diffusion between them, in different background strains and in the presence and absence of chemotactic stimuli were quantified. Tracking of individual CheY molecules had never before been attempted. The outcome of the investigations reported herein will guide further studies, either into the detailed effects of chemical stimuli on the dynamics of CheY, or the behavior of other chemotaxis proteins at the single molecule level.

6.2 CheY-FliM interaction: a brief summary

A short summary of section 1.3.3 about the state-of-the-art knowledge of the interaction between CheY and FliM is reported here for the reader's convenience.

One of the most notable properties of the *E. coli* flagellar motor is that it can switch direction in response to very small changes in the concentration of the signaling protein CheY-P, showing thereby a high degree of cooperativity[135]. The Hill coefficient for the sigmoidal curve that relates CheY-P concentration to motor rotational bias has been measured to be in fact ∼10 (reference 136). Despite in the last few decades a series of models have been proposed, the mechanism through which switching is achieved is not yet fully understood. A recently proposed allosteric model based on cooperative conformational spread in a ring of identical protomers, like FliM subunits, is able to qualitatively reproduce switching and Hill coefficient value measured for the rotary motor[133]. The interaction between CheY-P molecules and FliM subunits in the C-ring is believed to be responsible for determining the direction of rotation[1,74] and the possibility of cooperative binding between the two has been suggested to explain the motor's ultrasensitivity[90]. However, studies focused on this binding step have determined a Hill coefficient <1 for it, which eliminates the possibility that the amplification is driven by cooperative CheY-P binding to the motor and suggests that a separate, post-binding step within the switch complex is responsible[137,263]. Further evidence in support of the conformational spread model is the observation that flagellar motors can switch at low temperatures in the absence of CheY[264]. The authors of 141 suggest an alternative model: two FliM populations are envisioned to be present at the motor, one exchanging and one non exchanging, with the latter stabilising the C-ring; CheY-P molecules could bind the peripheral array of FliM subunits, which are in 1:1 stoichiometry with FliG, destabilising them and causing FliG to assume the conformation needed to generate CW rotation.

In *Afanzar, Di Paolo et al.* (in submission), the N-terminus of the switch protein FliM ($FliM_N$), which is known to be the high-affinity interaction site for CheY-P[123,263,265], is shown to be not essential for phosphorylation- and acetylation-mediated clockwise generation, chemotactic response, and switch modulation in $FliM_{\Delta N}$ background. Furthermore, evidence is provided that clockwise rotation is generated by

the cooperative binding of CheY to secondary low-affinity sites in the switch. The proposed function of $FliM_N$ is to recruit a high enough amount of CheY molecules to such sites, thereby compensating for their low affinity. A further suggestion made in the paper is that acetylation indirectly affects chemotaxis by modifying the threshold for phosphorylation-dependent switching. Experimental evidence supporting the existence of a secondary low-affinity binding site at the switch and of an acetate-induced effect on CheY-FliM interaction will be presented in section 6.5.

6.3 Tuning conditions

Those who choose electroporation as transformation method for their bacteria face several challenges, such as finding an opportune voltage to trade off between cell survival and internalisation efficiency, recovering electroporated cells to a healthy - ideally motile for this work's purposes - state as quickly as possible, imaging fluorescence from internalised molecules before it is reduced by cell division or intracellular degradation. Reasons why a 1.2 kV voltage was adopted for all the experiments described in this thesis are reported in section 3.4. Treatments to recover cell motility upon application of the electric pulse will be illustrated in chapter 7. In order to carry out single-molecule experiments, an additional challenge was to characterise the cellular uptake of labelled proteins upon electroporation and tune it to yield internalisation of very few molecules per cell (ideally less than 5 in average) to rule out artifacts caused by overlapping spots as much as possible. Based on the results obtained in section 4.2, a final labelled protein concentration of 15-30 nM in the electroporation cuvette was chosen.

6.4 Analysis tools

Channel mapping and cell segmentation

Fluorescence was recorded in two channels (green for FliM-YPet at the motors and red for Atto647 labelled chemotaxis proteins), each onto half of the camera chip; a bright-field image of each field of view in both channels was every time recorded, as well. To take into account possible distortions and tilts due to the optics, before performing any further analysis on the recorded movies, the green fluorescent channel was matched to the red one by means of a spatial transformation matrix obtained recording calibration images of fluorescent beads on the same day of the experiment. Fluorescence overlay images shown in the following were obtained by overlaying the averaged first 500 frames of corrected green channel and the red fluorescence channel (false colours).
Cells presenting a signal in both the green and the red channel in an overlay image were manually selected for further analysis.

6.4.1 Particle localisation

For each movie, spots corresponding to internalised labelled proteins were detected using automatically calculated high-pass filter. In general, the method of calculation was based on sorting all of the pixels in a given frame according to their intensity, with the intensity value that is farthest away from the line that connects the minimum and the maximum of the sorted pixels used for high-pass filtering, as shown in Figure 6.1. After applying the filter, a spot was defined as an area of at least 9 connected pixels. To account for cases in which several fluorophores shared the same spot area, a peak finding algorithm was applied to the area of the spot. If more than one local maximum was found, each peak was transformed into a spot the size of 5x5 pixels. Since detection was mostly based on pixel connectivity, a spot

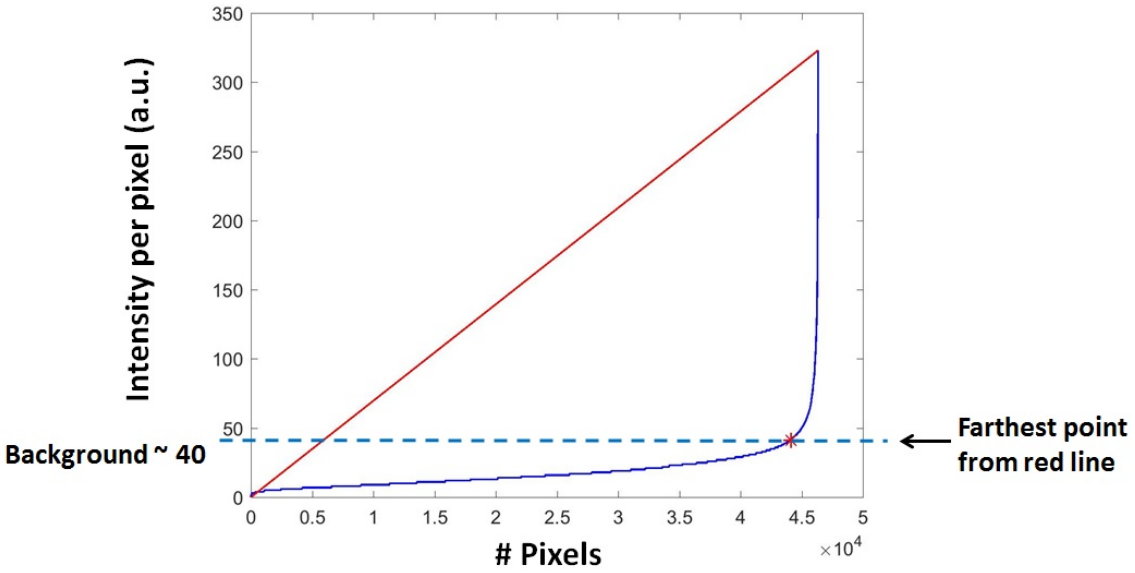

Figure 6.1: Fluorescence baseline subtraction in single-molecule experiments: for each frame, all pixels were sorted according to their intensities (blue curve) and the intensity value (red star) farthest away from the line (red straight line) that connects the minimum and the maximum of the sorted pixels was used for background thresholding (cyan, dashed line).

was identified as such even when its intensity was at the edge of the background level (i.e., a continuous region of pixels with low intensity values was considered as a spot whereas a region featuring a "salt and pepper" pattern was not). The area of each identified spot was fitted with a 2D Gaussian, and the estimated parameters were used for sub-pixel localisation.

An estimate of the Z position would be possible using the ratio of maximum $I(0)$ and measured $I(z)$ fluorescence intensities and theoretical TIRF penetration depth d according to the formula $z = d\ ln\frac{I(0)}{I(z)}$. Another possibility is to assess the Z position from the integral of the intensity from all the spots, considering that the most intense spots within the cell should be those at Z = 100 nm (the distance between the coverslip and the rotor). However, in the case of smeared spots, the intensity does not reflect the Z position of the particle but rather its velocity (i.e., highest intensity is where the particle spent most of its time in the frame) and therefore Z-estimation was for now neglected.

FliM spots were calculated from a series of 500 frames, in which the maximal intensity per pixel was recorded over time. The output image of this process was segmented using automatically calculated high-pass filter, and segmented regions were probed with peak finding algorithm to pixel resolution.

6.4.2 Localisation Uncertainty Estimation

The localisation uncertainty was previously experimentally measured by the author to be ∼30 nm for a static labelled CheY attached to the coverslip (Half Width Half Maximum (HWHM) of the fitted Gaussian); such value, considering the experimental setup and parameters used, is then the minimum expected for a labelled CheY in a cell. The localisation uncertainty was also estimated by the number of collected photons emitted according to the following formula, taken from 266:

$$\left\langle (\Delta x)^2 \right\rangle = \frac{s^2}{N} \left(\frac{16}{9} + \frac{8\pi s^2 b^2}{N a^2} \right) \tag{6.1}$$

where $s^2 = \sigma^2 + a^2/12$, with σ standard deviation of the point spread function and a pixel size (in nm), N number of collected photons and b standard deviation of the background fluorescence. The photon count was defined as the number of photons under the Gaussian subtracted by the equivalent background area according to the solution of the bidimensional Gaussian integral $N = 2\pi\, A\, S_x\, S_y$ with S_x and S_y Gaussian spreads in the two directions (in nm) and A Gaussian amplitude (photon count at peak).

As already mentioned above, due to the frame rate being for certain molecules slower than their velocity between two consecutive frames, some CheY spots look smeared in the movies. In cases in which the intensity values were too low and the predicted error was above 1 pixel, the error was arbitrarily assigned as 1 pixel and colocalisation determined with one pixel resolution at the coordinates of the pixel with the highest intensity.

6.4.3 Single-molecule tracking

Single-molecule tracking was performed by MATLAB implementation of a published algorithm[267]. Localised PSFs were linked to a track if they appeared in consecutive frames within a maximum distance corresponding to the length of the major axis of each analysed cell, to avoid false positives from molecules floating in the external surrounding medium. It is worth mentioning that spots outside the region of cell segmentation were not considered for tracking. The spots were tracked with a 1-frame memory parameter, e.g. the trajectory of a fluorophore that was lost for up to 10 ms due to blinking or to having left the TIRF field was recovered. The dye used for single-molecule tracking was however one of the most photostable on the market and the chance of it blinking could be therefore reasonably considered close to zero.

6.4.4 Criteria for colocalisation with FliM

Considering the center of the motor as the pixel with maximal fluorescence intensity, the expected distance between CheY and FliM in a binding event is given by the sum of the radius of the motor and the length of the N' terminus of FliM that acts as disordered polypeptide chain. The radius is ∼20-30 nm and the length of the chain is ∼20 nm, summing up to ∼40-50 nm in total. However, since FliM localisation was calculated with pixel resolution, the interaction distance was taken to be overall ∼1 pixel, as the maximal emission of a FliM spot could in some cases have been unequally split between two adjacent pixels. This means that, if CheY's XY coordinates are ∼1 pixel away from the motor's, an interaction between the two might occur. To be more restrictive, another criterion for binding events was also set, i.e. the distance travelled by CheY between two consecutive frames should be less than 200 nm, so that CheY molecules rapidly diffusing and passing nearby the motor without binding it would not be counted.

The CheY spots satisfying the listed criteria were tracked with a 1-frame memory parameter, e.g. a fluorophore that was lost for up to 10 ms due to blinking was recovered and considered the same one.

6.4.5 Dwell times

The Kaplan-Meier Survival Probability estimator is a non-parametric[1] statistic used to estimate the survival function from lifetime data[268]. In medical research, it is often used to measure the fraction of subjects living for a certain amount of time after treatment. The following example from 269 explains the need for such estimator very clearly: suppose that 100 subjects of a certain type were tracked over a period of time to determine how many survived for one year, two years, three years, and so forth. If all the subjects remained accessible throughout the entire length of the study, the estimation of year-by-year survival probabilities for subjects of this type in general would be an easy calculation. The survival of 87 subjects at the end of the first year would give a one-year survival probability estimate of $87/100 = 0.87$; the survival of 76 subjects at the end of the second year would yield a two-year estimate of $76/100 = 0.76$; and so forth. However, in real-life it rarely works out this neatly, as typically there are subjects lost along the way for reasons unrelated to the focus of the study. To illustrate the complication in this sort of situation, consider the following hypothetical scenario. Of the 100 subjects who are "at risk" at the beginning of the study, 3 become unavailable during the first year and 5 are known to have died by the end of the first year. Another 3 become unavailable during the second year and another 10 are known to have died by the end of the second year. And so on for the other years shown. The question in a situation of this sort is: what should be made of the subjects who become unavailable in a given

[1]Non-parametric statistics make no assumptions about the probability distributions of the variables being assessed. The difference between parametric models and non-parametric models is that the former have a fixed number of parameters, while the latter grow the number of parameters with the amount of training data[24].

time period? (Within the context of the Kaplan-Meier procedure, the subjects who become unavailable are spoken of as *censored*). It is not known, in fact, whether these subjects survived or died. Yet, if they were simply omitted from the study, valuable information would be lost: namely, that the 3 subjects who became unavailable during Year 2 survived at least through Year 1; that the 3 who became unavailable during Year 3 survived at least through Year 2; and so on. Kaplan and Meier, in the attempt to save this information, proposed that subjects who become unavailable during a given time period should be counted among those who survive through the end of that period, but then deleted from the number who are at risk for the next time period.

It should be now clear how such type of analysis suits the problem of describing the probability distribution of fluorescently labelled single CheY molecules dwelling for a certain amount of time at the motor spot and then disappearing due to either dissociation or bleaching. A plot of the Kaplan-Meier estimator is a series of declining horizontal steps which, with a large enough sample size, approaches the true survival function for that population. For each time interval, the estimated survival probability is calculated as the product-limit:

$$S(t_i) = \prod_{t_i \leq t} \left(1 - \frac{d_i}{n_i}\right) \tag{6.2}$$

where t_i is duration of study at point i, d_i is the number of deaths (i.e. molecules not dwelling at the motor anymore) up to point i and n_i is the number of individuals at risk (i.e. still dwelling at the motor) just prior to t_i. Thus, the probability of surviving (i.e. still dwelling) at any time point (frame) is the cumulative probability of surviving each of the preceding time intervals (calculated as the product of preceding probabilities). Although the probability calculated at any given interval might not be very accurate because of the small number of events, the overall probability of surviving to each point is more accurate. It is incorrect to join the calculated

points by sloping lines. The probability-dwell time plots shown in section 6.5 are of this type. The dwell time of CheY molecules with FliM spots was calculated as the number of consecutive frames in which CheY was localised <100 nm away from FliM, where each dwell time-point was documented in separate (e.g., for a total of 50 ms dwell time, dwell times of 10, 20 , 30 , 40 and 50 ms were recorded). After collecting the interaction data from all acquisitions, the survival probability of CheY dissociating from FliM was calculated as above described.

6.5 Results

In this section, results of single-molecule experiments with a series of electroporated labelled CheY mutants in different background strains of *E. coli* are reported. The intracellular diffusive behaviour of such molecules was investigated; furthermore, to verify that, indeed, the interaction of CheY with the motor involves a binding site other than $FliM_N$, as suggested in *Afanzar, Di Paolo et al.* (in submission), section 6.2), the dwell times near FliM switch complexes in single cells was measured. The results illustrated in this section will be part of a dedicated paper (*Single-molecule imaging of electroporated chemotaxis proteins in live bacteria*, *Di Paolo et al.*, submitted).

6.5.1 CheY dynamics

One of the aims of this work, listed in section 1.5, was to measure the diffusion coefficient of dye-labelled CheY molecules *in vivo*, without FP tags that might affect the mobility properties of the proteins: in the literature, a diffusion coefficient of 10 $\mu m^2/s$ *in vitro* was reported for CheY[89,270]. Two main techniques have been used to try and measure CheY's diffusion coefficient *in vivo*: Fluorescence Correlation Spectroscopy (FCS) and Fluorescence Recovery After Photobleaching (FRAP). The

former, in 136, yielded an average diffusion constant of the cytoplasmic CheY-GFP fusion of (4.6±0.8) $\mu m^2/s$; the latter, in 271, revealed that CheY had a very fast recovery after photobleaching, on the time scale of several seconds, which could not be clearly resolved from the recovery of the cytoplasmic fraction; the half-time for diffusional recovery ($t_{1/2}$) was therefore estimated and used to calculate its effective diffusion coefficient, using the relation $D = 0.07\ L^2/t_{1/2}$, where L is the cell length. Values found for CheY were $t_{1/2}$ = (0.61±0.12) s and hence D = (1.26±0.22) $\mu m^2/s$ for L = 3.3 μm (i.e. the length of an *E. coli* cell). which is several times higher than our estimate. The discrepancy between these two values can be attributed to the difference in the measurement techniques, with FRAP analysis underestimating the rapidly diffusing fraction of proteins due to the limited time resolution (0.33 s), and with FCS missing a slowly diffusing fraction. Electroporated dye-labelled CheY is expected to have a free diffusion coefficient higher than or comparable to the latter values (being the dye much smaller than GFP) but still not as high as 10 $\mu m^2/s$, which is the limit *in vitro*. The Mean Square Displacement (MSD) values were estimated from the MSDs of all individual trajectories and the diffusion coefficient D calculated according to the 2D formula MSD = 4Dt. Figure 6.2, a) shows a distribution of 50 equally dispersed bins for D values from all recognised trajectories. Two populations of slow and fast molecules were identified and fitted using a Gaussian mixture distribution model with two components (in-built MATLAB function *fitgmdist*, red solid lines). For clarity, also the sum of the two latter curves (red dashed line) and a single Gaussian fit to the data (blue solid line) are shown. A complete solution for a stochastic process is its *propagator*, i.e. the probability density for the final state at some time t_f given an initial condition at time t_i. For normal Brownian motion the propagator is a Gaussian distribution[272], hence the decision to use this fitting function. The R^2 value of the single Gaussian fit was found to be 0.88, versus a value of 0.91 for the two components fit, hence the choice to rely on the latter. A D = (2.3±2.4) $\mu m^2/s$ was found for the free diffusing mo-

lecules, and a D = (0.4±0.6) $\mu m^2/s$ for the slow diffusing ones, most of which are probably binding either the motor or the chemoreceptor cluster. The former value is in agreement with the one mentioned above measured in 136 for CheY-GFP, and is likely to be the lower limit for Atto647-(Cys)CheY diffusion. It is in fact possible that, due to the relatively slow acquisition rate (100 frames per second), molecules diffusing faster than this were discarded by the software in detection phase due to their low signal to noise ratio.

To study the interaction with the motor and the chemoreceptors, the low limit of CheY diffusion was considered (i.e. slow population in Figure 6.2). In wild type cells, it is known that response times for changes in FliM occupancy by CheY are determined by several sets of rates: (i) rates of receptor-linked CheA autophosphorylation, CheY phosphorylation by CheA-P, and CheY-P dephosphorylation by CheZ; (ii) on and off-rates of CheY-P binding to FliM; and (iii) CheY-P diffusion from receptor-kinase clusters on the cell pole across the cytoplasm to the flagellar motors or to cytoplasmic FliM. In 263, CheY-P decay rate constants were estimated as k = (2.2±0.1) s^{-1} and (0.085±0.001) s^{-1}, corresponding to decay half times of $t_{1/2} = 0.32$ s and 8 s, respectively. Assuming that the off rate of CheY-P from the FliM complex is fast relative to rate of dephosphorylation, these would be the half times for CheZ-catalyzed and spontaneous dephosphorylation, respectively. Moreover, based on an estimated CheA intracellular concentration of 5 μM, a dissociation constant for CheY-P from CheA of (3.7±0.4) μM was found. In the same paper, Fluorescence Resonance Energy Transfer (FRET) measurements between CheY-YFP and FliM-CFP in a Δ(*cheY, fliM, cheB, cheR, cheZ*) background estimated that CheY-P binds to FliM *in vivo* with a dissociation constant of about 3.7 μM. Assuming a diffusion-limited on-rate constant of (4 x 10^6) $M^{-1}s^{-1}$ and the just mentioned K_D, an off-rate of ∼15 s^{-1} (∼66 ms) was determined. More recently, an off-rate of 20 s^{-1} (dwell time of 50 ms) was measured for CheY and FliM in an *in vitro* population[137]. These values have been used since in various modelling studies and are consistent

with data-fitting work in the conformational spread model (Dr. Richard Branch, personal communication). However, in 211 a $K_{D,\ FliM_N}$ of 26 μM for CheY-P was measured *in vitro*: in this thesis, the apparent discrepancy between dissociation constant for CheY-P *in vitro* (26 μM)[211] and *in vivo* (3.7 μM)[263] is explained by means of the existence of secondary binding sites for CheY on $FliM_M$ or FliN.
In fact, the value for $K_{D,\ FliM_N}$(CheY)=30 μM (calculated assuming a diffusion-limited $k_{on} = (4 \times 10^6)\ M^{-1}s^{-1}$ [263]) and relative dwell time found for fast-dissociating molecules in the single-molecule experiments carried out in this work, as shown by the fitted probability distribution of CheY interaction with $FliM_N$ (green straight line) in Figure 6.2, b), are in good agreement with the value reported in 211. However, as it is also possible to notice in Figure 6.3 and in Figure 6.12, b) (magenta dots), longer dwell times were observed for electroporated Atto647-(Cys)CheY in FliM-YPet strain, as well, up to almost 400 ms. As mentioned in section 6.2, switching of the motor was described as a highly cooperative process (with a Hill coefficient of $\sim$10)[136], whereas CheY binding to full-length FliM was shown to be non-cooperative[137,263]: such long dwell times could therefore reflect binding of CheY to low-affinity sites, responsible for post-binding cooperativity, on either $FliM_M$ or FliN, which wold usually be masked in ensemble measurements by the binding of CheY to $FliM_N$. This is also the reason why a bi-linear fit was chosen for the semi-log plots, i.e. a bi-exponential behaviour is expected for two different types of binding site with different rate constants.

6.5.2 CheY** dynamics

Interaction with the motor was also investigated for the hyperactive mutant of CheY, CheY(D13K/Y106W), already presented in section 3.3.1 and also known as CheY**[173]. Being constitutively active, this mutant does not need to be phosphorylated to interact with the motor, and is also for this reason likely to interact

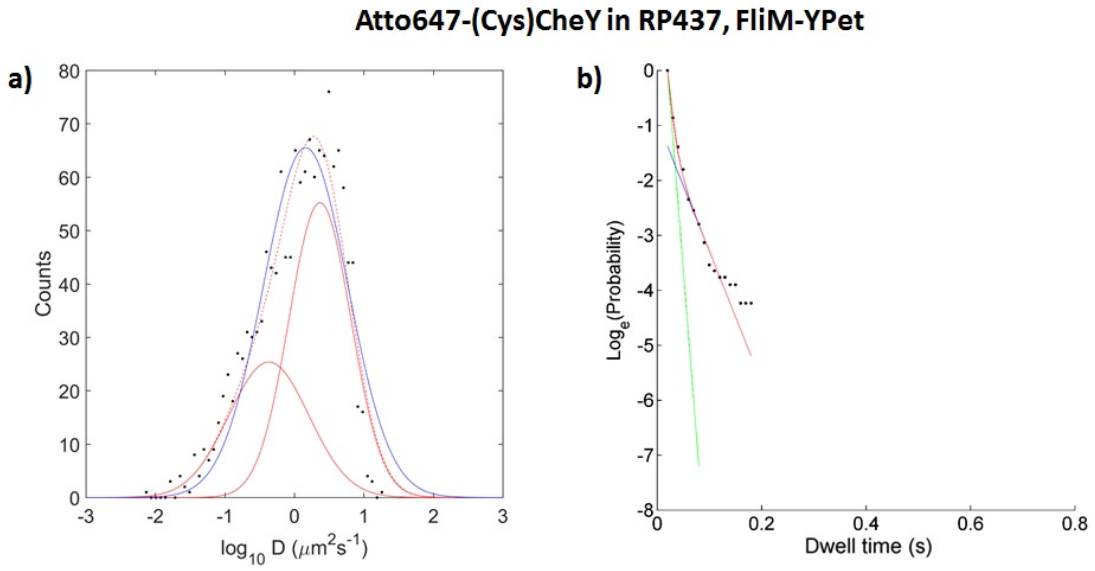

Figure 6.2: **a)** Diffusion coefficients' distribution for electroporated Atto647-(Cys)CheY in RP437, FliM-YPet *E. coli* cells. Histogram of 50 equally dispersed bins for D values from all recognised trajectories based on a data set consisting of 837 molecules in different acquisition dates. The two components Gaussian fit (red solid lines), the sum of the latter (red dashed line) and the single Gaussian fit (blue solid line) are shown. **b)** Distribution of dwell times at the motor for electroporated Atto647-(Cys)CheY in RP437, FliM-YPet *E. coli* cells. Bins with less than 5 counts were discarded (i.e. each data point is at least 5 events). The plot shows the experimental survival log-probability of switch-bound CheY to dissociate from it as a function of time. The red curve is a bi-exponential combined fit, whereas the green curve is the linear fit for CheY binding to $FliM_N$ and the blue curve is the linear fit for binding to the secondary sites (see Table 6.1 for the fitted values of $K_{D,\ FliM_N}$ and $k_{off,\ ss}$). Histogram based on a data set consisting of 48 cells in different acquisition dates. For both **a)** and **b)**: exposure time 10 ms, settings for YPet: 532 nm laser, 1 mW; settings for Atto647: 637 nm laser, 2.5 mW.

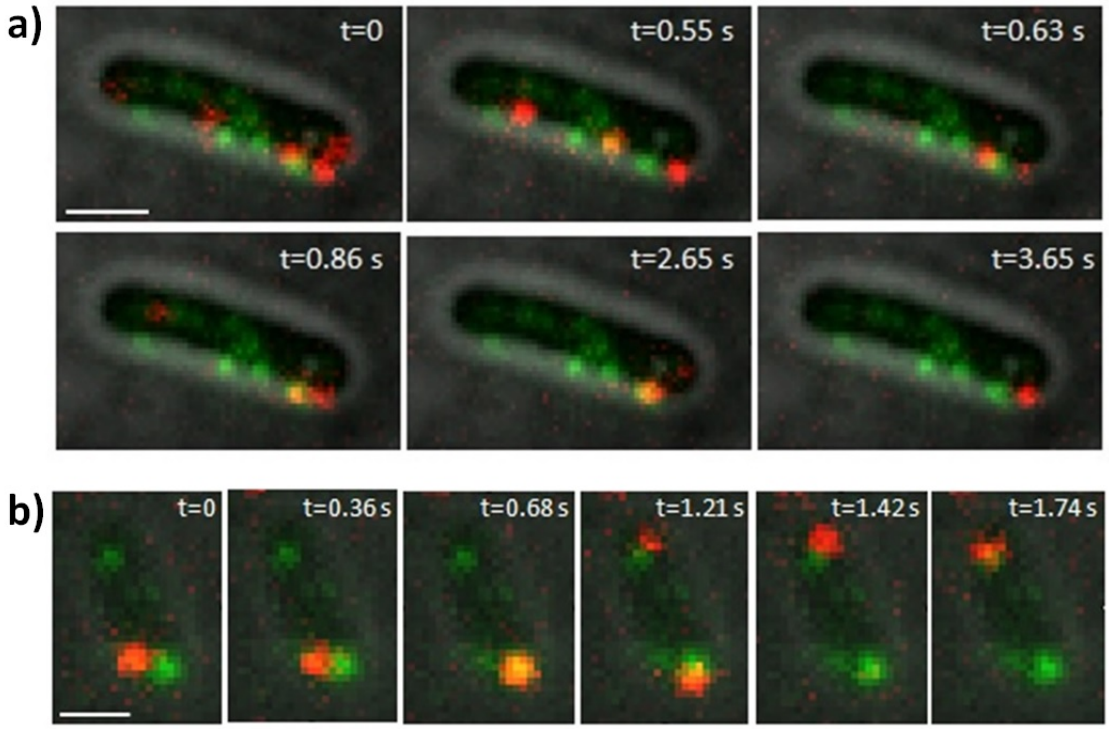

Figure 6.3: Frames from two-colors video microscopy showing single molecules diffusing/binding inside *E. coli* RP437 (FliM-YPet, FliC(sticky)) electrocompetent cells electroporated with 20 nM Atto647-(Cys)CheY: **a)** In this acquisition, performed over 20 s, CheY mostly localises with the green motor spots in the cell; it also dwells at some other unlabelled loci which could well correspond to polar or lateral chemoreceptor clusters, as especially visible in the last frame shown (t = 3.65 s). Scale bar = 1 μm. **b)** In this acquisition, performed over 40 s, at t = 0 CheY is located next to a motor at the bottom of the cell, travels to it after ∼550 ms and dwells there for ∼220 ms; at t = 1 s, another CheY molecule colocalises with the same motor, dwelling there for 230 ms; at t = 0.9 s, yet another CheY molecule localises with the top cell pole, for ∼800 ms; finally, a last CheY molecule appears at the top motor at t = 1.74 s, but disappears after only 20 ms. Scale bar = 500 nm. For both acquisitions: exposure time 10 ms, settings for YPet: 532 nm laser, 1 mW; settings for Atto647: 637 nm laser, 2.5 mW.(Substacks of full videos found on USB stick, *CheYcoloc1* and *CheYcoloc2* movies (20 fps), respectively).

with the chemoreceptors' cluster to a much lesser extent than CheY. For clarity, the sum of the two components Gaussian fit (red dashed line) and a single Gaussian fit to the data (blue solid line) are shown, as in Figure 6.2, a). The R^2 value of the latter was found to be 0.79, versus a value of 0.98 for the former, hence the choice to rely on the latter. The fit of coefficients for the fast diffusing population of molecules is centred at (2.2±1.4) $\mu m^2/s$ while the fit for the slow diffusing population at D =

(0.3±0.4) $\mu m^2/s$ (Figure 6.4, a)).

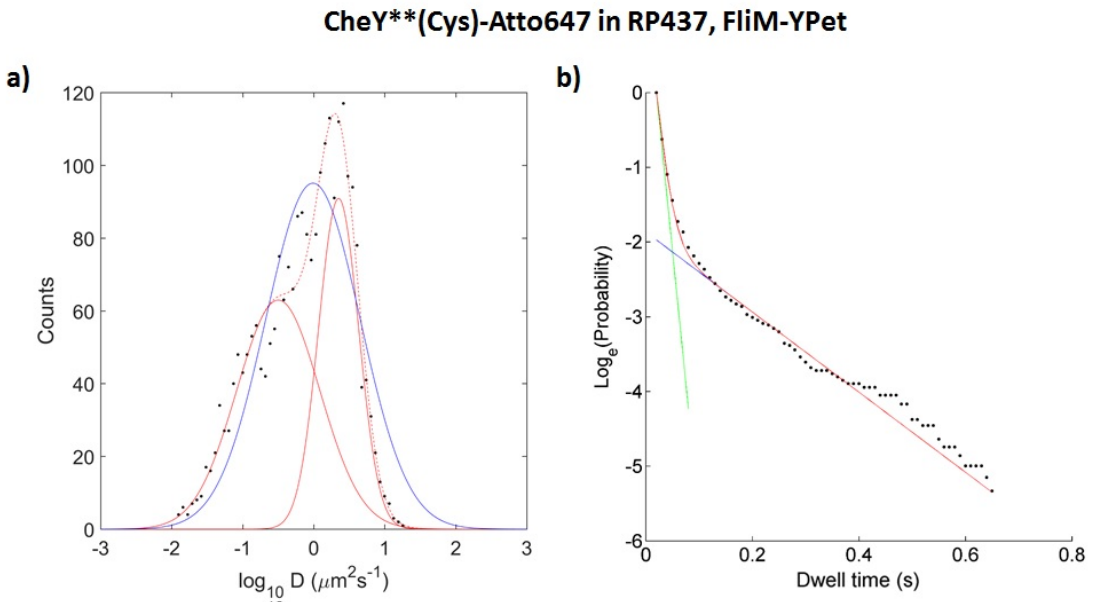

Figure 6.4: **a)** Diffusion coefficients' distribution for electroporated CheY**(Cys)-Atto647 in RP437, FliM-YPet *E. coli* cells. Histogram of 50 equally dispersed bins for D values from all recognised trajectories based on a data set consisting of 2269 molecules in different acquisition dates. The two components Gaussian fit (red solid lines), the sum of the latter (red dashed line) and the single Gaussian fit (blue solid line) are shown. **b)** Distribution of dwell times at the motor for electroporated CheY**(Cys)-Atto647 in RP437, FliM-YPet *E. coli* cells. Bins with less than 5 counts were discarded (i.e. each data point is at least 5 events). The plot shows the experimental survival log-probability of switch-bound CheY** to dissociate from it as a function of time. The red curve is a bi-exponential combined fit, whereas the green curve is the linear fit for CheY** binding to $FliM_N$and the blue curve is the linear fit for binding to the secondary sites (see Table 6.1 for the fitted values of $K_{D,\ FliM_N}$ and $k_{off,\ ss}$). Histogram based on a data set consisting of 28 cells in different acquisition dates. For both **a)** and **b)**: exposure time 10 ms, settings for YPet: 532 nm laser, 1 mW; settings for Atto647: 637 nm laser, 2.5 mW.

Figures 6.5 and 6.6 show frames extracted by two example movies of *E. coli* cells, in bright-field in inverted colors, electroporated with CheY**(Cys)Atto647. As in Figure 6.3, electroporated CheY** proteins are shown in red, motors in green. In comparison with CheY's behaviour shown in Figure 6.3, as expected, CheY** tends to spend much less time in loci in the cell which do not correspond to labelled motors; however, the trend to insistently localise at the motor spots is retained, with even

longer dwell times, as shown in Figure 6.4, b): it should be noted that CheY** is not likely to mimic CheY-P as it has been shown through fluorimetric assay to have inferior binding affinity for $FliM_N$ (K_D(CheY-P) = 26 μM vs K_D(CheY**) = 55 μM, as illustrated in Figure 6.7)[211,273]. However, it presents longer dwell times than CheY, which cannot be accounted for by a K_D of 55 μM, but could, in the light of the hypothesis proposed in section 6.5.1, be attributable to secondary sites' binding.

6.5.3 Dynamics of CheY(I95V) in Δ*che*Z background

To both increase the frequency of CheY interaction with the switch, thereby enhancing sampling, and to better distinguish the long dwell times observed for CheY, the labelled mutant CheY(I95V) and a Δ*che*Z background strain were used. In fact, both the phosphorylated and unphosphorylated forms of CheY(I95V) were shown to have an affinity for $FliM_N$ higher than both CheY and CheY** (K_D(CheY(I95V)-P) = 3.9 μM vs K_D(CheY-P) = 26 μM vs K_D(CheY**) = 55 μM)[211]. Residue Ile95 mediates the surface complementarity between CheY and FliM: in the active, phosphorylated form of CheY(I95V), the Tyr106 side chain is probably buried in the interior of a hydrophobic pocket and therefore does not affect FliM binding. This is supported by the unaltered FliM binding affinities of CheY mutants with substitutions at position 106 (reference 124). Mutants with substitutions at position 95, on the other hand, do have a dramatic impact on the binding affinity of CheY to the FliM N-terminal peptide[211]. Taken together, these findings suggest that Ile95 itself directly interacts with FliM. It is therefore likely that replacement of isoleucine with the slightly smaller valine might enhance the complementarity between the two proteins, allowing neighboring residues to bind to FliM more tightly.

In the single-molecule experiments carried out with this moiety, 0.3 pmoles (15 nM) of CheY(I95V)(Cys)-Atto647 were transformed by electroporation into FliM-YPet,

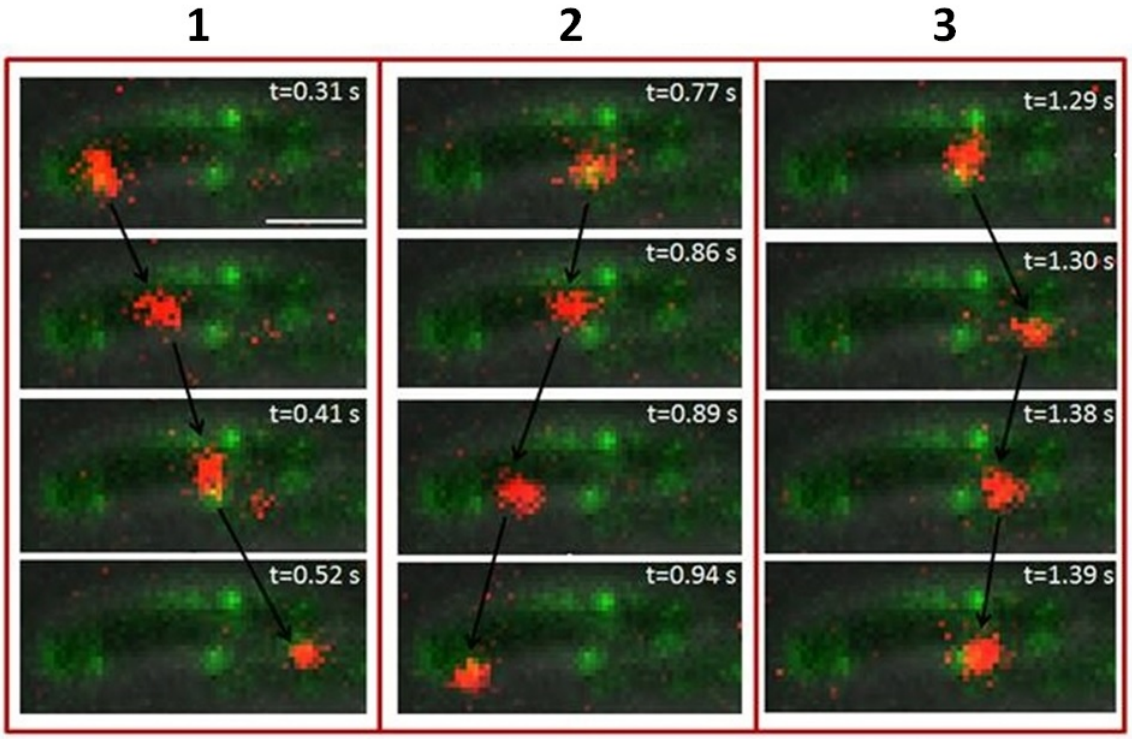

Figure 6.5: Frames from two-colors fluorescence video microscopy showing one single molecule diffusing/binding inside an electrocompetent *E. coli* RP437 (FliM-YPet, FliC(sticky)) cell electroporated with 30 nM CheY**(Cys)Atto647: in the top frame of the left box (t = 0.31 s), the molecule can be seen moving from the motor at the left pole (after having dwelled there for ∼50 ms) to the one located at mid-cell, getting there after 100 ms, and moving almost immediately on to the motor at the right pole of the cell (t = 0.52 s), where it stays for ∼200 ms; in the top frame of the central box, the same molecule returns to the mid-cell motor (t = 0.77 s), then moves to the motor at the left pole of the cell, dwelling there for ∼50 ms; finally, in the right box, the molecule is back at the mid-cell motor (t = 1.29 s), it then heads to the right pole motor again (dwell time ∼70 ms) and finally returns to the mid-cell one at t = 1.39 s. Exposure time 10 ms, settings for YPet: 532 nm laser, 1 mW; settings for Atto647: 637 nm laser, 2.5 mW. Scale bar = 1 μm. (Substack of full video found on USB stick, *CheYStarStarcoloc1* movie (20 fps)).

Δ*che*Z *E. coli* cells following the procedure described in 2.3.4; setting used for imaging were 10 ms exposure time, 532 nm laser with 1 mW power for YPet and 637 nm laser with 2.5 mW power for Atto647. Movies of electroporated fluorescent cells on agarose pads were recorded for 30 s and analysed with the software suite whose features are described in section 6.4. In Figure 6.8, a), a single Gaussian fit to the diffusion data (blue solid line, $R^2 = 0.97$), a two components Gaussian fit to the

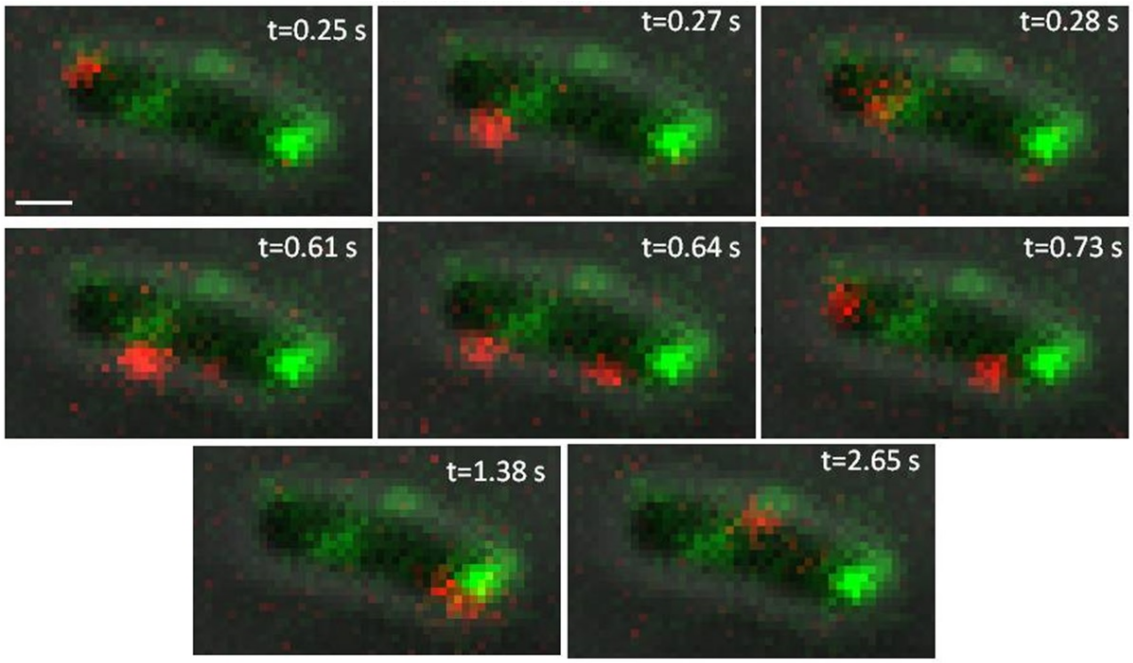

Figure 6.6: Frames from two-colors fluorescence video microscopy showing single molecules diffusing/binding inside an electrocompetent *E. coli* RP437 (FliM-YPet, FliC(sticky)) cell electroporated with 20 nM CheY**(Cys)Atto647: between t = 0 and t = 0.08 s, a single molecule of CheY** is located next to a motor at the left pole of the cell, reappearing again at frame 25 (shown) to then travel already in the next frame towards another motor spot underneath (t = 0.28 s); at t = 0.61 s, a red spot characterized by ∼twice the intensity of a single one appears close to the latter mentioned motor, splitting in the following frame into two single CheY** molecules; these travel in the cell colocalising, respectively, with the motors at each of the cell's poles (t = 0.73 s and t = 1.38 s). Finally, at t = 2.65 s, a CheY** molecule localising at the top mid-cell motor is visible. Exposure time 10 ms, settings for YPet: 532 nm laser, 1 mW; settings for Atto647: 637 nm laser, 2.5 mW. Scale bar = 500 nm. (Substack of full video found on USB stick, *CheYStarStarcoloc2* movie (20 fps)).

diffusion data (red solid lines) and a sum of the latter (red dashed line, $R^2 = 0.99$) are shown. The two components fit resulted the best, as judged by R^2 value, hence the decision to rely on that. A D = (2.3±1.7) $\mu m^2/s$ was found for the free diffusing molecules, and D = (0.5±0.7) $\mu m^2/s$ for the slow ones, probably binding to motor complexes. Both diffusion coefficient values are in agreement with those found for CheY, suggesting that the I95V mutation does not affect the diffusive behaviour of the protein.

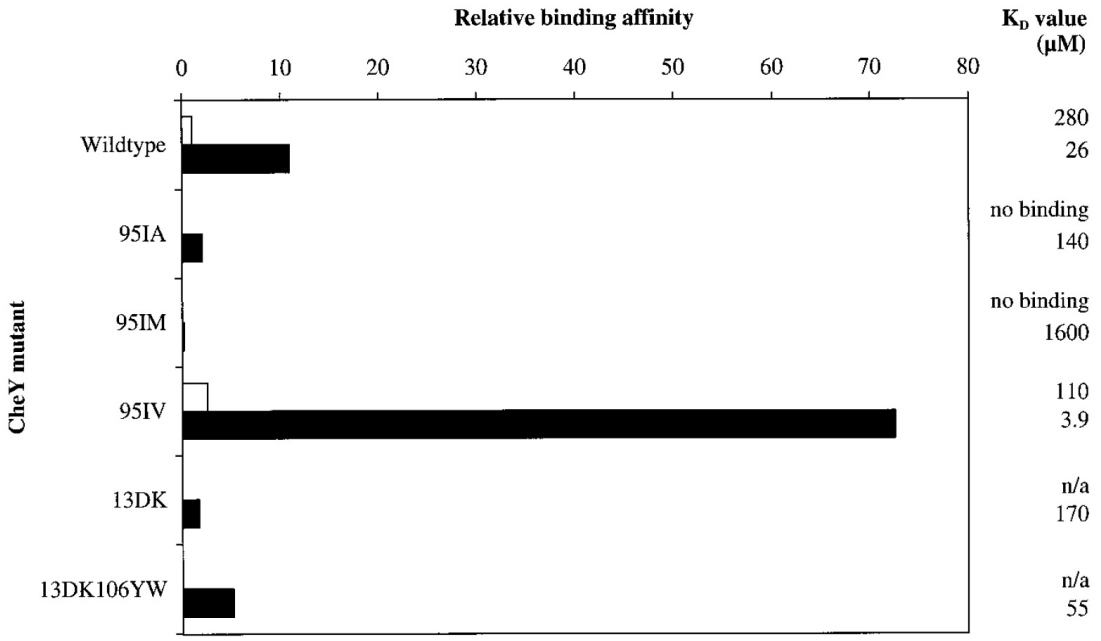

Figure 6.7: Calculated binding affinities of different CheY mutants to the peptide corresponding to the N-terminal 16 residues of FliM (MGDSILSQAEIDALLN). White bars denote the unphosphorylated, and black bars denote the phosphorylated forms. Binding reactions for CheY(D13K) and CheY(D13K/Y106W) (CheY**) were carried out are displayed in black bars because both proteins are assumed to represent the activated conformation[173]. Image taken from 211.

As for CheY and CheY**, most of the measured dwell times of CheY(I95V) at the switch resulted close to the sampling time comparable to the exposure time used (10 ms), likely representing the interaction of the protein with $FliM_N$ as well as random collisions and false positives (i.e., molecules in similar X- and Y-positions passing by the motor but at a different focal plane, i.e., different Z-position but in similar X- and Y-positions). However, some of the measured dwell times were much longer than those measured for CheY, lasting up to ∼0.3 s in the partial probability distribution shown in Figure 6.8, b) (bins with less than 5 counts discarded) and up to 0.7 s in Figure 6.12, b) (full probability distribution). Clearly, the dwelling profile is not the product of a simple first-order binding process, being different from the theoretical probability distribution for interaction with $FliM_N$ alone (green straight line in Figure 6.8, b)). This profile is suggestive of a secondary binding process. It is

reasonable that the short dwell times represent CheY(I95V) interaction with $FliM_N$ whereas the dwell times on the long tail in the curve of Figure 6.8, b) reflect binding to the low-affinity sites. These results endorse the conclusion that CheY interacts *in vivo* with a binding site different from $FliM_N$.

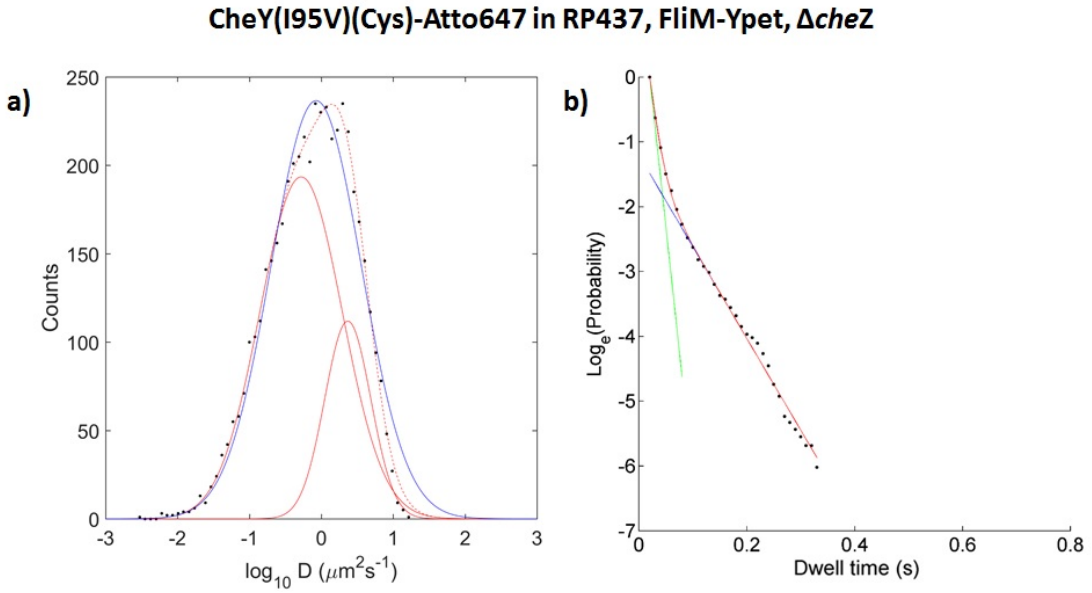

Figure 6.8: **a)** Diffusion coefficients' distribution for electroporated CheY(I95V)(Cys)-Atto647 in Δ*che*Z, FliM-YPet *E. coli* cells. Histogram of 50 equally dispersed bins for D values from all recognised trajectories based on a data set consisting of 4298 molecules in different acquisition dates. The two components Gaussian fit (red solid lines), the sum of the latter (red dashed line) and the single Gaussian fit (blue solid line) are shown. **b)** Distribution of dwell times at the motor for electroporated CheY(I95V)(Cys)-Atto647 in Δ*che*Z, FliM-YPet *E. coli* cells. Bins with less than 5 counts were discarded (i.e. each data point is at least 5 events). The plot shows the experimental survival log-probability of switch-bound CheY(I95V) to dissociate from it as a function of time. The red curve is a bi-exponential combined fit, whereas the green curve is the linear fit for CheY(I95V) binding to $FliM_N$and the blue curve is the linear fit for binding to the secondary sites (see Table 6.1 for the fitted values of $K_{D,\ FliM_N}$ and $k_{off,\ ss}$). Histogram based on a data set consisting of 87 cells in different acquisition dates. For both **a)** and **b)**: exposure time 10 ms, settings for YPet: 532 nm laser, 1 mW; settings for Atto647: 637 nm laser, 2.5 mW.

6.5.4 Dynamics of CheY(I95V) in Δ*che*A background

The results of the experiment described in the previous section, carried out in a Δ*che*Z background strain, are representative of the cooperative binding of CheY to the switch and in particular to a low affinity site on $FliM_M$ or on FliN. Since unphosphorylated CheY can bind FliM without producing CW rotation[211,274], and assuming that CW generation is triggered by the cooperative binding of CheY, a control representative of the non-cooperative binding to the switch was carried out in Δ*che*A, FliM-YPet *E. coli* cells. The use of this strain allowed also minimisation of CheY dwelling at the receptors patch, and therefore diffusion properties between this and the other strains used were compared. In Figure 6.9, a), a single Gaussian fit to the diffusion data (blue solid line, $R^2 = 0.94$), a two components Gaussian fit to the diffusion data (red solid lines) and a sum of the latter (red dashed line, $R^2 = 0.99$) are shown. The two components fit resulted the best, as judged by R^2 value, hence the decision to rely on that. A D = (2.8±1.6) $\mu m^2/s$ was found for the free diffusing molecules, and D = (0.5±0.6) $\mu m^2/s$ for the slow ones. From the values reported in Table 6.1, it is possible to say that the diffusion coefficients values are similar in magnitude to those previously measured for CheY, CheY** and CheY(I95V) in Δ*che*Z background. Unphosphorylated CheY(I95V) has been shown to have a $K_{D,\ FliM_N}$=110 μM (see Figure 6.7): it is therefore possible that it still interacts with the switch complex through a network of conserved residues that enable allosteric communication between the phosphorylation site (Asp57) and the target binding site on $FliM_N$[274]. Regarding the dwell times distribution, the measured dwell times were again much longer than those measured for CheY and slightly longer than those measured for the same mutant in Δ*che*Z background, lasting up to ∼0.4 s in the partial probability distribution shown in Figure 6.9, b) (bins with less than 5 counts discarded) and up to 0.8 s in Figure 6.12, b) (full probability distribution). It would be tempting to speculate that the absence of the

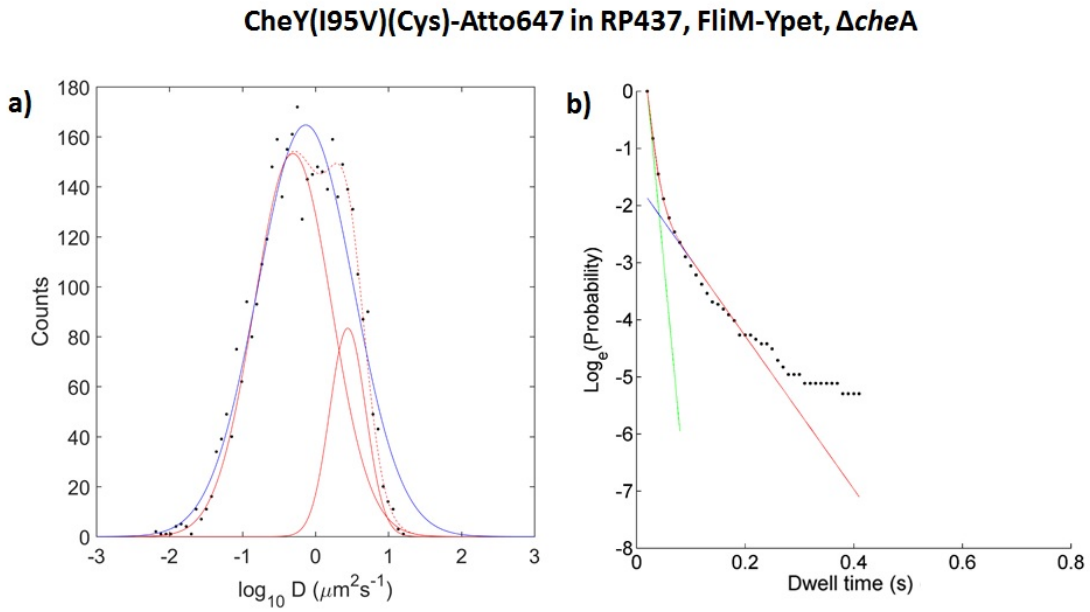

Figure 6.9: **a)** Diffusion coefficients' distribution for electroporated CheY(I95V)(Cys)-Atto647 in Δ*che*A, FliM-YPet *E. coli* cells. Histogram of 50 equally dispersed bins for D values from all recognised trajectories based on a data set consisting of 3388 molecules in different acquisition dates. The two components Gaussian fit (red solid lines), the sum of the latter (red dashed line) and the single Gaussian fit (blue solid line) are shown. **b)** Distribution of dwell times at the motor for electroporated CheY(I95V)(Cys)-Atto647 in Δ*che*A, FliM-YPet *E. coli* cells. Bins with less than 5 counts were discarded (i.e. each data point is at least 5 events). The plot shows the experimental survival log-probability of switch-bound CheY(I95V) to dissociate from it as a function of time. The red, green and blue curves are as described in Figure 6.8. Histogram based on a data set consisting of 63 cells in different acquisition dates. For both **a)** and **b)**: exposure time 10 ms, settings for YPet: 532 nm laser, 1 mW; settings for Atto647: 637 nm laser, 2.5 mW.

phosphate group on CheY could somehow facilitate the binding to the secondary site or stabilise such bond once it is formed.

6.6 Response to acetate

Phosphorylation is not the only chemical modification that CheY undergoes and not the only one that activates the protein. CheY also undergoes lysine acetylation, primarily at residues 92 and 109 (reference 79). This modification significantly increases the activity of CheY both *in vitro*[275] and *in vivo*[276] through what in *Afanzar, Di Paolo et al.* (in submission) is believed to be removal of conformational repression. However, unlike phosphorylation, acetylation does not affect the binding of CheY to FliM, suggesting that it is involved in a post-binding step[277]. Although it was recently demonstrated that this chemical modification is involved in chemotaxis (R. Barak and M. Eisenbach, unpublished data), its role is still an open question.

6.6.1 Effect of acetate on dwell times

To examine whether acetylation affects CheY binding to the switch, parallel experiments to those described in sections 6.5.3 and 6.5.4 were carried out in which the cells were also supplemented with 50 mM acetate (Ac). In Figure 6.10 a) and c), single Gaussian fits to the diffusion data (blue solid lines, R^2 for a) = 0.89, R^2 for b) = 0.86), a two components Gaussian fit to the diffusion data (red solid lines) and a sum of the latter (red dashed line, R^2 for a) = 0.97, R^2 for b) = 0.95) are shown. The two components fit resulted the best, as judged by R^2 value, hence the decision to rely on that. In a), a D = (2.5±2.1) $\mu m^2/s$ was found for the free diffusing molecules, and D = (0.4±0.6) $\mu m^2/s$ for the slow ones. In b), a D = (1.6±1.5) $\mu m^2/s$ was found for the free diffusing molecules, and D = (0.1±0.1) $\mu m^2/s$ for the slow ones. Comparing the distributions of diffusion coefficients D in Figure 6.10, a)

and c) with those in panels a) and b) of Figures 6.8 and 6.9, it is possible to make some considerations: at a first glance, the D values for bound fractions do not seem affected by the addition of acetate, being always close to zero; however, the shape of the distribution and the proportions of the slow and fast diffusing populations in Δ*che*A background seems to change substantially upon addition of acetate with respect to the case without acetate (see Table 6.1), becoming almost equal percentages for the 2 populations. In general, there seems to be the following hierarchy for the fast diffusing populations:

$$D_{I95V,dA} > D_{I95V,dA+Ac} > D_Y \simeq D_{I95V,dZ} > D_{Y^{**}} > D_{I95V,dZ+Ac}$$

This suggests that phosphorylation and even more phosphorylation+acetylation slow down the molecules in the cytoplasm, maybe increasing the probability that they interact with exchanging FliMs in the cytoplasm.

A change in the duration of dwell times was also observed upon addition of acetate, specifically a decrease to 0.5 s in Δ*che*A+Ac background and an increase to 1 s in Δ*che*Z+Ac background (Figure 6.12, b)). This result suggests that the complex generated between a CheY molecule that is both phosphorylated and acetylated and the secondary binding site at the switch is more stable than the complex generated with a CheY molecule that is phosphorylated only. In an earlier study involving all-atom Molecular Dynamics simulation, it was predicted that CheY acetylation promoted the local activation of the $\alpha 4\beta 5$ region of CheY[278], which is localised to the CheY-$FliM_M$ binding interface described in *Thermotoga maritima*[279]. Therefore, a possible interpretation for the measured higher dwell time of acetylated CheY at the switch is the enhanced CheY interaction with $FliM_M$. Collaborators examined the feasibility of this interpretation in a rigid-body docking model (Figure 6.11). In this analysis, a number of models for the binding of CheY to $FliM_M$ in *T. maritima* were produced, and the one that best fitted with the Nuclear Magnetic Resonance

(NMR) results of Dyer et al.[279] was chosen. This binding mode was translated to *E. coli* proteins by homology modeling for both active and inactive CheY (Figure 6.11 a) and b), respectively). It was observed that while the active conformation of CheY well docked onto $FliM_M$, the inactive conformation of the $\alpha4\beta5$ region of CheY clashed with the modelled $FliM_M$. In conclusion, the single-molecule results combined with the docking model suggest that acetylation generates clockwise rotation by enhancing the binding of CheY to $FliM_M$, and that this enhancement is achieved through modulation of the $\alpha4\beta5$ conformation.

Sample	D_{fast} [$\mu m^2/s$]	Fast %	D_{slow} [$\mu m^2/s$]	Slow %	$K_{D,\ FliM_N}$ [μM]	$k_{off,\ ss}$ [s^{-1}]
Atto647-(Cys)CheY	2.3±2.4	63	0.4±0.6	37	30.1	23.9
CheY**(Cys)-Atto647	2.2±1.4	41	0.3±0.4	59	17.6	5.4
CheY(I95V)(Cys)-Atto647, Δ*che*Z	2.3±1.7	24	0.5±0.7	76	19.3	14.1
CheY(I95V)(Cys)-Atto647, Δ*che*Z+Ac	1.6±1.5	52	0.4±0.6	48	17.6	10.7
CheY(I95V)(Cys)-Atto647, Δ*che*A	2.8±1.6	20	0.5±0.6	80	24.8	13.4
CheY(I95V)(Cys)-Atto647, Δ*che*A+Ac	2.5±2.1	48	0.4±0.6	52	25	21.1

Table 6.1: Experimentally measured fast and slow diffusion coefficients, relative population proportions as in previously shown normal distributions and kinetic constants for the *E. coli* CheY mutants and background strains used in this work. $K_{D,\ FliM_N}$ values were calculated from the fitted $k_{off,\ FliM_N}$ values (green curves in previously shown dwell time distributions) assuming a diffusion-limited k_{on} = (4 x 10^6) $M^{-1}s^{-1}$. $k_{off,\ ss}$ values for secondary binding sites (ss) are calculated from the slopes of the fitted blue curves in previously shown dwell time distributions.

6.6.2 FliM's acetate-induced dispersion

While performing the single-molecule experiments in the presence of 50 mM acetate in Δ*che*A and Δ*che*Z strains, a peculiar trend was noticed: the fluorescence intensity of the FliM-YPet proteins in the motor spots decreased with time, until a steady state was reached after 30-40 minutes in which there was no more trace of localised

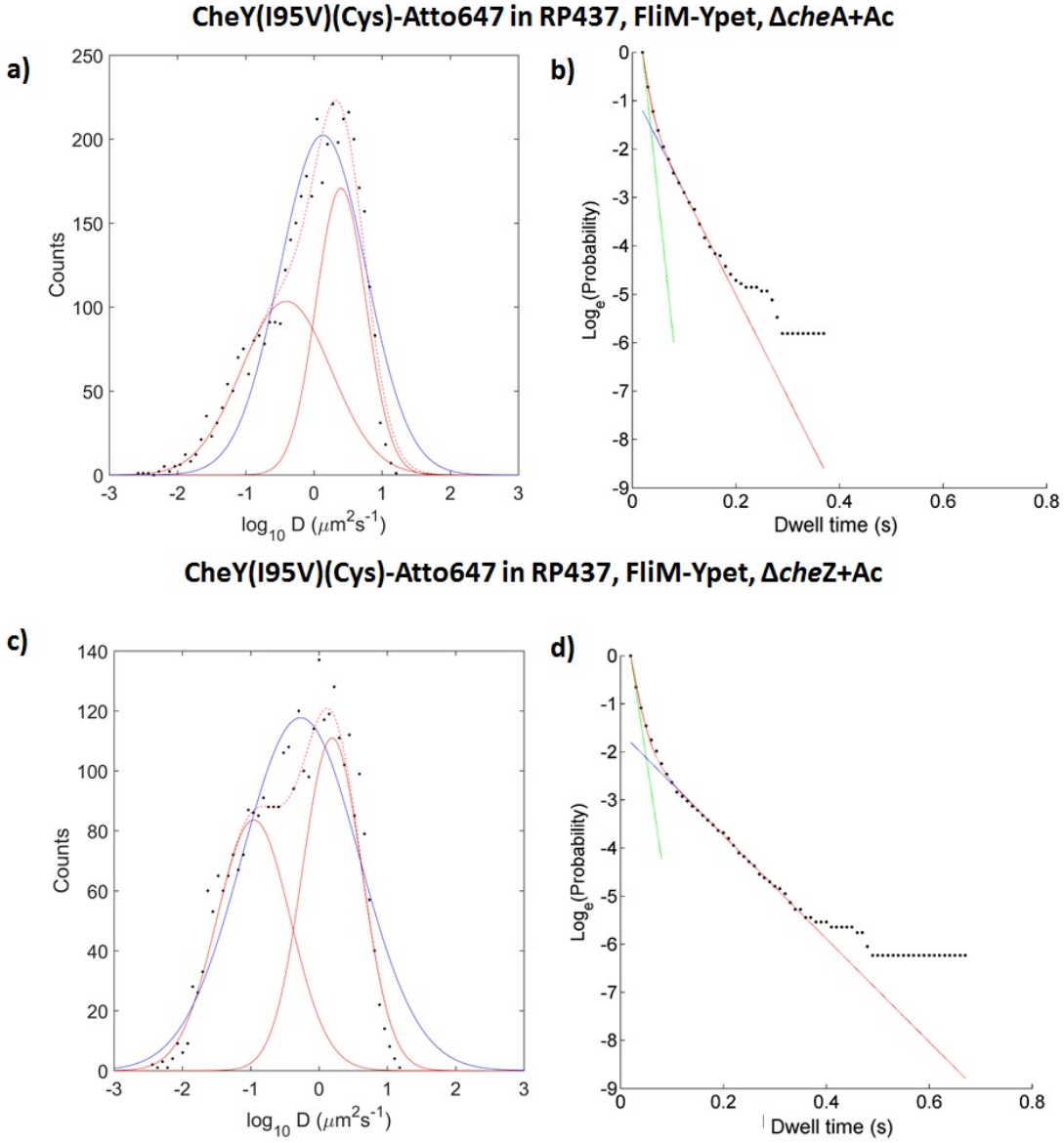

Figure 6.10: **a), c)** Diffusion coefficients' distributions for electroporated CheY(I95V)(Cys)-Atto647 in Δ*che*A/Δ*che*Z, FliM-YPet *E. coli* cells in the presence of 50 mM acetate. Histograms based on a data set consisting of 4308 molecules for a) and 3247 molecules for c) in different acquisition dates. The two components Gaussian fit (red solid lines), the sum of the latter (red dashed line) and the single Gaussian fit (blue solid line) are shown. **b), d)** Distributions of dwell times at the motor for electroporated CheY(I95V)(Cys)-Atto647 in Δ*che*A/Δ*che*Z, FliM-YPet *E. coli* cells in the presence of 50 mM acetate. Bins with less than 5 counts were discarded (i.e. each data point is at least 5 events). The plot shows the experimental survival log-probability of switch-bound CheY(I95V) to dissociate from it as a function of time. The red, green and blue lines are as in Figures 6.8, b) and 6.9, b). Histograms based on a data set consisting of 57 cells for Δ*che*A + acetate and 40 cells for Δ*che*Z + acetate imaged in different acquisition dates. For all the 4 panels: exposure time 10 ms, settings for YPet: 532 nm laser, 1 mW; settings for Atto647: 637 nm laser, 2.5 mW.

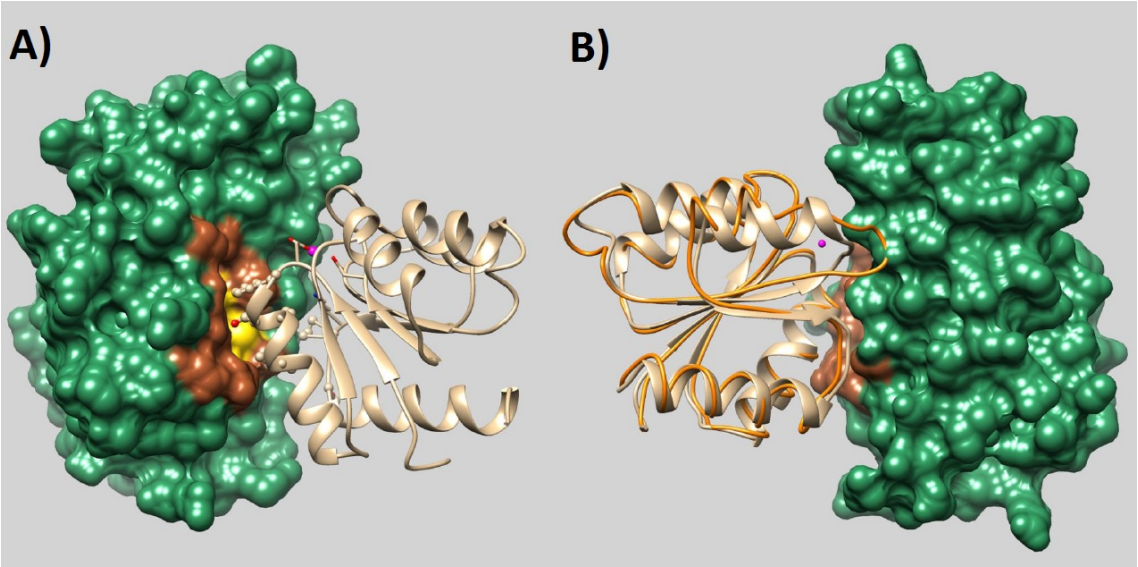

Figure 6.11: Predicted $FliM_M$-CheY binding modes in *E. coli*. The solvent accessible surface of $FliM_M$ is shown in green with a binding depression area and its surrounding ridge highlighted in yellow and brown, respectively. **A)** CheY is depicted as a beige ribbon, with residues F14, T16, M17, I20, P110 and T112 (shown as ball and stick) corresponding to the interacting residues in *T. maritima*. Except for T112, all these residues are interacting residues also in *E. coli*. **B)** The predicted interaction in *E. coli* rotated by approximately 180° about the vertical axis, showing that the inactivated conformation of CheY (orange coil) clashes with $FliM_M$.

green spots, but only a diffuse, low intensity cytoplasmic fluorescence. Figure 6.13 shows the probability distributions of FliM intensities in Δ*che*A, FliM-YPet (left) and in Δ*che*Z, FliM-YPet (right) *E. coli* cells in the absence (blue dots) and presence of 50 mM acetate (red dots). Each data point represents the maximum pixel intensity of a detected motor spot. Comparing the two blue and red distributions, it is possible to notice that for both genetic backgrounds, while in the absence of acetate the motor spots' intensities were scattered over a broader range (30-300 counts), upon addition of acetate the average intensity drops down to ∼25-30 counts.

The trends shown in Figure 6.13 for FliM intensity distributions in the presence and absence of acetate, joined with the findings about the diffusion coefficients described in section 6.6.1, support the hypothesis that CheY-Ac removes FliM from the switch by binding to its oligomerisation interface and mobilising it in the cytoplasm.

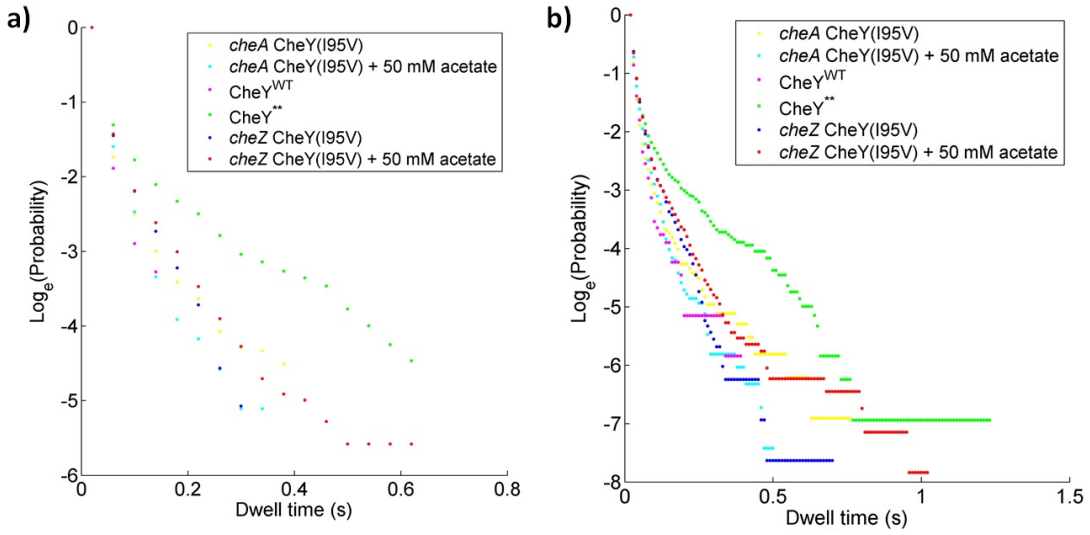

Figure 6.12: Short **(a)** and long **(b)** dwell time distributions for all CheY mutants and genetic backgrounds considered in this study. Bins with less than 5 counts were discarded in (a) (i.e. each data point is at least 5 events). Both plots show the experimental survival log-probability of switch-bound CheY mutants to dissociate from it as a function of time.

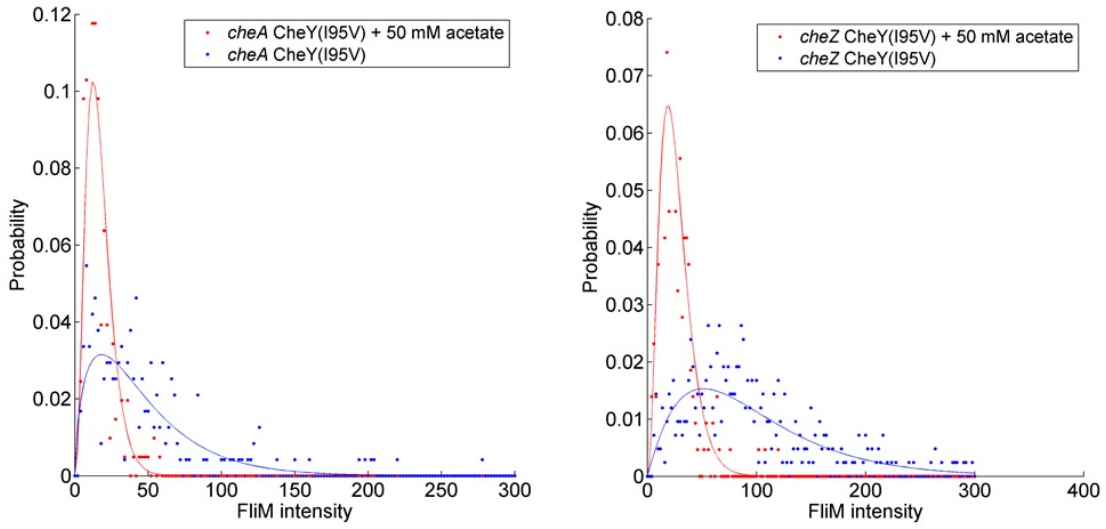

Figure 6.13: Probability distributions of FliM intensities in Δ*che*A, FliM-YPet (left) and in Δ*che*Z, FliM-YPet (right) *E. coli* cells in the absence (blue dots) and presence of 50 mM acetate (red dots). The solid lines, in corresponding colors, are Gamma fits obtained with the MATLAB in-built function *fitdist*. As discussed in the main text, the difference between the two distributions provides evidence for FliM's acetate-induced dispersion. Motor spots imaged in different acquisition dates in 150 (-acetate) and 97 (+acetate) cells using 10 ms exposure time, 532 nm laser, 1 mW power.

6.7 Summary

In this chapter, the main results of this thesis were reported. Single molecules of three labelled CheY mutants were imaged and tracked in their journey between the receptor clusters and the motors, via diffusion through the cytoplasm, in live cells. Binding kinetics to the motor, as well as diffusion between them and the chemoreceptor clusters, in three different background strains and in the presence and absence of chemotactic stimuli were quantified and summarised in Table 6.1. The presence of measured long dwell times at the motor which are not compatible with the dissociation constant to FliM commonly reported in the literature for *E. coli* $CheY^{263}$ supports the recently proposed hypothesis of the existence of a secondary binding site for CheY on either $FliM_M$ or FliN, which would be responsible for post-binding cooperativity and motor switching (*Afanzar, Di Paolo et al*, in submission). Finally, an interesting acetate-induced dispersal effect on FliM proteins was observed and characterised: that CheY-Ac removes FliM from the C-ring by binding to its oligomerisation interface and mobilising it in the cytoplasm was suggested.

Contributions

Oshri Afanzar (Department of Biological Chemistry, The Weizmann Institute of Science, Israel) wrote the MATLAB suite used to analyse single-molecule data and Milana Fraiberg (Department of Biological Chemistry, The Weizmann Institute of Science, Israel) performed docking analysis. Anne Plochowietz (Kapanidis group, Department of Physics, University of Oxford) provided the MATLAB script to perform channel mapping.

Chapter 7

Fluorescence Microscopy in *R. sphaeroides*

7.1 Motility and electroporation in *R. sphaeroides*

The correlation between motility and electroporation was also investigated in *R. sphaeroides*. Since in this case cells did not have a FliC(sticky) mutation, after transformation and washing steps they were tethered to the coverslip glass via anti-FliC antibody (procedure described in section 2.6.1). As for *E. coli*, the aim of these experiments was to confirm interaction of the electroporated labelled $CheY_6$ with the motor in a rotating tethered cell, to complement the observations in cells deposited onto agarose pads reported in section 7.3.3. For comparison, table 7.1 contains a summary of some relevant swimming parameters for *E. coli* and *R. sphaeroides*.

7.1.1 Single-molecule interaction with FliM in motile cells

The same approach as for *E. coli* described in section 5.1 was attempted first: electrocompetent *R. sphaeroides* was electroporated with 3.5 nM (i.e. 0.07 pmoles)

	E. coli	*R. sphaeroides*
Mean speed	16.5 μm/s[280]	40 μm/s
Mean run time	1 s	5 s
Mean tumble/stop length	0.1 s	0.66 s
Mean tumble/stop frequency		(0.31±0.19) $s^{-}1$
Mean run bias	0.6-0.7	(0.8±0.2)

Table 7.1: Swimming parameters for wild type *E. coli* (from 66 unless otherwise indicated) and *R. sphaeroides* (from 71).

$CheY_6$(A134C)-Atto647, recovered and washed as described in section 7.3.1. Since in the single-molecule experiments reported in section 7.3 it was found that *R. sphaeroides* cells were more permeable to labelled proteins in solution during the application of the electric pulse than *E. coli*, a lower amount of protein was used here (namely about 1/3 compared to what used in chapter 5) in order to guarantee the presence of ideally only one molecule per cell. Bright-field and two-colours TIRF microscopy (with the usual convention: $CheY_6$ in red, motor spots in green) revealed that, despite most (>95%) of the tethered cells not being motile after electroporation, in those that showed some extent of movement, however slow and jerky, $CheY_6$(A134C)-Atto647 was actually colocalising with the motor for periods as long as the whole duration of the acquisition (see *RSmot1BF* and *RSmot1* movies on USB stick for an example (bright-field and TIRF movies, respectively, 5.77 s acquisition in bright-field and 40 s in fluorescence, 10 ms exposure time, 60 fps). In order to rule out the possibility that the observed movement was only due to Brownian motion and not to a working motor, a different approach was taken, where cells were allowed to recover for longer and even grow and divide: a time-lapse experiment the same as the one described in section 5.1.4 for *E. coli*.

7.1.2 Time-lapse measurements

Differently from electroporated *E. coli* samples, in which it was possible to find properly spinning tethered cells, though not many, even after only 5 minutes recovery, electroporated *R. sphaeroides* turned out to preserve motility less well upon application of the electric pulse if allowed only a relatively short recovery. It was previously stated that *R. sphaeroides* seems to take up labelled molecules more easily than *E. coli*; however, motility and fluorescence have been shown by several pieces of evidence in this work and in 5 to be independent from one another, so a higher level of internalisation in *R. sphaeroides* than in *E. coli* is not likely to be the cause. Furthermore, *R. sphaeroides* was found to be more robust and viable than *E. coli* after electroporation, as it was observed by the author to grow and divide on agarose pads with almost no delay after application of the electric pulse; however, these observations were made on cells deposited onto agarose pads, and did not therefore give any information about the physical state of the motor nor its functionality. Hence the necessity to carry out tethered cell experiments to confirm the interaction of $CheY_6$ with FliM in working motors. As for *E. coli*, in order to have some fluorescence inside daughter cells, but keeping in mind that *R. sphaeroides* takes up molecules very easily, cells were initially incubated and electroporated with about 1.5-fold the amount of labelled protein used in section 7.1.1, namely 5 nM (i.e. 0.1 pmoles) $CheY_6$(A134C)-Atto647. Cells were first recovered for 20 minutes in SUX, then diluted 1:20 always in SUX to a starting volume of 10 ml ($OD_{700nm,\ t=0}$ = 0.113) and incubated at 30°C, 225 rpm in 125 ml flasks. Flasks were used instead of test tubes to prevent the bacteria from switching to photosynthetic growth due to lack of oxygen (see Discussion in section 7.2). Note that the optical density measurements for *R. sphaeroides* are carried out at 700 nm instead of at 600 nm as it is rich of red-absorbing pigments. The OD_{700nm} was measured every hour, 1 ml of cells washed and quickly imaged using phase contrast microscopy for a general

assessment of motility; cells were then flushed into a tunnel slide, left upside down in a humidity chamber for 10 minutes and washed extensively with SUX to remove unstuck cells; the tunnel's edges were sealed with nail polish to prevent evaporation and the sample in this way prepared was imaged in both bright-field and fluorescence. A NEP sample was prepared in the same way. The optical density curves for EP and NEP cells over time are shown in Figure 7.1: again, the latter grow faster than the former, but this time by about 30% compared to 20% in *E. coli* and only up to the first 3 hours of recovery, after which the NEP cells start growing exponentially faster than the EP ones. From the probability curves in the same figure, where values are normalised to a total number of 100 imaged cells for each time point, it is possible to infer that it is overall quite difficult to find a cell with a clearly spinning phenotype, being them always less than 10% anyway, in either sample. Movies *CheY6TimeLapse* and *CheY6TimeLapseBrightField* (60 fps) on USB stick show an example fluorescent and spinning tethered cell after about 3 hours from electroporation. However, it is interesting to notice that in the NEP sample the minimum number of spinners is observed in correspondence of OD_{700nm}∼0.3, which is when the two growth curves for this and EP sample start diverging.

7.2 Chromatophores in *R. sphaeroides*

With regard to the results illustrated in the previous section, it is worth mentioning some interesting fact that the author observed when carrying out experiments in *R. sphaeroides*: cells grown to OD_{700nm}∼0.3 and beyond imaged on the TIRF microscope could be seen to produce some cytoplasmic component excited by the 532 nm (green) laser and emitting in the red channel, causing a source of "out of focus" fluorescence that would make difficult accurate detection of the signal from the Atto647-labelled $CheY_6$ molecules. This could relate to the fact that most purple photosynthetic bacteria develop an extensive intracytoplasmic membrane (ICM) sys-

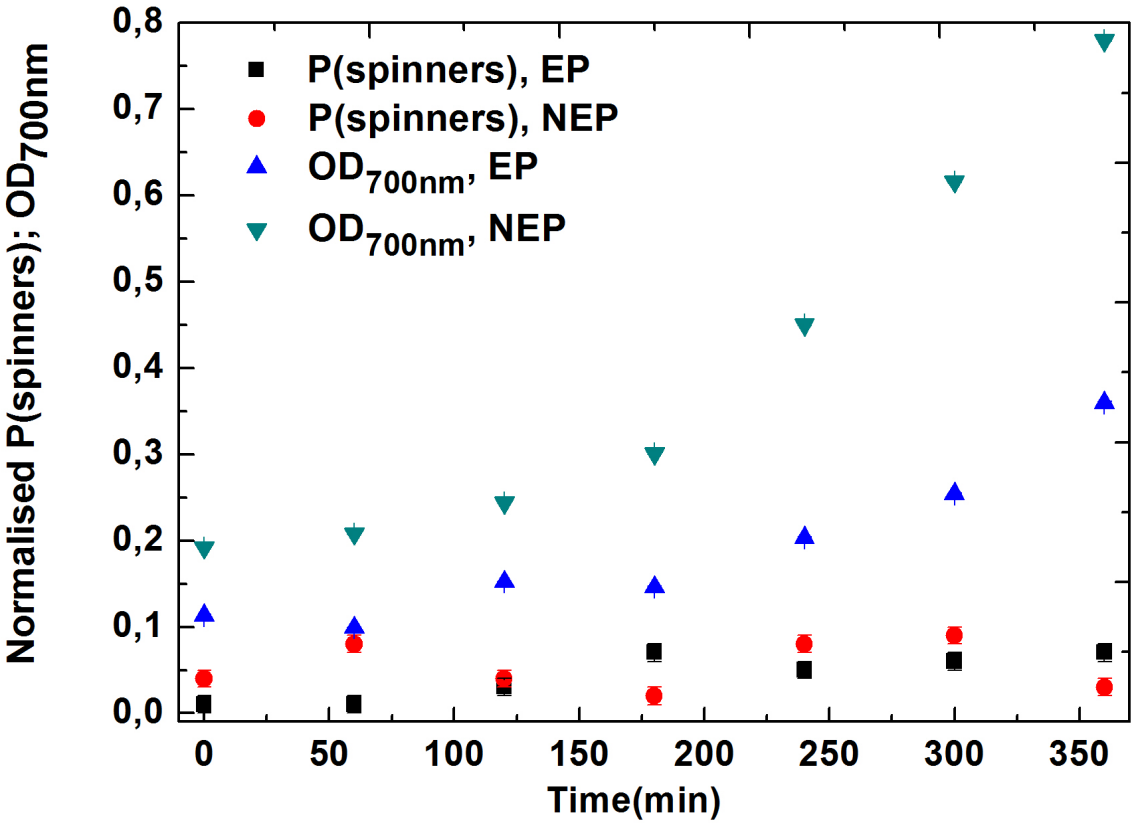

Figure 7.1: Correlation of motility and recovery length in *R. sphaeroides* cells electroporated with 5 nM (0.1 pmoles) $CheY_6$-Atto647: comparison of optical density and spinning probability curves over time for EP and NEP cells. Error bars on each data point are given by the normalised percentage error assuming 1 cell miscounting.

tem in response to a change from chemoheterotrophic to photoheterotrophic growth conditions (i.e. aerobic/anaerobic respiration)[281,282]. The ICM is also synthesized by *R. sphaeroides* during growth in the dark or light under conditions of limited oxygen availability (semi-aerobic growth)[283]. The composition and assembly of the ICM are known to be tightly regulated, with light intensity and oxygen tension being among the most prominent environmental stimuli which serve to control these processes. In *R. sphaeroides*, the ICM consists of interconnected vesicular structures of spherical shape and ∼60 nm diameter which originate from invaginations of the cytoplasmic membrane[284] and that can be isolated from cellular extracts as a rather homogeneous population of *chromatophores* (Figure 7.2 a) and b)). On a dry weight basis, purified chromatophores contain 5% phospholipid, 64% protein, and up to 5% pig-

ment, consisting mostly of bacteriochlorophylls (BChls) and carotenoids[285]. These chromatophore vesicles facilitate light harvesting and subsequent energy transfer to generate ATP within the bacteria. The photosynthetic apparatus is composed of three multimeric transmembrane protein complexes: the antenna or light-harvesting complexes (LHCs), the reaction center (RC) and the cytochrome (cyt) bc1 complex. The role of the LHCs, which non-covalently bind carotenoid and BChl molecules, is to collect incident light. Like most purple bacteria, *R. sphaeroides* has two types of LHCs, named LH1 and LH2 (see Figure 7.2 c)). The LH1, or B875, complex is synthesized in fixed stoichiometric amounts with the RC, forming the RCLH1 complexes. More peripheral to this fixed photosynthetic unit is the second complex, the LH2 or B800-850, whose amount is modulated by several factors, such as light intensity and oxygen partial pressure. Under semi-aerobic conditions, like those used in the time-lapse experiment described above, the production of the RC, B875, and B800-850 complexes can vary depending on the local oxygen concentrations. The syntheses of carotenoids and BChls vary in response to variations in light and/or oxygen. As shown in Figure 7.2 a) and b), electron tomography images show remarkably little apparent free cytoplasm in *R. sphaeroides* cells with full developed chromatophores[288]. As a further perspective of this work, electroporation of $CheY_6$ in aerobic and photoheterotrophic *R. sphaeroides* will be performed to allow both the true diffusion rate of this molecule *in vivo* and the effect of large numbers of physical barriers to that diffusion to be measured.

7.3 Single-molecule imaging of $CheY_6$ in *R. sphaeroides*

One of the most powerful features of the internalisation approach described in this work is that it can be applied to a range of proteins (up to 60 kDa molecular weight) and to many species of prokaryotes as well as eukaryotes[5]. The FP fusion method applied in the literature to determine $CheY_6$ localisation and measure motor

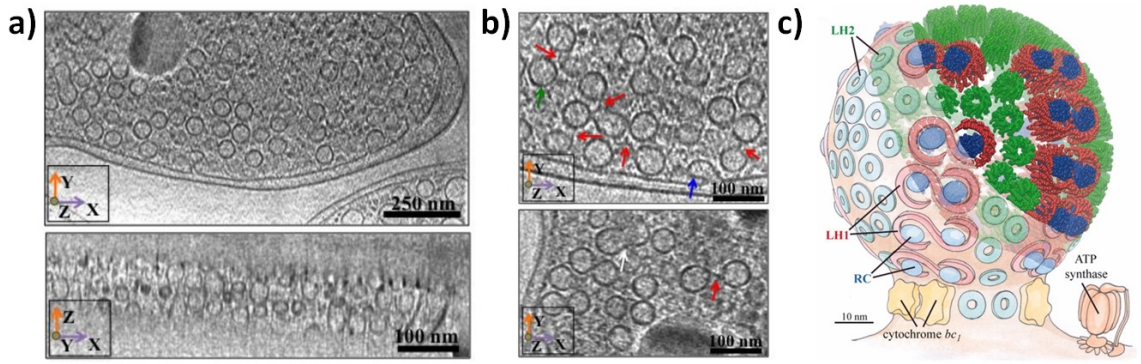

Figure 7.2: *R. sphaeroides* chromatophore vesicles. **a)** Architecture and constituents of a spherical chromatophore vesicle from *R. sphaeroides* constructed from atomic force microscopy and linear dichroism data. The light-harvesting complexes, LH2 (green) and LH1 (red), absorb light and transfer the resulting excitation to the RC (blue), which subsequently initiates electron transfers reducing quinone to hydroquinone; the bc 1 complex (yellow) oxidizes hydroquinone to create a proton gradient across the membrane, which in turn is used by ATP synthase (orange) for ATP production. Electrons are shuttled back to the RC by cytochrome c 2 (not shown). Taken from 286. **b)** Top: tomographic slide of a *R. sphaeroides* bacterium in the XY direction; bottom: visualisation of the same tomogram in the XZ direction. **c)** In the top panel it is possible to see chromatophores as isolated vesicles (green arrow), fused with the bacterial membrane (blue) or connected to one another in an extended reticulum (red); in the bottom panel two vesicles fused to each other are also visible. **b)** and **c)** taken from 287.

binding[155] suffers from some serious limitations; the main being that $CheY_6$ fusions are not functional and that if only a small percentage of a large population of proteins binds to either the motor or the chemoreceptor cluster, these events would be difficult if not impossible to distinguish against the background of free diffusing labelled molecules. Electroporation allows for internalisation of very few labelled $CheY_6$ molecules, hence removing background issues; moreover, the risk of non-functionality is limited by the small size of the organic dye used as label, much less invasive than a fluorescent protein usually at least 3 times as big as the protein itself and no downstream effects caused by adding the FP gene to the operon. For these reasons, in collaboration with Matthew W. Smith (Armitage group, Department of Biochemistry), work on *R. sphaeroides* was undertaken to investigate the behaviour *in vivo* of $CheY_6$, the equivalent of *E. coli* CheY in this species.

7.3.1 Experimental conditions

R. sphaeroides cells were made electrocompetent using the protocol in section 2.3.3, EP, NEP and *Negative Control* samples were prepared and, where applicable, electroporated as described in section 2.3.4 with a final concentration in solution of 5-10 nM $CheY_6$(A134C)-Atto647. Recovery time was ∼10 minutes for all the experiments and washing steps were carried out as described in section 2.3.4. Such recovery length was chosen to mirror a similar percentage of doubling time than 5 minutes represent for electrocompetent electroporated *E. coli* cells, which divide in ∼100 minutes (Figure 7.3, a)), while the calculated doubling time for electrocompetent electroporated *R. sphaeroides* resulted of ∼2.5 hours (Figure 7.3, b)). Samples were placed onto agarose pads and imaged using TIRF microscopy. Over 500 cells imaged, about 70% of EP and 10% of NEP cells internalised some labelled protein as judged by eye inspection, highlighting the greater membrane permeability of *R. sphaeroides* electrocompetent cells compared to their *E. coli* equivalents (see section 4.5). The position of the $CheY_6$ target was compared to a genomic fusion of FliM to either YFP or YPet or to a $CheW_4$-YFP fusion. Whilst $CheW_4$-YFP proved bright enough to locate the cytoplasmic cluster in the cell, due to the low copy number of FliM in the switch complex, FliM-YFP was not sufficiently bright to determine the motor location. A strain with FliM-YPet fusion was used for these experiments, instead.

7.3.2 Colocalisation with cytoplasmic cluster(s)

The same functionality test as for *E. coli* CheY was first carried out to check that the dye-labelled $CheY_6$ re-introduced in the cells by electroporation was localising this time at the cytoplasmic cluster(s), where it was previously shown to localise[155]. Depending on whether they are dividing or not, cells may contain either one or two cytoplasmic clusters[289]: in the first case, it would be placed at mid-cell, in the second

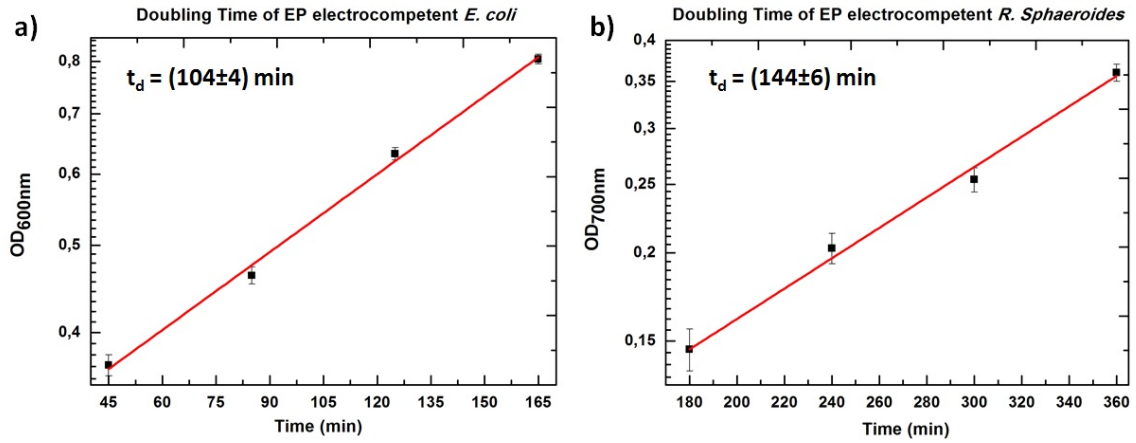

Figure 7.3: Experimentally determined doubling time for electrocompetent electroporated *E. coli* and *R. sphaeroides*(semi-log plots). Errorbars represent ±0.01 uncertainty on the OD measured value.

case at one-fourth and three-fourths of the cell main axis. As an indicator of where such cluster(s) was(were) in the cell, a *R. sphaeroides* strain with YFP labelled $CheW_4$ was employed, as such protein was shown to localise to the cytoplasmic cluster in several papers[156,290,291]. Colocalisation of $CheY_6$ with the cytoplasmic cluster was confirmed for 75% of the imaged cells which had internalised some fluorescence, two example images are shown in Figure 7.4: here it is possible to see that, besides being localised at cytoplasmic clusters, $CheY_6$ also dwells at some other locations in the cell which are not YFP-labelled and might correspond to motors or to the polar cluster (see next section).

7.3.3 Colocalisation with motors

Colocalisation of $CheY_6$ with the motor was then explored, using a FliM-YPet fusion as in the experiments reported earlier in this chapter for *E. coli*. Application of the electroporation approach to *R. sphaeroides* in this project turned out to be very promising and yielded good indications of $CheY_6$ colocalisation with the motor from the first attempts.

In the example cell shown in Figure 7.5, it is possible to identify two FliM-YPet

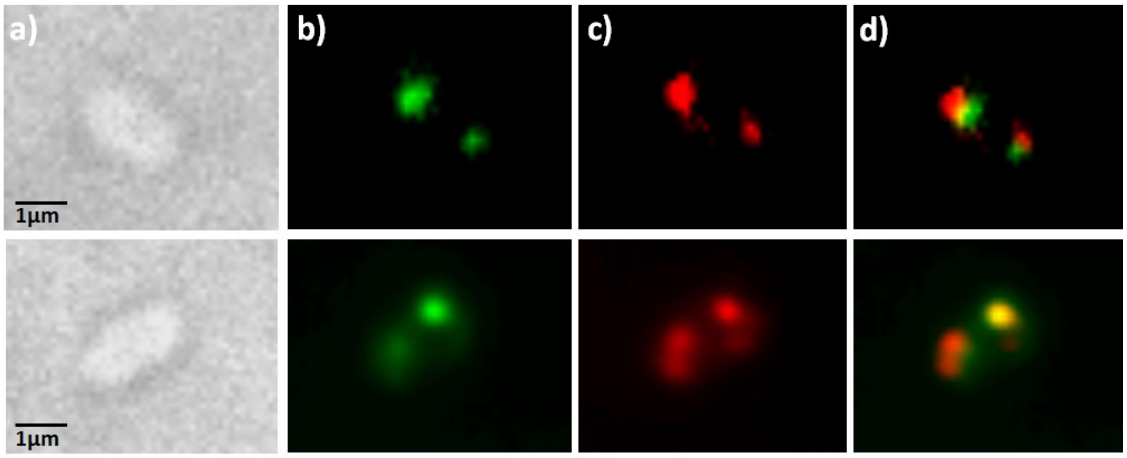

Figure 7.4: Colocalisation of $CheY_6$(A134C)-Atto647 with $CheW_4$ in two different electroporated cells (top and bottom rows): **a)** Bright-field image of the cell of interest in inverted colours; **b)** Position of the cytoplasmic cluster(s) as indicated by $CheW_4$-YFP (green, average over 4000 frames); **c)** Average position of $CheY_6$-Atto647 over 4000 frames (red); **d)** Overlay of the 3 channels. Total acquisition time 40 s, exposure time 10 ms, settings for YFP: 532 nm laser, 1 mW; settings for Atto647: 637 nm laser, 2.5 mW.

motor spots (in green, white arrows). It was previously shown that *R. sphaeroides* can have more than one FliM spot, especially if the cell is preparing to divide (Dr. C. W. Jones, Armitage lab, personal communication). The top right panel shows an overlay of the "preferred" $CheY_6$(A134C)-Atto647 localisations obtained by averaging all the positions occupied over 3 s of acquisition. $CheY_6$ is observed to dwell for as long as 800 ms at the top motor and 100-120 ms at the bottom motor. This difference in dwell time could be due to a diverse FliM composition of the two motors or to one of them being not a fully formed motor but only a C-ring, instead. However, in the same acquisition, $CheY_6$ is observed to also travel twice to two non-labelled regions in the right side and at the left pole of the cell, which could well be the cytoplasmic and the transmembrane clusters, respectively: it dwells 60 ms on average in both each time it travels there (see Figure 7.5). The polar chemotaxis cluster contains $CheA_2$, which has been shown to phosphorylate all six of the *R. sphaeroides* CheYs and both CheBs *in vitro*[151,155]. In contrast, the cytoplasmic chemotaxis cluster contains the atypical kinase formed by $CheA_3$ and

$CheA_4$, which can only phosphotransfer to $CheY_1$, $CheY_6$, and $CheB_2$. As already mentioned, phosphosignaling from both clusters has been shown to be essential for chemotaxis[143]. When $CheA_3$ or $CheA_4$ are inactivated or deleted without a concurrent $CheY_6$ mutation, smooth swimming results. This suggests strongly that the polar cluster cannot phosphorylate $CheY_6$ at physiologically relevant rates, at least during steady state swimming (Dr. J. A. de Beyer, personal communication). However, single $CheY_6$ molecules could still interact with the polar cluster to be phosphorylated by $CheA_2$.

In the example cell reported in Figure 7.6, the FliM-YPet spot at mid-cell (white arrow) is significantly brighter than values normally found for single motors (i.e. ∼4-fold more intense); since the cell is also dividing, it is speculated that they could actually be two motors, either both fully formed or one still in formation, maybe even with extra FliM molecules around them to support the construction. In this case, again $CheY_6$ is observed to localise at the cell bottom pole, and at a lateral region on the right side that could be the cytoplasmic cluster. The dwell time at the cytoplasmic cluster also is reproducible if compared with the example reported in Figure 7.5, i.e. about 50-60 ms. The dwell time at the pole looks in this case much longer, instead, with molecules visible there for up to 10 s continuosly, but this could also be due to the presence of a higher number of internalised $CheY_6$ copies. It is interesting to notice how at t = 4.41 s, a molecule detaches from the mid-cell FliM spot and travels to a region at mid-cell which could be the cytoplasmic cluster (red arrows, t = 4.42 s), going going back to the motor after ∼50 ms. This dynamic behaviour could be explained by the fact that the half life of spontaneous $CheY_6$-P autodephosphorylation is 4 s, compared to 14 s in *E. coli*[70]. $CheY_6$ could therefore be leaving FliM due to loss of its phosphoryl group, travel to the cytoplasmic $CheA_3A_4$ kinase complex to be re-phosphorylated, then move to the flagellar motor once again. Finally, in the example cell reported in Figure 7.7, only two $CheY_6$ molecules were internalised. Again, here the cell is dividing and the FliM-YPet spot

at mid-cell (white arrow) has an elongated shape, which could be consistent with the presence of two motors slightly spaced from each other but not enough to be optically resolved. The dwell times are reproducible here, as well: about 600 ms for the motor spot and ∼60 ms for the receptor cluster (average of two dwells at different times in the acquisition).

7.3.4 Discussion

The components of both the polar and cytoplasmic chemosensory clusters are required for a wild type chemotactic response in *R. sphaeroides*[70]. Cells must integrate the signals generated by these clusters to produce an appropriate balanced response to the sensory stimuli. A phosphorelay mechanism has been suggested in an ordinary differential equation (ODE) mathematical model[292]: cytoplasmic $CheA_3$ phosphorylates $CheB_2$, and $CheB_2$-P then phosphorylates polar $CheA_2$. $CheA_2$-P can subsequently phosphorylate any of its cognate response regulators, using the phosphoryl group originating from the cytoplasmic cluster (Figure 1.11). It has been shown that $CheY_6$ can be phosphorylated by both $CheA_3$-P and $CheA_2$-P *in vitro*, but the former takes place with a significantly higher rate than the latter. Despite phosphotransfer from $CheA_3$-P and $CheA_2$-P and dephosphorylation rates for $CheY_6$ have been estimated[143,151], to the authors' best knowledge, the values of the dissociation constants for *R. sphaeroides* Che proteins have not been measured. If the range reported in *E. coli* chemotaxis literature for K_D of CheY from CheA of 2-7 μM[263,293] is adopted to denote the dissociation constants between ligands and active transmembrane and cytoplasmic receptors in *R. sphaeroides*, as done in 294, then the dwell times of 60-80 ms at both the different types of receptor clusters measured in the experiments described above are of the expected order of magnitude, giving good indication that the values found in *E. coli* are valid for *R. sphaeroides*, too (see Table 7.2). Dwell times τ were calculated using the relation $k_{off}=\frac{1}{\tau}$ and

$K_D = \frac{k_{off}}{k_{on}}$, with diffusion-limited k_{on} = (4 x 10^6) $M^{-1}s^{-1}$. Furthermore, single-

	E. coli	*R. sphaeroides*
$< \tau_{\text{motor}} >$ [ms]	60	600
$K_{D,\text{ motor}}$ [μM]	4	0.4
$< \tau_{\text{cluster}} >$ [ms]	60-80	60-80
$K_{D,\text{ cluster}}$ [μM]	2-7	3-4

Table 7.2: Comparison between experimentally measured kinetic constants for the *R. sphaeroides* $CheY_6$ Cysteine mutant used in this work and those found in the literature for *E. coli*[263]. K_D values for the motor and the chemoreceptor clusters in both species were calculated assuming a diffusion-limited k_{on} = (4 x 10^6) $M^{-1}s^{-1}$.

molecule microscopy results reported in this section support the hypothesis that *R. sphaeroides* $CheY_6$ interacts with the flagellar motor, this being the first indication of such interaction *in vivo*. Interestingly enough, the average dwell time of $CheY_6$ at the motor spots indicated by FliM-YPet resulted of the same magnitude of the mean stop length measured in wild type *R. sphaeroides* cells via rotation of 0.83 μm beads on flagellar stubs (0.66 $\pm$ 1.01 s)[71] (see also Table 7.1). However, if the same diffusion-limited k_{on} as above is assumed, such dwell times at the motor yield a $K_D \sim 0.4$ μM, which is about 10-fold smaller than the value commonly found in the literature for CheY's affinity to the *E. coli* motor *in vivo*[263](see Table 7.2). Further statistics would be required to validate these preliminary results. Electroporating $CheY_6$ in *R. sphaeroides* containing FP-tagged $CheA_3$ and FliM would be then the next step to confirm that $CheY_6$'s function is indeed to transduce signals from the cytoplasmic cluster(s) to the flagellar motor(s). It would also be interesting to further investigate $CheY_6$ suggested interaction with the polar cluster via a FP-tagged $CheA_2$ or $CheW_3$.

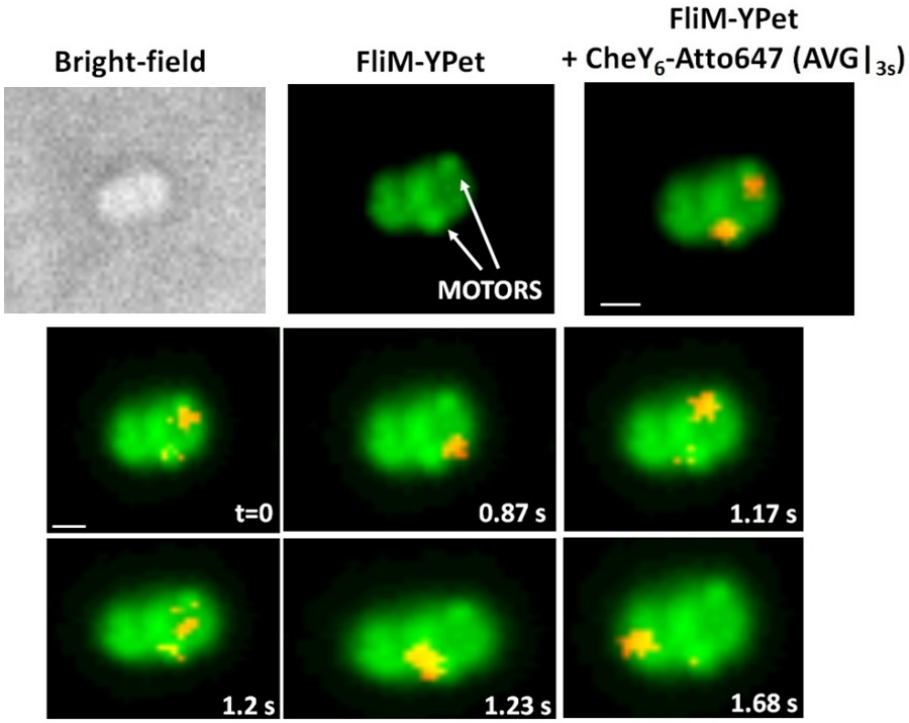

Figure 7.5: Frames from two-colours fluorescence video microscopy showing single molecules diffusing/binding inside an electrocompetent *R. sphaeroides* JPA1674 (FliM-YPet) cell electroporated with 10 nM $CheY_6$(A134C)-Atto647: in the top row, an image of the cell in bright-field (contrast adjusted), in the YPet fluorescence channel (green) with motors indicated by white arrows and an overlay of the "preferred" $CheY_6$(A134C)-Atto647 localisations obtained by averaging all the positions occupied over 3 s of acquisition (red) are shown. After dwelling at the top motor for ∼780 ms, a $CheY_6$ molecule moves to a side region which could correspond to a cytoplasmic cluster; it then moves back to the top motor only to travel after only 30 ms to the bottom motor (t = 1.23 s) where it dwells for 120 ms; from here, the molecule then spends ∼40 ms at the left pole of the cell, where the polar cluster might be. Dwellings at the polar and at the lateral regions are repeated once again after the frames shown in Figure, with a dwell time of 80 ms (at t = 2.48 s) and 60 ms (at t = 2.9 s), respectively. Total acquisition time 40 s, exposure time 10 ms, settings for YPet: 532 nm laser, 1 mW; settings for Atto647: 637 nm laser, 2.5 mW. Scale bars = 1 μm. (3s-substack of full video found on USB stick, *CheY6coloc1* movie (60 fps)).

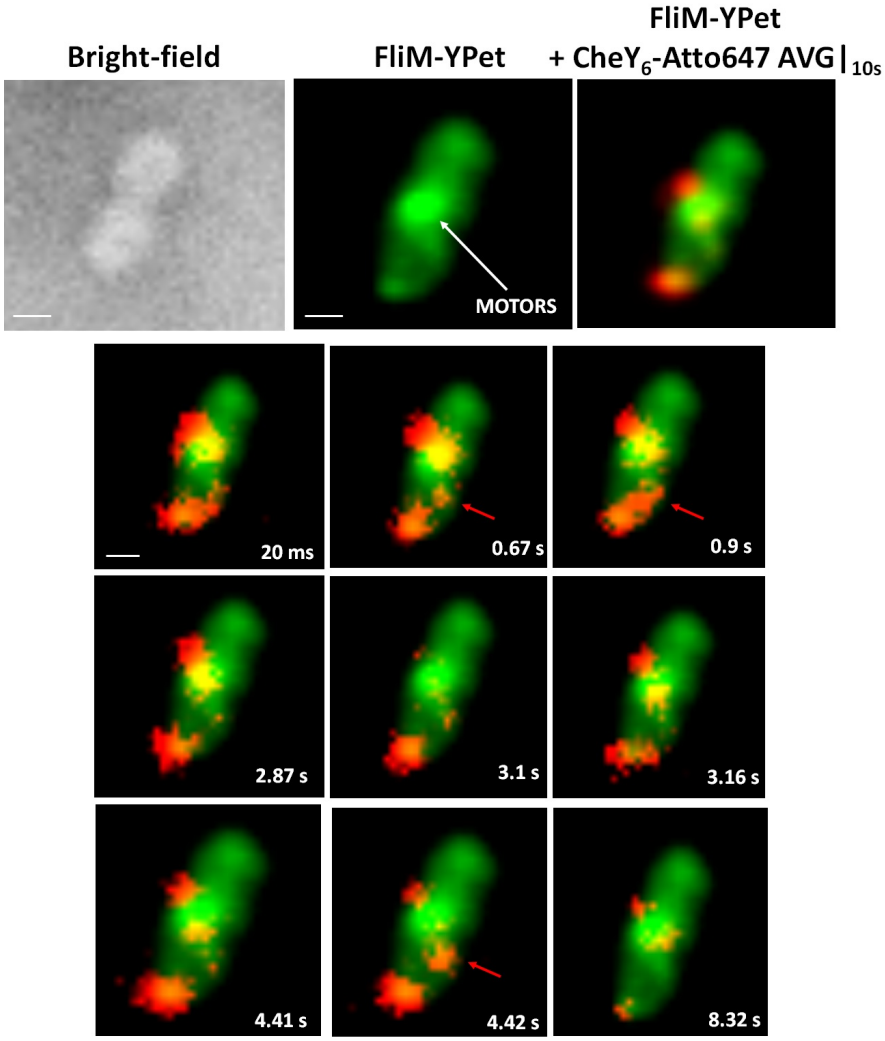

Figure 7.6: Frames from two-colours fluorescence video microscopy showing single molecules diffusing/binding inside an electrocompetent *R. sphaeroides* JPA1674 (FliM-YPet) cell electroporated with 10 nM $CheY_6$(A134C)-Atto647: in the top row, an image of the cell in bright-field (contrast adjusted), in the YPet fluorescence channel (green) with motor(s) indicated by white arrows and an overlay of the "preferred" $CheY_6$(A134C)-Atto647 localisations obtained by averaging all the positions occupied over 10 s of acquisition (red) are shown. Continuously for the first 2.2 s, two or more $CheY_6$ molecules are observed dwelling at the motor spot (indicated by the white arrow) and several at the bottom pole; at t = 0.67 s, a molecule travels from the pole to a non-labelled lateral region which could correspond to a cytoplasmic cluster, dwelling there for ∼50 ms (red arrow) to then go back where it came from; dwelling events in the same side location happen again at t = 0.9 s, with the molecule staying there for ∼60 ms and then going back to the bottom pole, and at t = 4.42 s, with the molecule this time coming from the mid-cell FliM spot in the previous frame (t = 4.41 s) and going back to it after ∼50 ms (red arrows); at t = 2.5 s two molecules reappear at the mid-cell motor(s) this time for 600 ms, simultaneously disappearing at t = 3.1 s; these (or other) two molecules come back one last time at t = 3.16 s and stay alternatively in one or two until bleaching at about 10 s of acquisition (frame at t = 8.32 s shown). Total acquisition time 40 s, exposure time 10 ms, settings for YPet: 532 nm laser, 1 mW; settings for Atto647: 637 nm laser, 2.5 mW. Scale bars = 1 μm. (10s-substack of full video found on USB stick, *CheY6coloc2* movie (60 fps)).

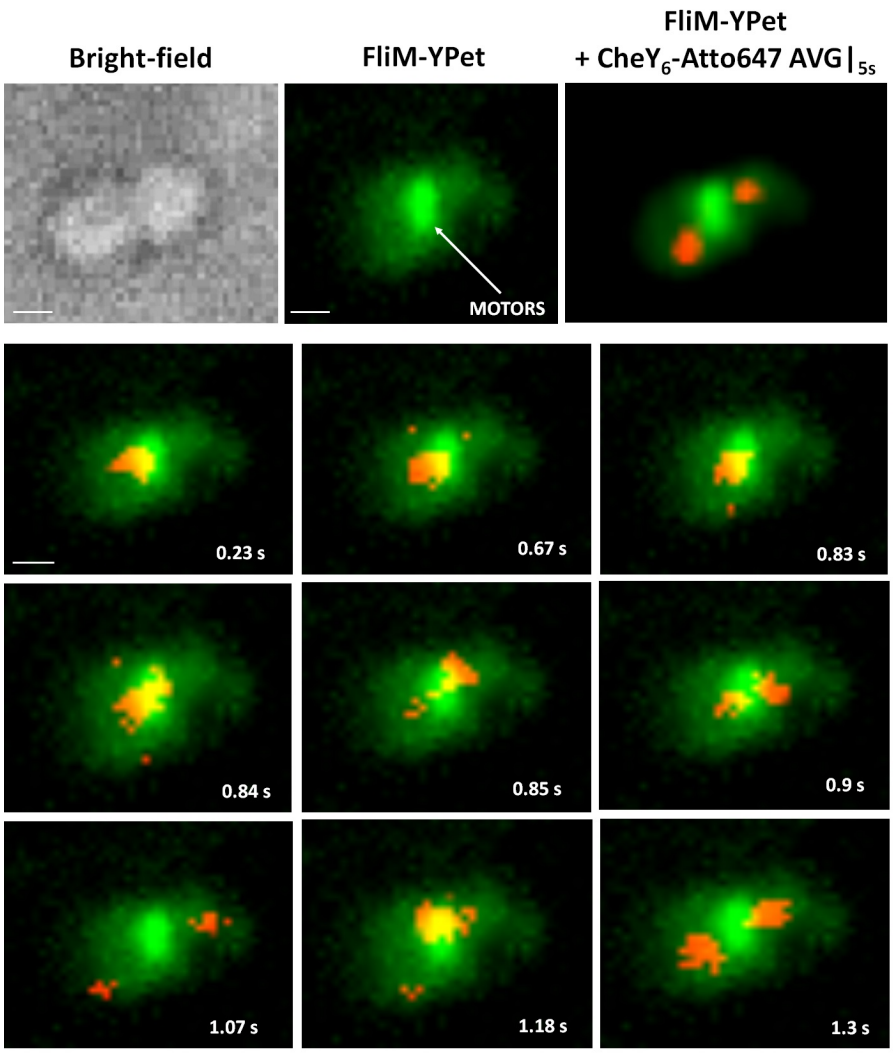

Figure 7.7: Frames from two-colours fluorescence video microscopy showing single molecules diffusing/binding inside an electrocompetent *R. sphaeroides* JPA1674 (FliM-YPet) cell electroporated with 5 nM $CheY_6$(A134C)-Atto647: in the top row, an image of the cell in bright-field (contrast adjusted), in the YPet fluorescence channel (green) with motor(s) indicated by white arrows and an overlay of the "preferred" $CheY_6$(A134C)-Atto647 localisations obtained by averaging all the positions occupied over 5 s of acquisition (red) are shown. A single $CheY_6$ molecule dwells on the left side of the elongated FliM-YPet focus for ∼600 ms, to then travel across it to its right side (t = 0.84-0.85 s) and stays there for ∼100 ms. The same molecule performs such exchange other two times during the acquisition. At t = 0.9 s, a second molecule adds up at the motor(s): its face-to-face position with the previous molecule supports the existence of two motors or C-rings in the mid-cell FliM-YPet focus. After parting at t = 1 s to travel towards two diagonally placed regions, one in the mother cell and one in the daughter cell, to probably interact with cytoplasmic or polar clusters, the two molecules join again at the motor spot. The same cycle is then once again repeated, with a similar characteristic time (∼65 ms in average). Total acquisition time 40 s, exposure time 10 ms, settings for YPet: 532 nm laser, 1 mW; settings for Atto647: 637 nm laser, 2.5 mW. Scale bars = 1 μm. (5s-substack of full video found on USB stick, *CheY6coloc3* movie (60 fps)).

Chapter 8

General Conclusions

As already stated in section 1.5, the aims of the work presented in this thesis were two: firstly, to establish a suitable procedure to apply the electroporation technique to the study of chemotaxis proteins in bacteria; secondly, to exploit such technique to elucidate the interactions of *E. coli* CheY and *R. sphaeroides* $CheY_6$ with the bacterial flagellar motor in order to further understand the switching mechanism and the chemotactic response. This chapter summarises the major results obtained and discusses prospects for further investigations.

8.1 Viability

Studies of cell viability upon electroporation showed that, upon recovery in rich medium, up to 68% of the *E. coli* cells resumed growth/division within one hour from electroporation, and 20% stay intact but not growing, a sort of frozen state in which, despite lack of growth/division, motility and chemotaxis are unaffected. No correlation was found between uptake of fluorescent molecules and cell viability, with loaded cells still largely viable upon internalisation of hundreds of proteins. Thanks to the damage-minimising protocols developed for both preparation of electrocom-

petent cells and electroporation, described in section 3.4, it was possible to increase with respect to previous values reported in the literature[219] both the proportion of loaded cells which could grow/divide after electroporation (38% vs 11%) and of cells remaining intact but not growing up to 3.5 hours from application of the electric pulse (43% vs 32%).

8.2 Internalisation

In order to avoid artifacts caused by overlapping spots in single-molecule experiments, the initial incubating concentration of labelled proteins was tuned to yield internalisation of less than 5 molecules per cell. Brightness measurements for Atto647-(Cys)CheY reported in section 4.2 gave a unitary fluorophore intensity *in vivo* of (7000±4800) photons per second: this is a much higher value than what previously estimated for a fluorescent protein like mCherry (less than 2800 photons per second[241]), further underlining that an unprecedented high localisation precision can be achieved in single-molecule tracking by preferring the electroporation approach adopted in this thesis to fluorescent protein fusions.

8.3 Recovery of motility

Evidence for the existence of a minimum lag time between start of recovery and time when cells start spinning/swimming again after application of the electric pulse was presented in section 4.6.1. Such delay, however, was less than the time required for cells to resume growth and division, indicating that it is possible to image fluorescence from the internalised molecules and a motile phenotype at the same time in the very cells present in solution at the moment of electroporation, losing none or, in the worst case, only some of the initial signal. This is a novel and very important

result not only for investigation of the interactions between CheY and FliM in a working motor as proposed in this thesis, but also for the general application of the electroporation technique to the study of the interactions *in vivo* of a range of other chemotaxis and motility proteins. In fact, previously reported experiments involving such technique in bacteria[5,219,241] did not consider its effects on cell motility at all, and actually even used a strain (DH5α) with a demonstrated poor-motility phenotype[295].

8.4 Cell loading and motility

Cell motility upon electroporation was shown to be independent of loading in section 5.1.2, as growth/division were demonstrated to be in chapter 4.3. The interaction of single labelled CheY/$CheY_6$ molecules with FliM (and with other loci in the cell) was observed in real time in rotating tethered *E. coli* and *R. sphaeroides* recovered for a short amount of time (few minutes) (sections 5.1.3 and 7.1.1) as well as for hours in a time-lapse experiment in rich medium (sections 5.1.4 and 7.1.2).

8.5 Electroporated proteins' functionality

Good indication of general functionality of the electroporated CheY labelled proteins in *E. coli* apart from interaction with the motor was given by the two-fluorescence colocalisation studies with CheZ-CFP at the cell poles reported in section 5.3. Through a similar functionality test, the dye-labelled $CheY_6$ re-introduced in *R. sphaeroides* by electroporation was shown to localise at the cytoplasmic cluster(s) through two-fluorescence colocalisation with YFP-$CheW_4$.

8.6 Single-molecule results in *E. coli*

One of the main aims of this work was to observe and quantify the working cycle of single CheY molecules while performing their role of response regulators in live cells. This was done using three different mutants (Cys-modified CheY, CheY** and CheY(I95V)), as many genetic backgrounds (FliM-YPet, FliM-YPet, Δ*che*Z and FliM-YPet, Δ*che*A) and presence or absence of repellent (acetate). Imaging of CheY proteins in living cells had previously been performed only via FP-genetic fusions. However, this approach presents some drawbacks: first, the protein's function could be affected by the presence of big probes as GFP[136] or YFP[263]; secondly, due to the low brightness of the FPs used, it was necessary to use long exposure times, which are incompatible with fast acquisition and observation of real-time behaviour; finally, on a related note, the low amount of photons that could be collected from FPs for frame and before bleaching did not allow for a high enough localisation precision to perform a reliable, prolonged single-molecule tracking.

Furthermore, it is known that in *E. coli* CheY binds to the N-terminus of the flagellar switch protein FliM to generate clockwise flagellar rotation, but the mechanism by which CheY switches the motor to clockwise rotation is still unknown. A fundamental problem in understanding this mechanism is the apparent discrepancy between cooperativity of clockwise generation and non-cooperative CheY binding to FliM, hence the rationale for quantifying the kinetics of individual CheY proteins at the switch.

In this work, single CheY molecules labelled with a small organic dye of choice were detected and tracked in their journey between the receptor clusters and the motors, via diffusion through the cytoplasm, in live cells with up to 10 ms temporal resolution and up to 40 s. Binding kinetics to the motor as well as diffusion between them, in different background strains and in the presence and absence of chemotactic stimuli were quantified. While the values found for the coefficient of freely diffusing

molecules reflected those previously reported in the literature ($\sim$4 μm^2/s)[136], something interesting was discovered with regard to the interaction between CheY and FliM. In fact, long dwell times at the motor were measured, in some cases >1 s: these are not compatible with the dissociation constant to FliM commonly reported in the literature for *E. coli* CheY of 3.7 μM[263], which would yield an average dwell time of CheY at the motor of $\sim$60-70 ms. Recent evidence has been brought forward that $FliM_N$ is not essential for phosphorylation- and acetylation-mediated clockwise generation, chemotactic responsiveness, and switch modulation (*Afanzar, Di Paolo et al*, in submission). Furthermore, the hypothesis that clockwise rotation is generated by the cooperative binding of CheY to secondary low-affinity sites in the switch has been proposed. The function of $FliM_N$ would be to generate high enough CheY concentration near the low-affinity sites, thereby compensating for their low affinity. The long dwell times measured in this work support the existence of a secondary binding site for CheY on either $FliM_M$ or FliN, which would be responsible for post-binding cooperativity and motor switching.

Finally, FliM proteins localised at motor spots in the cell were observed to disperse in the cytoplasm over time upon addition of acetate (see section 6.6.2): a possible explanation is that acetylated CheY removes FliM from the C-ring by binding to its oligomerisation interface and mobilises it in the cytoplasm.

8.7 Single-molecule results in *R. sphaeroides*

The rationale for extending the electroporation technique to *R. sphaeroides* is that the interaction of $CheY_6$ with the motor had never previously been observed *in vivo*, nor any of the dissociation constants for *R. sphaeroides* Che proteins from the receptor clusters or the motor had been measured. In this work, a protocol for the preparation of electrocompetent, motile *R. sphaeroides* cells was developed, and suitable parameters for electroporation in this species chosen; in the light of the

findings for *E. coli*, a recovery procedure for resuming motility in electroporated *R. sphaeroides* cells was devised, as well (sections 7.1.1, 7.3.1). Single-molecule imaging of electroporated dye-labelled $CheY_6$ in live *R. sphaeroides* allowed single-molecule imaging of them with temporal resolution of 10 ms and gave the first evidence of a $CheY_6$-FliM interaction *in vivo* (section 7.3.3).

8.8 *E. coli* and *R. sphaeroides*: a comparison

- On the one hand, according to what discussed in section 7.3.4, assuming the dissociation constants between ligands and active transmembrane and cytoplasmic receptors in *R. sphaeroides* of the same range reported in *E. coli* chemotaxis literature for K_D of CheY from CheA (i.e. 2-7 μM[263,293]), then the values of 60-80 ms measured for dwell times at both types of receptor clusters in this work would suggest that the values found in *E. coli* are also valid for *R. sphaeroides*.

- On the other hand, if the same diffusion-limited k_{on} as for *E. coli* is assumed ((4×10^6) $M^{-1}s^{-1}$), the measured dwell times of $CheY_6$ at the *R. sphaeroides* motor of ∼600 ms yield a dissociation constant which is about 10-fold smaller than the value commonly found in the literature for *E. coli* CheY affinity to FliM *in vivo*[263]. This would suggest that *R. sphaeroides* $CheY_6$ binds FliM with higher affinity than its equivalent in *E. coli*. As a matter of fact, the mutations that have been shown to activate *E. coli* CheY (D13K, Y106W, I95V) did not appear to activate any of the *R. sphaeroides* CheYs, including $CheY_6$[155]. This may suggest that although the *R. sphaeroides* $CheY_6$ and *E. coli* CheY are similar in that they require phosphorylation for activation, they may differ either in the subsequent conformational change caused by that phosphorylation or in their interaction with the flagellar motor. It was also

proposed in 155 that despite being unable to stop flagellar rotation, $CheY_3$ and $CheY_4$ might still compete for binding to FliM with $CheY_6$, the only one that can stop the motor. This competition, which could be central to integrating the signals from both the cytoplasmic and polar chemoreceptor clusters, could also be a cause for enhanced $CheY_6$ affinity to FliM. In conclusion, although *E. coli* CheY is often used as a model for response regulators across different bacterial species, the key residues and the interaction mechanisms with the motor, and in particular with FliM, between this and other response regulators should not automatically be translated.

8.9 Future work

Future work will include more about optimisation of the motility recovery process and study of the internalised fluorescence degradation. For comparison, wild type and other *E. coli* CheY mutants will be observed in cells deleted for unlabelled CheY (CCW motors) or with FliG mutations (CW motors), to investigate the effect of motor rotation direction on CheY binding and test the prediction of the conformational spread model that CW rotating motors bind more CheY[296]. Since it was shown in this thesis that electroporated cells can recover a motile phenotype, binding and unbinding events will also be correlated with switching events, which will allow testing of competing switching dynamics' models. Moreover, a quantitative analysis of diffusion properties and kinetic constants as the one reported in chapter 6 for *E. coli* will be carried out in *R. sphaeroides*, too, which for lack of time could not be included in this thesis. Further applications of the described electroporation technique in either the chemotaxis field or, more broadly, in the flagellar motor field are listed below.

Chemotaxis in *R. sphaeroides*

As described in section 1.3.4, *R. sphaeroides* has two expressed chemosensory pathways, the protein components of which are physically separated: one associates with transmembrane receptors and the other as a cluster at mid-cell with soluble receptors. Both pathways are required to control the single stop-start motor. The soluble pathway controls $CheY_6$, the only protein which can stop the motor, while the membrane cluster controls $CheY_3$ and $CheY_4$, which are both required for chemotaxis. The soluble cluster is linked to $CheA_2$ and adaptation proteins $CheR_2$ and $CheB_1$, the cytoplasmic cluster to $CheA_3A_4$, $CheR_3$ and $CheB_2$. Tomography has shown that both clusters have the same architecture, while extensive molecular genetics, biophysics and mathematical models have produced two different models for the mechanisms by which the two pathways integrate to control the single motor: (1) the CheYs compete at the motor, with attractant signals from the membrane receptors increasing $CheY_3$ and $CheY_4$ binding to the motor, blocking $CheY_6$ from binding to and stopping the motor or (2) signals from the cytoplasmic cluster increase levels of $CheB_2$-P, which both diffuses to the polar cluster to phosphorylate $CheA_2$, increasing $CheY_3$- and $CheY_4$-P levels, and acts as a phosphate sink, reducing $CheY_6$-P levels. There is currently no way of distinguishing the two models *in vivo*, as both fit the physiological data. The proteins of interest could be labelled with the chosen dye and electroporated into *R. sphaeroides*; the kinetics of binding and unbinding for different CheYs at the motor with and without stimulation of either cluster could be measured, and whether $CheB_2$ can actually diffuse to and bind to the polar cluster, as assumed in model 2, could be verified directly. Through single-molecule tracking, one of the two models described above could be identified as correct, or perhaps a new one could be proposed.

Flagellar filament assembly

As explained in section 1.2.4, flagellar filaments are built at their distal end by polymerisation of FliC exported through the growing filament by a Type-3 export system. The mechanism of protein secretion through the T3SS of the bacterial flagellar motor is controversial. Proteins are known to be delivered partially unfolded to the export apparatus and the unfolded protein to move down the central channel in the filament or needle. There are two different theories for the mechanism of transport through the filament channel, either diffusion or active head-to-tail transport driven by polymerisation at the growing tip. Thanks to the new electroporation technique, single-molecule tracking of dye-labelled FliC could be attempted. The dye is small, and therefore should not interfere with transport. Single labelled molecules could be visualised running down needles or helical filaments away from any background cell fluorescence. Their trajectories could provide a direct test of diffusive vs distal polymerisation chain models in the two related systems.

Protein exchange

Using fusion proteins, it has been shown that FliM and FliN in the rotor exchange in and out of the motor on a timescale of 30 s. Single-molecule tracking of electroporated proteins labelled with organic dyes will allow measurement of the individual dwell times of molecules both in and out of motors. Moreover, both FliM and FliN show differences in numbers associated with the core complex or differences in exchange rates under different conditions, suggesting different dwell times. This has led to suggestions that the FP fusion may change the interaction of the proteins in different conformations. It will be possible to address these questions directly using stable organic dyes on fully functional proteins.

Molecular crowding

It has recently become clear not only that the cytoplasm is extremely crowded, but that its physical state can change in response to growth state and conditions. It is very unclear whether the changing structures are homogenous or contain regions of lesser and greater fluidity, and also whether the charge of diffusing proteins alters their diffusive behaviour. As discussed in section 7.2, *R. sphaeroides* growing in low light photoheterotrophically is full of chromatophores, small membrane vesicles containing the photosynthetic system. Interestingly, aerobic and photoheterotrophic cells showed different sensitivity to chemosensory signals, perhaps indicating an effect on numbers of CheYs reaching the motor in a given time. Electroporating CheY in both will allow the true diffusion rate of CheY and the effect of large numbers of physical barriers to that diffusion to be measured.

Appendix A

Media and Solutions

Growth media

Luria-Bertani Broth (LB)

Ingredient	Quantity per litre
Yeast extract	5 g
Tryptone	10 g
NaCl	5 g

Made up to 1 litre with MilliQ water. Adjusted to pH 7.0. Autoclaved.

LB agar

Ingredient	Quantity per litre
Agar	16 g
Yeast extract	5 g
Tryptone	10 g
NaCl	5 g

Made up to 1 litre with MilliQ water. Adjusted to pH 7.0. Autoclaved.

Tryptone broth

Ingredient	Quantity per litre
Tryptone	10 g
NaCl	10 g

Made up to 1 litre with MilliQ water. pH adjusted to 7.0. Autoclaved.

2 x TY

Ingredient	Quantity per litre
Yeast extract	10 g
Tryptone	16 g
NaCl	5 g

Made up to 1 litre with MilliQ water. pH adjusted to 7.0. Autoclaved.

Succinate media

Ingredient	Quantity per litre
1M Phosphate buffer pH 7.0	20ml
Concentrated base (see below)	20ml
Growth factors (see below)	2ml
$(NH_4)_2$ SO_4	0.5g
NaCl	0.5g
Sodium succinate	2g
Casamino acids	1g

Made up to 1 litre with MilliQ water, pH adjusted to 7.2 with KOH, autoclaved.

SOC

Ingredient	Concentration
Glucose	20 mM
$MgCl_2$	10 mM
$MgSO_4$	10 mM
NaCl	10 mM
KCl	2.5 mM
Tryptone	20 g/l
Yeast extract	5 g/l

Autoclaved.

Buffers and solutions

Protein Purification - Lysis buffer

Ingredient	Quantity per litre
100% Glycerol	100 ml (10% final concentration)
1M Tris (pH 8.0)	50 ml
5M NaCl	30 ml
Imidazole	1.7 g (25 mM final concentration)

Made up to 1 litre with MilliQ water, pH adjusted to 8.0 using concentrated HCl.
Autoclaved.

Protein Purification - Elution Buffer

Ingredient	Quantity per litre
100% Glycerol	100 ml (10% final concentration)
1M Tris (pH 8.0)	50 ml
5M NaCl	30 ml
Imidazole	34 g (500 mM final concentration)

Made up to 1 litre with MilliQ water, pH adjusted to 8.0 using concentrated HCl.
Autoclaved.

Labelling Buffer

Ingredient	Concentration (mM))
Tris-HCl	50
NaCl	150
TCEP	0.1

Made up to 1 litre with MilliQ water, pH = 6.8 at RT (7.4 at 4°C). 0.45 μm -filtered and degassed.

Electroporation Buffer

Ingredient	Concentration (mM))
Tris-HCl	50
NaCl	25
TCEP	0.1

Made up to 1 litre with MilliQ water, pH = 7.5 at RT. 0.45 μm -filtered and degassed.

Motility Buffer -NaCl

Ingredient	Quantity (ml))
1M K2HPO4	6.2
1M KH2PO4	3.8
10mM EDTA	5

Made up to 1 litre with MilliQ water, pH = 7.0. Autoclaved and 0.45 μm -filter sterilised.

5 x DNA loading dye

Ingredient	Quantity (W/v)
Glycerol	70%
Bromophenol blue	0.25%
Xylene cyanol	0.25%
MilliQ water	29.5%

2 x non-stained SDS protein loading dye

250mM Tris, pH 6.8, 2

Ingredient	Quantity (W/v)
100% Glycerol	20%
Tris-HCl	250mM
SDS	2%
DTT	1mM

Made up to 1.5 ml with MilliQ water, pH = 7.5 at RT. 0.45 μm -filtered.

SDS-PAGE 1 x running buffer

1x Running Buffer 188g Glycine 30.2g Tris Base 100ml 1010L MilliQ Water

Ingredient	Quantity
Glycine	188 g
Tris-HCl	250mM
SDS	2%
DTT	1mM

10 x TBE

Ingredient	Quantity
TRIS base	108 g
Boric acid	55 g
EDTA pH 8.0	7.4 g

Made up to 1 litre with MilliQ water. pH adjusted to pH 8.3.

TFB I

Ingredient	Concentration
Potassiun acetate	30 mM
$RbCl_2$	100 mM
$CaCl_2$ $2H_2O$	10mM
$MnCl_2$ $4H_2O$	50 mM
Glycerol	15% (v/v)

TFB II

Ingredient	Concentration
PIPES	10 mM
$CaCl_2$ $2H_2O$	75mM
$RbCl_2$	10 mM
Glycerol	15 % (v/v)

Adjust pH to 6.8 with HCl. Filter sterilise.

GYT medium

Ingredient	Concentration
100% Glycerol	10% (v/v)
Yeast Extract	0.125% (w/v)
Tryptone	0.25% (w/v)

Sterilised by passing it through a prerinsed 0.22 μm filter. Stored in 1 ml aliquots at 4°C .

Appendix B

Primers

Name	Sequence (5' - 3')	Comments
pQE60-YNC-F	CATATCACATGTGTGC GGATAAAGAACTTAA	Forward primer used for cloning of WT CheY, N terminal Cys-CheY and Cys-CheY**
pQE60-YNC-R	GATATGAGATCTCATG CCCAGTTTCTC	Reverse primer used for cloning of WT CheY, N terminal Cys-CheY and Cys-CheY**
pQE60-YCC-F	CATATCCCATGGCGGA TAAAGAACTTAA	Forward primer used for cloning of C terminal Cys-CheY and Cys-CheY**
pQE60-YCC-R	GATATGAGATCTACAC ATGCCCAGTTTCTC	Reverse primer used for cloning of C terminal Cys-CheY and Cys-CheY**
pFloat-YNC-His-F	GAAGGAGATATACATA TGTGCGCGGATAAAG AACTTAAATTTTTG	Forward primer used for cloning of N terminal Cys-CheY with C terminal His-tag
pFloat-YNC-His-R	GGAACAGAACTTCCAG CATGCCCAGTTTCTCA AAGATTTTG	Reverse primer used for cloning of N terminal Cys-CheY with C terminal His-tag
pFloat-TAG-amp-fwd	GAGATCCGGCTGCTAA CAAAGCC	Forward primer used for cloning of N terminal Cys-CheY with N terminal SUMO-tag
pFloat-TAG-amp-rev	GGGCCCCTGGAACAGA ACTTCC	Reverse primer used for cloning of N terminal Cys-CheY with N terminal SUMO-tag
pQE80-Y6(A134C)-F	CGGACGCTGATGGCCT GCTGAAAGCTTAATTAG	Forward primer used for cloning of C terminal Cys-CheY$_6$
pQE80-Y6(A134C)-R	CTAATTAAGCTTTCAGC AGGCCATCAGCGTCCG	Reverse primer used for cloning of C terminal Cys-CheY$_6$

Bibliography

1. Sowa Y., Berry R.M. Bacterial flagellar motor. *Quarterly Reviews of Biophysics* **41**, 103–132 (2008). URL http://www.ncbi.nlm.nih.gov/pubmed/18812014.

2. M.A.B. Baker, Berry R.M. An introduction to the physics of the bacterial flagellar motor: a nanoscale rotary electric motor. *Contemporary Physics* **50**, 617–632 (2009). URL http://www.researchgate.net/publication/253922287_An_introduction_to_the_physics_of_the_bacterial_flagellar_motor_A_nanoscale_rotary_electric_motor.

3. Chen S., Beeby M., Murphy G.E., Leadbetter J.R., Hendrixson D.R., Briegel A., Li Z., Shi J., Tocheva E.I., Mller A., Dobro M.J. and Jensen G.J. Structural diversity of bacterial flagellar motors. *The EMBO Journal* **30**, 2972–81 (2011). URL http://www.ncbi.nlm.nih.gov/pubmed/21673657.

4. Diepold A., Kudryashev M., Delalez N.J., Berry R.M. and Armitage J.P. Composition, formation, and regulation of the cytosolic C-ring, a dynamic component of the Type III secretion injectisome. *PLoS Biology* **13**, e1002039 (2015). URL http://journals.plos.org/plosbiology/article?id=10.1371/journal.pbio.1002039.

5. Crawford R., Torella J.P., Aigrain L., Plochowietz A., Gryte K., Uphoff S. and Kapanidis A.N. Long-lived intracellular single-molecule fluorescence using electroporated molecules. *Biophysical Journal* **105**, 2439–50 (2013). URL http://www.ncbi.nlm.nih.gov/pubmed/24314075.

6. Ulrich L.E. and Zhulin I.B. The MiST2 database: a comprehensive genomics resource on microbial signal transduction. *Nucleic Acids Research* **38**, D401D407 (2010). URL http://www.ncbi.nlm.nih.gov/pmc/articles/PMC2808908/.

7. Jarrell K.F. and McBride M.J. The surprisingly diverse ways that prokaryotes move. *Nature Reviews Microbiology* **6**, 466–476 (2008). URL http://www.nature.com/nrmicro/journal/v6/n6/execsumm/nrmicro1900.html.

8. Burchard R.P. Gliding motility of prokaryotes: ultrastructure, physiology, and genetics. *Annual Review of Microbiology* **35**, 497–529 (1981). URL http://www.annualreviews.org/doi/abs/10.1146/annurev.mi.35.100181.002433.

9. McBride M.J. and Nakane D. *Flavobacterium* gliding motility and the type IX secretion system. *Current Opinion in Microbiology* **28**, 72–77 (2015). URL http://www.sciencedirect.com/science/article/pii/S1369527415001332.

10. Miyata M. and Hamaguchi T. Reprint of Prospects for the gliding mechanism of *Mycoplasma mobile*. *Current Opinion in Microbiology* **28**, 122–128 (2015). URL http://www.sciencedirect.com/science/article/pii/S1369527415001733.

11. Wolgemuth C., Hoiczyk E., Kaiser D. and Oster G. How *myxobacteria* glide. *Current Biology* **12**, R369–77 (2002). URL http://www.ncbi.nlm.nih.gov/pubmed/11882287.

12. Nan B., McBride M.J., Chen J., Zusman D.R. and Oster G. Bacteria that glide with helical tracks. *Current Biology* **24**, R169R173 (2014). URL http://www.ncbi.nlm.nih.gov/pmc/articles/PMC3964879/.

13. Mattick J.S. Type IV pili and twitching motility. *Annual Review of Microbiology* **56**, 289314 (2002). URL http://www.ncbi.nlm.nih.gov/pubmed/12142488.

14. Duggan P.S., Gottardello P. and Adams D.G. Molecular analysis of genes in *Nostoc punctiforme* involved in pilus biogenesis and plant infection. *Journal of Bacteriology* **189**, 4547–4551 (2007). URL http://www.ncbi.nlm.nih.gov/pmc/articles/PMC1913353/.

15. Varga J.J., Nguyen V., O'Brien D.K., Rodgers K., Walker R.A., Melville S.B. Type IV pili-dependent gliding motility in the Gram-positive pathogen *Clostridium perfringens* and other *Clostridia*. *Molecular Microbiology* **62**, 680–694 (2006). URL http://www.ncbi.nlm.nih.gov/pubmed/16999833.

16. Flagella. *Wikimedia Commons* (2007). URL https://en.wikipedia.org/wiki/File:Flagella.svg.

17. Bardy S.L., Ng S.Y.M. and Jarrell K.F. Prokaryotic motility structures. *Microbiology* **149**, 295–304 (2003). URL http://www.ncbi.nlm.nih.gov/pubmed/12624192.

18. Berg H.C. Bacterial flagellar motor. *Current Biology* **18**, R689–R691 (2008). URL http://www.sciencedirect.com/science/article/pii/S0960982208008816.

19. Lowe G., Meister M. and Berg H.C. Rapid rotation of flagellar bundles in swimming bacteria. *Nature* **325**, 637–640 (1987). URL http://www.nature.com/nature/journal/v325/n6105/abs/325637a0.html.

20. Lambert C. Evans K.J., Till R., Hobley L., Capeness M., Rendulic S., Schuster S.C., Aizawa S., Sockett R.E. Characterizing the flagellar filament and the role of motility in bacterial prey-penetration by *Bdellovibrio bacteriovorus*. *Molecular Microbiology* **60**, 274–286 (2006). URL http://www.ncbi.nlm.nih.gov/pubmed/16573680.

21. Aldridge P. and Hughes K.T. Regulation of flagellar assembly. *Current Opinion in Microbiology* **5**, 160–165 (2002). URL http://www.ncbi.nlm.nih.gov/pubmed/11934612.

22. Francis N.R., Sosinsky G.E., Thomas D. and Derosier D.J. Isolation, characterization and structure of bacterial flagellar motors containing the switch complex. *Journal of Molecular Biology* **235**, 1261–1270 (1994). URL http://www.ncbi.nlm.nih.gov/pubmed/8308888.

23. Thomas D.R. Francis N.R., Xu C., DeRosier D.J. The three-dimensional structure of the flagellar rotor from a clockwise-locked mutant of *Salmonella enterica serovar Typhimurium*. *Journal of Bacteriology* **188**, 7039–7048 (2006). URL http://www.ncbi.nlm.nih.gov/pubmed/17015643.

24. Murphy G.E., Leadbetter J.R., Jensen G.J. *In situ* structure of the complete *Treponema primitia* flagellar motor. *Journal of Bacteriology* **442**, 1062–1064 (2006). URL http://www.ncbi.nlm.nih.gov/pubmed/16885937.

25. Zhao X., Norris S.J. and Liu J. Molecular architecture of the bacterial flagellar motor in cells. *Biochemistry* **53**, 4323–4333 (2014). URL http://www.ncbi.nlm.nih.gov/pmc/articles/PMC4221660/.

26. Stock D., Namba K., Lee L.K. Nanorotors and self-assembling macromolecular machines: the torque ring of the bacterial flagellar motor. *Current Opinion in Microbiology* **23**, 545–554 (2012). URL http://www.sciencedirect.com/science/article/pii/S0958166912000201.

27. Morimoto Y.V. and Minamino T. Structure and function of the bi-directional bacterial flagellar motor. *Biomolecules* **4**, 217–234 (2014). URL http://www.mdpi.com/2218-273X/4/1/217.

28. Francis N.R., Irikura V.M., Yamaguchi S., DeRosier D.J., Macnab R.M. Localization of the *Salmonella typhimurium* flagellar switch protein FliG to the cytoplasmic M-ring face of the basal body. *Proceedings of the National Academy of Sciences* **89**, 6304–6308 (1992). URL http://www.ncbi.nlm.nih.gov/pmc/articles/PMC49489/.

29. Nakamura S., Kami-ike N., Yokota J.P., Minamino T., Namba K. Evidence for symmetry in the elementary process of bidirectional torque generation by the bacterial flagellar motor. *Proceedings of the National Academy of Sciences* **107**, 17616–17620 (2010). URL http://www.ncbi.nlm.nih.gov/pubmed/20876126.

30. Sowa Y., Rowe A.D., Leake M.C., Yakushi T., Homma M., Ishijima A. and Berry R.M. Direct observation of steps in rotation of the bacterial flagellar motor. *Nature* **437**, 916–919 (2005). URL http://www.nature.com/nature/journal/v437/n7060/abs/nature04003.html.

31. Young H.S., Dang H., Lai Y., DeRosier D.J. and Khan S. Variable symmetry in *Salmonella typhimurium* flagellar motors. *Biophysical Journal* **84**, 571–577 (2003). URL http://www.ncbi.nlm.nih.gov/pubmed/12524310.

32. Paul K., Gonzalez-Bonet G., Bilwes A.M., Crane B.R. and Blair D.F. Architecture of the flagellar rotor. *The EMBO Journal* **30**, 2962–2971 (2011). URL http://emboj.embopress.org/content/embojnl/30/14/2962.full.pdf.

33. Sato K. and Homma M. Functional reconstitution of the Na^+-driven polar flagellar motor component of *Vibrio alginolyticus*. *Journal of Biological Chemistry* **275**, 5718–5722 (2000). URL http://www.ncbi.nlm.nih.gov/pubmed/10681557.

34. Kojima S. and Blair D.F. Solubilization and purification of the MotA/MotB complex of *Escherichia coli*. *Biochemistry* **43**, 26–34 (2004). URL http://www.ncbi.nlm.nih.gov/pubmed/14705928.

35. Zhou J., Sharp L.L., Tang H.L., Lloyd S.A., Billings S., Braun T.F. and Blair D.F. Function of protonatable residues in the flagellar motor of *Escherichia coli*: A critical role for Asp 32 of MotB. *Journal of Bacteriology* **180**, 2729–2735 (1998). URL http://jb.asm.org/content/180/10/2729.short.

36. Blair D.F., Kim D.Y. and Berg H.C. Mutant MotB proteins in *Escherichia coli*. *Journal of Bacteriology* **173**, 4049–4055 (1991). URL http://www.ncbi.nlm.nih.gov/pubmed/2061285.

37. Garza A.G., Biran R., Wohlschlegel J. and Manson M.D. Mutations in *motB* suppressible by changes in stator or rotor components of the bacterial flagellar motor. *Journal of Molecular Biology* **173**, 270–285 (1996). URL http://www.ncbi.nlm.nih.gov/pubmed/8627625.

38. Erhardt M., Namba K., Hughes K.T. Bacterial nanomachines: the flagellum and type III injectisome. *Cold Spring Harbor Perspectives Biology* (2010). URL http://www.ncbi.nlm.nih.gov/pmc/articles/PMC2964186/.

39. Macnab R.M. Type III flagellar protein export and flagellar assembly. *Biochimica et Biophysica Acta* **1694**, 207–217 (2004). URL http://www.ncbi.nlm.nih.gov/pubmed/15546667.

40. Homma M., Komeda Y., Iino T. and Macnab R.M. The flaFIX gene product of *Salmonella typhimurium* is a flagellar basal body component with a signal peptide for export. *Journal of Bacteriology* **169**, 1493–1498 (1987). URL http://www.ncbi.nlm.nih.gov/pmc/articles/PMC211974/.

41. Jones C.J. and Macnab R.M. Flagellar assembly in *Salmonella typhimurium*: analysis with temperature-sensitive mutants. *Journal of Bacteriology* **172**, 1327–39 (1990). URL http://www.ncbi.nlm.nih.gov/pubmed/2407720/.

42. Homma M., Fujita H., Yamaguchi S. and Iino T. Excretion of unassembled flagellin by *Salmonella typhimurium* mutants defective in hook associated proteins. *Journal of Bacteriology* **159**, 1056–1059 (1984). URL http://www.ncbi.nlm.nih.gov/pubmed/6384179.

43. Homma M., Kuksukake K. and Iino T. Structural genes for flagellar hook associated proteins in *Salmonella typhimurium*. *Journal of Bacteriology* **163**, 464–471 (1985). URL http://www.ncbi.nlm.nih.gov/pubmed/2991190.

44. Samatey F.A., Imada K., Nagashima S., Vonderviszt F., Kumasaka T., Yamamoto M. and Namba K. Structure of the bacterial flagellar protofilament and implications for a switch for supercoiling. *Nature* **410**, 331–337 (2001). URL http://www.nature.com/nature/journal/v410/n6826/full/410331a0.html.

45. Yonekura K., Maki S., Morgan D.G., DeRosier D.J., Vonderviszt F., Imada K. and Namba K. The bacterial flagellar cap as the rotary promoter of flagellin self-assembly. *Science* **290**, 2148–2152 (2000). URL http://www.ncbi.nlm.nih.gov/pubmed/11118149.

46. Minamino T., Morimoto Y.V., Kinoshita M., Aldridge P.D. and Namba K. The bacterial flagellar protein export apparatus processively transports flagellar proteins even with extremely infrequent ATP hydrolysis. *Scientific Reports* **4** (2014). URL http://www.nature.com/articles/srep07579.

47. Bai F., Morimoto Y.V., Yoshimura S.D.J., Hara N., Kami-ike N., Namba K. and Minamino T. Assembly dynamics and the roles of FliI ATPase of the bacterial flagellar export apparatus. *Scientific Reports* **4** (2014). URL http://www.nature.com/articles/srep06528#f5.

48. Journet L., Agrain C., Broz P. and Cornelis G.R. The needle length of bacterial injectisomes is determined by a molecular ruler. *Science* **302**, 1757–1760 (2003). URL http://www.ncbi.nlm.nih.gov/pubmed/14657497.

49. Waters R.C., OToole P.W. and Ryan, K.A. The FliK protein and flagellar hook-length control. *Protein Science* **16**, 769–780 (2007). URL http://www.ncbi.nlm.nih.gov/pmc/articles/PMC2206646/.

50. Shibata S., Takahashi N., Chevance F.F., Karlinsey J.E., Hughes K.T., Aizawa S. FliK regulates flagellar hook length as an internal ruler. *Molecular Microbiology* **64**, 11404–1415 (2007). URL http://www.ncbi.nlm.nih.gov/pubmed/17542929.

51. Ferris H.U. and Minamino, T. Flipping the switch: bringing order to flagellar assembly. *Trends in Microbiology* **14**, 519–526 (2006). URL http://www.ncbi.nlm.nih.gov/pubmed/17067800.

52. Ferris H.U., Furukawa Y., Minamino T., Kroetz M.B., Kihara M., Namba K. and Macnab R.M. FlhB regulates ordered export of flagellar components via autocleavage mechanism. *Journal of Biological Chemistry* **280**, 41236–41242 (2005). URL http://www.ncbi.nlm.nih.gov/pubmed/16246842.

53. Minamino T., Ferris H.U., Moriya N., Kihara M. and Namba K. Two parts of the T3S4 domain of the hook length control protein FliK are essential for the substrate specificity switching of the flagellar type III export apparatus. *Journal of Molecular Biology* **362**, 1148–1158 (2006). URL http://www.ncbi.nlm.nih.gov/pubmed/16949608.

54. Kojima S. and Blair D.F. Conformational change in the stator of the bacterial flagellar motor. *Biochemistry* **40**, 13041–13050 (2001). URL http://pubs.acs.org/doi/abs/10.1021/bi011263o.

55. Braun T.F., Khubbar M. K., Saffarini D. A. and McBride M.J. *Flavobacterium johnsoniae* gliding motility genes identified by mariner mutagenesis. *Journal of Bacteriology* **187**, 69436952 (2005). URL http://www.ncbi.nlm.nih.gov/pubmed/16199564.

56. Blair D.F. and Berg H.C. Restoration of torque in defective flagellar motors. *Science* **242**, 1678–1681 (1988). URL http://www.ncbi.nlm.nih.gov/pubmed/2849208.

57. Reid S.W., Leake M.C., Chandler J.H., Lo C.J., Armitage J.P., and Berry R.M. The maximum number of torque-generating units in the flagellar motor of *Escherichia coli* is at least 11. *Proceedings of the National Academy of Sciences* **103**, 8066–8071 (2006). URL http://www.ncbi.nlm.nih.gov/pubmed/16698936.

58. Leake M. C., Chandler J.H., Wadhams G.H., Bai F., Berry R.M. and ARMITAGE J.P. Stoichiometry and turnover in single, functioning membrane protein complexes. *Nature* **443**, 355–358 (2006). URL http://www.ncbi.nlm.nih.gov/pubmed/16971952.

59. Fukuoka H., Inouea Y., Terasawab S., Takahashia H., Ishijima A. Exchange of rotor components in functioning bacterial flagellar motor. *Biochemical and Biophysical Research Communications* **394**, 130–135 (2010). URL http://www.sciencedirect.com/science/article/pii/S0006291X10003633.

60. Berg H.C. and Brown D.A. Chemotaxis in *Escherichia coli* analysed by three-dimensional tracking. *Nature* **239**, 500–4 (1972). URL http://www.nature.com/nature/journal/v239/n5374/abs/239500a0.html.

61. Turner L., Ryu W.S. and Berg H.C. Real-time imaging of fluorescent flagellar filaments. *Journal of Bacteriology* **182**, 2793–801 (2000). URL http://www.ncbi.nlm.nih.gov/pubmed/10781548.

62. Darnton N.C., Turner L., Rojevsky S. and Berg H.C. On torque and tumbling in swimming *Escherichia coli*. *Journal of Bacteriology* **189**, 1756–64 (2007). URL http://jb.asm.org/content/189/5/1756.abstract.

63. Kim M., Bird J.C., Van Parys A.J., Breuer K.S. and Powers T.R. A macroscopic scale model of bacterial flagellar bundling. *Proceedings of the National Academy of Sciences* **100**, 15481–5 (2003). URL http://www.pnas.org/content/100/26/15481.full.

64. Kim M., Bird J.C., Van Parys A.J., Breuer K.S. and Powers T.R. Real-time imaging of fluorescent flagellar filaments of *rhizobium lupini* H13-3: flagellar rotation and pH-induced polymorphic transitions. *Journal of Bacteriology* **184**, 5979–5986 (2002). URL http://www.ncbi.nlm.nih.gov/pmc/articles/PMC135403/.

65. Calladine C.R., Luisi B.F., , Pratap J.V. A "mechanistic" explanation of the multiple helical forms adopted by bacterial flagellar filaments. *Journal of Molecular Biology* **425**, 914–928 (2013). URL http://www.sciencedirect.com/science/article/pii/S0022283612009400.

66. Block S.M., Segall J.E. and Berg H.C. Adaptation kinetics in bacterial chemotaxis. *Journal of Molecular Biology* **154**, 312–323 (1983). URL http://jb.asm.org/content/154/1/312.full.pdf+html.

67. Shah D.S.H., Porter S.L., Martin A.C., Hamblin P.A. and Armitage J.P. Fine tuning bacterial chemotaxis: analysis of R*hodobacter sphaeroides* behaviour under aerobic and anaerobic conditions by mutation of the major chemotaxis operons and *cheY* genes. *EMBO Journal* **19**, 4601–4613 (2000). URL http://www.ncbi.nlm.nih.gov/pmc/articles/PMC302075/.

68. Armitage J.P. and Macnab R.M. Unidirectional intermittent rotation of the flagellum of *Rhodobacter sphaeroides*. *Journal of Bacteriology* **169**, 514–518 (1987). URL http://www.ncbi.nlm.nih.gov/pubmed/3492489.

69. Armitage J.P., Pitta T.P., Vigeant M.A.S., Packer H.L. and Ford R.M. Transformations in flagellar structure of *Rhodobacter sphaeroides* and possible relationship to changes in swimming speed. *Journal of Bacteriology* **181**, 4825–4833 (1999). URL http://www.ncbi.nlm.nih.gov/pubmed/10438751.

70. Porter S., Wadhams G. and Armitage J.P. *Rhodobacter sphaeroides*: complexity in chemotactic signalling. *Trends in microbiology* **16**, 251–60 (2008). URL URLhttp://www.ncbi.nlm.nih.gov/pubmed/18440816.

71. Pilizota T., Brown M.T., Leake M.C., Branch R.W., Berry R.M. and Armitage J.P. A molecular brake, not a clutch, stops the *Rhodobacter sphaeroides* flagellar motor. *Proceedings*

of the National Academy of Sciences **106**, 11582–11587 (2009). URL http://www.ncbi.nlm.nih.gov/pubmed/19571004.

72. Segall J.E., Block S.M. and Berg H.C. Temporal comparisons in bacterial chemotaxis. *Proceedings of the National Academy of Sciences* **83**, 8987–8991 (1986). URL http://www.ncbi.nlm.nih.gov/pmc/articles/PMC387059/.

73. Wolgemuth C.W. Collective swimming and the dynamics of bacterial turbulence. *Biophysical Journal* **95**, 1564–1574 (2008). URL http://www.ncbi.nlm.nih.gov/pmc/articles/PMC2483759/.

74. Wadhams G.H. and Armitage J.P. Making sense of it all: bacterial chemotaxis. *Nature Reviews. Molecular Cell Biology* **5**, 1024–1037 (2004). URL http://www.nature.com/nrm/journal/v5/n12/full/nrm1524.html.

75. Berg H.C. and Brown D.A. Temporal stimulation of chemotaxis in *Escherichia coli*. *Proceedings of the National Academy of Sciences* **71**, 1388–1392 (1974). URL http://www.ncbi.nlm.nih.gov/pmc/articles/PMC388234/.

76. Berg H.C. and Tedesco P.M. Transient response to chemotactic stimuli in *Escherichia coli*. *Proceedings of the National Academy of Sciences* **72**, 3235–3239 (1975). URL http://www.pnas.org/content/72/8/3235.

77. Purcell E.M. and Berg H.C. Physics of chemoreception. *Biophysical Journal* **20**, 193–219 (1977). URL http://www.ncbi.nlm.nih.gov/pmc/articles/PMC1473391/.

78. Falke J.J., Bass R.B., Butler S.L., Chervitz S.A. and Danielson M.A. The two-component signaling pathway of bacterial chemotaxis: a molecular view of signal transduction by receptors, kinases, and adaptation enzymes. *Annual Review of Cell and Developmental Biology* **13**, 457–512 (1997). URL http://www.ncbi.nlm.nih.gov/pmc/articles/PMC2899694/.

79. Bren A. and Eisenbach M. How signals are heard during bacterial chemotaxis: protein-protein interactions in sensory signal propagation. *Journal of Bacteriology* **182**, 6865–6873 (2000). URL http://jb.asm.org/content/182/24/6865.full.

80. West A.H. and Stock A.M. Histidine kinases and response regulator proteins in two-component signaling systems. *Trends in Biochemical Sciences* **26**, 6865–6873 (2001). URL http://www.sciencedirect.com/science/article/pii/S0968000401018527.

81. Bradshaw R., Dennis E. Handbook of cell signaling, three-volume set (1st Edition). URL http://store.elsevier.com/product.jsp?lid=0&iid=5&sid=0&isbn=9780080533575.

82. Falke J.J. and Hazelbauer G.L. Transmembrane signaling in bacterial chemoreceptors. *Trends in Biochemical Sciences* **26**, 257–265 (2001). URL http://www.ncbi.nlm.nih.gov/pubmed/11295559.

83. Weis R.M. and Koshland D.E. Jr. Reversible receptor methylation is essential for normal chemotaxis of *Escherichia coli* in gradients of aspartic acid. *Proceedings of the National Academy of Sciences* **85**, 83–87 (1988). URL http://www.ncbi.nlm.nih.gov/pubmed/2829179.

84. Porter S.L., Wadhams G.H. and Armitage J.P. Signal processing in complex chemotaxis pathways. *Nature Reviews Microbiology* **9**, 153–165 (2011). URL http://www.nature.com/nrmicro/journal/v9/n3/full/nrmicro2505.html.

85. Rebbapragada A., Johnson M.S., Harding G.P., Zuccarelli A.G., Fletcher H.M., Zhulin I.B. and Taylor B.L. The Aer protein and the serine chemoreceptor Tsr independently sense intracellular energy levels and transduce oxygen, redox, and energy signals for *Escherichia coli* behavior. . *Proceedings of the National Academy of Sciences* **94**, 10541–10546 (1997). URL http://www.pnas.org/content/94/20/10541.full.

86. Bibikov S.I., Barnes L.A., Gitin Y. and Parkinson J.S. Domain organization and flavin adenine dinucleotide-binding determinants in the aerotaxis signal transducer Aer of *Escherichia coli*. *Proceedings of the National Academy of Sciences* **97**, 5830–5835 (2000). URL http://www.ncbi.nlm.nih.gov/pubmed/10811894.

87. Morrison T.B. and Parkinson J.S. A fragment liberated from the *Escherichia coli* CheA kinase that blocks stimulatory, but not inhibitory, chemoreceptor signaling. *Journal of Bacteriology* **179**, 5543–5550 (1997). URL http://www.ncbi.nlm.nih.gov/pubmed/9287011.

88. Bilwes A.M., Alex L.A., Crane B.R. and Simon M.I. Structure of CheA, a signal-transducing histidine kinase. *Cell* **96**, 131–141 (1999). URL http://www.ncbi.nlm.nih.gov/pubmed/9989504.

89. Segall J.E., Manson M.D. and Berg H.C. Signal processing times in bacterial chemotaxis. *Nature* **296**, 855–857 (1982). URL http://www.nature.com/nature/journal/v296/n5860/abs/296855a0.html.

90. Sourjik V. and Berg H.C. Localization of components of the chemotaxis machinery of *Escherichia coli* using fluorescent protein fusions. *Molecular Microbiology* **37**, 740–751 (2000). URL http://www.ncbi.nlm.nih.gov/pubmed/10972797.

91. Blat Y. and Eisenbach M. Oligomerization of the phosphatase CheZ upon interaction with the phosphorylated form of CheY. The signal protein of bacterial chemotaxis. *Journal of Biological Chemistry* **271**, 1226–1231 (1996). URL http://www.ncbi.nlm.nih.gov/pubmed/8557654.

92. Blat Y., Gillespie B., Bren A., Dahlquist F.W. and Eisenbach M. Regulation of phosphatase activity in bacterial chemotaxis. *Journal of Molecular Biology* **284**, 1191–1199 (1998). URL http://www.ncbi.nlm.nih.gov/pubmed/9837737.

93. Lipkow K. Changing Cellular Location of CheZ Predicted by Molecular Simulations. *PLoS Computational Biology* **2**, e39 (2006). URL http://journals.plos.org/ploscompbiol/article?id=10.1371/journal.pcbi.0020039.

94. Manson M.D. Transmembrane signaling is anything but rigid. *Journal of Bacteriology* **193**, 5059–5061 (2011). URL http://jb.asm.org/content/193/19/5059.full.

95. Goy M.F., Springer M.S. and Adler J. Failure of sensory adaptation in bacterial mutants that are defective in a protein methylation reaction. *Cell* **15**, 1191–1199 (1978). URL http://www.ncbi.nlm.nih.gov/pubmed/365357.

96. Yonekawa H., Hayashl H. and Parklnson J.S. Requirement of the *cheB* function for sensory adaptation in *Escherichia coli*. *Journal of Bacteriology* **156**, 1228–1235 (1983). URL http://www.ncbi.nlm.nih.gov/pmc/articles/PMC217972/.

97. Li M. and Hazelbauer G.L. Cellular stoichiometry of the components of the chemotaxis signaling complex. *Journal of Bacteriology* **186**, 3687–94 (2004). URL http://www.ncbi.nlm.nih.gov/pubmed/15175281.

98. Maddock J.R. and Shapiro L. Polar location of the chemoreceptor complex in the *Escherichia coli* cell. *Science* **259**, 1717–1723 (1993). URL http://www.ncbi.nlm.nih.gov/pubmed/8456299.

99. Kim K.K., Yokota H. and Kim S.-H. Four-helical-bundle structure of the cytoplasmic domain of a serine chemotaxis receptor. *Nature* **400**, 787–792 (1999). URL http://www.nature.com/nature/journal/v400/n6746/full/400787a0.html.

100. Briegel A., Ladinsky M.S., Oikonomou C., Jones C.W., Harris M.J., Fowler D.J., Chang Y.-W., Thompson L.K., Armitage J.P. and Jensen G.J. Structure of bacterial cytoplasmic chemoreceptor arrays and implications for chemotactic signaling. *eLife* **3**, e02151 (2014). URL http://cdn.elifesciences.org/elife-articles/02151/pdf/elife02151.pdf.

101. Studdert C.A. and Parkinson J.S. Insights into the organization and dynamics of bacterial chemoreceptor clusters through in vivo crosslinking studies. *Proceedings of the National Academy of Sciences* **102**, 15623–8 (2005). URL http://www.ncbi.nlm.nih.gov/pubmed/16230637.

102. Shimizu T.S., Le Novre N., Levin M.D., Beavil A.J., Sutton B.J. and Bray D. Molecular model of a lattice of signalling proteins involved in bacterial chemotaxis. *Nature Cell Biology* **2**, 792–796 (2000). URL http://www.nature.com/ncb/journal/v2/n11/full/ncb1100_792.html.

103. Briegel A., Ortega D.R., Tocheva E.I., Wuichet K., Lia Z., Chen S., Muller A., Iancua C.V., Murphy G.E., Dobroa M.J., Zhulin I.B. and Jensen G.J. Universal architecture of bacterial chemoreceptor arrays. *Proceedings of the National Academy of Sciences* **106**, 17181–17186 (2009). URL http://www.pnas.org/content/106/40/17181.full.pdf.

104. Bray D., Levin M.D. and Morton F.C. Receptor clustering as a cellular mechanism to control sensitivity. *Nature* **393**, 85–88 (1998). URL http://www.ncbi.nlm.nih.gov/pubmed/9590695.

105. Sanders D.A., Gillece-Castro B.L., Stock A.M., Burlingame A.L. and Koshland D.E. Identification of the site of phosphorylation of the chemotaxis response regulator protein, CheY. *Journal of Biological Chemistry* **264**, 21770–8 (1989). URL http://www.ncbi.nlm.nih.gov/pubmed/2689446.

106. Volz K., Matsumura P. Crystal structure of *Escherichia coli* CheY refined at 1.7-Å resolution. *Journal of Biological Chemistry* **266**, 15511–15519 (1991). URL http://www.ncbi.nlm.nih.gov/pubmed/1869568?dopt=Abstract.

107. Ganguli S., Wang H., Matsumura P. and Volz K. Uncoupling phosphorylation and activation in bacterial chemotaxis: the 2.1 Å structure of a threonine to isoleucine mutant at position

87 of CheY. *Journal of Biological Chemistry* **270**, 17386–17393 (1995). URL http://www.ncbi.nlm.nih.gov/pubmed/22654654.

108. Lukat G.S., Lee B.H., Mottonen J.M., Stock A.M. and Stocks J.B. Roles of the highly conserved aspartate and lysine residues in the response regulator of bacterial chemotaxis. *Journal of Biological Chemistry* **266**, 8348–8354 (1991). URL http://www.jbc.org/content/266/13/8348.full.pdf.

109. Levit M., Liu Y., Surette M. and Stock J. Active site interference and asymmetric activation in the chemotaxis protein histidine kinase CheA. *Journal of Biological Chemistry* **271**, 32057–63 (1996). URL http://www.ncbi.nlm.nih.gov/pubmed/8943256.

110. Bourret R.B., Drake S.K., Chervitz S.A., Simon M.I. and Falke J.J. Activation of the phosphosignaling protein CheY. Analysis of activated mutants by F19 NMR and protein engineering. *Journal of Biological Chemistry* **268**, 13089–13096. (1993). URL http://www.ncbi.nlm.nih.gov/pubmed/8514750.

111. Lukat G.S., McCleary W.R., Stock A.M. and Stock J.B. Phosphorylation of bacterial response regulator proteins by low molecular weight phospho-donors. *Proceedings of the National Academy of Sciences* **89**, 718–722 (1992). URL http://www.ncbi.nlm.nih.gov/pmc/articles/PMC48310/.

112. Barak R. and Eisenbach, M. Acetylation of the response regulator, CheY, is involved in bacterial chemotaxis. *Molecular Microbiology* **40**, 731–743 (2001). URL http://www.ncbi.nlm.nih.gov/pubmed/11359578.

113. McCleary W. R., Stock J. B. Acetyl phosphate and the activation of two-component response regulators. *Journal of Biological Chemistry* **269**, 31567–31572 (1994). URL http://www.ncbi.nlm.nih.gov/pubmed/7989325.

114. Prüss B.M. and Wolfe A.J. Regulation of acetyl phosphate synthesis and degradation, and the control of flagellar expression in *Escherichia coli*. *Molecular Microbiology* **12**, 973–984 (1994). URL http://www.ncbi.nlm.nih.gov/pubmed/7934904.

115. Mayover T.L., Halkides C.J. and Stewart R.C. Kinetic characterization of CheY phosphorylation reactions: comparison of P-CheA and small-molecule phosphodonors. *Biochemistry* **38**, 2259–2271 (1999). URL http://www.ncbi.nlm.nih.gov/pubmed/10029518.

116. Schuster M., Silversmith R.E. and Bourret R.B. Conformational coupling in the chemotaxis response regulator CheY. *Proceedings of the National Academy of Sciences* **98**, 6003–6008 (2001). URL http://www.pnas.org/content/98/11/6003.full.pdf.

117. Paul K., Brunstetter D., Titen S. and Blair D.F. A molecular mechanism of direction switching in the flagellar motor of *Escherichia coli*. *Proceedings of the National Academy of Sciences* **108**, 17171–17176 (2011). URL http://www.ncbi.nlm.nih.gov/pmc/articles/PMC3193218/.

118. Parkinson J.S., Parker S.R., Talbert P.B., Houts S.E. Interactions between chemotaxis genes and flagellar genes in *Escherichia coli*. *Journal of Bacteriology* **155**, 265–74 (1983). URL http://www.ncbi.nlm.nih.gov/pubmed/6305913/.

119. Sockett H., Yamaguchi S., Kihara M., Irikura V.M. and Macnab R.M. Molecular analysis of the flagellar switch protein FliM of *Salmonella typhimurium*. *Journal of Bacteriology* **174**, 793–806 (1992). URL http://www.ncbi.nlm.nih.gov/pubmed/1732214.

120. Li J.Y., Swanson R.V., Simon M.I. and Weis R.M. The response regulators CheB and CheY exhibit competitive binding to the kinase CheA. *Biochemistry* **34**, 14626–14636 (1995).

121. Bourret R.B., Hess J.F. and Simon M.I. Conserved aspartate residues and phosphorylation in signal transduction by the chemotaxis protein CheY. *Proceedings of the National Academy of Sciences* **87**, 41–45 (1990). URL http://www.ncbi.nlm.nih.gov/pubmed/2404281.

122. Welch M., Oosawa K., Aizawa S.-I. and Eisenbach M. Effects of phosphorylation, Mg^{2+}, and conformation of the chemotaxis protein CheY on its binding to the flagellar switch protein FliM. *Biochemistry* **33**, 10470–10476 (1994). URL http://pubs.acs.org/doi/abs/10.1021/bi00200a031?journalCode=bichaw.

123. Welch M., Oosawa K., Aizawa S.-I. and Eisenbach M. Phosphorylation-dependent binding of a signal molecule to the flagellar switch of bacteria. *Journal of Biological Chemistry* **90**, 8787–8791 (1993). URL http://www.ncbi.nlm.nih.gov/pmc/articles/PMC47445/.

124. Zhu X., Amsler C.D., Volz K. and Matsumura P. Tyrosine 106 of CheY plays an important role in chemotaxis signal transduction in *Escherichia coli*. *Journal of Bacteriology* 4208–4215 (1996). URL http://jb.asm.org/content/178/14/4208.full.pdf+html.

125. Sarkar M.K., Paul K. and Blair D.F. Subunit organization and reversal-associated movements in the flagellar switch of *Escherichia coli*. *Journal of Biological Chemistry* **285**, 675–684 (2010). URL http://www.ncbi.nlm.nih.gov/pmc/articles/PMC2804215/.

126. Sarkar M.K., Paul K. and Blair D.F. Chemotaxis signaling protein CheY binds to the rotor protein FliN to control the direction of flagellar rotation in *E. coli*. *Proceedings of the National Academy of Sciences* **107**, 9370–9375 (2010). URL http://www.ncbi.nlm.nih.gov/pmc/articles/PMC2889077/.

127. Toker A.S., Kihara M. and Macnab R.M. Deletion analysis of the FliM flagellar switch protein of *Salmonella typhimurium*. *Proceedings of the National Academy of Sciences* **87**, 7069–7079 (1996). URL http://www.ncbi.nlm.nih.gov/pmc/articles/PMC178617/.

128. Mathews M.A.A., Tang H.L. and Blair D.F. Domain analysis of the FliM protein of *Escherichia coli*. *Journal of Bacteriology* **180**, 5580–5590 (1998). URL http://www.ncbi.nlm.nih.gov/pubmed/9791106.

129. Monod J., Wyman J. and Changeux J.P. On the nature of allosteric transitions: a plausible model. *Journal of Molecular Biology* **12** (1965). URL http://www.ncbi.nlm.nih.gov/pubmed/14343300.

130. Koshland Jr. D.E., Nmethy G. and Filmer D. Comparison of experimental binding data and theoretical models in proteins containing subunits. *Biochemistry* **5** (1966). URL http://www.ncbi.nlm.nih.gov/pubmed/5938952.

131. Fan B., Branch R.W., Nicolau Jr. D.V., Pilizota T., Steel B.C., Maini P.K. and Berry R.M. Conformational spread as a mechanism for cooperativity in the bacterial flagellar switch. *Science* **327** (2010). URL https://www.sciencemag.org/content/327/5966/685.full.

132. Eigen M. Immeasurably fast reactions. *Nobel Symposia* **5** (1967). URL http://www.nobelprize.org/nobel_prizes/chemistry/laureates/1967/eigen-lecture.pdf.

133. Duke T.A.J., Le Novre N. and Bray D. Conformational spread in a ring of proteins: a stochastic view of allostery. *Journal of Molecular Biology* **271**, 541–553 (2001). URL http://www.pdn.cam.ac.uk/groups/comp-cell/Papers/Duke01.pdf.

134. Bray D. and Duke T.A.J. Conformational spread: the propagation of allosteric states in large multiprotein complexes. *Annual Review of Biophysics and Biomolecular Structure* **33**, 53–73 (2004). URL http://www.ncbi.nlm.nih.gov/pubmed/15139804.

135. Ma Q., Nicolau Jr. D.V., Maini P.K., Berry R.M. and Fan B. Conformational spread in the flagellar motor switch: a model study. *PLoS Computational Biology* **8**, e1002523 (2012). URL http://www.ncbi.nlm.nih.gov/pubmed/22654654.

136. Cluzel P., Surette M. and Leibler S. An ultrasensitive bacterial motor revealed by monitoring signaling proteins in single cells. *Science* **287**, 1652–5 (2000). URL http://www.ncbi.nlm.nih.gov/pubmed/10698740.

137. Sagi Y., Khan S. and Eisenbach M. Binding of the chemotaxis response regulator CheY to the isolated, intact switch complex of the bacterial flagellar motor - lack of cooperativity. *Journal of Biological Chemistry* **278**, 25867–25871 (2003). URL http://www.ncbi.nlm.nih.gov/pubmed/12736245.

138. Sourjik V. and Berg H.C. Receptor sensitivity in bacterial chemotaxis. *Proceedings of the National Academy of Sciences* **99**, 123–127 (2002). URL http://www.pnas.org/content/99/1/123.full.

139. Bren A. and Eisenbach M. Changing the direction of flagellar rotation in bacteria by modulating the ratio between the rotational states of the switch protein FliM. *Journal of Molecular Biology* **312**, 699–709 (2001). URL http://www.sciencedirect.com/science/article/pii/S0022283601949927.

140. Yuan J., Branch R.W., Hosu B.G. and Berg H.C. Adaptation at the output of the chemotaxis signalling pathway. *Nature* **484** (2012). URL http://www.nature.com/nature/journal/v484/n7393/full/nature10964.html.

141. Delalez N., Berry R. M., Armitage J. P. Signal-dependent turnover of the bacterial flagellar switch protein FliM. *Proceedings of the National Academy of Sciences* **107**, 11347–11351 (2010). URL http://www.pnas.org/content/107/25/11347/F3.expansion.html.

142. Porter S.L., Warren A.V., Martin A.C. and Armitage J.P. The third chemotaxis locus of *Rhodobacter sphaeroides* is essential for chemotaxis. *Molecular Microbiology* **46**, 1081–1094 (2002). URL http://www.ncbi.nlm.nih.gov/pubmed/12421313.

143. Porter S.L. and Armitage J.P. Chemotaxis in *Rhodobacter sphaeroides* requires an atypical histidine protein kinase. *Journal of Biological Chemistry*

279, 573–580 (2004). URL http://www.jbc.org/content/279/52/54573?ijkey=c19831f5a0f7f9f7b868ced72d9cf8329c8594bd&keytype2=tf_ipsecsha.

144. Hamer R., Chen P.-Y., Armitage J.P., Reinert G. and Deane C.M. Deciphering chemotaxis pathways using cross species comparisons. *BMC Systems Biology* **4** (2010). URL http://www.ncbi.nlm.nih.gov/pmc/articles/PMC2829493/.

145. Hamblin P.A., Maguire B.A., Grishanin R.N. and Armitage J.P. Evidence for two chemosensory pathways in *Rhodobacter sphaeroides*. *Molecular Microbiology* **26**, 1083–1096 (1997). URL http://onlinelibrary.wiley.com/doi/10.1046/j.1365-2958.1997.6502022.x/epdf.

146. Martin A.C., Gould M., Byles E., Roberts M.A.J. and Armitage J.P. Two chemosensory operons of *Rhodobacter sphaeroides* are regulated independently by Sigma 28 and Sigma 54. *Journal of Bacteriology* **188**, 7932–7940 (2006). URL http://jb.asm.org/content/188/22/7932.full.

147. Wadhams G.H., Warren A.V., Martin A.C. and Armitage J.P. Targeting of two signal transduction pathways to different regions of the bacterial cell. *Molecular Microbiology* **50**, 763–770 (2003). URL http://onlinelibrary.wiley.com/doi/10.1046/j.1365-2958.2003.03716.x/epdf.

148. Mackenzie C., Choudhary M., Larimer F.W., Predki P.F., Stilwagen S., Armitage J.P., Barber R.D., Donohue T.J., Hosler J.P., Newman J.E., Shapleigh J.P., Sockett R.E., Zeilstra-Ryalls J. and Kaplan S. The home stretch, a first analysis of the nearly completed genome of *Rhodobacter sphaeroides*. *Photosynthesis Research* **70**, 19–41 (2001). URL http://www.ncbi.nlm.nih.gov/pubmed/16228360.

149. Poggio S., Abreu-Goodger C., Fabela S., Osorio A., Dreyfus G., Vinuesa P. and Camarena L. A complete set of flagellar genes acquired by horizontal transfer coexists with the endogenous flagellar system in *Rhodobacter sphaeroides*. *Journal of Bacteriology* **189**, 3208–3216 (2007). URL http://www.ncbi.nlm.nih.gov/pubmed/17293429.

150. Mackenzie C., Eraso J.M., Choudhary M., Roh J.H., Zeng X., Bruscella P., Pusks A. and Kaplan S. Postgenomic adventures with *Rhodobacter sphaeroides*. *Annual Reviews of Microbiology* **61**, 283–307 (2007). URL hhttp://www.ncbi.nlm.nih.gov/pubmed/17506668.

151. Porter S.L. and Armitage J.P. Phosphotransfer in *Rhodobacter sphaeroides* chemotaxis. *Journal of Molecular Biology* **324**, 35–45 (2002). URL http://www.ncbi.nlm.nih.gov/pubmed/12421557.

152. Martin A.C., Wadhams G.H. and Armitage J.P. The roles of the multiple CheW and CheA homologues in chemotaxis and in chemoreceptor localization in *Rhodobacter sphaeroides*. *Molecular Microbiology* **40**, 1261–1272 (2001). URL http://onlinelibrary.wiley.com/doi/10.1046/j.1365-2958.2001.02468.x/epdf.

153. Wadhams G. H., Warren A. V., Martin A. C., and Armitage J. P. Targeting of two signal transduction pathways to different regions of the bacterial cell. *Molecular Microbiology* **50**, 763–70 (2003). URL http://www.ncbi.nlm.nih.gov/pubmed/14617139.

154. Porter S.L., Roberts M.A.J., Manning C.S. and Armitage J.P. A bifunctional kinase-phosphatase in bacterial chemotaxis. *Proceedings of the National Academy of Sciences* **105**, 531–536 (2006). URL http://www.pnas.org/content/105/47/18531?ijkey=39c7d5f2895b47bcd35054a6834d610a30e4ae02&keytype2=tf_ipsecsha.

155. Porter S.L., Wadhams G.H., Martin A.C., Byles E.D., Lancaster D.E. and Armitage J.P. The CheYs of *R. sphaeroides*. *Journal of Biological Chemistry* **281**, 32694–32704 (2006). URL http://www.jbc.org/content/281/43/32694.long.

156. Wadhams G.H., Warren A.V., Martin A.C. and Armitage J.P. Targeting of two signal transduction pathways to different regions of the bacterial cell. *Molecular Microbiology* **50**, 763–770 (2003). URL http://onlinelibrary.wiley.com/doi/10.1046/j.1365-2958.2003.03716.x/full.

157. Ferre A., de la Mora J., Ballado T., Camarena L. and Dreyfus G. Biochemical study of multiple CheY response regulators of the chemotactic pathway of *R. sphaeroides*. *Journal of Bacteriology* **186**, 5172–5177 (2004). URL http://jb.asm.org/content/186/15/5172.full.

158. Murphy D.B., Oldfield R., Schwartz S. and Davidson M.W. Introduction to phase contrast microscopy. (2015). URL https://www.microscopyu.com/articles/phasecontrast/phasemicroscopy.html.

159. Murphy D.B., Spring K.R., Parry-Hill M., Sutter R.T. and Davidson M.W. DIC microscope component alignment. (2015). URL https://www.microscopyu.com/tutorials/java/dic/dicalignment/index.html.

160. Rottenfusser R., Wilson E.E. and Davidson M.W. Enhancing contrast in optical microscopy. (2015). URL http://zeiss-campus.magnet.fsu.edu/articles/basics/contrast.html.

161. Lichtman J.W. and Conchello J.A. Fluorescence microscopy. *Nature Methods* **2**, 910–919 (2005). URL http://www.nature.com/nmeth/journal/v2/n12/full/nmeth817.html.

162. Xia T., Li N. and Fang X. Single-molecule fluorescence imaging in living cells. *Annual Reviews of Physical Chemistry* **64**, 459–80 (2013). URL http://www.annualreviews.org/doi/pdf/10.1146/annurev-physchem-040412-110127.

163. Yu J., Xiao J., Ren X., Lao K. and Xie X.S. Probing gene expression in live cells, one protein molecule at a time. *Science* **311**, 1600–3 (2006). URL https://www.sciencemag.org/content/311/5767/1600.full.pdf.

164. Yang W.D., Gelles J. and Musser S.M. Imaging of single-molecule translocation through nuclear pore complexes. *Proceedings of the National Academy of Sciences* **101**, 12887–92 (2004). URL https://www.sciencemag.org/content/311/5767/1600.full.pdf.

165. Thompson N.L., Pearce K.H. and Hsieh H.V. Total internal-reflection fluorescence microscopy: application to substrate-supported planar membranes. *European Biophysics Journal* **22**, 367–78 (1993). URL http://www.annualreviews.org/doi/pdf/10.1146/annurev-physchem-040412-110127.

166. Tokunaga M., Imamoto N. and Sakata-Sogawa K. Highly inclined thin illumination enables clear single-molecule imaging cells. *Nature Methods* **5**, 159–161 (2008). URL http://www.nature.com/nmeth/journal/v5/n2/abs/nmeth1171.html.

167. Savage L. Improving plant cell analysis requires good TIRF. *Biophotonics* (2011). URL http://www.photonics.com/Article.aspx?AID=48690.

168. Baba T., Ara T., Hasegawa M., Takai Y., Okumura Y., Baba M., Datsenko K.A., Tomita M., Wanner B.L. and Mori H. Construction of *Escherichia coli* K-12 in-frame, single-gene knockout mutants: the Keio collection. *Molecular Systems Biology* **2**, 2006.0008 (2006). URL http://www.ncbi.nlm.nih.gov/pmc/articles/PMC1681482/.

169. Thomason L.C., Costantino N. and Court D.L. *Escherichia coli* genome manipulation by P1 transduction. *Current Protocols in Molecular Biology* **1.17**, 1–8 (2007). URL http://onlinelibrary.wiley.com/doi/10.1002/0471142727.mb0117s79/full.

170. Parkinson, J. Complementation analysis and deletion mapping of *Escherichia coli* mutants defective in chemotaxis. *Journal of Bacteriology* **10** (1978). URL http://jb.asm.org/content/135/1/45.short.

171. Sourjik V., Armitage J. P. Spatial organization in bacterial chemotaxis. *The EMBO journal* **29**, 2724–33 (2010). URL http://www.ncbi.nlm.nih.gov/pmc/articles/PMC2924652/.

172. Ind, A. C., Porter, S. L., Brown, M. T., Byles, E. D., de Beyer, J. a., Godfrey, S. a., Armitage, J. P. Inducible-expression plasmid for *Rhodobacter sphaeroides* and *Paracoccus denitrificans*. *Applied and environmental microbiology* **75**, 6613–5 (2009). URL http://www.ncbi.nlm.nih.gov/pubmed/19684165.

173. Turner L., Samuel A. D. T., Stern A. S., Berg H. C. Temperature dependence of switching of the bacterial flagellar motor by the protein $\mathrm{CheY}^{13DK106YW}$. *Biophysical Journal* **Vol 77**, 597–603 (1999). URL http://www.ncbi.nlm.nih.gov/pmc/articles/PMC1300356/.

174. Rogala K.B., Dynes N.J., Hatzopoulos G.N., Yan J., Pong Sheng K., Robinson C.V., Deane C.M., Gönczy P. and Vakonakis I. The *Caenorhabditis elegans* protein SAS-5 forms large oligomeric assemblies critical for centriole formation. *eLife Sciences Publications Limited* **10.7554/eLife.07410** (2015). URL http://elifesciences.org/content/early/2015/05/29/eLife.07410.

175. Schuster M., Abouhamad W.N., Silversmith R.E. and Bourret R.B. Chemotactic response regulator mutant CheY95IV exhibits enhanced binding to the flagellar switch and phosphorylation-dependent constitutive signalling. *Molecular Microbiology* **27**, 1065–1075 (1998). URL http://onlinelibrary.wiley.com/doi/10.1046/j.1365-2958.1998.00756.x/epdf.

176. Kitagawa M., Ara T., Arifuzzaman M., Ioka-Nakamichi T., Inamoto E., Toyonaga H. and Mori H. Complete set of ORF clones of *Escherichia coli* ASKA library (a complete set of *E. coli* K-12 ORF archive): unique resources for biological research. *DNA Research* 12291–299 (2005). URL http://www.ncbi.nlm.nih.gov/pubmed/16769691.

177. Gibson D.G., Young L., Chuang R.Y., Venter J.C., Hutchison C.A. 3rd and Smith H.O. Enzymatic assembly of DNA molecules up to several hundred kilobases. *Nature Methods* **6**,

343–345 (2009). URL http://www.nature.com/nmeth/journal/v6/n5/full/nmeth.1318.html.

178. J. Sambrook , D. W. Russell. Molecular cloning: a laboratory manual - 3rd edition. *Cold Spring Harbor Laboratory Press* **I** (2001).

179. Adler J. and Templeton B. The effect of environmental conditions on the motility of *Escherichia coli*. *Journal of general microbiology* **46**, 175–184 (1967). URL http://www.ncbi.nlm.nih.gov/pubmed/4961758.

180. Matsumura P., Rydel J. J., Linzmeier R. and Vacante D. Overexpression and sequence of the *Escherichia coli cheY* gene and biochemical activities of the CheY protein. *Journal of Bacteriology* **160**, 36–41 (1984). URL http://www.ncbi.nlm.nih.gov/pubmed/6090423.

181. Macherey-Nagel GmbH & Co. KG. User manuals: purification of His-tag proteins. *Rev. 06* (2014). URL http://www.mn-net.com/Portals/8/attachments/Redakteure_Bio/Protocols/Protino/UM_ProtinoNi_TED.pdf.

182. Bradford M. M. A rapid and sensitive method for the quantitation of microgram quantities of protein utilizing the principle of protein-dye binding. *Analytical Biochemistry* **72**, 248–54 (2008). URL http://www.ncbi.nlm.nih.gov/pubmed/942051.

183. Kim Y., Ho S. O., Gassman N. R., et al. Efficient site-specific labeling of proteins via cysteines. *Bioconjugate chemistry* **19**, 786–791 (2008). URL http://www.ncbi.nlm.nih.gov/pmc/articles/PMC3086356/.

184. Prasher D.C., Eckenrode V.K., Ward W.W., Prendergast F.G. and Cormier M.J. Primary structure of the Aequorea victoria green-fluorescent protein. *Gene* **111**, 229–233 (1992). URL http://www.ncbi.nlm.nih.gov/pubmed/1347277.

185. Cody C.W., Prasher D.C., Westler W.M., Prendergast F.G., and Ward W.W. Chemical structure of the hexapeptide chromophore of the Aequorea green-fluorescent protein. *Biochemistry* **32**, 1212–1218 (1993). URL http://pubs.acs.org/doi/abs/10.1021/bi00056a003/.

186. Day R.N. and Davidson M.W. The fluorescent protein palette: tools for cellular imaging. *Chemical Society Reviews* **38**, 2887–2921 (2009). URL http://www.ncbi.nlm.nih.gov/pmc/articles/PMC2910338/.

187. Plautz J.D., Day R.N., Dailey G.M., Welsh S.B., Hall J.C., Halpain S. and Kay S.A. Green fluorescent protein and its derivatives as versatile markers for gene expression in living *Drosophila melanogaster*, plant and mammalian cells. *Gene* **173**, 83–7 (1996). URL http://www.ncbi.nlm.nih.gov/pubmed/8707061.

188. C. Neal Stewart. Go with the glow: fluorescent proteins to light transgenic organisms. *Trends in Biotechnology* **24**, 155–162 (2006). URL http://www.sciencedirect.com/science/article/pii/S0167779906000308.

189. Campbell R.E. et al. A monomeric red fluorescent protein. *Proceedings of the National Academy of Sciences* **99**, 7877–7882 (2002). URL http://www.pnas.org/content/99/12/7877.full.pdf.

190. I.I. Shemiakina et al. A monomeric red fluorescent protein with low cytotoxicity. *Nature Communications* **3** (2012). URL http://www.nature.com/ncomms/journal/v3/n11/full/ncomms2208.html.

191. Hammar P., Leroy P. and Elf J. The lac repressor displays facilitated diffusion in living cells. *Science* **336**, 1595–1598 (2012). URL http://www.ncbi.nlm.nih.gov/pubmed/22723426.

192. Miesenbock G., De Angelis D.A. and Rothman J.E. Visualizing secretion and synaptic transmission with pH-sensitive green fluorescent proteins. *Nature* **394**, 192–5 (1998). URL http://www.ncbi.nlm.nih.gov/pubmed/9671304.

193. Delalez N. et al. Signal-dependent turnover of the bacterial flagellar switch protein FliM. *Proceedings of the National Academy of Sciences* **107**, 11347–11351 (2010). URL http://www.ncbi.nlm.nih.gov/pubmed/20498085.

194. Delalez N., Berry R.M. and Armitage J.P. Stoichiometry and turnover of the bacterial flagellar switch protein FliN. *mBio* **5**, e01216–14 (2014). URL http://mbio.asm.org/content/5/4/e01216-14.full.

195. Dempsey, G.T., Vaughan, J.C., Chen, K.H., Bates, M. and Zhuang, X. Evaluation of fluorophores for optimal performance in localization-based super-resolution imaging. *Nature Methods* **8**, 1027–1036 (2011). URL http://www.nature.com/nmeth/journal/v8/n12/full/nmeth.1768.html.

196. Shaner, N.C., Steinbach, P.A. and Tsien, R.Y. A guide to choosing fluorescent proteins. *Nature Methods* **2**, 905–909 (2005). URL http://www.nature.com/nmeth/journal/v2/n12/abs/nmeth819.html.

197. Hinner M.J. and Johnsson K. How to obtain labeled proteins and what to do with them. *Current Opinion in Biotechnology* **21**, 766–776 (2010). URL http://www.ncbi.nlm.nih.gov/pubmed/21030243.

198. Keppler A., Gendreizig S., Gronemeyer T., Pick H., Vogel H. and Johnsson K. A general method for the covalent labeling of fusion proteins with small molecules *in vivo*. *Nature Biotechnology* **21**, 86–89 (2003). URL http://www.nature.com/nbt/journal/v21/n1/abs/nbt765.html.

199. McNeil P.L., Murphy R.F., Lanni F., Taylor D.L. A method for incorporating macromolecules into adherent cells. *The Journal of Cell Biology* **98**, 1556–1564 (1984). URL http://www.ncbi.nlm.nih.gov/pubmed/6201494.

200. Clarke M.S., McNeil P.L. Syringe loading introduces macromolecules into living mammalian cell cytosol. *Journal of Cell Science* **102**, 533–541 (1992). URL http://www.ncbi.nlm.nih.gov/pubmed/1506433.

201. Taylor L.S. Electromagnetic syringe. *IEEE Transactions on Biomedical Engineering* **25**, 303–304 (1978). URL http://ieeexplore.ieee.org/stamp/stamp.jsp?arnumber=4122834.

202. Riveline D. and Nurse P. 'Injecting' yeast. *Nature Methods* **6**, 513–514 (2009). URL http://www.nature.com/nmeth/journal/v6/n7/abs/nmeth.1335.html.

203. Aigrain L., Sustarsic M., Crawford R., Plochowietz A. and Kapanidis A.N. Internalization and observation of fluorescent biomolecules in living microorganisms via electroporation. *Journal of Visualized Experiments* **96**, 52208 (2015). URL http://www.ncbi.nlm.nih.gov/pmc/articles/PMC4354625/.

204. Weaver J.C. Electroporation theory. Concepts and mechanisms. *Methods in Molecular Biology* **47**, 1–26 (1995). URL http://www.ncbi.nlm.nih.gov/pubmed/7550723.

205. Tsong T.Y. Electroporation of cell membranes. *Biophysical Journal* **60**, 297–306 (1991). URL http://www.ncbi.nlm.nih.gov/pubmed/1912274.

206. Tokman M., Lee J.H., Levine Z.A., Ho M.-C., Colvin M.E., Vernier P.T. Electric field-driven water dipoles: nanoscale architecture of electroporation. *PLoS One* **8**, e61111 (2013). URL http://journals.plos.org/plosone/article?id=10.1371/journal.pone.0061111.

207. Kotnik T., Kramar P., Pucihar G., Miklavcic D. and Tarek M. Cell membrane electroporation - part 1: the phenomenon. *IEEE Electrical Insulation Magazine* (2012). URL http://ieeexplore.ieee.org/stamp/stamp.jsp?arnumber=62684382012.

208. Deamer D.W. and Bramhall J. Permeability of lipid bilayers to water and ionic solutes. *Chemistry and Physics of Lipids* **40**, 167–188 (1986). URL http://www.sciencedirect.com/science/article/pii/0009308486900691.

209. M. Jansen and A. Blume. A comparative study of diffusive and osmotic water permeation across bilayers composed of phospholipids with different headgroups and fatty acyl chains. *Biophysical Journal* **68**, 997–1008 (1995). URL http://www.ncbi.nlm.nih.gov/pubmed/7756562.

210. Scharf B.E., Fahrner K. A., Turner L. and Berg H.C. Control of direction of flagellar rotation in bacterial chemotaxis. *Proceedings of the National Academy of Sciences* **95**, 201–206 (1998). URL http://www.pnas.org/content/95/1/201.abstract.

211. Schuster M., Zhao R., Bourret R.B. and Collins E.J. Correlated switch binding and signaling in bacterial chemotaxis. *Journal of Biological Chemistry* **275**, 19752–8 (2000). URL http://www.jbc.org/content/early/2000/03/29/jbc.M909908199.full.pdf.

212. Halkides C.J., McEvoy M.M., Casper E., Matsumura P., Volz K. and Dahlquist F.W. The 1.9 Å resolution crystal structure of phosphono-CheY, an analogue of the active form of the response regulator, CheY. *Biochemistry* **39**, 5280–6 (2000). URL http://www.ncbi.nlm.nih.gov/pubmed/10819997/.

213. Cho H.S., Lee S.Y., Yan D., Pan X., Parkinson J.S., Kustu S., Wemmer D.E., Pelton J.G. NMR structure of activated CheY. *Journal of Molecular Biology* **297**, 543–551 (2000). URL http://www.ncbi.nlm.nih.gov/pubmed/10731410.

214. Welch M., Chinardet N., Mourey L., Birck C. and Samama J.-P. NMR structure of activated CheY. *Nature Structural Biology* **5**, 25–29 (1998). URL http://www.ncbi.nlm.nih.gov/pubmed/9437425.

215. Yuan Y., Wang X., Mei B., Zhang D., Tang A., An L., He X., Jiang J. and Liang G. Labeling thiols on proteins, living cells, and tissues with enhanced emission induced by FRET.

Scientific Reports **3** (2013). URL http://www.nature.com/srep/2013/131217/srep03523/full/srep03523.html.

216. Mo G., Zhou H., Kawamura T. and Dahlquist F.W. Solution structure of a complex of the histidine autokinase CheA with its substrate CheY. *Biochemistry* **51**, 3786–3798 (2012). URL http://www.ncbi.nlm.nih.gov/pmc/articles/PMC3365488/.

217. Bell C.H., Porter S.L., Strawson A., Stuart D.I., Armitage J.P. Using structural information to change the phosphotransfer specificity of a two-component chemotaxis signalling complex. *Plos Biology* **8**, e1000306–e1000306 (2010). URL http://www.ncbi.nlm.nih.gov/pubmed/20161720?dopt=Abstract.

218. DeLano Scientific, LLC. The PyMOL Molecular Graphics System, Version 1.1eval. (2008). URL https://www.pymol.org/.

219. Sustarsic M., Plochowietz A., Aigrain L., Yuzenkova Y., Zenkin N. and Kapanidis A. Optimized delivery of fluorescently labeled proteins in live bacteria using electroporation. *Histochemistry and Cell Biology* **142**, 113–24 (2014). URL http://www.ncbi.nlm.nih.gov/pubmed/24696085.

220. Dower W. J., Miller J. F., Ragsdale C. W. High efficiency transformation of *E. coli* by high voltage electroporation. *Nucleic Acids Research* **16**, 6127–6145 (1988). URL http://www.ncbi.nlm.nih.gov/pmc/articles/PMC336852/.

221. Donohue T.J., Kaplan S. Genetic techniques in *Rhodospirillaceae*. *Methods in Enzymology* **204**, 459–485 (1991). URL http://www.ncbi.nlm.nih.gov/pubmed/1658568.

222. Jun D., Saer R.G., Madden J.D., Beatty J.T. Use of new strains of *Rhodobacter sphaeroides* and a modified simple culture medium to increase yield and facilitate purification of the reaction centre. *Photosynthesis Research* **120**, 197–205 (2014). URL http://www.ncbi.nlm.nih.gov/pubmed/23765434.

223. Gill S.C., von Hippel P.H. Calculation of protein extinction coefficients from amino acid sequence data. *Analytical Biochemistry* **182**, 319–326 (1999). URL http://www.ncbi.nlm.nih.gov/pubmed/2610349.

224. Walker J.M. The proteomics protocols handbook. *Humana Press* 571–607 (2005). URL http://www.springer.com/gb/book/9781588293435.

225. Bachmair, A., Finley, D., and Varshavsky, A. *In vivo* half-life of a protein is a function of its amino-terminal residue. *Science* **234**, 179–186 (1986). URL http://www.ncbi.nlm.nih.gov/pubmed/3018930.

226. Gonda D.K., Bachmair A., Wunning I., Tobias J.W., Lane W.S. and Varshavsky A.J. Universality and structure of the N-end rule. *Journal of Biological Chemistry* **264**, 700–16 (1989). URL http://www.ncbi.nlm.nih.gov/pubmed/2506181.

227. Tobias J.W., Shrader T.E., Rocap G., and Varshavsky A. The N-end rule in bacteria. *Science* **254**, 1374–1377 (1991). URL http://www.ncbi.nlm.nih.gov/pubmed/1962196.

228. Pace C.N.,Vajdos F., Fee L., Grimsley G. and Gray T. How to measure and predict the molar absorption coefficient of a protein. *Protein Science* **4**, 2411–2423 (1995). URL http://www.ncbi.nlm.nih.gov/pubmed/8563639.

229. Zanetti-Domingues L.C., Tynan C.J., Rolfe D.J., Clarke D.T., Martin-Fernandez M. Hydrophobic fluorescent probes introduce artifacts into single molecule tracking experiments due to nonspecific binding. *PLOS ONE* **8**, e74200 (2013). URL http://journals.plos.org/plosone/article?id=10.1371/journal.pone.0074200#pone.0074200-Yao1.

230. ATTO-TEC GmbH (2011). URL http://www.atto-tec.com/fileadmin/user_upload/Katalog_Flyer_Support/ATTO_647N.pdf.

231. Hughes L.D., Rawle R.J. and Boxer S.G. Choose your label wisely: water-soluble fluorophores often interact with lipid bilayers. *PLOS ONE* **19**, e87649 (2014). URL http://journals.plos.org/plosone/article?id=10.1371/journal.pone.0087649#s4.

232. ATTO-TEC GmbH (2010). URL https://www.atto-tec.com/fileadmin/user_upload/Katalog_Flyer_Support/Catalogue_2009_2010.pdf.

233. Buschmann V., Weston K.D. and Sauer M. Spectroscopic study and evaluation of red-absorbing fluorescent dyes. *Bioconjugate Chemistry* **14**, 195–204 (2003). URL http://pubs.acs.org/doi/abs/10.1021/bc025600x.

234. Wirpsza L., Krasnoperov L. and Mustaev A. New quinolone-based thiol-reactive lanthanide luminescent probes. *Journal of Photochemistry and Photobiology A: Chemistry* **251**, 30–37 (2013). URL http://www.ncbi.nlm.nih.gov/pmc/articles/PMC3700551/.

235. Netto L.E. and Stadtman E.R. The iron-catalyzed oxidation of Dithiothreitol is a biphasic process: hydrogen peroxide is involved in the initiation of a free radical chain of reactions. *Archives of Biochemistry and Biophysics* **333**, 233–42 (1996). URL http://www.ncbi.nlm.nih.gov/pubmed/8806776.

236. Burns J.A., Butler J.C., Moran J. and Whitesides G.M. Selective reduction of disulfides by Tris(2-carboxyethy1)phosphine. *The Journal of Organic Chemistry* **56**, 2648–2650 (1991). URL https://gmwgroup.harvard.edu/pubs/pdf/310.pdf.

237. Burmeister Getz E., Xiao M., Chakrabarty T., Cooke R. and Selvin P.R. A comparison between the sulfhydryl reductants Tris(2-carboxyethyl)phosphine and Dithiothreitol for use in protein biochemistry. *Analytical Biochemistry* **273**, 73–80 (1999). URL http://protomnis.com/wp-content/uploads/2014/04/TCEP-vs-DTT-publication1.pdf.

238. Haugland R.P. Handbook of fluorescent probes and research chemicals. *Molecular Probes* (1996). URL http://www.researchgate.net/publication/244463954_Handbook_Of_Fluorescent_Probes_And_Research_Chemicals.

239. Tyagarajan K., Pretzer E. and Wiktorowicz J.E. Thiol-reactive dyes for fluorescence labeling of proteomic samples. *Electrophoresis* **24**, 2348–2358 (2003). URL http://www.ncbi.nlm.nih.gov/pubmed/12874870.

240. Shafer D.E., Inman J.K., Lees A. Reaction of Tris(2-carboxyethyl)phosphine (TCEP) with maleimide and alpha-haloacyl groups: anomalous elution of TCEP by gel filtration. *Ana-*

lytical Biochemistry **282**, 161–4 (2000). URL http://www.ncbi.nlm.nih.gov/pubmed?cmd=Retrieve&dopt=AbstractPlus&list_uids=10860517.

241. Plochowietz A., Crawford R. and Kapanidis A.N. Characterization of organic fluorophores for in vivo FRET studies based on electroporated molecules. *Physical Chemistry Chemical Physics* **16**, 12688–94 (2014). URL http://www.ncbi.nlm.nih.gov/pubmed/24837080.

242. Young J.W., Locke J.C.W:, Altinok A., Rosenfeld N., Bacarian T., Swain P.S., Mjolsness E. and Elowitz M.B. Measuring single-cell gene expression dynamics in bacteria using fluorescence time-lapse microscopy. *Nature Protocols* **7**, 80–88 (2012). URL http://www.nature.com/nprot/journal/v7/n1/full/nprot.2011.432.html.

243. Kretschy N. and Somoza M.M. Comparison of the sequence-dependent fluorescence of the Cyanine dyes Cy3, Cy5, DyLight DY547 and DyLight DY647 on single-stranded DNA. *PLOS ONE* **9**, e85605 (2014). URL http://journals.plos.org/plosone/article?id=10.1371/journal.pone.0085605.

244. Yang L., Zhou Y., Zhu S., Huang T., Wu L. and Yan X. Detection and quantification of bacterial autofluorescence at the single-cell level by a laboratory-built high-sensitivity flow cytometer. *Analytical Chemistry* **84**, 1526–1532 (2012). URL http://pubs.acs.org/doi/abs/10.1021/ac2031332.

245. Terasaki M. and Dailey M.E. Confocal microscopy on living cells. In Handbook of biological confocal microscopy. *Plenum Press* **Ed. 2nd ed.**, 327–346 (1995). URL http://www.springer.com/us/book/9780387259215.

246. Kolmakov K., Belov V.N., Bierwagen J., Ringemann C., Mller V., Eggeling C. and Hell S.W. Red-emitting rhodamine dyes for fluorescence microscopy and nanoscopy. *Chemistry - A European Journal* **16**, 158–166 (2010). URL http://www3.mpibpc.mpg.de/groups/hell/publications/pdf/Chem.Eur.J._16_158-166.pdf.

247. Yao J.Z., Uttamapinant C., Poloukhtine A., Baskin J.M., Codelli J.A., Sletten E.M., Bertozzi C.R., Popik V.V. and Ting A.Y. Fluorophore targeting to cellular proteins via enzyme-mediated azide ligation and strain-promoted cycloaddition. *Journal of the American Chemical Society* **134**, 3720–3728 (2012). URL http://www.ncbi.nlm.nih.gov/pubmed/22239252.

248. R. E. Thompson, D. R. Larson and W. W. Webb. Precise nanometer localization analysis for individual fluorescent probes. *Biophysical Journal* **182**, 32775–2783 (2002). URL http://www.ncbi.nlm.nih.gov/pmc/articles/PMC1302065/.

249. Ravid S. and Eisenbach M. Minimal requirements for rotation of bacterial flagella. *Journal of Bacteriology* **158**, 1208–1210 (1984). URL http://www.ncbi.nlm.nih.gov/pmc/articles/PMC215579/.

250. Neidhardt F.C., Bloch P.L., and Smith D.F. Culture medium for enterobacteria. *Journal of Bacteriology* **119**, 736–47 (1974). URL http://www.teknova.com/EZ-RICH-DEFINED-MEDIUM-KIT-p/m2105.html.

251. Payne J.W. and Gilvarg C. Size restriction on peptide utilization in *Escherichia coli*. *Journal of Biological Chemistry* **243**, 6291–9 (1968). URL http://www.ncbi.nlm.nih.gov/pubmed/4881360.

252. Sezonov G., Joseleau-Petit D. and D'Ari R. *Escherichia coli* physiology in Luria-Bertani broth. *Journal of Bacteriology* **189**, 8746–8749 (2007). URL http://jb.asm.org/content/189/23/8746.full.

253. Hanahan D. Studies on transformation of *Escherichia coli* with plasmids. *Journal of Molecular Biology* **166**, 557–80 (1983). URL http://www.ncbi.nlm.nih.gov/pubmed/6345791.

254. Papp-Wallace K. and Maguire M. Magnesium transport and magnesium homeostasis. *EcoSal Plus* **3** (2008). URL http://www.asmscience.org/content/journal/ecosalplus/10.1128/ecosalplus.5.4.4.2.

255. Monod J. Recherches sur la croissance des cultures bactriennes. (1941). URL http://www.worldcat.org/title/recherches-sur-la-croissance-des-cultures-bacteriennes/oclc/493163067.

256. Gorke B. and Stulke J. Carbon catabolite repression in bacteria: many ways to make the most out of nutrients. *Nature Reviews Microbiology* **6**, 613–624 (2008). URL http://www.ncbi.nlm.nih.gov/pubmed/18628769.

257. Hibino M., Itoh H. and Kinosita K. Jr. Time courses of cell electroporation as revealed by submicrosecond imaging of transmembrane potential. *Biophysical Journal* **64**, 1789–1800 (1993). URL http://www.ncbi.nlm.nih.gov/pmc/articles/PMC1262513/.

258. Pucihar G., Kotnik T., Miklavcic D. and Teissi J. Kinetics of transmembrane transport of small molecules into electropermeabilized cells. *Biophysical Journal* **95**, 2837–2848 (2008). URL http://www.ncbi.nlm.nih.gov/pmc/articles/PMC2527253/.

259. Driver E.C. and Kelley M.W. Transfection of mouse cochlear explants by electroporation. *Current Protocols in Neuroscience* **Chapter: Unit 4** (2010). URL http://www.ncbi.nlm.nih.gov/pmc/articles/PMC2921770/.

260. Franklin S., Ibey B.L., Nash K. and Beier H.T. Measurement of changes in plasma membrane phospholipid polarization following nanosecond pulsed electric field exposure. *Proc. SPIE 8585, Terahertz and Ultrashort Electromagnetic Pulses for Biomedical Applications* **85850S** (2013). URL http://spie.org/Publications/Proceedings/Paper/10.1117/12.2005091.

261. Greenfield D., McEvoy A.L., Shroff H., Crooks G.E., Wingreen N.S., Betzig E. and Liphardt J. Self-organization of the *Escherichia coli* chemotaxis network imaged with super-resolution light microscopy. *PLoS Biology* **7**, e1000137 (2009). URL http://www.ncbi.nlm.nih.gov/pubmed/19547746?access_num=19547746&link_type=MED&dopt=Abstract.

262. Cantwell B.J., Draheim R.R., Weart R.B., Nguyen C., Stewart R.C. and Manson M.D. CheZ phosphatase localizes to chemoreceptor patches via CheA-short. *Journal of Bacteriology* **185**, 2354–2361 (2003). URL http://www.ncbi.nlm.nih.gov/pubmed/12644507.

263. Sourjik V. and Berg H.C. Binding of the *E. coli* response regulator CheY to its target measured in vivo by fluorescence resonance energy transfer. *Proceedings of the National Academy of Sciences* **99**, 12669–12674 (2002). URL http://www.pnas.org/content/99/20/12669.full.

264. Turner L., Caplan S.R. and Berg H.C. Temperature-induced switching of the bacterial flagellar motor. *Biophysical Journal* **71**, 2227–2233 (1996). URL http://www.ncbi.nlm.nih.gov/pmc/articles/PMC1233691/.

265. Bren A. and Eisenbach M. The N terminus of the flagellar switch protein, FliM, is the binding domain for the chemotactic response regulator, CheY. *Journal of Molecular Biology* **278**, 507–514 (1998). URL http://www.sciencedirect.com/science/article/pii/S0022283698917302.

266. Mortensen K.I., Stirling Churchman L., Spudich J.A. and Flyvbjerg H. Optimized localization analysis for single-molecule tracking and super-resolution microscopy. *Nature Methods* **7**, 377–381 (2010). URL http://www.nature.com/nmeth/journal/v7/n5/abs/nmeth.1447.html.

267. Crocker J.C. and Grier D.G. Methods of digital video microscopy for colloidal studies. *Journal of Colloid and Interface Science* **179**, 298–310 (1996). URL http://glinda.lrsm.upenn.edu/~weeks/idl.

268. Kaplan E.L. and Meier P. Nonparametric estimation from incomplete observations. *Journal of the American Statistical Association* **53**, 457–481 (1958). URL http://www.jstor.org/stable/2281868?seq=1#page_scan_tab_contents.

269. Lowry R. Kaplan-Meier survival probability estimates. *VassarStats website* (1998-2015). URL http://vassarstats.net/survival.html.

270. Elowitz M.B., Surrette M.G., Wolf P.-E., Stock J.B. and Leibler S. Protein mobility in the cytoplasm of *E. coli*. *Journal of Bacteriology* **181**, 197–203 (1999). URL http://www.ncbi.nlm.nih.gov/pmc/articles/PMC103549/.

271. Schulmeister S., Ruttorf M., Thiem S., Kentner D., Lebiedz D. and Sourjik V. Protein exchange dynamics at chemoreceptor clusters in *Escherichia coli*. *Proceedings of the National Academy of Sciences* **105**, 6403–8 (2008). URL http://www.ncbi.nlm.nih.gov/pubmed/18427119.

272. Jianrong W. and Berland K.M. Propagators and time-dependent diffusion coefficients for anomalous diffusion. *Biophysical Journal* **95**, 2049–2052 (2008). URL http://www.sciencedirect.com/science/article/pii/S0006349508701620.

273. McEvoy M.M., Bren A., Eisenbach M. and Dahlquist F.W. Identification of the binding interfaces on CheY for two of its targets, the phosphatase CheZ and the flagellar switch protein FliM. *Journal of Molecular Biology* **289**, 1423–1433 (1999). URL http://www.ncbi.nlm.nih.gov/pmc/articles/PMC3327947/.

274. Dyer C.M. and Dahlquist F.W. Switched or not?: the structure of unphosphorylated CheY bound to the N terminus of FliM. *Journal of Bacteriology* **188**, 25867–25871 (2006). URL http://www.ncbi.nlm.nih.gov/pmc/articles/PMC1636273/.

275. Barak R., Welch M., Yanovsky A., Oosawa K. and Eisenbach M. Acetyladenylate or its derivative acetylates the chemotaxis protein CheY in vitro and increases its activity at the flagellar switch. *Biochemistry* **31**, 10099–10107 (1992). URL http://www.ncbi.nlm.nih.gov/pubmed/1390767.

276. Barak R., Abouhamad W.N. and Eisenbach M. Both acetate kinase and acetyl coenzyme A synthetase are involved in acetate-stimulated change in the direction of flagellar rotation in *Escherichia coli*. *Journal of Bacteriology* **180**, 985–988 (1998). URL http://www.ncbi.nlm.nih.gov/pmc/articles/PMC106981/.

277. Ramakrishnan R., Schuster M. and Bourret R.B. Acetylation at Lys-92 enhances signaling by the chemotaxis response regulator protein CheY. *Proceedings of the National Academy of Sciences* **95**, 4918–4923 (1992). URL http://www.ncbi.nlm.nih.gov/pmc/articles/PMC20188/.

278. Fraiberg M., Afanzar O., Cassidy C.K., Gabashvili A., Schulten K., Levin Y. and Eisenbach M. CheY's acetylation sites responsible for generating clockwise flagellar rotation in *Escherichia coli*. *Molecular Microbiology* **95**, 231–244 (2015). URL http://www.ncbi.nlm.nih.gov/pubmed/25388160.

279. Dyer C.M., Vartanian A.S., Zhou H. and Dahlquist F.W. A molecular mechanism of bacterial flagellar motor switching. *Journal of Molecular Biology* **388**, 71–84 (2009). URL http://www.ncbi.nlm.nih.gov/pmc/articles/PMC3327947/.

280. Alon U., Camarena L., Surette M.G., Aguera y Arcas B., Liu Y., Leibler S. and Stock J.B. Response regulator output in bacterial chemotaxis. *The European Molecular Biology Organization Journal* **17**, 4238–4248 (1998). URL http://www.ncbi.nlm.nih.gov/pmc/articles/PMC1170757/.

281. Chory J., Donohue T.J., Varga A.R., Staehelin L.A. and Kaplan S. Induction of the photosynthetic membranes of *Rhodopseudomonas sphaeroides*: biochemical and morphological studies. *Journal of Bacteriology* **159**, 540–554 (1984). URL http://jb.asm.org/content/159/2/540.full.pdf.

282. Tucker J.D., Siebert C.A., Escalante M., Adams P.G., Olsen J.D., Otto C., Stokes D.L. and Hunter C.N. Membrane invagination in *Rhodobacter sphaeroides* is initiated at curved regions of the cytoplasmic membrane, then forms both budded and fully detached spherical vesicles. *Molecular Microbiology* **76**, 833–847 (2010). URL http://onlinelibrary.wiley.com/doi/10.1111/j.1365-2958.2010.07153.x/full.

283. Yeliseev A.A., Eraso J.M. and Kaplan S. Differential carotenoid composition of the B875 and B800-850 photosynthetic antenna complexes in *R. sphaeroides* 2.4.1: involvement of spheroidene and spheroidenone in adaptation to changes in light intensity and oxygen availability. *Journal of Bacteriology* **178**, 5877–5883 (1996). URL http://www.ncbi.nlm.nih.gov/pmc/articles/PMC178441/pdf/1785877.pdf.

284. Niederman R.A and Gibson K.D. The photosynthetic bacteria (Clayton R.K. and Sistrom W.R., eds). *Plenum Press, New York* 79–118 (1978).

285. Theiler R. and Niederman R.A. Localization of chromatophore proteins of *R. sphaeroides*. *Journal of Biological Chemistry* **266**, 23157–62 (1991). URL http://www.ncbi.nlm.nih.gov/pubmed/1744115.

286. Sener M.K., Olsen J.D., Hunter C.N. and Schulten K. Atomic-level structural and functional model of a bacterial photosynthetic membrane vesicle. *Proceedings of the National Academy*

of Sciences **104**, 15723–15728 (2007). URL http://www.pnas.org/content/104/40/15723.full.

287. Noble J.M., Lubieniecki J., Plitzko J., Baumeister W., Engelhardt H. and Kourkoutis L.F. Cryo-electron tomography of chromatophore in *R. sphaeroides*. *Microscopy and Microanalysis Meeting* (2015). URL http://conference.microscopy.org/MandM/2015/program/abstracts/PDP_17-147.pdf.

288. Scheuring S., Nevo R., Liu L.-N., Mangenot S., Charuvi D., Boudier T., Prima V., Hubert P., Sturgis J.N. and Reich Z. The architecture of *R. sphaeroides* chromatophores. *Biochimica et Biophysica Acta (BBA) - Bioenergetics* **1837**, 1263–1270 (2014). URL http://www.sciencedirect.com/science/article/pii/S000527281400098X.

289. Thompson S., Wadhams G.H. and Armitage J.P. The positioning of cytoplasmic protein clusters in bacteria. *Proceedings of the National Academy of Sciences* **103**, 8209–8214 (2006). URL http://www.pnas.org/content/103/21/8209?ijkey=9e033f9e3cc8693751efd98209a5a316aaa81752&keytype2=tf_ipsecsha.

290. Wadhams G.H., Martin A.C., Porter S.L., Maddock J.R., Mantotta J.C., King H.M. and Armitage J.P. TlpC, a novel chemotaxis protein in *R. sphaeroides*, localizes to a discrete region in the cytoplasm. *Molecular Microbiology* **46**, 1211–1221 (2002). URL http://onlinelibrary.wiley.com/doi/10.1046/j.1365-2958.2002.03252.x/full.

291. Wadhams G.H., Martin A.C., Warren A.V. and Armitage J.P. Requirements for chemotaxis protein localization in *R. sphaeroides*. *Molecular Microbiology* **58**, 895–902 (2005). URL http://onlinelibrary.wiley.com/doi/10.1111/j.1365-2958.2005.04880.x/full.

292. Tindall M.J., Porter S.L., Maini P.K. and Armitage J.P. Modeling chemotaxis reveals the role of reversed phosphotransfer and a bi-functional kinase-phosphatase. *PLoS Computational Biology* **6**, e1000896 (2010). URL http://www.ncbi.nlm.nih.gov/pubmed/20808885.

293. Li J., Swanson R.V., Simon M.I. and Weis R.M. Response regulators CheB and CheY exhibit competitive binding to the kinase CheA. *Biochemistry* **34**, 14626–14636 (1995). URL http://pubs.acs.org/doi/abs/10.1021/bi00045a003.

294. Hamadeh A., Ingalls B. and Sontag E. Transient dynamic phenotypes as criteria for model discrimination: fold-change detection in *R. sphaeroides* chemotaxis. *Journal of The Royal Society Interface* **10**, 20120935 (2013). URL http://www.ncbi.nlm.nih.gov/pmc/articles/PMC3565743/.

295. Wood T.K., Gonzalez Barrios A.F., Herzberg M. and Lee J. Motility influences biofilm architecture in *Escherichia coli*. *Applied Microbiology and Biotechnology* **72**, 361–7 (2006). URL http://www.ncbi.nlm.nih.gov/pubmed/16397770.

296. Fukuoka H., Sagawa T., Inoue Y., Takahashi H., Ishijima A. Direct imaging of intracellular signaling components that regulate bacterial chemotaxis. *Science Signaling* **7**, ra32 (2014). URL http://stke.sciencemag.org/content/7/319/ra32.